École Doctorale 388

Development of the NCI method: High performance optimization and visualization

THÈSE

présentée et soutenue publiquement le 13 septembre 2016

pour l'obtention du

Doctorat de l'Université Pierre et Marie Curie

par

Roberto A. Boto

Composition du jury

Rapporteurs :	Prof. Frank De Proft
	Prof. Clémence Corminboeuf
Examinateurs :	Dr. Vincent Tognetti
	Prof. Ángel Martín Pendás
Co-encadrants :	Prof. Jean-Philip Piquemal
	Dr. Julien Tierny
Directrice de thèse :	Dr. Julia Contreras-García

Laboratoire de Chimie Théorique – UMR 7616

Mis en page avec la classe thesul.

À mes parents
À mon frère
À Will

Acknowledgements

Les travaux présentés dans cette mémoire ont été réalises au Laboratoire de Chimie le Laboratoire de Chimie Théorique de la Université Pierre et Marie Curie. Je remercie tout d'abord à Olivier Parisel, pour m'avoir accueillie pendant ces trois années et m'avoir procuré des conditions optimales pour réaliser cette thèse.

Je tiens à remercier à mes trois encadrants Julia Contreras García, Jean-Philip Piquemal et Julien Tierny, d'avoir accepté d'entreprendre cette aventure avec moi. Je les remercie sincèrement pour leur confiance et leur patience. Ils ont su m'accompagner aussi bien au niveau scientifique qu'au niveau personnel dans tous les développement de cette thèse en me laissant beaucoup de libertés et en étant toujours disponible pour répondre à mes nombreuses questions.

Un grand merci à tous les membres du Laboratoire de Chimie Théorique pour les moments que nous avons partagés. En particulier je voudrais remercier à Odile, Christophe et Mónica. Odile qui m'a aidé avec tout les démarches et à qui je le souhaite tout le bonheur pour l'avenir. Christophe, grâce à qui je suis capable de m'exprimer en français, malgré tout. Et Mónica qui m'a introduit à la bonne gastronomie asiatique-française.

I would like to thank all the members of my PhD committee Vincent Tognetti and Ángel Martín Pendás, and especially Frank de Proft and Clémence Corminboeuf for accepting to review my work and to attend to my defense.

I would like to thank to Paul Geerlings and Frank de Proft for accepting me in the ALGC group in Brussels. Dank aan alle leden van ALGC voor een fantastische stage. Vooral aan Mercedes, Tatiana, Ann-Sophie, Zino, Thijs en Jan.

No podría terminar sin dar las gracias a todos los miembros del grupo de química cuántica de la Universidad de Oviedo, donde di mis primeros pasos en ese incierto mundo de la mecánica quántica. A ellos les debo mi manera de ver la química cuántica y la ciencia en general.

Esta tesis jamás hubiera visto la luz sin el apoyo de mis amigos y mi familia. Sobre todo gracias a mis padres y a mi hermano, quienes a pesar de la distancia y de mis dificultades para explicarles el contenido de este manuscrito están presentes en cada una de las palabras que él contiene.

Roberto A. Boto

Paris, le 4 juillet de 2016

Preface to the revised version

In the present version I have included all the suggestions and corrected the mistakes highlighted by the reviewers. In addition, the conditions for non-AIM-CPs of the reduced density gradient in Chapter 3 and 4 have been completed, and the list of publications has been updated.

During the revision process, I felt tempted to modify some of the chapters and the overall structure of this manuscript. However, I preferred to conserve the original spirit of the work, and to keep to a minimum any modification.

Roberto A. Boto

Aveiro, 28 June 2018

Contents

Introduction

1

Methods of quantum mechanics

2

Mathematical foundations

3

Quantum chemical topology

4

The NCI method

5

NCIPLOT: A program for plotting and computing properties within non-covalent interaction regions

6

Bonding analysis by means of the NCI method I: Covalent and ionic interactions

7

Bonding analysis by means of the NCI method II: Non-covalent interactions

8

Bonding analysis by means of the NCI method III: Reactivity

9

Conclusions and outlook

List of publications

Introduction

Back in 2010 Erin Johnson and co-workers came up with a new tool for analyzing non-covalent interactions, the NCI method. This tool allows for a fast and visual characterization of chemical interactions. The warm reception of the method by the community was so, that the second article on the NCI method was among the ten most read articles in the *Journal of Chemical Theory and Computation* in 2011. Supporters and detractors of the method grew equally and questions about the theoretical basis of the method and its reliability beyond correlation with "chemical intuition" expectations arose. The present manuscript is aimed at rebutting such criticisms, showing in a comprehensive manner the advantages, limitations and possibilities of the method. I have tried to collect the state of the art of the NCI method, weaving some new thoughts and ideas aiming at further pushing its limits .

Before describing the structure of this manuscript, it is worth to frame the exceptional conditions that enabled the rapid success of the NCI method. The reader may figure out that all this story starts with the chemical bonding and the ever-lasting quest for a definitive consensus on its definition. Contrary to other observables such as energy polarizability, momentum, the chemical bond is not a physical observable, and thus a pure quantum mechanical definition of chemical bonding does not exist. Perhaps because it is a concept and not a property, seeking for their corresponding operator is senseless. I would not like to disappoint the reader so early, but I do not have the answer yet. Other cornerstone ideas in chemistry such as atomic shell, lone pair, (hyper-)conjugation, aromaticity, etc suffer from the same pathology. Nevertheless all of them constitute such a rich set of "fuzzy", yet invaluably set of concepts, that many efforts have been devoted to understand their underlying mechanistic nature.

In face of this quandary, many people follow Coulson's point of view *"Sometimes it seems to me that a bond between two atoms has become so real, so tangible, so friendly, that I can almost see it. Then I awake with a little shock, for a chemical bond is not a real thing. It does not exist. No one has ever seen one. No one ever can. It is a figment of our own imagination"*. In keeping with this comment, chemical bond was compared to a unicorn *"a mythical but useful creature, which brings law [...] in an otherwise chaotic world"*. These "imaginary" and discouraging thinkings trace back to the early observations about the transformation of matter that took place at the dawn of chemistry as a scientific branch. At that time, physics or mathematics were not developed enough to provide a formalism able to account for such observations. The advent of quantum mechanics paved the way for the understanding of such phenomena, a way we are still walking.

Almost 90 years latter of Dirac's utterance *"the underlying physical laws necessary for the mathematical theory of a large part of physics and the whole of chemistry are thus completely known, and the difficulty is only that the exact application of these laws leads to equations much too complicated to be soluble. It therefore becomes desirable that* *approximate practical methods of applying quantum mechanics should be developed, which can lead to an explanation of the main feature of complex atomic systems without to much computation.”*, we haven’t overcome the mathematical difficulties encountered in solving the Schrödinger equation for molecular systems. Even for the most “simple” chemical bond, covalent bonding, there is even controversy on its its mechanistic origin. This situation has been clearly stated in the very recent paper entitled “The Nature of the Fourth Bond in the Ground State of C_2: The Quadruple Bond Conundrum” by Danovich *et al* [1].

In trying to overcome this dichotomy, it is worth to focus on simpler objects than the wave function as uttered by Coulson *“in recognizing the bond as a figment of our imagination [but that it is] worthwhile to adopt pragmatic schemes for getting molecular structure out of wave functions whenever possible”*. Hohenberg and Kohn were apparently the first to reckon the importance of the electron density, setting the basis of the density functional theory. The electron density is the starting point of the topological approaches, which ascribe chemical concepts to the topological features of some scalar field defined from the electron density or reduced density matrices in general.

Topological approaches or real space approaches offer a series of advantages over other traditional ones widely used to understand molecular structure such as molecular orbital theory. First, they are independent on the route taken for computing the wave function, that is the theory level. Secondly, they are orbital invariant, and finally, they are defined in real space, where chemical concepts have been historically set. In this regard, they enable the visualization of these “pieces of our imagination” and their connection with quantum mechanical objects.

However, a mismatching between the solution provided by these topological approaches and the traditional chemical wisdom is very often found. This is the case for instance of non- covalent interactions (NCI). The lacking of chemical bonding definition hampers the design of suitable indicators able to properly characterize all interaction types, while matching “chemical intuition”. One may thing that using “chemical intuition” and not physics as guideline may hamper the discovering of new insight into the nature chemical matter. For the moment, we will consider this “inherited knowledge” as correct.

The NCI method presents a compromise solution for characterizing different interaction types no matter their strength. We shall not attempt to summarize all the literature on the NCI method, but to present in a comprehensive manner the theory and applications of the method along four chapters divided into three blocks: theory (Chapter 4), implementation (Chapter 5) and application (Chapters 6 to 8), thus yielding a comprehensive view of the the NCI method within the fields of theoretical and computational chemistry.

Chapter 1

The first chapter is a brief summary of the main methods used for computing the electron density. It is oriented to readers unfamiliar with quantum chemistry. We will specially focus on those methods more used all along the manuscript, albeit CCSD and solid state calculations are performed in Chapters 5 and 7 respectively, they are not presented here since they remain punctual. The reader is directed to textbooks like *Modern Quantum Chemistry: Introduction to Advanced Electronic Structure Theory* by Atila Szabo and Neil S. Ostlund, *Molecular Electronic-Structure Theory* by Trygve Helgaker, Poul Jorgensen and Jeppe Olsen, *Density-Functional Theory of Atoms and Molecules* by Robert G. Parr and Weitao Yang and *A Chemist’s Guide to Density Functional Theory* by Wolfram Koch and Max C. Holthausen for a complete compilation of methods in a rather educational framework.

Chapter 2

Throughout this manuscript chemical bonding is mainly analyzed by topological approaches. Thus, we considered adequate to collect in a stand alone chapter the most relevant topological aspects of the analysis of chemical bonding. Additionally, we present some notions and algorithms commonly used in the visualization community. For further reading we recommend the book *Computational Topology: An Introduction* by Herbert Edelsbrunner and John L. Harer.

Chapter 3

Chapter 3 is devoted to introducing topological approaches and emphasizing quantum chemical topology. This part will set the basis for the rest of the manuscript. In the zoo of functions encompassed under the umbrella of quantum chemical topology, I have tried to focus on those more related to the NCI method. The number of textbook that collects all topological approaches is quite limited so far. For the interested readers I recommend *Atoms in Molecules, A Quantum Theory* by Richard F. W. Bader and *Applications of Topological Methods in Molecular Chemistry* by R. Chauvin, C. Lepetit, B. Silvi and E. Alikhani.

Chapter 4

This chapter is entirely devoted to the NCI method; theoretical basis and *modus operandi*. In the first part we connect the theoretical grounds of the method with some of the concepts introduced in Chapter 3. Then some examples of its application to the analysis of non-covalent interactions are presented.

Chapter 5

All the NCI calculations herein presented were performed with the NCIPLOT code. This chapter intends to summarize the technical aspects of the code and its possibilities in a tutorial-like manner. Additionally, the method is tested on a list of a benchmark calculations in order to disclose its dependency with the method and basis used to compute the electron density.

Chapter 6

Three chapters are devoted to apply the NCI method to the analysis of different bonding patterns. Covalent, ionic and charge-shift bonding constitute the scope of the Chapter 6.

Chapter 7

The NCI method is applied to the analysis of non-conventional weak bonding patterns in Chapter 7. This chapter is divided in two sections. First, quantitative NCI analyses are performed on non-covalent directional interactions: pnictogen, halogen and weak-hydrogen bonding. Then, bonding in complex systems as self-assembly monolayers and metallocenes is explored. All the results obtained in this chapter are eventually collected in form of answer to a semantic question related to the nomenclature of chemical interactions.

Chapter 8

Chemical reactions are characterized by the interplay of chemical interactions of different strengths. This chapter is devoted to chemical reactivity. The NCI method is applied to understand the outcome of some prototype chemical reactions in terms of the role of non-covalent interactions in the transition state.

Chapter 1

Methods of quantum mechanics

Sommaire

Any problem concerning the electronic structure of matter is covered by the Schrödinger equation [2]

$$i\hbar\frac{\partial\Psi(\mathbf{x},t)}{\partial t}=\widehat{H}\Psi(\mathbf{x},t), \tag{1.1}$$

where $\widehat{H}$ is the Hamiltonian operator, $\Psi(\mathbf{x},t)$ is the wave function of a N particle system, $\mathbf{x}=\{\mathbf{x}_1,\ \mathbf{x}_2,...,\mathbf{x}_N\}$ stands for the collection of all space-spin coordinates needed to describe each of the N particles and t for the time. For conservative or stationary systems, where the potential energy part of the Hamiltonian is not a function of time, a possible solution of Equation 1.1 is

$$\Psi(\mathbf{x},t)=\psi(\mathbf{x},t)e^{-iEt/\hbar}, \tag{1.2}$$

where E is the energy of the system. Inserting this factorized form of the wave function in 1.1, leads to a time-independent equation

$$\hat{H}\psi(\mathbf{x})=E\psi(\mathbf{x}). \tag{1.3}$$

Equation 1.3 is the so-called time-independent Schrödinger equation.

1.1 Born-Oppenheimer approximation

In the non-relativistic approach, the Hamiltonian operator of a system formed by N electrons moving around M nuclei, considering all the terms in atomic units, is given by

$$\widehat{H}=-\frac{1}{2}\sum_{A=1}^{M}\frac{\nabla_A^2}{M_A}-\frac{1}{2}\sum_{i}^{N}\nabla_i^2+\sum_{i>j}\frac{1}{r_{ij}}-\sum_{A,i}\frac{Z_A}{|r_i-R_A|}+\sum_{A>B}\frac{Z_AZ_B}{|R_A-R_B|}, \tag{1.4}$$

where the indexes A,B and i,j designate nuclei and electrons, respectively, M_A is the mass of atom A, Z_A, Z_B are the nuclear charges of atoms A and B respectively, and ∇_i^2 ,∇_A^2 are the electron and nuclear Laplacian operators, respectively. The Hamiltonian of Equation 1.4 is composed of five terms: the two first terms are the electronic and the nuclear kinetic energy respectively, and the remaining three terms are the electron-electron, nucleus-electron and nucleus-nucleus Coulomb interactions respectively. These five contributions may be grouped in electronic $\widehat{H}_{el}$, nuclear $\widehat{H}_{nuc}$, and nucleus-electron $\widehat{H}_{el-nuc}$ terms:

$$\widehat{H}=\underbrace{-\frac{1}{2}\sum_{A=1}^{M}\frac{\nabla_A^2}{M_A}+\sum_{A>B}\frac{Z_AZ_B}{|R_A-R_B|}}_{\widehat{H}_{nuc}}\underbrace{-\frac{1}{2}\sum_{i}^{N}\nabla_i^2+\sum_{i>j}\frac{1}{r_{ij}}}_{\widehat{H}_{el}}\underbrace{-\sum_{A,i}\frac{Z_A}{|r_i-R_A|}}_{\widehat{H}_{el-nuc}}, \tag{1.5}$$

The corresponding wave function must contain both, nuclear and electronic coordinates. The Hamiltonian of Equation 1.4 may be simplified if we notice the huge difference in the mass of electrons and nuclei (a factor of 10^3-10^5). The nuclei are much heavier and consequently they move considerably slower than electrons. Under this consideration nuclear kinetic energies may be neglected and the nuclear electrostatic interaction may be considered as constant. Then the whole term $\widehat{H}_{nuc}$ becomes constant. This approximation is known as the Born-Oppenheimer approximation and its main consequence is the decoupling of the electron and the nuclear motion, in such a way that the total wave function may be factorized in an electronic and nuclear part

$$\Psi(\mathbf{x},\mathbf{R}) = \Psi_{el}(\mathbf{x};\mathbf{R})\Psi_{nuc}(\mathbf{R}), \tag{1.6}$$

The electronic wave function $\Psi_{el}(\mathbf{x};\mathbf{R})$ describes the motion of electrons at a fixed position of nuclei. It depends on the electronic coordinates and parametrically of the nuclear coordinates $\mathbf{R}$. Under the Born-Oppenheimer approximation the electronic problem may be set as

$$\Big(\widehat{H}_{el} + \widehat{H}_{el-nuc}\Big)\Psi_{el}(\mathbf{x};\mathbf{R}) = E_{el}\Psi_{el}(\mathbf{x};\mathbf{R}), \tag{1.7}$$

where E_{el} is the electronic energy. The total energy is defined as the addition of E_{el} and the nuclear electrostatic interaction

$$E(\mathbf{R}) = E_{el} + \sum_{A>B}\frac{Z_A Z_B}{|R_A - R_B|}. \tag{1.8}$$

The nuclear wave function $\Psi_{nuc}(\mathbf{R})$ is the solution of the corresponding nuclear Schrödinger equation

$$\Big(-\frac{1}{2}\sum_{A=1}^{M}\frac{\nabla_A^2}{M_A} + E(\mathbf{R})\Big)\Psi_{nuc}(\mathbf{R}) = E_{nuc}\Psi_{nuc}(\mathbf{R}). \tag{1.9}$$

In what follows, we will focus on how to solve the electronic problem, posed by Equation 1.7. On referring to $\widehat{H}_{elec}$, Ψ_{elec} and E_{elec} we will drop the subscript.

1.1.1 Electron spin

The electron wave function obtained by solving Equation 1.7 depends on spin-space coordinates $\mathbf{x}$ and parametrically on the nuclear arrangement $\mathbf{R}$. To completely describe an electron it is necessary to specify not only its spatial coordinates $\mathbf{r}$, but also an intrinsic angular momentum called spin. Electrons are known to have a value of the spin quantum number equal to $\frac{1}{2}\hbar$, whose z component may take two possible values $+\frac{1}{2}\hbar$ and -$\frac{1}{2}\hbar$. Under the non-relativistic model, the spin coordinates (σ) are included on the wave function by two spin functions $\alpha(\sigma)$ and $\beta(\sigma)$, corresponding to eigenvalues of the z component of the spin operator equal to $+\frac{1}{2}\hbar$ and -$\frac{1}{2}\hbar$ respectively. These two spin functions are orthonormal,

$$\int \alpha^*(\sigma)\alpha(\sigma)d\sigma = \int \beta^*(\sigma)\beta(\sigma)d\sigma = 1, \tag{1.10}$$

$$\int \alpha^*(\sigma)\beta(\sigma)d\sigma = \int \beta^*(\sigma)\alpha(\sigma)d\sigma = 0. \tag{1.11}$$

The electronic generic coordinates $\mathbf{x}$ may be defined as the composition of spatial $\mathbf{r}$=$\{x,y,z\}$ and spin cordinates (σ), and they are called spatial-spin coordinates $\mathbf{x}$=$\{\mathbf{r},\sigma\}$.

1.1.2 Spin orbitals

Strictly speaking an orbital is the solutions of Equation 1.3 for the hydrogen atom (or any hydrogen-like ion). From here on we shall refer to orbital as a one-electron wave function. For an atom, one has atomic orbitals and for molecules, molecular orbitals. As it has been already said, an electron is characterized by its spatial and spin coordinates, and in the non-relativisitc approach spatial-spin coordinates are defined as composition of both. Similarly, we may define spatial and spin orbitals. A spatial orbital $\psi_i(\mathbf{r})$ is a function of the position vector $\mathbf{r}$ and describes the spatial distribution of the *i-th* electron, such that $|\psi_i(\mathbf{r})|^2 d\mathbf{r}$ is the probability of finding the electron i in the small volume element $d\mathbf{r}$ surrounding the position $\mathbf{r}$, Similar to spin function $\alpha(\sigma)$ and $\beta(\sigma)$, spatial orbitals are assumed to form an orthonormal set:

$$\int \psi_i^*(\mathbf{r})\psi_j(\mathbf{r})dr \quad = \quad \delta_{ij}, \tag{1.12}$$

where δ_{ij} is Dirac's delta. If the spin part is added, we can define a spin orbital $\phi_i(\mathbf{x})$ as a one electron wave function that describes both space and spin coordinates. In the non-relativistic approach a spin-orbital may be defined as the direct product of a spatial orbital and a spin function.

$$\begin{aligned} \phi_i^\alpha(\mathbf{x}) &= \psi_i(\mathbf{r})\alpha(\sigma), \\ \phi_i^\beta(\mathbf{x}) &= \psi_i(\mathbf{r})\beta(\sigma). \end{aligned} \tag{1.13}$$

Since both spatial orbitals and spin function form orthonormal sets, spin orbitals are therefore orthonormal

$$\int \phi_i^*(\mathbf{x})\phi_j(\mathbf{x})d\mathbf{x} = \delta_{ij}. \tag{1.14}$$

In what follows, we will refer to spatial orbitals as orbitals and will reserve the term spin orbital when spin functions are added.

1.1.3 The symmetry of the wave function

The fact that electrons are identical particles must be reflected on the wave function. Suppose a two electron system at spin space coordinates $\mathbf{x}_1$ and $\mathbf{x}_2$ and with wave function $\Psi(\mathbf{x}_1, \mathbf{x}_2)$. The probability of finding both electrons simultaneously in volume elements $d\mathbf{x}_1$ and $d\mathbf{x}_2$ around points $\mathbf{x}_1$ and $\mathbf{x}_2$ is given by $|\Psi(\mathbf{x_1}, \mathbf{x_2})|^2 d\mathbf{x}_1 d\mathbf{x}_2$. If the two particles are interchanged, the corresponding probability $|\Psi(\mathbf{x}_2, \mathbf{x}_1)|^2 d\mathbf{x}_1 d\mathbf{x}_2$ should be the same, since electrons are indistinguishable particles,

$$|\Psi(\mathbf{x}_1, \mathbf{x}_2)|^2 = |\Psi(\mathbf{x}_2, \mathbf{x}_1)|^2. \tag{1.15}$$

This property is satisfied only if the wave function is either symmetric or antisymmetric with respect to the interchange of the coordinates of both electrons

$$\begin{aligned} \Psi(\mathbf{x}_1, \mathbf{x}_2) &= \Psi(\mathbf{x}_2, \mathbf{x}_1) \text{ (symmetric)}, \\ \Psi(\mathbf{x}_1, \mathbf{x}_2) &= -\Psi(\mathbf{x}_2, \mathbf{x}_1) \text{ (antisymmetric)}. \end{aligned} \tag{1.16}$$

Pauli's exclusion principle imposes wave function the antisymmetric choice. Such conclusion may be generalized to many electron case resulting in the antisymmetry principle:

Antisymmetry Principle *The wave function $\Psi(\boldsymbol{x}_1, \boldsymbol{x}_2, ..., \boldsymbol{x}_N)$ describing any state of an N-electron system is antisymmetric under any permutation of any two electrons:*

$$\widehat{P}\Psi(\boldsymbol{x}_1, \boldsymbol{x}_2, ..., \boldsymbol{x}_N) = (-1)^p \Psi(\boldsymbol{x}_1, \boldsymbol{x}_2, ..., \boldsymbol{x}_N)$$

where $\widehat{P}$ is a permutation operator and p is the number of permuted electron pairs.

1.1.4 The independent particle model

A first approach to solve Equation 1.7 consists of neglecting the electron-electron interaction term $\sum_{i>j} \frac{1}{r_{ij}}$. Let us consider electrons as non-interacting particles moving in a nuclear potential. This model is known as independent particle model (IPM). Under this approximation the electronic Hamiltonian may be written as a sum of one-electron Hamiltonians $\widehat{h}_i$

$$\begin{aligned} \widehat{H} &= \sum_{i=1}^{N} \widehat{h}_i, \\ \widehat{h}_i &= -\frac{1}{2}\nabla_i^2 - \sum_{A=1}^{M} \frac{Z_A}{|r_i - R_A|}. \end{aligned} \quad (1.17)$$

The wave function provided by this model is nothing but the product of spin orbitals, known as the Hartree product (HP)

$$\Psi_{HP}(\mathbf{x}_1, \mathbf{x}_2, ..., \mathbf{x}_N) = \phi_1(\mathbf{x}_1)\phi_2(\mathbf{x}_2)...\phi_N(\mathbf{x}_N), \quad (1.18)$$

and the electronic energy is given by the action of $\widehat{H}$ on Ψ_{HP}

$$\begin{aligned} E &= \langle \Psi_{HP} | \widehat{H} | \Psi_{HP} \rangle, \quad (1.19) \\ &= \sum_{i=1}^{N} \langle \Psi_{HP} | \widehat{h}_i | \Psi_{HP} \rangle, \\ &= \sum_{i}^{N} \epsilon_i, \end{aligned}$$

where ϵ_i is the eigenvalue of $\widehat{h}_i$,

$$\widehat{h}_i \phi_i(\mathbf{x}_i) = \epsilon_i \phi_i(\mathbf{x}_i). \quad (1.20)$$

The HP possesses a fundamental deficiency: it does not follow the antisymmetry principle because

$$\begin{aligned} |\Psi(\mathbf{x}_1, \mathbf{x}_2, ..., \mathbf{x}_N)|^2 d\mathbf{x}_1 d\mathbf{x}_2 ... d\mathbf{x}_N &= \quad (1.21) \\ |\phi_1(\mathbf{x}_1)|^2 d\mathbf{x}_1 |\phi_2(\mathbf{x}_2)|^2 d\mathbf{x}_2 .. |\phi_N(\mathbf{x}_N)|^2 d\mathbf{x}_N, \end{aligned}$$

which states that the simultaneous probability of finding electron 1 in the volume $d\mathbf{x}_1$, centered at $\mathbf{x}_1$, electron 2 in $d\mathbf{x}_2$ centered at $\mathbf{x}_2$, etc, is equal to the probability of finding electron 1 in $d\mathbf{x}_1$ times the probability that electron 2 in $d\mathbf{x}_2$ and so on. This statement does not take account of electron indistinguishability, but differentiates between electron 1 occupying spin orbital ϕ_1, electron 2 in spin orbital ϕ_2, and so on. Contrary to what is imposed by the antisymmetry principles, the HP does distinguish between identical particles.

We can construct a correct wave function by linear combination of HPs. Lets consider a two electron case with spin orbitals ϕ_i and ϕ_j. It is possible to construct two HPs, Ψ_{12}^{HP} with electron one in ϕ_i and electron two in ϕ_j, and the opposite distribution Ψ_{21}^{HP} with electron one in ϕ_j and electron two in ϕ_i

$$\begin{aligned}\Psi_{12}^{HP}(\mathbf{x}_1,\mathbf{x}_2) &= \phi_i(\mathbf{x}_1)\phi_j(\mathbf{x}_2), &(1.22)\\ \Psi_{21}^{HP}(\mathbf{x}_1,\mathbf{x}_2) &= \phi_i(\mathbf{x}_2)\phi_j(\mathbf{x}_1). &(1.23)\end{aligned}$$

Taking an appropriate linear combination of Ψ_{12}^{HP} and Ψ_{21}^{HP} we can obtain a correct antisymmetrized wave function

$$\begin{aligned}\Psi(\mathbf{x}_1,\mathbf{x}_2) &= \frac{1}{\sqrt{2}}\Big(\Psi_{12}^{HP}(\mathbf{x}_1,\mathbf{x}_2) - \Psi_{21}^{HP}(\mathbf{x}_1,\mathbf{x}_2)\Big), &(1.24)\\ &= \frac{1}{\sqrt{2}}|\phi_i(\mathbf{x}_1)\phi_j(\mathbf{x}_2) - \phi_i(\mathbf{x}_2)\phi_j(\mathbf{x}_1)|, &(1.25)\\ &= \frac{1}{\sqrt{2}}\begin{vmatrix}\phi_i(\mathbf{x}_1) & \phi_j(\mathbf{x}_1)\\ \phi_i(\mathbf{x}_2) & \phi_j(\mathbf{x}_2)\end{vmatrix}, &(1.26)\end{aligned}$$

where $1/\sqrt{2}$ is a normalization factor. This determinantal form of the wave function is known as Slater determinant. For an N-electron system it reads as

$$\Psi = \frac{1}{\sqrt{N!}}\begin{vmatrix}\phi_1(\mathbf{x}_1) & \phi_2(\mathbf{x}_1) & \dots & \phi_N(\mathbf{x}_1)\\ \phi_1(\mathbf{x}_2) & \phi_2(\mathbf{x}_2) & \dots & \phi_N(\mathbf{x}_2)\\ \vdots & \vdots & \ddots & \vdots\\ \phi_1(\mathbf{x}_N) & \phi_2(\mathbf{x}_N) & \dots & \phi_N(\mathbf{x}_N)\end{vmatrix}. \tag{1.27}$$

Slater determinants satisfy the antisymmetry principle: if two rows or two columns are swapped, $\Psi(\mathbf{x}_1,\mathbf{x}_2,\dots,\mathbf{x}_i,\mathbf{x}_j,\dots,\mathbf{x}_n) = -\Psi(\mathbf{x}_1,\mathbf{x}_2,\dots,\mathbf{x}_j,\mathbf{x}_i,\dots,\mathbf{x}_n)$. By extension the Pauli exclusion principle is also satisfied, i.e two identical fermions cannot be found in the same quantum state. If $\phi_i = \phi_j$, two rows are identical and therefore, $\Psi = 0$. Slater determinants are often called in terms of the N occupied spin orbital $\phi_i, \phi_j, \phi_k, \dots, \phi_N$, we note $\Psi(\mathbf{x}_1,\mathbf{x}_2,\dots,\mathbf{x}_N) = |\dots i \dots k \dots\rangle$.

In contrast to the HP, which is a truly independent-electron wave function, a Slater determinant correlates same spin electrons through Pauli exclusion principle, this is known as exchange or Fermi correlation. Since different spin electrons remain uncorrelated, a single determinantal wave function is referred as uncorrelated wave function, although Fermi correlation is included.

1.2 The Hartree-Fock approximation

The Hartree-Fock (HF) method is the next step to solve Equation 1.7. The HF approximation is a single determinantal theory which searches variationally for the set of orthonormalized spin orbitals such that, the single determinant formed by them minimizes the electronic energy of the system. The HF hamiltonian for a many electron system adds electron-electron interaction to the IPM hamiltonian

$$\widehat{H} = \sum_i^N \widehat{h}_i + \sum_{j\neq i}^N \widehat{v}_{ij}, \tag{1.28}$$

where $\widehat{h}_i$ is the one-electron operator introduce in IPM and $\widehat{v}_{ij}$ is a two-electron operator which represents the Coulomb electron-electron interaction, and is given by

$$\widehat{v}_{ij} = \frac{1}{|\mathbf{r}_i - \mathbf{r}_j|} = \frac{1}{r_{ij}}. \tag{1.29}$$

The expectation value of the HF energy E_{HF} is given by inserting the HF wave function Ψ_{HF} in Equation 1.28

$$E_{HF} = \langle \Psi_{HF} | \hat{H} | \Psi_{HF} \rangle = \sum_i^N h_i + \frac{1}{2} \sum_i^N \sum_j^N (J_{ij} - K_{ij}), \tag{1.30}$$

where

$$h_i = \int \phi_i^*(\mathbf{x}) \left[-\frac{1}{2} \nabla_i^2 - \sum_{A=1}^M \frac{Z_A}{|r_i - R_A|} \right] \phi_i(\mathbf{x}) d\mathbf{x}, \tag{1.31}$$

is the average kinetic energy and potential energy for the electrostatic attraction between the nuclei and the electron described by ϕ_i, and they define a core hamiltonian operator $\widehat{h}_i$. The integrals J_{ij} and K_{ij} are two electron integrals called Coulomb and exchange integrals respectively,

$$J_{ij} = \int \int \phi_i(\mathbf{x}_1) \phi_i^*(\mathbf{x}_1) \frac{1}{r_{12}} \phi_j(\mathbf{x}_2) \phi_j^*(\mathbf{x}_2) d\mathbf{x}_1 d\mathbf{x}_2, \tag{1.32}$$

$$K_{ij} = \int \int \phi_i(\mathbf{x}_1) \phi_i^*(\mathbf{x}_2) \frac{1}{r_{12}} \phi_j(\mathbf{x}_2) \phi_j^*(\mathbf{x}_1) d\mathbf{x}_1 d\mathbf{x}_2. \tag{1.33}$$

J_{ij} may be understood as the Coulomb interaction between electron i in ϕ_i and an average local potential given by

$$j_k(\mathbf{x}_1) = \int [\phi_k^*(\mathbf{x}_2) \frac{1}{r_{12}} \phi_k(\mathbf{x}_2)] d\mathbf{x}_2. \tag{1.34}$$

Following this interpretation we may define a Coulomb operator acting on $\phi_i(\mathbf{x}_1)$

$$\hat{j}_k(\mathbf{x}_1) \phi_i(\mathbf{x}_1) = \int [\phi_k^*(\mathbf{x}_2) \frac{1}{r_{12}} \phi_k(\mathbf{x}_2)] d\mathbf{x}_2 \phi_i(\mathbf{x}_1). \tag{1.35}$$

The exchange term arises from the antisymmetric nature of the wave function and contrary to j_{ij}, it does not have a simple classical interpretation. Similarly to the Coulomb operator, we may define a exchange operator $\widehat{k}_j(\mathbf{x}_1)$, by its action on a spin orbital ϕ_i

$$\hat{k}_j(\mathbf{x}_1) \phi_i(\mathbf{x}_1) = \int [\phi_j^*(\mathbf{x}_2) \frac{1}{r_{12}} \phi_i(\mathbf{x}_2)] d\mathbf{x}_2 \phi_j(\mathbf{x}_1). \tag{1.36}$$

Whereas the Coulomb operator is nothing but a local operator, the exchange operator is a non-local operator, in the sense that there does not exist a unique multiplicative operator uniquely defined at a position $\mathbf{x}_1$. From $\widehat{h}$, $\hat{k}$ and $\hat{j}$, we define the Fock operator $\widehat{F}_i$ as

$$\widehat{F}_i = \widehat{h}_i + \sum_{j \neq i}^N \hat{j}_j - \hat{k}_j. \tag{1.37}$$

Since $\widehat{F}$ is identical for all electrons we drop the subindex i, $\widehat{F}_i = \widehat{F}$. In the following section, we shall see that $\widehat{F}$ arises in a natural way in the derivation of the HF equations. It is important to notice the key difference between the HF Hamiltonian

(Equation 1.28) and the Fock operator (Equation 1.37). The former returns the energy of the many-electron system, the latter is nothing but the sum of one-electron operators whose eigenvectors are the set of spin orbitals from which the HF wave function is constructed.

1.2.1 Hartree-Fock equations

As aforementioned, the HF method target is the set of spin orbitals that minimize E_{HF} under the orthonormalization condition $\langle \phi_i | \phi_j \rangle = \delta_{ij}$. We may face the problem using Lagrange multipliers. We consider therefore the Lagrangian

$$\mathcal{L}_{HF} = E_{HF} - \sum_{ij}^{N} \lambda_{ij} (\langle \phi_i | \phi_j \rangle - \delta_{ij}), \tag{1.38}$$

where λ_{ij} are the Langrange multipliers. $\mathcal{L}_{HF}$ is stationary with respect to small changes in spin orbitals

$$\delta\mathcal{L}_{HF} = \delta E_{HF} - \sum_{ij}^{N} \lambda_{ij} (\langle \delta\phi_i | \phi_j \rangle - \langle \phi_i | \delta\phi_j \rangle) = 0. \tag{1.39}$$

We may express this equation in terms of the Fock operator

$$\delta E_{HF} = \sum_{i}^{N} (\langle \delta\phi_i | \widehat{F}_i | \phi_i \rangle - \langle \phi_i | \widehat{F}_i | \delta\phi_i \rangle). \tag{1.40}$$

Equation 1.40 leads to

$$\delta\mathcal{L}_{HF} = \sum_{i}^{N} \langle \delta\phi_i | \big[\widehat{F} | \phi_i \rangle - \sum_{i}^{N} \lambda_{ij} | \phi_j \rangle \big] + c.c. = 0, \tag{1.41}$$

where *c.c.* denotes the complex conjugate. Since $\delta\phi_i$ is arbitrary, the term in the squared bracket should be zero for all i. Therefore,

$$\widehat{F} | \phi_i \rangle = \sum_{j}^{N} \lambda_{ij} | \phi_j \rangle. \tag{1.42}$$

Since $\widehat{F}$ is an hermitian operator, the matrix form by Langrange multipliers λ_{ij} is also hermitian and therefore, it can be diagonalized by a unitary transformation $\mathbf{U}$

$$\mathbf{U}^{\dagger} \lambda \mathbf{U} = \lambda^{'} = \begin{cases} \lambda^{'}_{ij} = 0, \\ \lambda^{'}_{ii} = \epsilon_i. \end{cases} \tag{1.43}$$

Applying the same unitary transformation to spin orbital ϕ_i, we transform the above equation into a diagonal form leading to the canonical Hartree-Fock equations

$$\widehat{F} | \phi_i \rangle = \epsilon_i | \phi_i \rangle. \tag{1.44}$$

The corresponding spin orbitals are the canonical Hartree-Fock spin orbitals and the eigenvalues ϵ_i are known as orbital energies. Under the canonical formulation, we note that the HF method is an independent-particle model, in the sense that each spin orbital is an eigenfunction of an effective one-electron operator, the Fock operator $\hat{F}$.

The electron-electron interaction is only taken into account in an averaged form; each electron does not feel the instantaneous field generated by the remaining $N-1$ electrons of the system, but an average field given by the Coulomb and exchange operators.

The Hartree-Fock energy may be recovered from the orbital energies as

$$E_{HF} = \sum_{i}^{N} \epsilon_i - \frac{1}{2}\sum_{i,j}^{N} J_{ij} - K_{ij}. \tag{1.45}$$

The second term discounts the electronic repulsion energy that is counted twice in $\sum_i \epsilon_i$.

Although canonical HF equations are written as linear eigenvalue equations, they are non-linear equations, since the Fock operator depends on the spin orbital ϕ_i through the Coulomb and exchange operators. Hence they must be solved by an iterative procedure.

1.2.2 Restricted and unrestricted Hartree-Fock

The above Hartree-Fock equations have been presented for a general set of spin orbitals $\{\phi_i\}$. As discussed in section 1.1.2, a spin orbital herein considered is defined as the product of an orbital ϕ_i and a $\alpha(\sigma)$ or $\beta(\sigma)$ spin function. In the general case the spatial parts of both α and β spin orbitals are different, leading to the unrestricted Hartree- Fock formalism (UHF). By contrast, if the spatial parts are forced to be identical it leads to the restricted Hartree-Fock formalism (RHF). Being the spin functions already defined, we may rewrite Equation 1.44 in terms of the orbitals

$$\widehat{F}^{\alpha}\psi_i^{\alpha}(\mathbf{r}) = \epsilon_i^{\alpha}\psi_i^{\alpha}(\mathbf{r}), \tag{1.46}$$

$$\widehat{F}^{\beta}\psi_i^{\beta}(\mathbf{r}) = \epsilon_i^{\beta}\psi_i^{\beta}(\mathbf{r}). \tag{1.47}$$

These two set of equations depend on the formalism we are working in. In the UHF case both equations are coupled since $\widehat{F}^{\alpha}$ acts over α and β orbitals

$$\widehat{F}^{\alpha} = \widehat{h}_i^{\alpha} + \sum_{j\neq i}^{N_\alpha}(\hat{j}_j^{\alpha} - \hat{k}_j^{\alpha}) + \sum_{j\neq i}^{N_\beta}\hat{j}_j^{\beta}, \tag{1.48}$$

where $\widehat{h}_i^{\alpha}$, $\widehat{j}_{ij}^{\alpha}$ and $\widehat{k}_{ij}^{\alpha}$ act over N_α orbitals, ψ_i^{α}, occupied by α electrons. The additional term $\widehat{j}_{ij}^{\beta}$ acts over $N_\beta = N - N_\alpha$ orbitals occupied by β electrons. An equivalent equation may be written for $\widehat{F}^{\beta}$. The last Coulomb term in Equation 1.48 prevents solving it independently, since $\widehat{F}^{\alpha}$ depends on the occupied β functions, ψ_i^{β}, and $\widehat{F}^{\alpha}$ depends on the occupied α functions, ψ_i^{α}. Therefore, the two equations must be solved simultaneously.

The RHF formalism is only applicable if the electronic state under consideration has an even number of electrons N, such that there are $N/2$ doubly occupied orbitals, $\{\phi_i\}$. Since α and β orbitals are restricted to be identical $\psi_i^{\alpha}(\mathbf{r}) = \psi_i^{\beta}(\mathbf{r}) = \psi_i(\mathbf{r})$, and the number of occupied α and β orbitals are identical and equal to $N/2$, Equation 1.48 becomes

$$\widehat{F}_i\psi_i(\mathbf{r}) = \epsilon_i\psi_i(\mathbf{r}), \tag{1.49}$$

where

$$\widehat{F}_i = \widehat{h}_i + \sum_{j\neq i}^{N/2}(2\hat{j}_j - \hat{k}_j). \tag{1.50}$$

The core hamiltonian operator $\widehat{h}_i$ is independent of the spin, thus it is the same in the UHF and in the RHF formalism. Since α and β spin orbitals have the same spatial form in the restricted formalism, Equation 1.44 is the same for both α and β spin orbitals. By contrast,the UHF formalism is more involved, although it may be applied to describe either open or closed shell electronic states.

1.2.3 Roothaan equations

Hartree-Fock Equation 1.44 is in general too complicated to be solved numerically. In 1950's Roothaan showed how, by using a basis sets expansion approach, the HF integro-differential equations may be converted to an algebraic set of equations and solved by standard matrix techniques. The generalization of this method to deal with the UHF equations 1.46 and 1.47 was given by Pople and Nesbet, and we do not describe it in this manuscript. In the Roothaan method each spatial function, ψ_i, is expanded in a linear expansion of N_{basis} known spatial functions χ_ν

$$\psi_i = \sum_{\nu}^{N_{basis}} C_{\nu i}\chi_\nu(\mathbf{r}). \tag{1.51}$$

The functions $\chi_\nu(\mathbf{r})$ are usually atomic orbitals, this approach is thus known as linear combination of atomic orbitals method (LCAO). If the set $\{\chi_\nu\}$ were complete, expansion 1.51 would be exact. In practice, we are limited to a finite set of N_{basis} functions, and the orbitals $\{\psi_i\}$ are thus approximated solutions of the HF equations. N_{basis} should be at least as large as the number of spin orbitals $N_{basis} = N$. In practice as N_{basis} increases, the closer to the completeness the basis set is, so in most cases $N_{basis} > N$. Inserting the expansion 1.51 into Equation 1.44 and multiplying by $\langle\chi_\nu|$ we obtain

$$\sum_{\nu}^{N_{basis}} C_{\nu i}\langle\chi_\mu|\widehat{F}|\chi_\nu\rangle = \epsilon_i \sum_{\nu}^{N_{basis}} C_{\nu i}\langle\chi_\mu|\chi_\nu\rangle. \tag{1.52}$$

We now define the overlap matrix $\mathbf{S}$ with elements

$$S_{\mu\nu} = \langle\chi_\mu|\chi_\nu\rangle, \tag{1.53}$$

and the Fock matrix with elements

$$F_{\mu\nu} = \langle\chi_\mu|\widehat{F}|\chi_\nu\rangle. \tag{1.54}$$

Equation 1.44 may now be rewritten as

$$\sum_{\nu}^{N_{basis}} F_{\mu\nu}C_{\nu i} = \epsilon_i \sum_{\nu}^{N_{basis}} S_{\mu\nu}C_{\nu i}. \tag{1.55}$$

These are the so-called Roothaan equations, that can be written more compactly as

$$\mathbf{FC} = \mathbf{SC}\epsilon, \tag{1.56}$$

where $\mathbf{C}$ is the matrix of expansion coefficients $C_{\nu i}$ and ϵ is a diagonal matrix of orbital energies ϵ_i. So far we have replaced the integro-differential Equation 1.44 by matrix Equation 1.56. To obtain the matrices $\mathbf{C}$ and ϵ, we need an explicit expression for the Fock matrix elements, $F_{\mu\nu}$

$$F_{\mu\nu} = H_{\mu\nu}^{core} + \sum_{\sigma\lambda} P_{\sigma\lambda}[\langle\mu\lambda|\nu\sigma\rangle - \frac{1}{2}\langle\mu\lambda|\sigma\nu\rangle], \tag{1.57}$$

where we have introduced a core Hamiltonian matrix

$$H_{\mu\nu}^{core} = \langle\mu|\widehat{h}|\nu\rangle, \tag{1.58}$$

and a density matrix

$$P_{\mu\nu} = 2\sum_{j}^{N/2} C_{\mu j}C_{\nu j}, \tag{1.59}$$

Because the Fock matrix depends on the expansion coefficients through the density matrix, Roothaan equations are non-linear

$$\mathbf{F}(\mathbf{C})\mathbf{C} = \mathbf{S}\mathbf{C}\epsilon, \tag{1.60}$$

and therefore they will be solved by an iterative procedure. To transform the Equation 1.60 into a conventional eigenvalue problem we need to orthonormalize the basis by a unitary transformation $\mathbf{U}$

$$\mathbf{U}^{\dagger}\mathbf{S}\mathbf{U} = \mathbf{I}, \tag{1.61}$$

where $\mathbf{U}^{\dagger}$ is the adjoint matrix of $\mathbf{U}$, and $\mathbf{I}$ is the identity matrix. As long as $\mathbf{U}$ is non-singular, Roothaan equations can be written as

$$(\mathbf{U}^{\dagger}\mathbf{F}\mathbf{U})(\mathbf{U}^{-1}\mathbf{C}) = (\mathbf{U}^{\dagger}\mathbf{S}\mathbf{U})(\mathbf{U}^{-1}\mathbf{C})\epsilon, \tag{1.62}$$

If we define the matrices $\mathbf{F}^{'}$ and $\mathbf{C}^{'}$

$$\mathbf{F}' = \mathbf{U}^{\dagger}\mathbf{F}\mathbf{U}, \tag{1.63}$$

$$\mathbf{C} = \mathbf{U}\mathbf{C}'. \tag{1.64}$$

Equation 1.60 is transformed into

$$\mathbf{F}'\mathbf{C}' = \mathbf{C}'\epsilon. \tag{1.65}$$

Equations 1.63-1.65 are the transformed Roothaan equations, which can be solved by diagonalizing $\mathbf{F}'$. However, these equations are still nonlinear; $\mathbf{F}'$ depends on the matrix $\mathbf{C}$, so we need to provide an initial guess of a set of orbitals. With this guess, approximate $\mathbf{F}'$ matrices can be constructed and diagonalized, and therefore, a new set of orbitals is obtained. Similarly, with this new orbitals a new Fock matrix is constructed and diagonalized and so on. This procedure is repeated until the change in the density matrix or the total electronic energy between two successive iterations is below a given threshold. When the convergence is attained, we say that such orbitals represent the self-consistent-field (SCF) solution. This approach is thus referred as the Self-Consistent-Field method. The size of all the matrices presented in Roothaan equations is $N_{basis} \times N_{basis}$, this means that the number of eigenvectors of $\mathbf{F}'$ is N_{basis}. The ground state wave function are constructed by filling the eigenvectors with lower orbital energies with N electrons and ignoring the remaining ones. These eigenvectors are referred to as occupied orbitals, while the remaining empty eigenvectors are known as virtual orbitals. Note that only occupied orbitals are used in the construction of the Fock operator, and therefore, they are the only ones which are optimized in the SCF procedure.

1.3 Electron correlation

As we have seen, the HF theory makes the basic assumption that each electron moves in the static average field created by all the other electrons regardless their instantaneous positions. This image is obviously wrong: there is a mutual correlation in the motion of electrons that reduces the probability of finding two electrons close each other, as we shall see later 1.7.1. This effect is called electron correlation. The HF theory only correlates electrons with parallel spins through the Pauli principle, since the probability of finding two like spin electrons at the same point of space is zero. That is Fermi or exchange correlation. However, at HF level unlike spin electrons are treated as though they were independent particles, in other words, they are uncorrelated.

Conventionally the correlation energy E_{corr} is defined as the difference between the exact non-relativistic energy of the system (E_{exact}) and the Hartree-Fock energy (E_{HF}) at the complete basis set limit

$$E_{corr} = E_{exact} - E_{HF}. \tag{1.66}$$

Since E_{HF} is an upper bound to E_{exact}, E_{corr} is always negative. Sometimes electron correlation is described in terms of two effects: dynamic correlation and static correlation [3].

- **Dynamic correlation**

Dynamic correlation arises from the Coulomb repulsion term in the Hamiltonian, r_{ij}^{-1}. The correlation cusp condition states that in regions where $r_{ij} = 0$, the exact wave function contains a cusp. The HF wave function does not show this cusp, and consequently does not describe correctly dynamic correlation. Since Coulomb repulsion is spin independent, spin-like electrons feel both Fermi and dynamic correlation.

- **Static correlation**

Static or non-dynamical correlation arises when many HF configurations have nearby or exactly the same energy. For this reason it is also referred to as near-degeneracy correlation. In this case, the flaw of the HF approximation is not so much that the correlated motion of electrons is neglected, but rather than a single determinant wave function is not able to describe this effect. As we will see, this kind of correlation can be usually dealt with by adding more Slater determinants to the wave function.

In the rest of this chapter we will focus on how to improve the HF approximation by including electron correlation in the wave function.

1.4 Configuration interaction

The configuration interaction (CI) method is the next step for improving the electronic structure description. Lets expand the wave function in terms of a set of Slater determinants D_i

$$\Psi = \sum_i C_i D_i, \tag{1.67}$$

$$D_i = \frac{1}{\sqrt{N!}} |\phi_{i_1}(\mathbf{x}_1) \ldots \phi_{i_N}(\mathbf{x}_N)|. \tag{1.68}$$

For a N electrons system and M functions basis set, $\{\phi_i\}$ constitutes a set of M spin orbitals, ϕ_{i_1}, ϕ_{i_2},…,ϕ_{i_N} with $N < M$, used to construct the determinant D_i, and C_i are coefficients obtained variationally by minimizing the total energy, $E = \langle\Psi|\widehat{H}|\Psi\rangle$. When all possible independent combinations of determinants are included in the expansion 1.67 the method is called *full CI* and it is the exact solution for a given basis set $\{\phi_i\}$. However, this limit is computationally very demanding, being only possible to perform *full CI* calculations for relatively small systems. The CI expansion is usually truncated at a given excitation level, giving a hierarchy of methods: CIS (includes all single excitations), CISD (includes all single and double excitations) and so on. The CISD is the most usual truncation, since single and doubly excitations are the most important ones for lowering the ground state energy.

1.4.1 CI matrix

The CI energy is obtained by diagonalizing the matrix of the electronic Hamiltonian in the basis of Slater determinants. To show the structure of this CI matrix, we express the ground state wave function of the system Ψ_o in a symbolic form

$$|\Psi_o\rangle = c_o|\Phi_o\rangle + c_S|S\rangle + c_D|D\rangle + c_T|T\rangle + \ldots, \tag{1.69}$$

where $|\Phi_o\rangle$ is the ground state Hartree-Fock wave function, $|S\rangle$ is the set of single excitations, $|D\rangle$ the set of double excitations and so on. The Brillouin's theorem and the Slater rules simplify the structure of the CI matrix.

Brillouin's Theorem *Singly excited determinants will not interact directly with a reference Hartree-Fock determinant.*

This theorem cancels all the elements of the form $\langle\Phi_o|\widehat{H}|S\rangle$. The Slater rules cancel all those matrix elements which couple two determinants that differ in more than two spin orbitals, i.e.,$\langle\Phi_o|\widehat{H}|T\rangle, \langle S|\widehat{H}|Q\rangle, \ldots$. The CI matrix takes then a block structure

$$\begin{bmatrix} \langle\Phi_o|\widehat{H}|\Phi_o\rangle & 0 & \langle\Phi_o|\widehat{H}|D\rangle & 0 & 0 & \ldots \\ 0 & \langle S|\widehat{H}|S\rangle & \langle S|\widehat{H}|D\rangle & \langle S|\widehat{H}|T\rangle & 0 & \ldots \\ \langle D|\widehat{H}|\Phi_o\rangle & \langle D|\widehat{H}|S\rangle & \langle D|\widehat{H}|D\rangle & \langle D|\widehat{H}|T\rangle & \langle D|\widehat{H}|Q\rangle & \ldots \\ \vdots & \vdots & \vdots & \vdots & \vdots & \ldots \end{bmatrix}.$$

1.4.2 Correlation energy

The correlation energy E_{corr} was defined in Equation 1.66. In this section, we will show how to recover it at the *full* CI level for the ground state of a molecular system. First we write again Equation 1.69 in more detail:

$$|\Psi_o\rangle = |\Phi_o\rangle + \sum_{ar} c_a^r|\Phi_a^r\rangle + \sum_{a<b,r<s} c_{ab}^{rs}|\Phi_{ab}^{rs}\rangle + \ldots, \tag{1.70}$$

where $|\Phi_a^r\rangle$ means a determinant created replacing the spin orbital a by the spin orbital r in $|\Psi_o\rangle$, $|\Phi_{ab}^{rs}\rangle$ is a determinant created replacing the spin orbitals a and b with the spin orbitals r and s respectively, and so on. Now, we impose an intermediate normalization condition

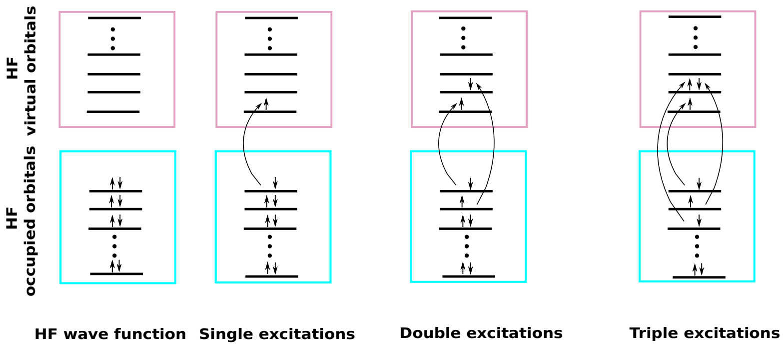

$$\Phi = c_0|\Psi_o\rangle + \sum_{\substack{a\\r}} c_a^r|\Psi_a^r\rangle + \sum_{\substack{a<b\\r<s}} c_{ab}^{rs}|\Psi_{ab}^{rs}\rangle + \sum_{\substack{a<b<c\\r<s<t}} c_{abc}^{rst}|\Psi_{abc}^{rst}\rangle + ...$$

Figure 1.1: Diagramatic representations of the configurations involved in the CI wave function.

$$\langle\Psi_o|\Phi_o\rangle = 1. \tag{1.71}$$

The greater the contribution of the HF configuration to $|\Psi_o\rangle$, the more exact the intermediate approximation is. Similarly to the HF case, the ground state energy E_o is the solution of the equation

$$\widehat{H}|\Psi_o\rangle = E_o|\Psi_o\rangle. \tag{1.72}$$

Applying the correlation energy definition (Equation 1.66), and multiplying both sides of the above equation by $\langle\Phi_o|$ we have

$$\langle\Phi_o|\widehat{H} - E_{HF}|\Psi_o\rangle = \langle\Phi_o|E_o - E_{HF}|\Psi_o\rangle = E_{corr}, \tag{1.73}$$

where the intermediate condition was used. Combining the Brioullin's theorem and the Slater rules, E_{corr} becomes:

$$E_{corr} = \sum_{a<b,r<s} c_{ab}^{rs}\langle\Psi_o|\widehat{H}|\Psi_{ab}^{rs}\rangle. \tag{1.74}$$

With the intermediate normalization condition, the correlation energy is solely determined by the double excitations. The single excitations only contribute indirectly by coupling with the double excitations. Although third and higher excitations are also coupled, their weights in the CI wave function are much lower. That is why single and double truncation are the most employed.

The main advantage of truncated CI methods is they offer a systematic procedure to improve the HF approximation in a variational way; the higher the degree of truncation, the closer to the *full* CI limit, which is the exact solution of Equation 1.3 for a given basis set. Unlike the HF and the *full* CI methods, the truncated CI approximations are not size-consistent, nor size-extensive. The size-consistency refers to the fact that the energy of two infinitely separated systems should be equal to the sum of each individual system.

The size-extensivity property indicates that the energy of a system should increases linearly with the number of subsystems.

1.5 Multiconfigurational methods

CI calculations use canonical Hartree-Fock orbitals to construct configurations. Since virtual orbitals do not contribute to the HF energy they are not optimized at this level of calculation. The philosophy of multiconfigurational methods (MCSCF) is to find the best choice for all orbitals: occupied and virtual orbitals. In this approximation, the wave function is expanded in terms of a set of configurations, $\{|\Psi_i\rangle\}$,

$$|\Psi_{MCSCF}\rangle = \sum_i C_i |\Psi_i\rangle. \tag{1.75}$$

Unlike the CI method, in which only C_i coefficients are optimized, in the MCSCF procedure both, C_i and the orbitals that define $|\Psi_i\rangle$ are optimized. This makes the process much more computationally demanding, limiting then the number of configurations that can be included in the calculation. The choice of the configurations depends on some *a priori* knowledge of the problem; which occupied and virtual orbitals are expected to be involved in the chemical phenomenon.

The cost of MCSCF may be reduced by choosing not only the orbitals to be included in each configuration, but also the number of electrons to be excited from the HF configuration. That is, the orbitals are split in two sets; frozen and active orbitals. The former will have occupations equal to two in all the configurations. The latter are allowed to have occupations lower than two. The active space is specified by the number of electrons to be excited (m) and the number of active orbital (n). This kind of MCSCF method is known as Complete Active Space Self Consisted Field (CASSCF). A CASSCF (m, n) means that all the configurations coming from distributing m electrons in n orbital, are included in the wave function.

1.6 Perturbation theory

Alternative to variational methods, electron correlation effects, namely dynamical correlation, may be tackled by means of perturbation theory. In what follows we shall consider the non-degenerate Rayleigh-Schrödinger perturbation theory, particularly the Möller-Plesset (MP) perturbation theory. In this approach, the Hamiltonian of the system is divided in two pieces: a zero-order part, $\widehat{H}_0$, whose solution is known, and a perturbation, $\widehat{V}$.

$$\widehat{H} = \widehat{H}_0 + \lambda \widehat{V};\ \widehat{H}_0 |\Psi_i^0\rangle = E_i^0 |\Psi_i^0\rangle, \tag{1.76}$$

where H_0 is the Hartree-Fock hamiltonian, λ is an ordering parameter, $|\Psi_i^0\rangle$, and E_i^0 are its $i-th$ eigenvector and eigenfunction respectively. To improve the eigenvalues and eigenfunctions of H, from the HF $(\lambda = 0)$ to the fully correlated solution $(\lambda = 1)$, $|\Psi_i\rangle$ and E_i are expanded in a Taylor series in λ

$$\begin{aligned} E_i &= E_i^0 + \lambda E_i^1 + \lambda^2 E_i^2 + \dots, & (1.77)\\ |\Psi_i\rangle &= |\Psi_i^0\rangle + \lambda |\Psi_i^1\rangle + \lambda^2 |\Psi_i^2\rangle + \dots & (1.78) \end{aligned}$$

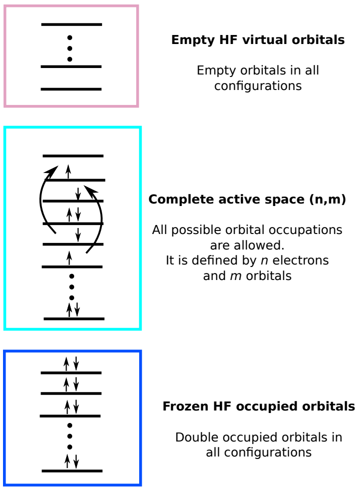

Figure 1.2: Diagramatic representations of the configurations involved in the CASSCF wave function.

The terms E_i^n and $|\Psi_i^n\rangle$ are the n order energy and wave function, respectively. To express these quantities in terms of the zero order energies and wave functions, we choose the intermediate normalization condition as we did before (Equation 1.71)

$$\begin{aligned} \langle\Psi_i|\Psi_i^0\rangle &= 1, && (1.79)\\ \langle\Psi_i^0|\Psi_i^n\rangle &= 0 \quad \forall\ n \neq 0. && (1.80) \end{aligned}$$

The expression for E_i^n may be found by grouping all the terms that multiplied λ^n and multiplying by $\langle\Psi_i^0|$

$$\begin{aligned} E_i^0 &= \langle\Psi_i^0|\widehat{H}_0|\Psi_i^0\rangle, && (1.81)\\ E_i^1 &= \langle\Psi_i^0|\widehat{V}|\Psi_i^0\rangle, && (1.82)\\ E_i^2 &= \langle\Psi_i^0|\widehat{V}|\Psi_i^1\rangle, && (1.83)\\ E_i^2 &= \langle\Psi_i^0|\widehat{V}|\Psi_i^2\rangle. && (1.84) \end{aligned}$$

To find the expression for the n order wave function, $|\Psi_i^n\rangle$ is expanded in term of the eigenfunctions of $\widehat{H}_0$, $|\Psi_j^0\rangle$

$$|\Psi_i^n\rangle = \sum_j c_j^i|\Psi_j^0\rangle. \tag{1.85}$$

Since the set $\{|\Psi_n^0\rangle\}$ forms an orthonormal set, the previous equation may be written as

$$|\Psi_i^n\rangle = \sum_j |\Psi_j^0\rangle\langle\Psi_j^0||\Psi_i^n\rangle. \tag{1.86}$$

First order corrections to E_n and $|\Psi_i\rangle$ are given by

$$
\begin{aligned}
E_i^1 &= \sum_{n>0} \frac{\langle \Psi_0^0 | \widehat{V} | \Psi_n^0 \rangle}{E_i^0 - E_n^0}, && (1.87) \\
|\Psi_i\rangle &= |\Psi_i^0\rangle + \sum_{n>0} \frac{\langle \Psi_0^0 | \widehat{V} | \Psi_n^0 \rangle}{E_i^0 - E_n^0} |\Psi_n^0\rangle. && (1.88)
\end{aligned}
$$

E^1 is the sum of the $0th$ and first order energies, that is the HF energy. The second order correction (E^2) is the first term which includes electron correlation

$$
E_i^2 = \sum_{n>0} \frac{\langle \Psi_0^0 | \widehat{V} | \Psi_n^0 \rangle \langle \Psi_0^0 | \widehat{V} | \Psi_n^0 \rangle}{E_i^0 - E_n^0}. \tag{1.89}
$$

The second order MP (MP2) method is probably the cheapest approach for dealing with dynamical correlation and typically accounts for 80-95% of the correlation energy. Unlikely truncated CI methods, MP theory is size-extensive.

1.7 Electron density and related functions

All of the methods described so far obtain the properties of the system from the wave function. However electronic wave functions are in general objects so complex that a further simplification is required in order to extract any chemical insight. The reduced density matrices provide us with a feasible formalism to recover not only the collective behavior of electrons but also any property of the system as state by the Hohenberg-Kohn theorems [4]. In the following section we will not explain the overall reduced density matrices formalism, but we will only present their more physically sound part: their diagonal elements [5].

1.7.1 The electron distribution

The wave functions obtained by each of the methods described in the previous sections are built by not observable objects defined in the Fock space, spin orbitals. According to the statistical interpretation of the quantum mechanics, only the square of the wave function has a true physical meaning.

Considering a single electron in orbital $\phi_i(\mathbf{r})$ with spin $\alpha(\sigma)$. The wave function is then $\psi_i(\mathbf{x}) = \phi_i(\mathbf{r})\alpha(\sigma)$. The probability of finding a particle in the volume element $d\mathbf{r}$ and with spin σ and $\sigma + d\sigma$ is given by

$$
\rho(\mathbf{x}) = |\psi_i(\mathbf{x})|^2 d\mathbf{x} = |\phi_i(\mathbf{r})|^2 |\alpha(\sigma)|^2 d\mathbf{r} d\sigma. \tag{1.90}
$$

The probability of finding the electron in a volume d$\mathbf{r}$ with any spin, is given by integration over the spin coordinates

$$
P(\mathbf{r}) d\mathbf{r} = d\mathbf{r} \int |\psi_i(\mathbf{x})|^2 d\mathbf{s}, \tag{1.91}
$$

$\rho(\mathbf{x})$ and $P(\mathbf{r})$ are then probability densities. They admit a generalization if ψ_i is replaced by a many electron wave function $\Psi(\mathbf{x}_1, \mathbf{x}_2, \ldots, \mathbf{x}_n)$. The probability of finding electron 1 in a volume $d\mathbf{x}_1$, electron 2 in a volume $d\mathbf{x}_2$ and the electron n in $d\mathbf{x}_n$ is given by

$$\Psi(\mathbf{x}_1, \mathbf{x}_2, \ldots, \mathbf{x}_N)\Psi^*(\mathbf{x}_1, \mathbf{x}_2, \ldots, \mathbf{x}_N)d\mathbf{x}_1, d\mathbf{x}_2, \ldots, d\mathbf{x}_N. \tag{1.92}$$

If $\Psi(\mathbf{x}_1, \mathbf{x}_2, \ldots, \mathbf{x}_N)$ is normalized, the electron distribution 1.92 satisfies

$$\int \Psi(\mathbf{x}_1, \mathbf{x}_2, \ldots, \mathbf{x}_N)\Psi^*(\mathbf{x}_1, \mathbf{x}_2, \ldots, \mathbf{x}_N)d\mathbf{x}_1, d\mathbf{x}_2, \ldots, d\mathbf{x}_N = N. \tag{1.93}$$

These probability functions may be “reduced” to those that lead to the probability of finding a set of n electrons in $d\mathbf{x}_1, \ldots, d\mathbf{x}_n$, given by integration over all the N electrons of the system but n.

$$d\mathbf{x}_1, d\mathbf{x}_2, \ldots, d\mathbf{x}_n \int \Psi(\mathbf{x}_1, \mathbf{x}_2, \ldots, \mathbf{x}_N)\Psi^*(\mathbf{x}_1, \mathbf{x}_2, \ldots, \mathbf{x}_N)d\mathbf{x}_{n+1}, \ldots, d\mathbf{x}_N. \tag{1.94}$$

Due to the indistinguishability of the electrons, $\binom{N}{n}n!$ times Equation 1.94 gives the probability of finding any set of n electrons. Thus the probability density associated with such n electrons is given by

$$\rho_n(\mathbf{x}_1, \ldots, \mathbf{x}_n) = \binom{N}{n} n! \int \Psi(\mathbf{x}_1, \mathbf{x}_2, \ldots, \mathbf{x}_N)\Psi^*(\mathbf{x}_1, \mathbf{x}_2, \ldots, \mathbf{x}_N)d\mathbf{x}_{n+1}, \ldots, d\mathbf{x}_N. \tag{1.95}$$

Similarly to Equation 1.91, the spinless counterpart of $\rho_n(\mathbf{x}_1, \ldots, \mathbf{x}_n)$ may be obtained by integration over the spin coordinates

$$\rho_n(\mathbf{r}_1, \ldots, \mathbf{r}_n) = \int \rho_n(\mathbf{x}_1, \ldots, \mathbf{x}_n)d\mathbf{s}_1, \ldots, d\mathbf{s}_n. \tag{1.96}$$

For $n = 1$, we get the ordinary electron function obtained in the DFT calculations and by X-ray crystallographers at experimental level. For $n = 2$, the so-called pair density is obtained. All ρ_n are normalized to the $n - tuple$ of electrons

$$\int \rho_n(\mathbf{r}_1, \ldots, \mathbf{r}_n)d\mathbf{r}_1, \ldots, d\mathbf{r}_n = \binom{N}{n} n!, \tag{1.97}$$

i.e. for $n = 1$ and $n = 2$

- $n = 1$

$$\int \rho_1(\mathbf{r}_1)d\mathbf{r}_1 = N, \tag{1.98}$$

- $n = 2$

$$\int \rho_2(\mathbf{r}_1, \mathbf{r}_2)d\mathbf{r}_1 d\mathbf{r}_2 = N(N - 1). \tag{1.99}$$

1.7.2 Pair density and electron correlation

The probability of finding two electrons at points $\mathbf{r}_1$ and $\mathbf{r}_2$ with any combination of spins is given by $\rho_2(\mathbf{r}_1, \mathbf{r}_2)$, and therefore, any information about electron correlation, as a pairwise effect, is contained in it. It is convenient to divide $\rho_2(\mathbf{r}_1, \mathbf{r}_2)$ into two components,

$$\rho_2(\mathbf{r}_1, \mathbf{r}_2) = \rho_1(\mathbf{r}_1)\rho_1(\mathbf{r}_2) - \rho_{xc}(\mathbf{r}_1, \mathbf{r}_2). \tag{1.100}$$

$$\tag{1.101}$$

The first term is the simple product on independent densities and does not contain any information about the electron correlation at all. The second term adds the influence of the Fermi and Coulomb correlation to $\rho_2(\mathbf{r}_1, \mathbf{r}_2)$. It is therefore known as exchange-correlation density, $\rho_{xc}(\mathbf{r}_1, \mathbf{r}_2)$

One may wonder now how likely is to find an electron at $\mathbf{r}_2$ knowing that there is a reference electron at $\mathbf{r}_1$. To define such statistical event we define the conditional probability $P_{cond}(\mathbf{r}_1|\mathbf{r}_2)$, [6]

$$P_{cond}(\mathbf{r}_1|\mathbf{r}_2) = \frac{\rho_2(\mathbf{r}_1, \mathbf{r}_2)}{\rho(\mathbf{r}_1)}. \tag{1.102}$$

Since the reference electron is arbitrarily fixed at $\mathbf{r}_1$, $P_{cond}(\mathbf{r}_1|\mathbf{r}_2)$ integrates to $N-1$

$$\int P_{cond}(\mathbf{r}_1|\mathbf{r}_2) d\mathbf{r}_1 d\mathbf{r}_2 = N - 1. \tag{1.103}$$

The effect of a reference electron on $\rho(\mathbf{r})$ may be explored by the exchange-correlation hole $h_{xc}(\mathbf{r}_1|\mathbf{r}_2)$

$$\begin{aligned} h_{xc}(\mathbf{r}_1|\mathbf{r}_2) &= P_{cond}(\mathbf{r}_1|\mathbf{r}_2) - \rho(\mathbf{r}_1), \\ &= -\frac{\rho_{xc}(\mathbf{r}_1, \mathbf{r}_2)}{\rho(\mathbf{r}_2)}. \end{aligned} \tag{1.104}$$

Thus $h_{xc}(\mathbf{r}_1|\mathbf{r}_2)$ accounts for the number of electrons excluded by electron at $\mathbf{r}_2$ due to the presence of a reference electron at $\mathbf{r_1}$, that is, electron correlation. $h_{xc}(\mathbf{r}_1|\mathbf{r}_2)$ satisfies the following properties

$$\int h_{xc}(\mathbf{r}_1|\mathbf{r}_2) d\mathbf{r_2} = -1, \tag{1.105}$$

$$h_{xc}(\mathbf{r}_1 \to \mathbf{r}_2|\mathbf{r}_2) = -\rho(\mathbf{r}_1). \tag{1.106}$$

$$\tag{1.107}$$

We now go a step further and distinguish the correlation effects only between spin like electrons

$$h_{xc}(\mathbf{r}_1|\mathbf{x}_2) = h_{xc}^{s_1=s_2}(\mathbf{r}_1|\mathbf{r}_2) + h_{xc}^{s_1,s_2}(\mathbf{r}_1|\mathbf{r}_2) \tag{1.108}$$

$$= h_F(\mathbf{r}_1|\mathbf{r}_2) + h_C(\mathbf{r}_1|\mathbf{r}_2) \tag{1.109}$$

$h_F(\mathbf{r}_1|\mathbf{r}_2)$ is known as the Fermi hole, and takes into account the correlation between electrons with the same spin (Fermi correlation) as a consequence of the exclusion principle. $h_C(\mathbf{r}_1|\mathbf{r}_2)$ contains the correlation between electrons of either spin (Coulomb correlation) and its known as the Coulomb hole. It is a consequence of the repulsion suffered by the electron due to its charge no matter the spin. Strictly speaking only $h_{xc}(\mathbf{r}_1|\mathbf{r}_2)$ has a true physical meaning, leaving $h_F(\mathbf{r}_1|\mathbf{r}_2)$ and $h_C(\mathbf{r}_1|\mathbf{r}_2)$ as mere artefacts to analyze electron correlation. It is worthy noticing that the Fermi and Coulomb classification of electron correlation is completely independent of that introduced in section 1.3, i.e the HF wave function only shows Fermi correlation even if dynamic and static correlation are absent. It is interesting to analyze separately $h_F(\mathbf{r}_1|\mathbf{r}_2)$ and $h_C(\mathbf{r}_1|\mathbf{r}_2)$:

- $h_F(\mathbf{r}_1|\mathbf{r}_2)$ is the main contribution to $h_{xc}(\mathbf{r}_1|\mathbf{r}_2)$ and it shows some interesting properties

  $$\int h_F(\mathbf{r}_1|\mathbf{r}_2)d\mathbf{r}_2 = -1. \tag{1.110}$$

  The presence of a reference electron with spin σ excludes this electron from the electron distribution. Thus $P_{cond}(\mathbf{r}_1|\mathbf{r}_2)$ integrates to $N_\sigma - 1$, where N_σ is there number of electron with spins $\mathbf{s}$.

  $$h_F(\mathbf{r}_1 \to \mathbf{r}_2|\mathbf{r}_2) = -\rho(\mathbf{r}_1). \tag{1.111}$$

  Since the Pauli principle does not allow two like spin electrons to be at the same position of space, $h_F(\mathbf{r}_1|\mathbf{r}_2)$ tends to the value of the density at the position of the reference electron, $\mathbf{r}_1$, as $\mathbf{r}_2 \to \mathbf{r}_1$.

  $$h_F(\mathbf{r}_1|\mathbf{r}_2) < 0. \tag{1.112}$$

- By contrast, $h_C(\mathbf{r}_1|\mathbf{r}_2)$ does not satisfy so many properties as $h_F(\mathbf{r}_1|\mathbf{r}_2)$ does. We have

  $$\int h_C(\mathbf{r}_1|\mathbf{r}_2)d\mathbf{r}_2 = 0. \tag{1.113}$$

  $P_{cond}(\mathbf{r}_1|\mathbf{r}_2)$ integrates to $N_\mathbf{s}$ for electrons of unlike spin. This result also implies that contrary to $h_F(\mathbf{r}_1|\mathbf{r}_2)$, $h_C(\mathbf{r}_1|\mathbf{r}_2)$ may take positive and negative values. The coulombic nature of $h_C(\mathbf{r}_1|\mathbf{r}_2)$ forces it to show a cusp as $\mathbf{r}_1 \to \mathbf{r}_2$.

1.8 Density functional theory

The Density Functional Theory (DFT) is a different approach that extracts, in principle, any property of the system not from the wave function but from a simpler object: the electron density [7]. Besides an statistical distribution, $\rho(\mathbf{r})$ is closely connected to energetics through the Hohenberg-Kohn theorems [4].

1.8.1 First Hohenberg-Kohn theorem

First Hohenberg-Kohn Theorem *For any system of interacting particles in an external potential $V_{ext}(\mathbf{r})$, this potential is determined uniquely, except for a constant, by the ground state particle density $\rho(\mathbf{r})$.*

From this theorem it follows that since the Hamiltonian of the system is fully determined by $V_{ext}(\mathbf{r})$, all the properties of the system are completely determined given $\rho(\mathbf{r})$.

Proof. Suppose that there were two different external potentials $V_{ext}^{(1)}(\mathbf{r})$ and $V_{ext}^{(2)}(\mathbf{r})$ which differ in more than a constant and which lead to the same ground state density $\rho(\mathbf{r})$. The two potentials lead to different Hamiltonians , $\widehat{H}^{(1)}$ and $\widehat{H}^{(2)}$, with different ground state wave functions, $\Psi^{(1)}$ and $\Psi^{(2)}$. Since $\Psi^{(2)}$ is not the ground state of $\widehat{H}^{(1)}$, from the variational principle it follows that

$$E^{(1)} = \langle \Psi^{(1)} | \widehat{H}^{(1)} | \Psi^{(1)} \rangle < \langle \Psi^{(2)} | \widehat{H}^{(1)} | \Psi^{(2)} \rangle. \tag{1.114}$$

It is supposed that the ground state is non-degenerate. Otherwise it would not be possible to assure the above inequality. The last term may be rewritten as

$$\begin{aligned} \langle \Psi^{(2)} | \widehat{H}^{(1)} | \Psi^{(2)} \rangle &= \langle \Psi^{(2)} | \widehat{H}^{(2)} | \Psi^{(2)} \rangle + \langle \Psi^{(2)} | \widehat{H}^{(1)} - \widehat{H}^{(2)} | \Psi^{(2)} \rangle & (1.115) \\ &= E^{(2)} + \int [\widehat{V}_{ext}^{(1)}(\mathbf{r}) - \widehat{V}_{ext}^{(2)}(\mathbf{r})] \rho(\mathbf{r}) d\mathbf{r}, & (1.116) \end{aligned}$$

so that

$$E^{(1)} < E^{(2)} + \int [\widehat{V}_{ext}^{(1)}(\mathbf{r}) - \widehat{V}_{ext}^{(2)}(\mathbf{r})] \rho(\mathbf{r}) d\mathbf{r}. \tag{1.117}$$

Considering $E^{(2)}$ in the same way as $E^{(1)}$ leads to

$$E^{(2)} < E^{(1)} + \int [\widehat{V}_{ext}^{(2)}(\mathbf{r}) - \widehat{V}_{ext}^{(1)}(\mathbf{r})] \rho(\mathbf{r}) d\mathbf{r}. \tag{1.118}$$

Adding the two equations, it yields a contradictory inequality $E^{(1)} + E^{(2)} < E^{(1)} + E^{(2)}$.

This establishes that there cannot be two different external potentials differing by more than a constant which give rise to the same non-degenerate ground state charge state density.

1.8.2 Second Hohenberg-Kohn theorem

Second Hohenberg-Kohn Theorem *A functional for the energy $E[\rho]$ in terms of the density $\rho(\mathbf{r})$ can be defined valid for any external potential $V_{ext}(\mathbf{r})$. The exact ground state energy of the system is given by the global minimum value of such functional, and the exact ground state density is the one that minimizes it.*

Proof. Since all the properties are determined by $\rho(\mathbf{r})$, each energy term may be defined as a functional of $\rho(\mathbf{r})$

$$E[\rho] = F_{HK}[\rho] + \int V_{ext} \rho(\mathbf{r}) d\mathbf{r}, \tag{1.119}$$

where $F_{HK}[\rho]$ is a universal functional of the density which contains the kinetic and electron-electron interaction energy,

$$F_{HK}[\rho] = T[\rho] + V_{ee}[\rho]. \tag{1.120}$$

The energy of a system with ground state density $\rho^{(1)}(\mathbf{r})$, external potential $V_{ext}^{(1)}$ and wave function $\Psi^{(1)}$ is given by the energy functional $E^{(1)}[\rho^{(1)}]$

$$E^{(1)}[\rho^{(1)}] = \langle \Psi^{(1)} | \widehat{H}^{(1)} | \Psi^{1} \rangle. \tag{1.121}$$

According to the first Hohenberg-Kohn theorem, any trial electron density, $\rho^{(2)}(\mathbf{r})$ determines its own external potential $V_{ext}^{(2)}$, hamiltonian $H^{(2)}$, and eventually, wave function $|\Psi^{2}\rangle$.

The variational principle assures that

$$E^{(1)}[\rho^{(1)}] = \langle \Psi^{(1)} | \widehat{H}^{(1)} | \Psi^{(1)} \rangle \leq \langle \Psi^{(2)} | \widehat{H}^{(1)} | \Psi^{(2)} \rangle = E^{(1)}[\rho^{(2)}]. \tag{1.122}$$

The map $\rho \rightarrow V_{ext} \rightarrow \widehat{H} \rightarrow \Psi$, allows for a formulation of the variational principle in terms of ρ: any trial density different from the exact leads to an upper limit to the exact ground state energy. Therefore, the exact ground state density satisfies the stationary principle:

$$\delta\Big(E^{(1)}[\rho] - \mu\Big[\int \rho(\mathbf{r}) d\mathbf{r} - N\Big]\Big) = 0, \tag{1.123}$$

where the Lagrange multiplier μ ensures that ρ integrates to the number of electrons N.

In the Hohenberg-Kohn original work the search of densities was constrained to those densities associated with some external potential V_{ext}. These densities are called *V-representable.* This condition may be relaxed by the *N-representability* constrain introduced by Levy [8, 9, 10]. A density is said to be *N-representable* if it derives from a well-behaved wave function and integrates to the correct number of electrons. The formulation given by Levy, not only replaces the *V-representability* constrain by the $N-$ *representability* constraint, but extends the Hohenberg-Kohn theorems to degenerated ground states.

From the second theorem of Hohenberg-Kohn it follows that if $F_{HK}[\rho]$ is known, the ground state density and the energy are available by minimization of the total energy of the system with respect to the density. However, $F_{HK}[\rho]$ is not known. The Kohn-Sham approach tackles this problem replacing true the kinetic energy by that of a set of non-interacting electrons, and the electron correlation is modeled as density functionals.

1.9 Kohn-Sham formulation

The Hohenberg-Kohn theorems provide a method for calculating ground-state properties such that if a form of $F[\rho]$ can be found, we have to minimize $E[\rho]$. But the task of finding good approximations to $F[\rho]$ is not easy. There is a problem with the expression of the kinetic part $T[\rho]$ in terms of the density, which represents the main drawback of the Thomas-Fermi approach, the old practical application of DFT.

In 1965, Kohn and Sham (KS) introduced a method for evaluating $T[\rho]$ by replacing the kinetic energy of the interacting electrons with an equivalent non-interacting reference system whose ground-state density is that of the interacting one ρ_o [11]. Assuming that ρ_o is the ground-state density of the non-interacting Hamiltonian $\widehat{H}_{KS}$

$$\hat{H}_{KS} = \hat{T} + \hat{V}_{KS}, \tag{1.124}$$

where $\hat{V}_{KS}$ is the external local Kohn-Sham potential $\hat{V}_{KS} = \int v_{ks}(\mathbf{r})\widehat{\rho}(\mathbf{r})d\mathbf{r}$, and the potential $v_{KS}(\mathbf{r})$ is such that:

1. its wave function is a single Slater determinant $\Phi[\rho]$ from which the ground-state density may be derived $\rho_o = \langle\Phi[\rho]|\hat{\rho}(\mathbf{r})|\Phi[\rho]\rangle$,
2. it minimizes the expectation value of $\hat{T}$.

The ground state energy is then given by

$$E_{KS} = \min_\rho \Big[\int v_{KS}(\mathbf{r})\rho(\mathbf{r})d\mathbf{r} + T_s[\rho] \Big] = \int v_{KS}(\mathbf{r})\rho_o(\mathbf{r})d\mathbf{r} + T_s[\rho_o], \tag{1.125}$$

where $T_s[\rho] = \langle\Phi[\rho]|\hat{T}|\Phi[\rho]\rangle$ is a non-interacting kinetic energy functional. Rearranging Equation 1.120, it is possible to include $T_s[\rho]$ in $F[\rho]$

$$F[\rho] = T_s[\rho] + E_H[\rho] + E_{xc}[\rho], \tag{1.126}$$

where

$$E_H[\rho] = \frac{1}{2}\int\int \frac{\rho(\mathbf{r})\rho(\mathbf{r}')}{|\mathbf{r}-\mathbf{r}'|} d\mathbf{r}d\mathbf{r}', \tag{1.127}$$

is the classical electrostatic Hartree energy functional and $E_{xc}[\rho]$ is the unknown exchange-correlation energy functional

$$E_{xc}[\rho] = T[\rho] - T_s[\rho] + V_{ee}[\rho] - E_H[\rho]. \tag{1.128}$$

The minimization of Equation 1.125 leads to the KS equations for determining the lowest N eigenfunctions of $\hat{H}_{KS}$, ψ_i, which form the minimizing determinant $\Phi[\rho]$

$$\hat{H}_{KS}|\psi_i\rangle = \epsilon_i|\psi_i\rangle, \tag{1.129}$$

where ϵ_i is the eigenvalue corresponding to the *i-th* eigenfunction ψ_i. Just as in Hartree-Fock theory, these equations must be solved self-consistently since $\hat{H}_{KS}$ depends on $\rho(\mathbf{r})$, and where the self-consistency is achieved $\rho(\mathbf{r}) = \rho_o(\mathbf{r})$. The KS method is in principle exact, though in practice we must find approximations for $E_{xc}[\rho]$. In this regard, it is worthy to notice that $E_{xc}[\rho]$ admits a further partition into exchange and correlation contributions

$$E_{xc}[\rho] = E_x[\rho] + E_c[\rho], \tag{1.130}$$

where $E_x[\rho]$ is the exchange energy functional

$$E_x[\rho] = \langle\Phi[\rho]|\hat{V}_{ee}|\Phi[\rho]\rangle - E_H[\rho], \tag{1.131}$$

and $E_c[\rho]$ is the correlation energy functional

$$E_c[\rho] = \langle\Psi[\rho]|\hat{T} + \hat{V}_{ee}|\Psi[\rho]\rangle - \langle\Phi[\rho]|\hat{T} + \hat{V}_{ee}|\Phi[\rho]\rangle, \tag{1.132}$$

where $\Psi[\rho]$ is the true wave function of the system. Moreover, the correlation energy may split into kinetic and potential components

$$E_c[\rho] = T_c[\rho] + V_c[\rho], \tag{1.133}$$

where $T_c[\rho] = T[\rho] - T_s[\rho]$ and $V_c[\rho] = V_{ee}[\rho] - (E_H[\rho] + E_x[\rho])$.

It is possible to analyse this partition in terms of $\rho_2(\mathbf{r}_1, \mathbf{r}_2)$

$$V_{ee}[\rho] = \langle\Phi[\rho]|\hat{V}_{ee}|\Phi[\rho]\rangle = \frac{1}{2}\int\int \frac{\rho_2(\mathbf{r}_1, \mathbf{r}_2)}{r_{12}} d\mathbf{r}_1 d\mathbf{r}_2. \tag{1.134}$$

We can rewrite $\rho_2(\mathbf{r}_1, \mathbf{r}_2)$ in terms of $h_{xc}(\mathbf{r}_1|\mathbf{r}_2)$

$$\rho_2(\mathbf{r}_1, \mathbf{r}_2) = \rho(\mathbf{r}_1)\rho(\mathbf{r}_2) + h_F(\mathbf{r}_1|\mathbf{r}_2)\rho(\mathbf{r_1}) + h_C(\mathbf{r}_1|\mathbf{r}_2)\rho(\mathbf{r_1}). \tag{1.135}$$

Then

$$\begin{aligned} V_{ee}[\rho] &= \frac{1}{2}\int\int \frac{\rho_2(\mathbf{r}_1, \mathbf{r}_2)}{r_{12}} d\mathbf{r}_1 d\mathbf{r}_2, & (1.136) \\ &= \frac{1}{2}\int\int \frac{\rho(\mathbf{r}_1)\rho(\mathbf{r}_2)}{r_{12}} d\mathbf{r}_1 d\mathbf{r}_2 + \frac{1}{2}\int\int \frac{\rho(\mathbf{r}_1)h_F(\mathbf{r}_1|\mathbf{r}_2)}{r_{12}} d\mathbf{r}_1 d\mathbf{r}_2 + \\ &+ \frac{1}{2}\int\int \frac{\rho(\mathbf{r}_1)h_C(\mathbf{r}_1|\mathbf{r}_2)}{r_{12}} d\mathbf{r}_1 d\mathbf{r}_2, \\ &= J[\rho] + E_x[\rho] + E_c[\rho]. & (1.137) \end{aligned}$$

From the latter formulation of $V_{ee}[\rho]$, it is possible to define the exchange correlation density $\epsilon_{xc}(\mathbf{r})$

$$\begin{aligned} \epsilon_{xc}(\mathbf{r}_1) &= \frac{1}{2}\int \frac{h_{xc}(\mathbf{r}_1|\mathbf{r}_2)}{r_{12}} d\mathbf{r}_2, & (1.138) \\ E_{xc}[\rho] &= \frac{1}{2}\int\int \frac{\rho(\mathbf{r}_1)h_{xc}(\mathbf{r}_1|\mathbf{r}_2)}{r_{12}} d\mathbf{r}_1 d\mathbf{r}_2, \\ &= \int \rho(\mathbf{r})\epsilon_{xc}(\mathbf{r}) d\mathbf{r}, & (1.139) \end{aligned}$$

Similarly to $h_{xc}(\mathbf{r}_1|\mathbf{r}_2)$, ϵ_{xc} is usually split into exchange ϵ_x and correlation ϵ_c contributions

$$\epsilon_{xc}(\mathbf{r}) = \epsilon_x(\mathbf{r}) + \epsilon_c(\mathbf{r}) \tag{1.140}$$

Although the KS equation (Equation 1.129) provides us with the exact ρ and E, it is extremely complicate to solve it due to the $\epsilon_{xc}(\mathbf{r})$ term. Equation 1.138 is only valid for the exact wave function Ψ which is solution of the Hamiltonian described by Equation 1.3 and not $\widehat{H}_{ks}$. The main difference between these two Hamiltonians comes from T_s. In order to provide a proper E_{xc} derived from $\widehat{H}_{KS}$, Becke outlined the adiabatic connection formulation. In a nutshell, the adiabatic connection envisages a path that connects the non-interacting reference system whose Hamiltonian does not posses the coulombic r_{ij}^{-1} and the real system where this term operates at full strength. These two systems are connected by increasing the coupling strength parameter λ from 0 to 1 whereas ρ always equals that of the fully interacting system. The main result of this formulation is that Equation 1.138 is replaced by

$$E_{xc}[\rho] = \frac{1}{2}\int\int \frac{\rho(\mathbf{r}_1)\bar{h}_{xc}(\mathbf{r}_1|\mathbf{r}_2)}{r_{12}} d\mathbf{r}_1 d\mathbf{r}_2, \tag{1.141}$$

where $\bar{h}_{xc}$ is the coupling strength integrated exchange-correlation hole

$$\bar{h}_{xc}(\mathbf{r}_1|\mathbf{r}_2) = \int_0^1 h_{xc}(\mathbf{r}_1|\mathbf{r}_2) d\lambda. \tag{1.142}$$

Fortunately $\bar{h}_{xc}(\mathbf{r}_1|\mathbf{r}_2)$ and $h_{xc}(\mathbf{r}_1|\mathbf{r}_2)$ share the same properties. The DFT challenge relies on a proper modeling of $\epsilon_{xc}(\mathbf{r})$, and specially $h_{xc}(\mathbf{r}_1|\mathbf{r}_2)$. Different models lead to different exchange-correlation functionals, whose quality rely on how well they reproduce the properties of the exact h_{xc} aforementioned.

1.9.1 Exchange-correlation functionals

Local density approximations

The simplest approach for computing $E_{xc}[\rho]$ is found in the Thomas-Fermi-Dirac (TFD) model. This approximation considers the electronic system as a uniform electron gas which moves on a positive background charge distribution such that the total ensemble is electrically neutral. The electron density of such system attains a constant value everywhere. Thus this model is commonly known as homogeneous electron gas (HEG). In the traditional Thomas-Femi (TF) model, electron-electron interaction is solely replaced by the Coulomb term in Equation 1.136 $J[\rho]$ and the kinetic energy is derived form the HEG model.

$$T_{HEG} = C_F \int \rho^{5/3}(\mathbf{r})d\mathbf{r}, \qquad C_F = \frac{3}{10}(3\pi^2)^{2/3}, \tag{1.143}$$

where C_F is the Fermi constant. Similarly to E_{xc}, we may define the TF kinetic energy density

$$\epsilon_{TF}(\rho) = -C_F\rho^{2/3}. \tag{1.144}$$

All kinetic energy density functionals are somehow based on the TF model. The TFD model adds the exchange contribution to electron-electron interaction leading to the famous exchange-energy Dirac formula

$$K_D = -C_x \int \rho^{4/3}(\mathbf{r})d\mathbf{r}, \qquad C_x = \frac{3}{4}\left(\frac{3}{\pi}\right)^{1/3}. \tag{1.145}$$

and the HEG exchange energy density ϵ_{xc}^{HEG}, frequently called Salter exchange, is defined as

$$\epsilon_{xc}^{HEG} = C_x\rho^{1/3}(\mathbf{r}). \tag{1.146}$$

The local density approximation (LDA) is defined by using $\epsilon_x^{HEG}(\mathbf{r})$ as exchange functional into KS equations. For the correlation part $\epsilon_c^{LDA}(\mathbf{r})$ no such explicit formula is known. However, some expressions are available from highly accurate numerical quantum Monte-Carlo simulations [12] and further parametrisation schemes, as those developed by Vosko, Wilk, and Nusair [13] or the most recently proposed by Perdew and Wang [14].

LDA may be adapted to deal with spin polarized systems; $\rho(\mathbf{r})$ is split into $\alpha(\rho\uparrow(\mathbf{r}))$ and $\beta(\rho\downarrow(\mathbf{r}))$ spin densities such that $\rho(\mathbf{r}) = \rho\uparrow(\mathbf{r}) + \rho\downarrow(\mathbf{r})$. Equation 1.145 becomes

$$\begin{aligned} E_x^{LSD} &= -2^{1/3}\frac{1}{2}C_x \int \rho^{4/3}(\mathbf{r})\Big[(1+\zeta(\mathbf{r}))^{4/3} + (1-\zeta(\mathbf{r}))^{4/3}\Big]d\mathbf{r}, \\ &= \int \rho(\mathbf{r})\epsilon_x(\rho,\zeta)d\mathbf{r}, \end{aligned} \tag{1.147}$$

where

$$
\begin{aligned}
\epsilon_x(\rho,\zeta) &= \epsilon(\rho,0) + [\epsilon_x(\rho,1) - \epsilon_x(\rho,0)]f(\zeta), && (1.148)\\
f(\zeta) &= \frac{1}{2(2^{1/3}-1)}[(1+\zeta(\mathbf{r}))^{4/3} + (1-\zeta(\mathbf{r}))^{4/3} - 2]. && (1.149)
\end{aligned}
$$

The degree of spin polarisation is accounted by the spin polarisation density $\zeta(\mathbf{r})$

$$\zeta(\mathbf{r}) = \frac{\rho\uparrow(\mathbf{r}) - \rho\downarrow(\mathbf{r})}{\rho(\mathbf{r})}. \tag{1.150}$$

ζ attains values from 0 for spin compensated system to 1 for full spin polarized systems. $\rho\uparrow(\mathbf{r})$ and $\rho\uparrow(\mathbf{r})$ may be written in terms of $\zeta(\mathbf{r})$

$$\rho\uparrow(\mathbf{r}) = \frac{1}{2}(1+\zeta(\mathbf{r})\rho(\mathbf{r}), \quad \rho\downarrow(\mathbf{r}) = \frac{1}{2}(1-\zeta(\mathbf{r}))\rho(\mathbf{r}). \tag{1.151}$$

The resulting formalism is known as the local spin density approximation (LSDA) and the exchange-correlation energy is now a function of $\rho(\mathbf{r})$ and $\zeta(\mathbf{r})$

$$E_x^{LSDA}[\rho\uparrow(\mathbf{r}),\rho\downarrow(\mathbf{r})] = \int[\rho\uparrow(\mathbf{r}) + \rho\downarrow(\mathbf{r})]\epsilon_{xc}^{HEG}(\rho(\mathbf{r}),\zeta(\mathbf{r}))d\mathbf{r}. \tag{1.152}$$

The LDA works well in systems where the electron density is quite uniform such as bulk metals. However as expected for a simple model such as HEG, it is a very crude approximation for systems where the density varies rapidly such as atoms and molecules. The origin of such deficiencies may be found in the structure of the LDA exchange hole. Although it satisfies the properties above mentioned for the exact exchange hole, it is always symmetric around the reference electron while the exact hole has a pronounced angular structure.

Generalized gradient approximation

The erratic homogeneous behavior of LDA may be corrected by adding density derivatives to $E_{xc}^{LDA}[\rho]$ trough a gradient expansion of E_{xc}. The Generalized Gradient Approximation (GGA) [15] improves LDA results by including not only $\rho(\mathbf{r})$, but also derivatives of $\rho(\mathbf{r})$ in E_{xc}

$$
\begin{aligned}
E_x^{GEA}[\rho\uparrow(\mathbf{r}),\rho\downarrow(\mathbf{r})] &= \int \rho(\mathbf{r})\epsilon_{xc}(\rho\uparrow(\mathbf{r}),\rho\downarrow(\mathbf{r}))d\mathbf{r}\\
&+ \sum_{\sigma,\sigma'}\int C_{xc}^{\sigma,\sigma'}(\rho\uparrow(\mathbf{r}),\rho\downarrow(\mathbf{r}))\frac{|\vec{\nabla}\rho_\sigma(\mathbf{r})|^2}{\rho_\sigma^{4/3}(\mathbf{r})}d\mathbf{r} + \ldots && (1.153)
\end{aligned}
$$

where GEA means gradient expansion approximation. This kind of expansions was introduced by Hohenberg and Kohn [4] and they showed that they require: 1) slow varying and 2) uniform density. The first condition may be mathematically describes as

$$\frac{|\vec{\nabla}\rho(\mathbf{r})|}{\rho(\mathbf{r})} << k_F(\mathbf{r}), \qquad k_F(\mathbf{r}) = (3\pi^2\rho(\mathbf{r}))^{1/3}, \tag{1.154}$$

where $k_F(\mathbf{r})$ is the Fermi wave momentum. The second condition prevents ρ from showing short-wavelength oscillations. Mathematically it requires

$$\frac{|H_{ij}(\rho)(\mathbf{r})|}{|\vec{\nabla}\rho(\mathbf{r})|} << k_F(\mathbf{r}), \tag{1.155}$$

where $H_{ij}(\rho)(\mathbf{r})$ is the element i, j of the Hessian matrix of $\rho(\mathbf{r})$. Surprisingly GEA functionals do not improved LDA results since GEA $h_{xc}(\mathbf{r}_1|\mathbf{r}_2)$ does not fulfill any of the properties aforementioned (Equations 1.110, 1.111,and 1.112), nor the negative condition. To define well-behaved exchange-correlation functionals based on the GEA, Perdew prosed to truncate $h_F(\mathbf{r}_1|\mathbf{r}_2)$ and $h_C(\mathbf{r}_1|\mathbf{r}_2)$ to integrate to -1 and 0 respectively. Functionals that include the gradient of ρ and are forced to satisfy the properties of the exact $h_{xc}(\mathbf{r}_1|\mathbf{r}_2)$ are referred, to as generalize gradient approximations (GGA) [15]. The GGA exchange contributions to $E_{xc}^{GGA}[\rho]$ may be written as

$$E_x^{GGA}[\rho] = \int \rho(\mathbf{r})\epsilon_x^{HEG} F_x(s, |\vec{\nabla}\rho(\mathbf{r})|)d\mathbf{r}, \tag{1.156}$$

where the function $F_{xc}[\rho]$ is an enhancement function constructed to satisfy the properties of the exact $h_{xc}(\mathbf{r}_1|\mathbf{r}_2)$. It is a function of the reduced density gradient $s(\mathbf{r})$

$$\begin{aligned} s(\mathbf{r}) &= \frac{|\vec{\nabla}\rho(\mathbf{r})|}{2k_F(\mathbf{r})\rho(\mathbf{r})}, \\ &= \frac{|\vec{\nabla}\rho(\mathbf{r})|}{2(3\pi^2)^{1/3}\rho^{4/3}(\mathbf{r})}. \end{aligned} \tag{1.157}$$

$s(\mathbf{r})$ accounts for the local inhomogeneity, therefore for the HEG $s(\mathbf{r})$=0 and $F(s) = 1$. As shown in Equation 1.154 gradient expansion requires $s(\mathbf{r}) << 1$ to convergence. It assumes very large values in regions where not only the gradient is large, but also where density is small, such as the exponential tails far from the nuclei. By contrast, $s(\mathbf{r})$ takes small values for small gradients, but also for large densities as in bonding regions and close to nuclear positions. It is worthy to say that the 4/3 exponent in the denominator is not an arbitrary choice, but is needed to make $s(\mathbf{r})$ a dimensionless variable. The function F_x defines the E_x^{GGA} functional. We may distinguish between those functionals that use some empirical parameter to fit E_x^{GGA} to the exact exchange energy of some reference system, such as B88 of Becke [16] or PW91 developed by Perdew Burke and Wang, and those functionals that are free of semiempirical parameter, i.e B86 by Becke, PBE developed by Perdew, Becke and Ernzerhof [15].

The GGA correlation energy E_c^{GGA} has in general a more complicated shape than the exchange and we will not enter into details. Among the most popular E_c^{GGA} we find the parameter free PW91 by Perdew and Wang, and the one empirical parameter LYP developed by Lee Yang and Parr [17].

Meta-generalized gradient approximations

A further improvement in exchange-correlation functional may be achieved if instead of looking at GEA of E_{xc} we analyze the spherical average of $\rho_x(\mathbf{r}_1|\mathbf{r}_2)$,$\langle\rho_{x\sigma}(\mathbf{r_{12}})\rangle$ at small interelectronic distance.

$$\langle\rho_{x\sigma}(\mathbf{r_{12}})\rangle = \rho_\sigma(\mathbf{r}) + \frac{1}{6}\Big[\nabla^2\rho_\sigma(\mathbf{r}) - 2\tau_\sigma + \frac{1}{2}\frac{|\vec{\nabla}\rho_\sigma(\mathbf{r})|^2}{\rho_\sigma}\Big]\mathbf{r}_{12}^2 + \dots. \tag{1.158}$$

This expansion was firstly developed by Becke [18, 19]. He highlighted that not only $|\vec{\nabla}\rho(\mathbf{r})|$ is a key component at small $\mathbf{r_{12}}$, but also the Laplacian of $\rho(\mathbf{r})$, $\nabla^2\rho(\mathbf{r})$ and the positive definite kinetic energy density for a HEG $\tau(\mathbf{r})$

$$\tau(\mathbf{r}) = \frac{1}{2}\sum_{i=1}^{occ}|\vec{\nabla}\phi_i(\mathbf{r})|^2. \tag{1.159}$$

As showed by Becke, the coefficient of the quadratic term may be used as a predictor for further corrections to the LSDA hole, without imposing sharp cut-offs to $h_{xc}(\mathbf{r}_1|\mathbf{r}_2)$ as GGA does. Functionals that includes $\tau(\mathbf{r})$ have been termed as meta-GGA,

$$E_x^{meta-GGA}[\rho] = \int \rho(\mathbf{r})\epsilon_x^{HEG}F_x(|\vec{\nabla}\rho|, \tau, \tau_w)d\mathbf{r}, \tag{1.160}$$

where $\tau_w(\mathbf{r})$ denotes the von Weizsäcker kinetic energy density

$$\tau^w(\mathbf{r}) = \frac{1}{8}\frac{|\vec{\nabla}\rho(\mathbf{r})|^2}{\rho(\mathbf{r})}. \tag{1.161}$$

Meta-GGA functionals offer two main improvements with respect to GGA functions; in the one hand their main variable $\tau(\mathbf{r})$ admits a clearest physically interpretation than the dimensionless variable $s(\mathbf{r})$. In Chapter 4 we shall show that is possible to understand $s(\mathbf{r})$ in terms of kinetic energy densities.

One of the most sound problems of exchange-correlation functional is the self-interaction error. For a one electron system, such as the hydrogen atom the $E_H[\rho]$ and $E_{xc}[\rho]$ terms in Equation 1.126 should cancel each other out. For many functional this is not the case. One strategy for designing self-interaction free functionals is based on the relationship between $\tau(\mathbf{r})$ and $\tau_w(\mathbf{r})$ [20]. Self-Correlation Corrections (SCC) are based on the following property

$$\tau_w(\mathbf{r}) \leq \tau(\mathbf{r}), \tag{1.162}$$

where the equality only holds if $\rho(\mathbf{r})$ is represented by a single orbital. This property is usually used to define SCC

$$\eta^{SCC}(\mathbf{r}) = 1 - \frac{\tau_w(\mathbf{r})}{\tau(\mathbf{r})}. \tag{1.163}$$

From Equation 1.162 it follows that $\eta^{SCC}(\mathbf{r}) \leq 1$ and it vanishes for any one-orbital system. In the following chapters we shall revisit $\tau_w(\mathbf{r})$ properties to construct bonding descriptors.

SCC is not possible at GGA level since only $s(\mathbf{r})$(and not $\tau(\mathbf{r})$) is used as a main variable. Among the most famous meta-GGA functionals we found the Becke's 1995 correlation functional (B95) [21] Perdew-Kurth-Zupan-Blaha(PKZB) [22] correlation functional, Tao-Perdew-Staroverov-Scuseria (TPSS) exchange-correlation functional [23] or Krieger-Chen-Iafrate-Savin (KCIS) exchange correlation functional [24].

Hybrids

All the approximations hitherto presented reproduce to different extents $h_{xc}(\mathbf{r}_1|\mathbf{r}_2)$. However it is known that $h_F(\mathbf{r}_1|\mathbf{r}_2)$ is the main component of $h_{xc}(\mathbf{r}_1|\mathbf{r}_2)$ and it may be exactly computed from the HF wave function by Equation 1.33. Including a rational portion of the exact exchange and combining it with some correlation functionals is the spirit of hybrids functionals. The main issue of this approach rests on the incapacity of $h_F(\mathbf{r}_1|\mathbf{r}_2)$ and $h_C(\mathbf{r}_1|\mathbf{r}_2)$, taken individually, for reproducing the properties of $h_{xc}(\mathbf{r}_1|\mathbf{r}_2)$; $h_F(\mathbf{r}_1|\mathbf{r}_2)$ should be complemented by $h_C(\mathbf{r}_1|\mathbf{r}_2)$. In terms of the adiabatic connection we may consider hybrids functionals as interpolation schemes between the exact exchange ($\lambda = 0$) and the exact exchange-correlation functionals ($\lambda = 1$). The simplest approach is to assume a linear extrapolation of λ, leading to the half-and-half (HH) exchange-correlation functional introduced by Becke [25].

$$E_{xc}^{HH} = \frac{1}{2}E_{xc}^{\lambda=0} + \frac{1}{2}E_{xc}^{\lambda=1}. \tag{1.164}$$

Becke used E_{xc}^{LDA} for $E_{xc}^{\lambda=1}$. Further improvements on the interpolation scheme leads to more sophisticated exchange-correlation functionals where the amount of exact exchange and the approximative exchange and correlation contributions is determined by some parametrization scheme. Among the hybrid functionals we find the most widely used functional, the exchange-correlaton B3LYP functional [26]

$$E_{xc}^{B3LYP} = aE_x^{HF} + (1-a)E_x^{LSDA} + bE_x^{b88} + cE_c^{LYP} + (1-c)Ec^{VWN}, \tag{1.165}$$

where the parameters ($a = 0.2$, $b = 0.72$, $c = 0.81$) were adjusted to the G2 set of experimental data. Many efforts have be done to reduce the number of parameter, as B1B95 due to Becke [27, 25] which reduces the number of parameters to one. However there are certain technical disadvantages that make B1B95 less appealing than B3LYP.

Aside from hybrid functionals based on empirical parametrizations, Perdew Burke and Erhzerhof proposed a parameter-free hybrid where the amount was derived from theoretical derivations

$$E_{xc}^{hybrid} = E_{xc}^{GGA} + 0.25(E_x^{HF} - E_x^{GGA}). \tag{1.166}$$

The most successful of these functional is the PBE1PBE functional (also known as PBE0) where the PBE exchange-correlation functional is chosen as the GGA component [28].

Range-separated hybrids

It is well known that approximate $v_{xc}(\mathbf{r})$ fails in reproducing the asymptotic behavior the exact potential; none of them has the correct $-\mathbf{r}^{-1}$ decay, they rather decrease exponentially, and therefore they are less attractive that the exact potential at large $\mathbf{r}$; i.e. at distances far from the atoms. This ill-behavior turns out to be critical for those properties that not only depend on the occupied KS orbitals, but also on the virtual orbital, such as polarizabilities or excitation energies. In the spirit of hybrid functionals, one may include some amount of the exact exchange and correlation to correct the long-range behavior of approximated $v_{xc}(\mathbf{r})$. Range-separated functionals [29, 30] separate electron-electron interaction into short and long range terms

$$\frac{1}{r_{12}} = \frac{erf(\mu r_{12})}{r_{12}} + \frac{erfc(\mu r_{12})}{r_{12}}, \tag{1.167}$$

where the parameter μ controls the separation between the long-range ($\mathrm{erf}(\mu r_{12})/r_{12}$) and the short-range ($\mathrm{erfc}(\mu r_{12}/r_{12}$) interactions. This is equivalent to representing E_{xc} as

$$E_{xc} = E_{xc}^{SR}(\mu) + E_{xc}^{LR}(\mu). \tag{1.168}$$

This partition scheme admits the combination of wave function and DFT methods depending if a long-range corrected or a screened functional is sought. The first mix long-range HF with short range DFT providing the proper $-\mathbf{r}^{-1}$ decay of $v_{xc}(\mathbf{r})$, and therefore, improving properties such as charge-transfer, Rydberg excitations and van der Waals interactions [31, 32, 33]. There is room for improvements if the HF contribution is replaced by MCSCF, leading to the multiconfigurational hybrid functionals. This way, then non-dynamical correlation may be included. The latter approach is mainly used in solid state physics and where mixing long-range DFT with short range HF to define a screened potential, improves band-gaps, lattice constants, etc [34, 35, 36, 37].

Chapter 2

Mathematical foundations

Sommaire

In Chapter 1 we have shown that a chemical system is characterized by its wave function and how the quality of this magnitude may be systematically improved by means of the variational principle or perturbation theory. Along with the wave function, one may obtain the averaged value of any property, as long as it has an associated quantum operator, this is, if it is an observable. However, chemical concepts were introduced many years before the birth of quantum mechanics, and recovering these ideas in a quantum mechanical manner is not an easy task at all. In the forthcoming chapters, we shall introduce an approach that has successfully recovered many of the firmly rooted chemist ideas from quantum mechanics, quantum chemical topology. In a nutshell, this approach exploits the topology of any chemically or physically-sound scalar field defined from reduced density matrices. The aim of the present chapter is to let the reader become acquainted with some of the topological concepts that will be used in the rest of the manuscript. Additionally, some of the algorithms and formalism used for computing different topological properties will be presented.

The birth of Topology as a scientific branch dates from Euler's publication on the Königsberg bridge problem. This seminal work showed a property of graphs that is true regardless of their geometry. Soon after he proposed his formula for polyhedra: $V - E + F = 2$ (where V refers to the number of vertexes of the polyhedron, E refers to the number of edges and F refers to the numbers of faces). Several years later Simon Lhuilier corrected this Euler's formula to account for genus (G):$V - E + F = 2 - 2G$. The Königsberg problem revealed the topology as a the study of aspects of space, regardless of geometric metrics. Much of the formal structure used in topology was formalized in 1895 by Jules Poincaré, who introduced the ideas of homotopy, homology and Betti numbers to characterize the topology of an object.

2.1 Topological spaces

The notion of topological space was established in order to tackle questions related to the connectivity of point sets. The topology of a point set defines which points are close without defining how close they are from each other, that is, without defining a particular metric. A topology on a point set $\mathbb{X}$ is a collection $\mathcal{U}$ of subsets of $\mathbb{X}$, called open sets, such that

- $\mathbb{X}$ is open and the empty set $\emptyset$ is open;
- if U_1 and U_2 are open, then $U_1 \bigcap U_2$ is open;
- if U_i is open for all i in some possibly infinite, possible uncountable, index set, then the union of all U_i is open.

The pair ($\mathbb{X}$, $\mathcal{U}$) is called a topological space, and $\mathcal{U}$ is said to be a topology of $\mathbb{X}$. Through the combination of open sets that satisfies the three above conditions, different topologies may be built. These open sets form the basis of a topology on $\mathbb{X}$.

Definition 2.1 *A basis of a topology on a point set $\mathbb{X}$ is a collection $\mathcal{B}$ of subsets of $\mathbb{X}$, called basis elements, such that each $x \in \mathbb{X}$ is contained in at least one $B \subseteq \mathcal{B}$ and $x \in B_1 \bigcup B_2$ implies there is a third basis element with $x \subseteq B_3 \subseteq B_1 \bigcap B_2$. The topology $\mathcal{U}$ generated by $\mathcal{B}$ consists of all sets $U \subseteq \mathbb{X}$ for which $x \in U$ implies there is a basis element $x \in B \subseteq U$.*

As an example, consider the real line, $\mathbb{R}$, and let $\mathcal{B}$ be the collection of all open intervals in $\mathbb{R}$. Let x, be any number in $\mathbb{R}$, and B_3 an open interval around x, $B_3 = (x - \epsilon, x + \epsilon)$

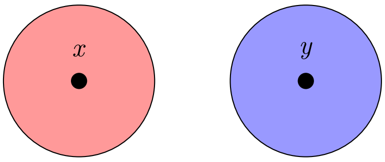

Figure 2.1: Hausdorff condition for two points $x, y \in \mathbb{R}^2$

with $\epsilon > 0$. It is always possible to find two open intervals $B_1 = (x - k_1\epsilon, x + k_1\epsilon)$ and $B_2 = (x - k_2\epsilon, x + k_2\epsilon)$, with k_1 and $k_2 \geq 1$, such that $B_3 \subseteq B_1 \bigcap B_2$. The union of all possible B_3 constructs a topology on $\mathbb{R}$.

As pointed out at the beginning of this chapter, the topology of a point set, say $\mathbb{X}$, defines how close are the points of $\mathbb{X}$ between them without reference to any metric. This is done through the concept of neighborhood.

A subset $\mathbb{Y} \subseteq \mathbb{X}$ is a neighborhood of $x \in \mathbb{Y}$ if there exists an open set U such that $x \in U \subseteq Y$.

Furthermore, if for every $x, y \in \mathbb{X}$, $x \neq y$, there are neighborhoods A, B of x, y, respectively such that $A \bigcap B = \emptyset$, $\mathbb{X}$ is said to be a Hausdorff space (see Figure 2.1). The separability of a topological space is guaranteed if it has a countable basis of neighborhoods, then it is said that a topological space is separable.

The concept of neighborhood defines the inner structure of a topological space. In Topology, it is also interesting, and necessary, to compare different topological spaces. This is can be done through the notion of homeomorphism.

Definition 2.2 *Given two topological spaces, $\mathbb{X}$ and $\mathbb{Y}$, a homeomorphism is a bijective function $f : \mathbb{X} \to \mathbb{Y}$, such that f and its inverse f^{-1} are continuous. If such an f exits, $\mathbb{X}$ is said to be homeomorphic to $\mathbb{Y}$, and that $\mathbb{X}$ and $\mathbb{Y}$ have the same topological type.*

In practice, we deal with metric spaces, such as Euclidean spaces. A metric space $\mathbb{S}$ is a set with a metric function $d : \mathbb{S} \times \mathbb{S} \to \mathbb{R}$ such that,

- Positivity. For all $x, y \in \mathbb{S}, d(x, y) \geq 0$.
- Non-degeneracy. If $d(x, y) = 0$, then $x = y$.
- Symmetry. For all $x, y \in \mathbb{S}, d(x, y) = d(y, x)$.
- Triangle inequality. $\forall\ x, y, z \in \mathbb{S}, d(x, y) + d(y, z) \geq d(x, z)$.

For example, if $d(x, y) = \sqrt{\left(\sum_{i=0}^{n}(x_i - y_i)^2\right)}$ we may define the n-dimensional Euclidean space $\mathbb{R}^n$ as the Cartesian product of n copies of the real line $\mathbb{R}$ with metric $d(x, y)$. Alternatively a metric space may be defined as a topological space, where open balls serve as basis neighborhoods for a topology of a set.[1] All metric space is Hausdorff; being $\mathbb{S}$ a metric space, and $x, y \in \mathbb{S}$, it is possible to define two balls of radius $d(x, y)/2$ around each point, such that they do not overlap.

---

[1] An open ball $B(x, r)$ with center x and radius $r > 0$ with respect to metric $d(x, y)$ is defined as $B(x, r) = \{y | d(x, y) < r\}$.

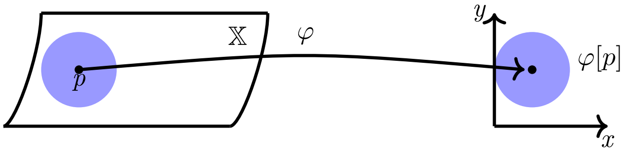

Figure 2.2: Homeomorphism (φ) onto an open subset of $\mathbb{R}^2$. The pair $(U,\ \varphi)$, where $U \subseteq \mathbb{X}$, forms a chart at $p \in \mathbb{X}$.

2.1.1 Manifolds

Before introducing a formal definition of manifold, let's imagine an Euclidean space $\mathbb{M}$, such that, for each point $P \in \mathbb{M}$, there exists a neighborhood homeomorphism, φ, to an open set in $\mathbb{R}^m$,

$$\begin{aligned} \varphi : \mathbb{M} &\rightarrow \mathbb{R}^m \\ P &\rightarrow (x_1, x_2, \ldots, x_m), \end{aligned}$$

that is, for every P, $\varphi[P]$ defines a local set of coordinates $(x_1, x_2, \ldots, x_m)$ in $\mathbb{R}^m$. Figure 2.2 shows an homeomorphism to an open set in $\mathbb{R}^2$. This local homeomorphism is accounted by charts,

Definition 2.3 *A chart at $x \in \mathbb{X}$ is the pair $(U,\ \varphi)$, where $U \subseteq \mathbb{X}$ is an open set containing x, and φ is a homeomorphism onto an open subset of $\mathbb{R}^m$. The dimension of the chart φ is m.*

In order to prevent two different charts $(U,\ \varphi_1)$, $(V,\ \varphi_2)$ from pointing into the same local coordinates $(x_1, x_2, \ldots, x_m) \in \mathbb{R}^m$, we impose both charts to be C^∞-related,

Definition 2.4 *Given a topological space $\mathbb{X}$ and two charts $(U,\ \varphi_1)$ and $(V,\ \varphi_2)$ such that*

$$\varphi_1 : U \subset \mathbb{X} \rightarrow \mathbb{R}^m \tag{2.1}$$
$$\varphi_2 : V \subset \mathbb{X} \rightarrow \mathbb{R}^m, \tag{2.2}$$

they are said to be C^∞-related if

$$U \bigcap V = \emptyset,$$

else if $\varphi_1 \circ \varphi_2^{-1}$ and $\varphi_2 \circ \varphi_1^{-1}$ are smooth [2].

$$\varphi_2 \circ \varphi_1^{-1} : \varphi_1[U_1 \bigcup U_2] \subset \mathbb{R}^m \rightarrow \varphi_2[U_1 \bigcup U_2] \subset \mathbb{R}^m. \tag{2.3}$$

A C^∞-related pair of charts is depicted in Figure 2.3. Formally, a d-manifold is a separable Hausdorff space $\mathbb{X}$ if at every point $x \in \mathbb{X}$ there is a d-dimensional chart. This means that every point $x \in \mathbb{X}$ has a neighborhood homeomorphic to $\mathbb{R}^d$.

---

[2] A function $f : U \rightarrow \mathbb{R}^d$ is smooth or C^∞-continuous or C^∞ if all coordinate functions have partial derivatives for all orders and types.

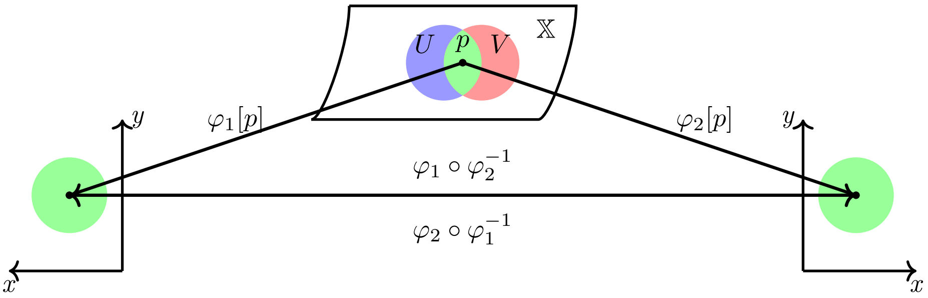

Figure 2.3: Two C^∞-related charts (U, φ_1),(V, φ_2) through the conditions $\varphi_1 \circ \varphi_2^{-1}$ and $\varphi_2 \circ \varphi_1^{-1}$ to be smooth, and $U \bigcap V \neq \emptyset$.

The set of charts (U, φ) that covers a d-manifold $\mathbb{X}$, defines the atlas of $\mathbb{X}$. Furthermore if any pair of charts in the atlas of $\mathbb{X}$ are C^∞-related, this atlas is C^∞. To admit a chart in a C^∞ atlas, it has to be C^∞-related to every chart in the atlas, and it is said that this chart is admissible to that C^∞-atlas. If a given C^∞-atlas contains all admissible charts, it is known as an atlas maximum, and it defines a C^∞-manifold

Definition 2.5 *A C^∞-manifold is a topological manifold together with all the admissible charts of some C^∞-atlas.*

C^∞-manifolds play a major role in the Morse theory, thus for the sake of simplicity, the term manifold is used as synonym of C^∞-manifold.

2.2 Morse theory

Morse theory deals with the relationship between the structures of spaces, and functions defined on those spaces. Specially, this theory draws the relationship between critical points of a smooth function defined on a manifold and the global topology of that manifold. Smooth functions are ideal for data analysis; they are dense, and they can be represented in abstract terms, such as Reeb graphs or Morse-Smale complexes. Although smooth functions admit derivatives of any order in practices, most commonly we just need derivatives of first and second order. Using the first order derivatives of a smooth function $f : \mathbb{R}^n \to \mathbb{R}$, we may define the gradient of f, $\vec{\nabla} f$, as

$$\vec{\nabla} f = \Big(\frac{\partial f}{\partial x_1}, \ldots, \frac{\partial f}{\partial x_n}\Big). \tag{2.4}$$

The gradient of a scalar function is a vector field that points in the direction of steepest ascent. Given a point $p \in \mathbb{R}^n$, $p = (x_1, x_2, \ldots, x_n)$, it is said to be a regular point of f if $\nabla f(p) \neq 0$, and a critical point (CP) otherwise,

$$\frac{\partial f}{\partial x_1}(p) = \frac{\partial f}{\partial x_2}(p) = \ldots = \frac{\partial f}{\partial x_n}(p) = 0. \tag{2.5}$$

The image of a CP, $f(p)$, is called a *critical value* of f. All other values are *regular values* of f. We use second derivatives to further distinguish between different types of CPs. The Hessian of f at the point p_0 is the matrix of second derivatives, i.e. in $\mathbb{M}^3$:

$$\mathbb{H}(p = p_0) = \left(\begin{array}{ccc} \frac{\partial^2 f}{\partial x^2} & \frac{\partial^2 f}{\partial x \partial y} & \frac{\partial^2 f}{\partial x \partial z} \\ \frac{\partial^2 f}{\partial y \partial x} & \frac{\partial^2 f}{\partial y^2} & \frac{\partial^2 f}{\partial y \partial z} \\ \frac{\partial^2 f}{\partial z \partial x} & \frac{\partial^2 f}{\partial z \partial y} & \frac{\partial^2 f}{\partial z^2} \end{array} \right)_{p=p_0} . \tag{2.6}$$

A CP x is *non-degenerate* if the Hessian is non-singular, that is, $\det\mathbb{H}(x) \neq 0$, and degenerate otherwise. The Morse theory deals with a special type of smooth functions, called Morse functions;

Definition 2.6 *Given a smooth function* $f : \mathbb{M} :\rightarrow \mathbb{R}$*, it is a Morse function if*

- *all its CPs are non-degenerate,*
- *all its CPs have distinct function values.*

It is worth to say that the second condition is sometimes dropped. A unique feature of Morse functions is their behavior near CPs, where the gradient is negligible. Given a Morse function in $\mathbb{M}^d$, $f : \mathbb{M}^d \rightarrow \mathbb{R}$, its behavior in a small neighborhood around a CP u, is dominated by the quadratic terms. Even more, we can find local coordinates of $u = (0, 0, \ldots, 0)$ such that there are no higher-order terms

$$f(p) = f(u) - x_1^2 - \ldots - x_q^2 + x_{q+1}^2 + \ldots + x_d^2, \tag{2.7}$$

for every point $p = (x_1, x_2, \ldots, x_d)$ in a small neighborhood of u. This result is known as Morse lemma. From this, it can be shown that u is the only CP in such neighborhood and therefore, u is said to be isolated. The number of minus signs in the quadratic polynomial is the index of the CP, $\text{index}(u) = q$. This index classifies the non-degenerate CPs into d+1 types. This result is equivalent to say that the index of a CP is equal to the number of negative eigenvalues of the Hessian at such critical point. For a 3-manifold, we have four types, minima with index 0, 1-saddles with index 1, 2-saddles with index 2 and maxima with index 3. CPs are often classified in terms of their rank r, and their signature, s, by the notation (r, s). The rank is the number of non-zero eigenvalues of the Hessian matrix at the CP, and the signature is defined as the difference between the number of positive and negative eigenvalues. For instance in $\mathbb{M}^3$, maxima, 2-saddles, 1-saddles and minima are denoted by (3,-3), (3,-1), (3,-2) and (3,3) respectively.

A major result of Morse theory is its ability to define the global shape of a manifold in terms of its CPs since non-degenerate CPs are isolated, and therefore, the topology of its isosurface (also known as level set) is guaranteed not to change between CPs. This results may be summarized in the following theorem;

Definition 2.7 *Let* $\mathbb{M}$ *be a closed manifold and* $f : \mathbb{M} \rightarrow \mathbb{R}$ *a Morse function. Let* $\mathbb{M}_t = \{p \in \mathbb{M} | f(p) \leq t\}$ *for a value* t *of* f*. If* f *has no CPs in [a,b]*$\in \mathbb{R}$*, then* $\mathbb{M}_a$ *and* $\mathbb{M}_b$ *are homeomorphic.*

If there is a CP in $[a, b]$, there is not a homeomorphism between $\mathbb{M}_a$ and $\mathbb{M}_b$ any more. To overcome this hurdle, we need to attach a q-handle to $\mathbb{M}_a$.

Definition 2.8 *A q-handle* D_q^d *corresponding to a CP* p *with index* q *such that* $f(a) < f(p) < f(b)$*, is a d-manifold homeomorphic to a d-ball that is attached through a disjoint union to* M_a*, so that,* $M_a \bigcup D_q^d$ *is diffeomophic to* M_b*.*

A manifold may be constructed by handle decomposition, that is by gluing handles to the manifolds, as seen in Figure 2.4. When handles are attached in increasing order of CPs, the handle decomposition discloses the topological features of a manifold.

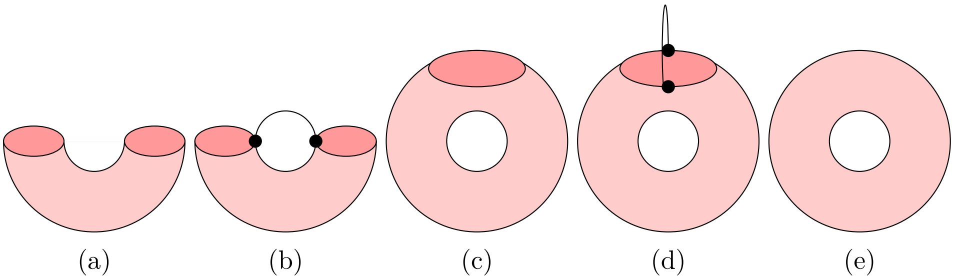

Figure 2.4: Handle decomposition of a torus. Attaching 1-handle corresponding to a 1-saddle (b) to a cylinder (a) is homeomorphic to a capped torus (c). Adding a 2-handle corresponding to a maximum to a capped torus (d) is homeomorphic to a torus (e).

2.2.1 Morse inequalities

The number of CPs of a Morse function $f : \mathbb{M} \to \mathbb{R}$ is limited by the Morse inequalities. The weak and the strong Morse inequalities provide lower bounds to the number of CPs of some index q, c_q, in terms of Betti numbers of the *qth* homology group of $\mathbb{M}$, $\beta_q(\mathbb{M})$ [3]:

Definition 2.9 *Let $\mathbb{M}$ be a manifold of dimension d and $f : \mathbb{M} \to \mathbb{R}$ a Morse function. Then*

(i) weak: $c_q \geq \beta(\mathbb{M})$ *for all q*

(ii) strong: $\sum_{j=0}^{q}(-1)^{q-j}c_j \geq \sum_{j=0}^{q}(-1)^{q-j}\beta_j(\mathbb{M})$ *for all q,*

The strong Morse inequality becomes an equality for $j = d$. Morse inequalities connect the number of CPs of $\mathbb{M}$ with its Euler characteristic, $\chi(\mathbb{M})$, through the Euler-Poincare theorem

$$\chi(\mathbb{M}) = \sum_{q\geq 0}^{d}(-1)^q\beta_q(\mathbb{M}),$$

then

$$\chi(\mathbb{M}) = \sum_{q=0}^{d}(-1)^q\beta_q(\mathbb{M}) = \sum_{q=0}^{d}(-1)^q c_q.$$

2.3 Manifold partitioning

The Morse theory states that all the relevant features of a Morse function and the manifolds defined by its isosurfaces rest on its critical points and the connection between them. Therefore, one may try to decompose a Morse manifold in subsets containing the relevant features of some Morse function defined on it. In many applications understanding the response of a system to a external perturbation is only possible if each of its parts may be analyzed separately, thus a partition of space defined by our physical system is

---

[3] Informally the *qth* Betti number may be understood as the number of q-dimensional holes on a topological surface, i.e. β_0 is the number of connected components, β_1 is the number of “circular” holes, β_2 is the number of two-dimensional “cavities”,...

required. Morse theory provides us with an invaluable topological arsenal for performing such task. Usually the partitioning engines are based on the behavior of level sets (Reeb graphs) or on the the behavior of the gradient (Morse Complex).

2.3.1 Reeb graphs

The creation, destruction, merging, and splitting of connected components of level sets may be recovered by Reeb graphs. Intuitively, the Reeb graph is the result of contracting each connected component of a level set to a point, such that, every node in the graph corresponds to a level set containing a CP and arcs between nodes represent the evolution of the connected components of the level sets between CPs. Formally, the Reeb graph sets an equivalence relationship between points belonging to a common connected component of a level set of a scalar function $f : \mathbb{M} \to \mathbb{R}$

ReebGraph 2.10 *Let $f : \mathbb{M} \to \mathbb{R}$ be a scalar function on a compact manifold $\mathbb{M}$. The Reeb graph of f is the quotient space f in $\mathbb{M} \times \mathbb{R}$ by the equivalence relation $\sim$:*

$$(X_1, f(X_1)) \sim (X_2, f(X_2))$$

if and only if $f(X_1) = f(X_2)$, and X_1, X_2 belong to the same connected component of $f^{-1}(f(X_1))$.

The evolution of the level set of a height function defined on a torus is shown in Figure 2.5. If the Reeb graph is defined over a simply connected Euclidean space, it is a called contour tree.

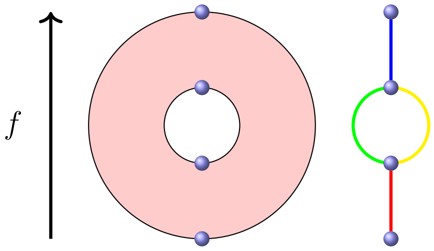

Figure 2.5: (Right) Reeb graph of the height function (f) defined on a torus (left). The CPs of f are the nodes of the Reeb graph, and the arcs divide the torus into sections where level sets have a single connected component.

2.3.2 Morse complex

A manifold may be also be split in submanifolds of lower order whose union leads to the notion of complex. The relationship between level sets, highlighted in Reeb graphs, may be understood in terms of the gradient. Given a Morse function, the gradient flow may be used to decompose a manifold depending on where the flow originated and where it ends. The gradient flow is defined by integral lines and they lead to Morse and Morse-Smale complexes.

Definition 2.11 *Given a Morse function $f : \mathbb{M} \to \mathbb{R}$, a curve $\gamma(t)$ is an integral line of f if $\frac{\partial \gamma(t)}{\partial t} = \nabla f(\gamma(t))$ for all $t \in \mathbb{R}$.*

Because γ is defined for all $t \in \mathbb{R}$, the integral line necessarily approaches a CP, both for t going to $+\infty$ and to $-\infty$. We call these limits the origin *org* and the destination *dest* of the integral line,

$$\begin{aligned} org(\gamma) &= \lim_{t \to -\infty} \gamma(t), & (2.8) \\ dest(\gamma) &= \lim_{t \to \infty} \gamma(t). & (2.9) \end{aligned}$$

f increases along the integral lines which implies that $org(\gamma) \neq dest(\gamma)$. Integral lines exhibit the following properties:

1. Two integral lines are either disjoint or the same.
2. Integral lines cover all $\mathbb{M}$.
3. The origin and destination of an integral line is either a CP of f or ∞.

The first property is a consequence of the existence and Uniqueness Theorems of differential equations, and it implies that every point in $\mathbb{M}$ has exactly one integral line passing through it. This property suggests we may decompose the manifold into integral lines or unions of integral lines with shared characteristics.

Definition 2.12 *The stable manifold of a CP u of f, $S(u)$, is the point itself together with all regular points whose integral lines end at u. Symmetrically, the unstable manifold of u, $U(u)$, is the point itself together with all regular points whose integral lines originate at u. More formally,*

$$\begin{aligned} S(u) &= u \cup x \in \mathbb{M} | dest(\gamma_x) = u, & (2.10) \\ U(u) &= u \cup x \in \mathbb{M} | org(\gamma_x) = u. & (2.11) \end{aligned}$$

The function increases along integral lines. It follows that $f(u) \geq f(x)$ for all point x in $S(u)$. This is the reason why $S(u)$ is sometimes referred as the descending manifold of u. Symmetrically, $f(u) \leq f(y)$ for all points y in $U(u)$ and it is sometimes referred to as ascending manifold of u. Viewing $\mathbb{M}$ as a terrain, $S(u)$ and $U(u)$ correspond to “basins” and “mountains” respectively. Subsets of $S(u)$ and $U(u)$ of a function in $\mathbb{R}^3$ are shown in Figure 2.6.

Suppose the dimension of $\mathbb{M}$ is d and the index of the CP u is q. Then there is a q-sphere of directions along which integral lines approach u. It can be proved that together with u, these integral lines form an open ball of dimension q, called open q-cell and the $S(u)$ is a submanifold homeomorphic to $\mathbb{R}^q$ that is immersed in $\mathbb{M}$. The complex formed by the descending manifolds of a Morse function $f : \mathbb{M} \to \mathbb{R}$, is called the Morse complex.

For instance, let’s analyse the Morse complex of the function $f(x, y) = -x^4 + 4(x^2 - y^2) - 3$.

$$\begin{aligned} \mathbb{R}^2 &\to \mathbb{R} & (2.12) \\ f(x,y) &\to -x^4 + 4(x^2 - y^2) - 3, \end{aligned}$$

The CPs of this function are such points where its gradient vanishes, $\vec{\nabla} f(x, y)$

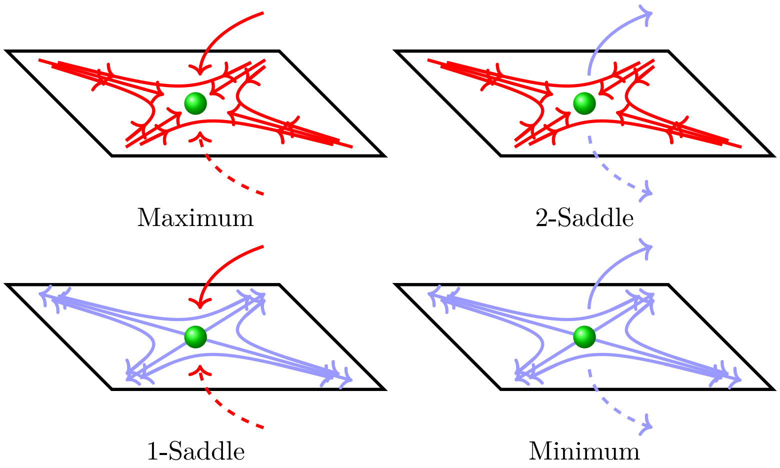

Maximum

2-Saddle

1-Saddle

Minimum

Figure 2.6: Subsets of S (red) and U (blue) manifolds of $f : \mathbb{R}^3 \to \mathbb{R}$ for the four kinds of CPs of f.

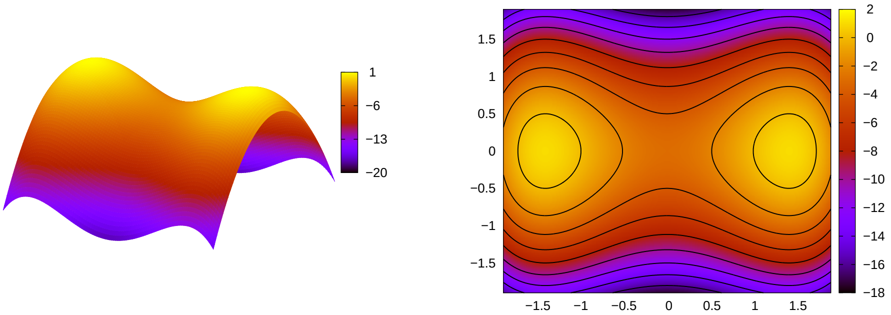

Figure 2.7: (Left) $f(x,y) = -x^4 + 4(x^2 - y^2) - 3$ and (right) its contour lines.

$$\vec{\nabla} f(x,y) = (-4x^3 + 8x)\vec{i} - 8y\vec{j} = 0\vec{i}, 0\vec{j}. \tag{2.13}$$

$f(x,y)$ exhibits three CPs $(\sqrt{2},0)$, $(-\sqrt{2},0)$ and $(0,0)$. Glancing at Figure 2.7, we can realize that maxima are at $(\sqrt{2},0)$ and $(-\sqrt{2},0)$, and the saddle point at $(0,0)$. Nevertheless, a complete analysis of the function requires the calculation of its Hessian matrix and its eigenvalues at the CPs

$$\mathbb{H}(x,y) = \begin{pmatrix} -12x^2 + 8 & 0 \\ 0 & -8 \end{pmatrix}$$

Since $\mathbb{H}(x,y)$ is diagonal everywhere, its eigenvalues at every point of $\mathbb{R}^2$ are $-12x^2+8$ and -8. At $(\sqrt{2},0)$ and $(-\sqrt{2},0)$ both eigenvalues are negatives (-16,-8), then maxima are located at these positions. At the origin, $(0,0)$, $\mathbb{H}$ eigenvalues have different sign (8,-8), indicating therefore the presence of a saddle point. The indices of CPs in $\mathbb{R}^2$ are two for maxima and one saddle points.

Although the integral lines of $f(x,y)$ are not here displayed, the behavior of $\vec{\nabla} f(x,y)$ is showed in Figure 2.8. Since integral lines are tangent at every point of space to $\vec{\nabla} f(x,y)$, they exhibit a similar behavior; all of them die at maxima forming a plane (a 2-sphere), that is, $(\sqrt{2},0)$ and $(-\sqrt{2},0)$ are $dest(\gamma)$ of these lines. The stable manifold of $(-\sqrt{2},0)$ and $(\sqrt{2},0)$, Ω_a and Ω_b respectively are displayed in Figure 2.8. The stable and unstable manifold of the saddle point form lines (1-sphere) parallel to the Y and X directions respectively. The Morse complex of $f(x,y)$ is formed by two disjoint regions as shown in Figure 2.8.

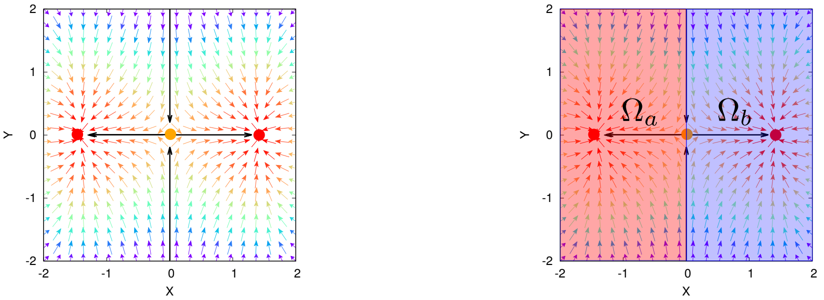

Figure 2.8: (Left) $f(x,y) = -x^4 + 4(x^2 - y^2) - 3$ vector field, $\vec{\nabla} f(x,y)$. The thick black lines are symbolic representations of the integral lines connecting the CPs. (Right) Topological partition obtained from $\vec{\nabla} f(x,y)$. Ω_a and Ω_b stand for the stable manifolds of each of the maxima of $f(x,y)$.

It is also possible to classify points according to both $dest(\gamma)$ and $org(\gamma)$, leading to a generalization of the Morse complex, called the Morse-Smale complex. To consistently define this complex it is required that S and U intersect transversally;

Definition 2.13 *Two submanifolds $\mathbb{M}_a$ and $\mathbb{M}_b$ with dimension a and b respectively, belonging to $\mathbb{M}$ with dimension d, are said to intersect transversally if the tangent space of $\mathbb{M}_a$ and the tangent space of $\mathbb{M}_b$ generate the tangent space of $\mathbb{M}$, or when their intersection is empty. When $a+b=d$, the intersection is a single point.*

Similarly to the Morse complex, the Morse-Smale complex is defined in terms of the integral lines of some Morse-Smale function

Definition 2.14 *A Morse function is Morse-Smale if its stable and unstable manifolds only intersect transversally.*

This condition implies that a pair of CPs of a Morse-Smale function f connected by an integral line cannot have the same index, and, the index of the CP at the origin of such integral line is less than the index of the CP at the destination. Similarly to the Morse complex, we may define a Morse-Smale complex as follows:

Definition 2.15 *Given a Morse-Smale function f, the Morse-Smale complex of f is the complex formed by the intersection of the Morse complex of f and the Morse complex of $-f$.*

The cells of the Morse-Smale complex are formed by the set of points whose associated integral lines share a common *orig* and *dest*.

Since the Morse complex of f and $-f$ are transversal, the boundary of every $S(u)$ is a union of $S(u)$s of lower dimension. The intersection of a S of dimension q of $f \in \mathbb{M}_d$ and an U of dimension p of the same Morse function has dimension $q+p-d$. The intersections of $S(u)$s constructs the Morse Smale complex adding one dimension at a time.

2.4 Dynamical systems

Morse theory provides us with the proper machinery to analyze the topology a manifold in terms of the CPs of some Morse function defined in such manifold. Quantum chemical topology was originally formulated within dynamical systems theory. The aim of this section is to show that many of the concepts used in both theories are equivalent.

Consider a system of n differential equations, F. We are interested in its set of solutions $y_j(t; x \in \mathbb{R}^N, c_\alpha \in W)$ defined over a manifold $\mathbb{M}$

$$F_i\Big(y_i; c_\alpha; t; \frac{\partial y_j}{\partial t}, \frac{\partial^2 y_j}{\partial t^2}, \ldots; x_l; \frac{\partial y_j}{\partial x_l}, \frac{\partial^2 y_j}{\partial x_l x_m}, \ldots; \int dx_1, \ldots\Big) = 0, \tag{2.14}$$

where

$$\begin{array}{ccc} 1 \leq i & , & j \leq n \\ 1 \leq l & , & m \leq N \\ 1 \leq & \alpha & \leq k \end{array} \tag{2.15}$$

where c_α denotes the control parameters which are the elements of the set W referred to as the control space of dimension k. x and t may be regarded as space and time coordinates. In order to make the problem much more tractable, we can apply a sequence of simplifications;

1. We assume that the Equation 2.14 involves neither integrals, space derivatives nor space dependence:

$$F_i = \Big(y_i; c_\alpha; t; \frac{\partial y_j}{\partial t}, \frac{\partial^2 y_j}{\partial t^2}, \ldots,\Big) = 0. \tag{2.16}$$

2. Moreover, we assume that Equation 2.16 has no higher derivatives than the first order $\frac{\partial y_i}{\partial t}$:

$$F_i = \frac{\partial y_i}{\partial t} - f_i(y_j; c_\alpha; t) = 0. \tag{2.17}$$

   Systems of equations described by Equation 2.17 are called dynamical systems.

3. Further simplification is achieved if $f_i(y_j; c_\alpha; t)$ is time independent:

$$F_i = \frac{\partial y_i}{\partial t} - f_i(y_j; c_\alpha) = 0. \tag{2.18}$$

   A system of equations given by Equation 2.18 is called an autonomous dynamical system.

The integration of Equation 2.17 under some initial conditions yields a unique set of solutions $y(c_\alpha, t)$, which are known as trajectories in $\mathbb{M}$. Any trajectory fulfills the properties previously cited for the gradient lines of some scalar field (Section 2.3.2). Conversely trajectories do not start or end at CPs of some scalar field, but at points where $f_i(y_j; c_\alpha; t) = 0$ (we shall see that for a particular kind of dynamical system these CPs match with those of some scalar field). These points are the CPs of the dynamical system, also called singular or equilibrium points. CPs of a dynamical system may be classified through the analysis of its trajectories y_j, in the neighborhood of a CP, $t_c, y^c = y(t_c; c_\alpha)$. A linear expansion of y_j near t_c leads to

$$\frac{\partial y_i}{\partial t} = f_i(y_j; c_\alpha; t_c) \approx f_i(y^c; c_\alpha; t_c) + \mathbb{J}(t - t_c) = \mathbb{J}(t - t_c), \tag{2.19}$$

$$\tag{2.20}$$

where $\mathbb{J}$ is the Jacobian matrix of the system at t_c,

$$\mathbb{J} = \frac{\partial f(y_i; c_\alpha; t_c)}{\partial t}\Big|_{y_i = y^c}. \tag{2.21}$$

Shifting the coordinates origin to t_c, the linear system may be written as

$$\frac{\partial y_i}{\partial t} = \mathbb{J}(t). \tag{2.22}$$

Being $\mathbb{J}$ a symmetric matrix it is possible to find an orthogonal matrix $\mathbb{U}$ that diagonalizes $\mathbb{J}$ at t_c,

$$\mathbb{U}^t \mathbb{J} \mathbb{U} = diag(\lambda_i), \tag{2.23}$$

where λ_i are the eigenvalues of $\mathbb{J}$. The eigenvectors of $\mathbb{J}$, η, define a new coordinate system,

$$y = \mathbb{U}\eta \tag{2.24}$$

$$\frac{\partial y}{\partial t} = \mathbb{U}\frac{\partial \eta}{\partial t} \tag{2.25}$$

$$\tag{2.26}$$

Replacing in the previous equations,

$$\frac{\partial \eta}{\partial t} = diag(\lambda_i)\eta, \tag{2.27}$$

whose trivial solution is

$$\eta_i(t) = \eta_i(t_o)e^{\lambda_i(t - t_o)}. \tag{2.28}$$

The eigenvalues of $\mathbb{J}$, λ_i, are the characteristic or Lyapunov's exponents, and define the behavior of the dynamical system in the neighborhood of a CP. λ_i are in general complex numbers. A CP is called hyperbolic if none of its characteristic exponents have a zero real part. Otherwise it is a non-hyperbolic CP, and the linear expansion is not enough to characterize it. The index of a CP, $I(f, y^c)$, is defined by the number of positive Lyapunov's exponents. Similarly to the Morse rule, the Poincaré-Hopf theorem limits the number of CPs of a dynamical system: if $\mathbb{M}$ is a compact manifold and $f(y; c_\alpha, t)$ has only isolated hyperbolic CPs, then they fulfill the following relation:

$$\sum (-1)^{I(f,y^s)} = \chi(\mathbb{M}), \tag{2.29}$$

where $\chi(\mathbb{M})$ is the Euler characteristic of the manifold $\mathbb{M}$. A hyperbolic CP may be a maximum, a minimum or a saddle point. For a given point $y_o \in \mathbb{M}^q$ the limit sets of $y_o(c_\alpha, t)$ for $t \to -\infty$ and $t \to +\infty$ are referred to as α-limit and ω-limit, respectively. A maximum is characterized by $I(X, y^s) = 0$, and is also known as attractor. The set of trajectories that have an attractor as ω-limit defines the stable manifold of such CP, and all the points within constitutes the basin (Ω) of such attractor. The boundary points between basins are called separatrices, defined by the so-called zero flux condition:

$$\int_\Omega f(f_i(y_j; c_\alpha; t))dt = 0. \tag{2.30}$$

α and ω-limits lead to a partition of $\mathbb{M}$ into basins and separatrices similar to that defines by the Morse complex. Conversely, a minimum or repeller in $\mathbb{R}^q$ is characterized by $I(X, y^s) = q$. The set of trajectories that have an attractor as α-limit defines the unstable manifold of such CP.

An interesting property of autonomous dynamical systems (Equation 2.18) is that they can be derived from the gradient of some potential function $V(y_j; c_\alpha)$, $f(y_j; c_\alpha) = \nabla V(y_j; c_\alpha)$. Such system is called a gradient dynamical system,

$$f_i(y_j; c_\alpha; t) = \frac{\partial y_i(c_\alpha; t)}{\partial t} = \frac{\partial V(y_j; c_\alpha)}{\partial y_i}, \tag{2.31}$$

and the CPs of the system are defined by

$$\frac{\partial V(y_j; c_\alpha)}{\partial y_i} = 0. \tag{2.32}$$

Furthermore, if V is a Morse function all the concepts previously defined within the Morse theory find some equivalent in the dynamical systems theory. The trajectories of the gradient dynamical system defined by $\vec{\nabla} V$ are nothing but the integral lines of V, and they may be written as a set of parametric equations

$$y(t) = y(t_o) + \int_{t_o}^{t} \vec{\nabla} V(y_j; c_\alpha)dt. \tag{2.33}$$

α and ω limit definitions match with those of $org(y)$ and $dest(y)$ in the Morse theory jargon, and therefore, the stable and unstable definitions are also the same. Furthermore the basins of such dynamical system, are exactly the basins of the Morse complex of the potential function V, leading thereby to the same topological partition of $\mathbb{M}$.

The nomenclature of the CPs, by contrast, is ambiguous; whereas the number of positive eigenvalues of the Hessian matrix is used as index in the dynamical systems framework, the number of negative eigenvalues is used the Morse theory. In what follows we shall use the nomenclature (r, s) for convenience.

It is worthy to notice that for a gradient dynamical system the following relationship holds,

$$\mathbb{J}(f) = \mathbb{J}(\vec{\nabla} V) = \mathbb{H}(V), \tag{2.34}$$

Critical Point	I	λ	(r, s)
Maximum (attractor)	0	3	(3,-3)
2-saddle	1	2	(3,-1)
1-saddle	2	1	(3, 1)
Minimum (repeller)	3	0	(3, 3)

Table 2.1: Classification of the critical points for a $\mathbb{M}^3$ manifold. I and λ and (r,s) stand for the dynamical system, Morse theory and $(r,\ s)$ nomenclature, respectively.

where $\mathbb{H}(V)$ is the Hessian matrix of V. Thus, the Lyapunov's exponents are the eigenvalues of $\mathbb{H}(V)$. Since this matrix is symmetric, it only shows real eigenvalues, and therefore, only hyperbolic CPs are present in gradient dynamical systems.

Chapter 3

Quantum chemical topology

Sommaire

There is no doubt that chemistry is founded in three main aspects; chemical structure, properties and reactivity. The former is completely associated with the arrangement of atoms in the space. The second and the third aspects are consequences of the interactions between atoms through chemical bonds. Therefore, atoms and chemical bonds constitutes the fundamental blocks in chemistry. Although many strategies have been put forward for defining atoms in a quantum mechanical framework, the quest for an unambiguous quantum definition of chemical bond still remains. The lack of quantum mechanical operator associated with chemical bonding has created a gap between classical concepts such as electron shells, lone pairs, aromaticity, (hyper-) conjugation, strain, etc and quantum theory, and thus hampers any understanding of their mechanistic origin.

To overcome this gap several approaches have been developed to provide a quantum mechanical equivalent of such “fuzzy” concepts in Hilbert and in real space. Whereas Hilbert space approaches are based on some unitary transformation of the occupied orbitals of the system, they are somehow unbiased since they depend on the initial set of orbitals. Real space approaches completely exploit the topological properties of some scalar field as explained in Chapter 2. In this chapter we will focus in this second approach that is often termed as quantum chemical topology.

3.1 Quantum chemical topology

Quantum chemical topology (QCT) [38] embraces all work that shares the central idea of the gradient vector field of some scalar function as partitioning scheme of a quantum system. As shown in Chapter 2 any vectorial field may be defined as a dynamical system able to split a manifold into basins (Ω_a), defined as the set of trajectories which share a common ω-limit. In QCT the dynamical system is defined by the gradient vector field of some 3D scalar field, therefore this partition is equivalent to those obtained by the Morse complex of such scalar field. As any trajectory (or integral line) belongs to one and only one basin, it does not transverse the surface of any basin. This result is known as “zero flux condition” and is mathematically expressed as

$$\vec{\nabla} f(\mathbf{r}) \cdot \vec{n}(\mathbf{r}) = 0, \tag{3.1}$$

where $\vec{n}(\mathbf{r})$ is a normal vector to the surface at point $\mathbf{r}$ and $\vec{\nabla} f(\mathbf{r})$ is the gradient of $f(\mathbf{r})$ at $\mathbf{r}$. One consequence of the zero flux condition is that the partition obtained for some vectorial field is always exhaustive

$$\cup_a^M \Omega_a = \mathbb{R}^3, \qquad \Omega_a \cap \Omega_b = \emptyset, \qquad a \neq b, \tag{3.2}$$

where M is the number of basins. Once the system is split into non-overlapping regions, the next step in QCT is to assign a physical/chemical significance to these regions in order to recover the distribution in real space of some property. The meaning of Ω_a is inherited from the scalar field whose gradient has been used as partitioning engine. The scalar fields used in QCT are usually defined in terms of density matrices and may be easily visualized by the representation of their isosurfaces or contour lines.

3.2 Topology of the electron density

The electron density $\rho(\mathbf{r})$ was already introduced in Chapter 1 as well as its paramount role in the electronic structure of matter through the Hohenberg and Kohn theorems [4].

Its gross form is dominated by maxima at the nuclear positions. However, at these positions its gradient shows a discontinuity resulting in in a cusp. As shown by Kato [39] this cusp condition may be mathematically described as

$$\lim_{\mathbf{r_{iA}}\to 0}\left[\frac{\partial\bar{\rho}(\mathbf{r})}{\partial\mathbf{r}}+2Z_A\bar{\rho}(\mathbf{r})\right]=0, \tag{3.3}$$

where $\bar{\rho}(\mathbf{r})$, Z_A and $\mathbf{r_{iA}}$ are the spherical average of $\rho(\mathbf{r})$, the nuclear charge and the coordinates of the nucleus A, respectively. Conversely the behavior of $\rho(\mathbf{r})$ far from nuclei positions is described by an exponential decay [40]

$$\rho(\mathbf{r}) \propto e^{-(\sqrt{2\mathrm{I}})\mathbf{r}}, \tag{3.4}$$

where I is the first ionization potential. The cusp condition avoids $\rho(\mathbf{r})$ to be a true differentiable field. However it is possible to replace the cusp at nuclear positions by maxima, identifying the nuclear positions as (3,-3) CPs. Quantum atoms may be defined then as basins of $\rho(\mathbf{r})$. Since (3,-1) CPs always take place between maxima, they have been identified as indicators of chemical bonding, and therefore they are known as bond critical points (BCPs). It is said that there is a chemical bond between two atoms if they are connected through a BCP. From the topology of $\rho(\mathbf{r})$, a molecular system may be envisaged as a set of atoms connected through interatomic surfaces (IASs). We note that an IAS only appears if there is a BCP between two basins (atoms). The CPs of $\rho(\mathbf{r})$ do not only identify chemical bonds, but also provide insight about their nature. $\vec{\nabla}\rho(\mathbf{r})$ represents the charge flow through the system, thus stable and unstable manifolds of CPs of $\rho(\mathbf{r})$ represent directions of charge concentration and depletion respectively. Maxima are characterized by 3D stable manifolds, this is a charge concentration in all directions. By contrast, stable and unstable manifolds of a BCP form a plane and a line, respectively; the charge is depleted through a integral line which connects the two bonded atoms, known as bond path, and there is a charge concentration in the plane perpendicular to such line. The presence of BCP may be then identified with the accumulation of $\rho(\mathbf{r})$ in a plane. The two blocks of chemistry are therefore recovered; atoms and bonds. Joining all maxima through BCPs following bond paths we may render the molecular graph of a chemical system, and therefore, its molecular structure.

Further CPs have less clear chemical meaning and they are often connected with regions where it is expected to find some kind of strain. (3,1) CPs appear in plains limited by BCPs, and they represent a plane of charge depletion (the unstable manifold of a (3,-1) CP is a plane). Minima are characterize by charge depletion along all directions and they are identified as (3,3) CPs.

Besides of identifying atoms, the basins of $\rho(\mathbf{r})$ are the only regions where the virial theorem is defined (apart from $\mathbb{R}^3$) and they may be considered as open quantum subsystems leading to the quantum theory of atom in molecules (QTAIM) owed to Bader [41]. In the literature QTAIM is often used for referring to the topological analysis of $\rho(\mathbf{r})$.

3.3 The electron localisation function

The electron localization function (ELF) [42] is a powerful tool to identify regions where electrons are localized. The ELF was derived by Becke et Edgecombe expanding the Hartree-Fock spherically averaged same-spin conditional probability density

$$P^{\sigma\sigma}_{cond}(\mathbf{r},s)=\frac{1}{3}\left[\tau_\sigma(\mathbf{r})-\frac{1}{4}\frac{|\vec{\nabla}\rho_\sigma(\mathbf{r})|^2}{\rho(\mathbf{r})_\sigma}(\mathbf{r})\right]\mathbf{s}^2+\ldots, \tag{3.5}$$

where the arguments $(\mathbf{r}, \mathbf{s})$ denote the spherically averaged on a shell of radius $\mathbf{s}$ about the reference point $\mathbf{r}$, and $\tau_\sigma(\mathbf{r})$ is the positive definite kinetic energy density introduced in the meta-GGA framework 1.159.

A number of insights may be extracted from $P^{\sigma\sigma}_{cond}(\mathbf{r}, \mathbf{s})$; the smaller the probability of finding a second like-spin electron near the reference point, the higher the localization of the reference electron. Hence, the coefficient of the quadratic term in Equation 3.5 is an index of electron localization

$$D_\sigma(\mathbf{r}) = \tau_\sigma(\mathbf{r}) - \frac{1}{4}\frac{|\vec{\nabla}\rho_\sigma(\mathbf{r})|^2}{\rho_\sigma(\mathbf{r})}. \tag{3.6}$$

It may be proved that D_σ is necessarily non-negative and it vanishes in the special case of one-electron systems and hence also vanishes in multielectron systems in regions dominated by a single localized σ-spin orbital, reinforcing therefore the interpretation of D_σ as a measure of electron delocalization. To provide an index of electron localization that renders a proper visualization, Becke and Edgecombe defined ELF as

$$\mathrm{ELF}(\mathbf{r}) = (1 + \chi_\sigma(\mathbf{r})^2)^{-1}, \tag{3.7}$$

where

$$\chi_\sigma(\mathbf{r}) = \frac{D_\sigma(\mathbf{r})}{D^0_\sigma(\mathbf{r})}, \qquad D^0_\sigma(\mathbf{r}) = \frac{3}{5}(6\pi^2)\rho^{5/3}_\sigma(\mathbf{r}). \tag{3.8}$$

$D^0_\sigma(\mathbf{r})$ corresponds to an HEG with equal spin density as the real system. ELF is bounded from below and above,

$$0 \leq \mathrm{ELF}(\mathbf{r}) \leq 1, \tag{3.9}$$

The upper limit ELF($\mathbf{r}$)=1 corresponds to perfect localization, and the value ELF($\mathbf{r}$)=1/2 to electron gas-like behavior. Strictly speaking ELF($\mathbf{r}$) maxima identify regions dominated by a single spin-orbital. Since at Hartee-Fock level, unlike spin electrons are independent $D_\alpha(\mathbf{r})$ and $D_\beta(\mathbf{r})$ are identical, and therefore ELF($\mathbf{r}$) maxima identify regions with high probability of finding an electron pair, i.e. atomic shells, core, bonding, or lone pairs. Contrary to the topological analysis of $\rho(\mathbf{r})$, CPs further than maxima do not convey any clear chemical significance, and therefore the topological analysis of ELF($\mathbf{r}$) is limited to the localization of its maxima and the characterization of its basins.

Classification of the ELF(r) basins

The geometrical arrangement of the ELF($\mathbf{r}$) maxima allows to differentiate two types of basins: core and valence. The former are highly localized around nuclei with Z > 2 and denoted by C(A) where A stands for the atomic symbol of the atom. The latter fill the remaining spaces. The localization of valence basins closely matches with the electron pair arrangements defined by Gillespie in the Valence Shell Electron Pair Repulsion model (VSEPR), and therefore it provides a mathematical support for Lewis' valence theory and for VSEPR. Valence basins are denoted by V(A,B), where A and B are the atomic center which share the basin. The synaptic order of a valence basin [43] is defined as the number of core basins which have a common boundary with it. According to their synaptic order the valence basins can be asynaptic (synaptic order zero), monosynaptic, disynaptic or polysinaptic (see Table 3.1). F centers in solid state, lone pairs, two-center bonds are examples of asysnaptic, monosynaptic and dysnaptic basins, respectively. Basins with synaptic higher order are characteristic of polyatomic bonding, such as the trisynaptic basin V(H,B,H) in diborane [43].

Synaptic order	Name	Symbol
0	Asynaptic	
1	Monosynaptic	V(A)
2	Disynaptic	V(A,B)
3	Trisynaptic	V(A,B,C)
>3	Polysynaptic	V(A,B,C,...)

Table 3.1: ELF($\mathbf{r}$) basin classification according its synapticity.

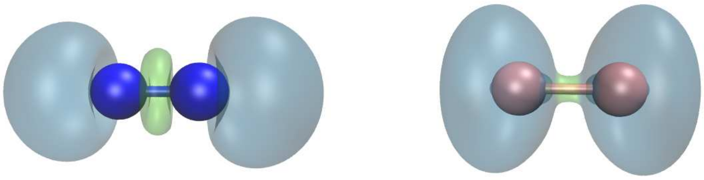

Figure 3.1: ELF($\mathbf{r}$) localisation domains for: N_2(f=0.8)(left), F_2(f=0.6)(right). Monosynaptic and disynaptic basins are coloured in cyan and green respectively.

Contrary to $\rho(\mathbf{r})$, ELF($\mathbf{r}$) is specially well suited for visualization analysis, since it is bounded from above and from below. Additionally to the partition induced by the gradient of ELF($\mathbf{r}$), we can analyze the partition defined by its level sets, i.e. the Reeb Graph. In the ELF($\mathbf{r}$) parlance, a domain is defined as a region bounded by a closed level set ELF($\mathbf{r}$)=f. An f-localization domain [44] is the subset of points such that each point satisfies ELF($\mathbf{r}$)>f. If a localization domain surrounds as much as one maximum it is called irreducible, otherwise it is reducible. Depending on the nature of the basins contained in a domain, it is possible to differentiate three types of domains. Core domains only contain core maxima, valence domains only valence maxima and composite domains contain both valence and core ones (see Figure 3.1).

3.4 Kinetic energy density based descriptors

Among the scalar fields proposed to analyze chemical interactions, scalar fields based on any of the forms of the kinetic energy density are specially useful for the visual analysis of chemical interactions. The success of this family of scalar fields rests on the decrease in the interatomic kinetic energy during the formation of a covalent interaction [45, 46, 47]; therefore any function able to map this variations should be a good candidate as a real space bonding indicator. It is well known that there is an infinity of kinetic energy densities; the only requirement is that they integrate to the total kinetic energy of the system T. [48, 49]

$$T = \int d\mathbf{r}\tau_g(\mathbf{r}), \tag{3.10}$$

where $\tau_g(\mathbf{r})$ is any form of the kinetic energy density. Two particular forms of τ_g have been widely use in the literature $\tau(\mathbf{r})$ and $K(\mathbf{r})$

$$\begin{aligned} K(\mathbf{r}) &= -\frac{1}{2}\sum_i^{occ} n_i\psi_i(\mathbf{r})\nabla^2\psi_i(\mathbf{r}) && (3.11)\\ \tau(\mathbf{r}) &= \frac{1}{2}\sum_i^{occ} n_i\vec{\nabla}\psi_i(\mathbf{r})\vec{\nabla}\psi_i(\mathbf{r}), && (3.12)\end{aligned}$$

where ψ_i are real natural orbital and n_i their occupation numbers such that $\rho(\mathbf{r}) = \sum_i n_i\psi_i(\mathbf{r})\psi_i(\mathbf{r})$. As kinetic energy densities both of these function integrates to the same total kinetic energy density, but they differ locally. Whereas $\tau(\mathbf{r})$ is positive everywhere, $K(\mathbf{r})$ exhibits positive and negative values and is the definition used by Schrödinger. Both definition are related via the Laplacian of the electron density.

$$K(\mathbf{r}) = -\frac{1}{4}\nabla^2\rho(\mathbf{r}) + \tau(\mathbf{r}). \tag{3.13}$$

Since $\nabla^2\rho(\mathbf{r})$ is a divergence term, its net contribution to T cancels

$$\int \nabla^2\rho(\mathbf{r}) = 0. \tag{3.14}$$

The positive definite condition of $\tau(\mathbf{r})$ enables the interpretation of its local behavior in terms of classical effects, and thus many chemical bonding descriptors have profited from this property. It worthy noticing that for a Hartree-Fock wave function Equation 3.11 becomes

$$\tau(\mathbf{r}) = \frac{1}{2}\sum_{i=1}^{occ} |\vec{\nabla}\psi_i(\mathbf{r})|^2, \tag{3.15}$$

where $\psi_i(\mathbf{r})$ are occupied Hartree-Fock orbitals. If ψ_i are replaced by Kohn-Sham orbitals Equation 1.159 of Chapter 1 is obtained. Contrary to Equation 3.15 , Equation 1.159 integrates to the Kohn-Sham kinetic energy.

The limiting behavior of $\tau(\mathbf{r})$ at $\mathbf{r} = 0$ and $\mathbf{r} \to \infty$ is determined by the von Weizsäcker kinetic energy density [50] $\tau_w(\mathbf{r})$ as introduced in Equation 1.161 of Chapter 1. It may be shown that it constitutes a rigorous lower bound for $\tau(\mathbf{r})$. Although $\tau_w(\mathbf{r})$ is not a kinetic energy density in the sense that it does not satisfies Equation 3.10 and it integrates to the von Weizsäcker correction to the Thomas-Fermi model, it constitutes a useful tool for revealing atomic and molecular structure [51, 52].

3.4.1 Bonding descriptors based on $\tau(\mathbf{r})$

The chemical content of $\tau(\mathbf{r})$, was already used by Schmider and Becke to define the localized-orbital locator (LOL) [53]. LOL is defined from the dimensionless variable $t(\mathbf{r})$

$$t(\mathbf{r}) = \frac{\tau_{TF}(\mathbf{r})}{\tau(\mathbf{r})}. \tag{3.16}$$

The function $t(\mathbf{r})$ is bounded by zero from below, but has no an upper boundary:

$$0 \leq t(\mathbf{r}) < \infty. \tag{3.17}$$

To circumvent this problem, they proposed to map $t(\mathbf{r})$ onto the range [0,1]. They referred to this map as ν:

$$\nu(\mathbf{r}) = \frac{t(\mathbf{r})}{1+t(\mathbf{r})} = \frac{1}{1+\frac{\tau(\mathbf{r})}{\tau_{TF}(\mathbf{r})}}. \tag{3.18}$$

LOL refers both to $t(\mathbf{r})$ and to its bounded counterpart $\nu(\mathbf{r})$. In what follows, we shall refer to $t_{LOL}(\mathbf{r}) = \tau(\mathbf{r})/\tau_{TF}(\mathbf{r})$ as the LOL kernel. The properties of this dimensionless ratio were already discussed by Finzel [54]. At the positions of the stationary points of localized orbitals, $t_{LOL}(\mathbf{r})$ is driven to small values ($\nu \to 1$). In regions dominated by the overlap of localized orbitals, $t_{LOL}(\mathbf{r})$ attains large values ($\nu \to 0$). Thus, the chemical content of LOL is similar to that of ELF($\mathbf{r}$).

3.4.2 Bonding descriptors based on $\tau_w(\mathbf{r})$

The term $\tau_w(\mathbf{r})$ is the kinetic energy density in the absence of the Pauli principle, hence it accounts for the bosonic character of the system. As aforementioned, $\tau(\mathbf{r})$ is bounded from below by $\tau_w(\mathbf{r})$, they exhibit the same limiting behavior at near and far way from the nuclear coordinates. Moreover $\tau_w(\mathbf{r})$ is exact for any system described by a single spatial orbital [55]. In many electron systems, it also approaches $\tau(\mathbf{r})$ for those systems that are well described by strongly localized orbitals in separate regions. Additionally, $\tau_w(\mathbf{r})$ is the kinetic energy density of the marginal probability amplitude introduced by Hunter some time ago [56]. $\tau_w(\mathbf{r})$ may be thereby understood as a measure of the single particle character of the system. Because a localized electron pair behaves as a single particle, namely as a boson, its kinetic energy density is given by $\tau_w(\mathbf{r})$. This was already noticed by Bohórquez *et al.* who proposed a partition of molecular space based on the local behavior of $\tau_w(\mathbf{r})/\rho(\mathbf{r})$, valid for every pair of atoms connected through a BCP[51]. They also introduced the localized electron detector LED defined as the local momentum associated with $\tau_w(\mathbf{r})/\rho(\mathbf{r})$, $\tilde{P}(\mathbf{r})$:

$$\tilde{P}(\mathbf{r}) = -\frac{\vec{\nabla}\rho(\mathbf{r})}{2\rho(\mathbf{r})}. \tag{3.19}$$

Contrary to all descriptors hitherto introduced, $\tilde{P}(\mathbf{r})$ is not a scalar field, but a vectorial field. The analysis of LED is based on the visualization of the modulus of $\tilde{P}(\mathbf{r})$, ($|\tilde{P}(\mathbf{r})|$), and not on the partition induced by $\tilde{P}(\mathbf{r})$ itself. As argued by Bohórquez *et al.* , critical points of $\tilde{P}(\mathbf{r})$ match with those of $\rho(\mathbf{r})$, and therefore not further partitions need to be analyzed. Just as for $t_{LOL}(\mathbf{r})$, we may rescale $\tau_w(\mathbf{r})$ by $\tau_{TF}(\mathbf{r})$ defining the dimensionless variable $t_{bose}(\mathbf{r})$ [52] as:

$$t_{bose}(\mathbf{r}) = \frac{\tau_w(\mathbf{r})}{\tau_{TF}(\mathbf{r})}, \tag{3.20}$$

$t_{bose}(\mathbf{r})$ carries the same chemical information as $\tau_w(\mathbf{r})$; both account for the single particle character of the system.

Similar to $\tau_w(\mathbf{r})$ and $\tau(\mathbf{r})$, $t_{bose}(\mathbf{r})$ is a lower bound to $t_{LOL}(\mathbf{r})$, and they approach each other in regions well described by a single orbital, as it occurs where there is electron pair localization [57]. We may establish a parallelism between both functions: if t_{LOL} is understood as an indicator of positions where localized orbitals attain their stationary points, t_{bose} may be understood as a locator of the stationary points of the electron density. As explained by Savin, at regions where localized orbitals attain their maxima, $|\vec{\nabla}\rho(\mathbf{r})|$ is expected to be close to 0, and both functions t_{LOL} and t_{bose} are driven to small values [58]. Thus, one requirement (though not sufficient) for electron localization is small values of $|\vec{\nabla}\rho(\mathbf{r})|$, and therefore of $\tau_w(\mathbf{r})$ as well as t_{bose}. Note that the opposite is not true; not all regions of low values of $|\vec{\nabla}\rho(\mathbf{r})|$ involve maxima of localized orbitals. In this regard $t_{bose}(\mathbf{r})$ contains more chemical information than $t_{LOL}(\mathbf{r})$; it shows minima at regions where the Pauli repulsion accounted for the Pauli kinetic energy (see following subsection) is relatively low.

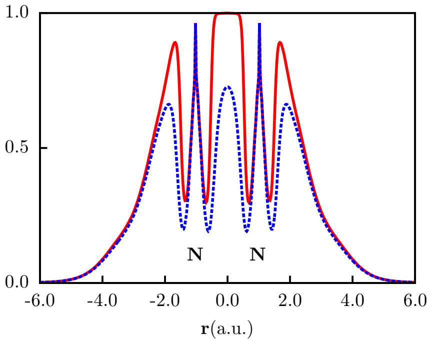

Figure 3.2: $\beta(\mathbf{r})$ (solid red line) and LOL (dashed blue line) along internuclear axis for N_2. The zero was set at the BCP.

For the sake of comparison with LOL, we define $\beta(\mathbf{r}) = 1/(1 + t_{bose}(\mathbf{r}))$, as an upper limit to LOL($\mathbf{r}$) (Fig. 7.1). It may be seen that the chemical picture obtained by the two functions is the same; maxima account for regions of electron-pair localization, i.e. cores, lone and bonding electron pairs.

This interpretation is also valid for any function derived from $\tau_w(\mathbf{r})$, such as $\tau_w(\mathbf{r})/\rho(\mathbf{r})$ or LED. As noted by Bohórquez *et al.* [59] both $\tau_w(\mathbf{r})/\rho(\mathbf{r})$ and LED are bounded by physical limits, whereas $t_{bose}(\mathbf{r})$ is an unbounded variable.

Contrary to the bonding descriptors based on $\tau(\mathrm{r})$, $\tau_w(\mathrm{r})$ bonding descriptors have the unique feature of revealing not only atomic shells, bonding and lone electron pairs, but also non-covalent interactions as we shall see in Section 3.5

3.4.3 Bonding descriptors based on $\tau(\mathbf{r})$ and $\tau_w(\mathbf{r})$

Since $\tau_w(\mathbf{r})$ contains the bosonic information of the system, for a single determinantal wave function the difference between $\tau(\mathbf{r})$ and $\tau(\mathbf{r})_w$ is a measure of the excess of kinetic energy density due to the Pauli principle. This difference is known as the Pauli kinetic energy density $t_p(\mathbf{r})$[57]

$$t_p = \tau(\mathbf{r}) - \tau_w(\mathbf{r}). \tag{3.21}$$

The right hand term of Equation 3.21 matches with the Laplacian of the conditional probability density $D(\mathbf{r})$ introduced to define ELF [42]. Additionally the term $D_\sigma^0 = \frac{3}{5}(6\pi^2)\rho_\sigma^{5/3}$ is the Thomas-Fermi kinetic energy density $\tau_{TF}(\mathbf{r})$. As proposed by Savin *et al* [57] ELF may be understood as the excess of kinetic energy compared with a system of bosons of the same density due to the Pauli principle, all of it scaled by the Thomas-Fermi term.

$$\chi(\mathbf{r}) = \frac{t_p(\mathbf{r})}{\tau_{TF}(\mathbf{r})} = \frac{\tau(\mathbf{r}) - \tau_w(\mathbf{r})}{\tau_{TF}(\mathbf{r})}. \tag{3.22}$$

From this kinematic interpretation of ELF, all the chemical meaning of ELF is contained in $t_p(\mathbf{r})$ as the only measure of electron localization [60]. Nevertheless it is known that $t_p(\mathbf{r})$ is not able to reveal chemical structure features. As explained by Schmider *et al.* [61] the origin of this may be found in the scaling relation between the kinetic energy $\tau(\mathbf{r})$ and the density; $\tau(\mathbf{r})$ is completely dominated by the core regions. To circumvent this problem, Becke and Edgecombe chose $\tau_{TF}(\mathbf{r})$ as reference. Within the local quantum theory framework, Bohórquez *et al.* chose the electron density as reference [51]. They analyzed the local values of all the functions involved in $t_p(\mathbf{r})$, $t_p(\mathbf{r})/\rho(\mathbf{r})$, $\tau(\mathbf{r})/\rho(\mathbf{r})$ and $\tau_w(\mathbf{r})/\rho(\mathbf{r})$. They have not only shown, that $t_p(\mathbf{r})/\rho(\mathbf{r})$ provides a better depiction of electron localization than $t_p(\mathbf{r})$, but $\tau(\mathbf{r})/\rho(\mathbf{r})$ and $\tau_w(\mathbf{r})/\rho(\mathbf{r})$ are useful chemical bonding descriptors too.

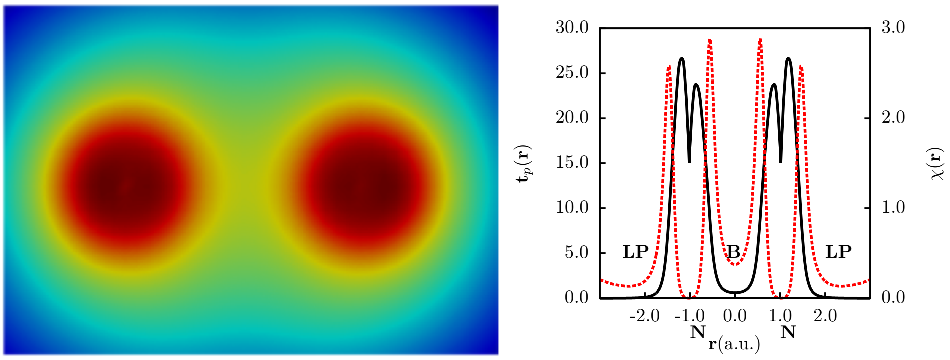

Figure 3.3: $t_p(\mathbf{r})$ isocontours (left) and (right) $t_p(\mathbf{r})$(solid black line) along with the ELF kernel $\chi(\mathbf{r}) = t_p(\mathbf{r})/t_{TF}(\mathbf{r})$ values along the internuclear axis (right) for N_2. **LP** and **B** stand for lone and bonding pair, respectively.

Although $\chi(\mathbf{r})$ is given by the difference between $t_{LOL}(\mathbf{r})$ and $t_{bose}(\mathbf{r})$, its features as bonding descriptor are closer to those of $t_{LOL}(\mathbf{r})$ than to those of $t_{bose}(\mathbf{r})$. For instance, non-covalent interactions are identified as saddle points of $\chi(\mathbf{r})$ and $t_{LOL}(\mathbf{r})$ while they are easily identified as minima of $t_{bose}(\mathbf{r})$. For visualization purposes it is much better to work with extrema, i.e. maxima and minima, than saddle points.

The ratio between $\tau(\mathbf{r})$ and $\tau_w(\mathbf{r})$ has been widely used to define self-correlation-free meta-GGAs and local hybrid functionals [20, 62].

$$g(\mathbf{r}) = \frac{\tau_w(\mathbf{r})}{\tau(\mathbf{r})}. \tag{3.23}$$

Similarly to $t_p(\mathbf{r})$, $g(\mathbf{r})$ detects regions where the density is dominated by a single orbital ("iso-orbital" regions). Unlike $t_p(\mathbf{r})$, $t_{LOL}(\mathbf{r})$ or $t_{bose}(\mathbf{r})$, $g(\mathbf{r})$ is a bounded function

$$0 \leq g(\mathbf{r}) \leq 1, \tag{3.24}$$

"Iso-orbital" regions are characterized by $g(\mathbf{r}) \to 1$. In Figure 3.4 $g(\mathbf{r})$ is computed for H_2 and N_2 at B3LYP level. For H_2 the electron density is computed using only one Kohn-Sham orbital and $g(\mathbf{r}) = 1$ is expected everywhere. For $g(\mathbf{r})$ cancels at the bond critical point and it displays a higher $g(\mathbf{r})$ value minima at nuclear positions. Between these two regions $g(\mathbf{r})$ attains its maximum value 1. Far away from nuclear positions $\tau_w(\mathbf{r}) \to \tau(\mathbf{r})$ and thus $g(\mathbf{r})$ approaches to 1

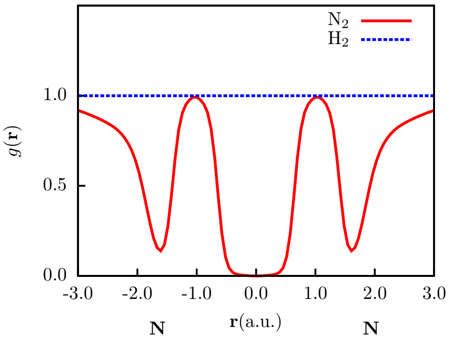

Figure 3.4: $g(\mathbf{r})$ along internuclear axis for N_2 (red line) and H_2 (blue dashed line).

Although $g(\mathbf{r})$ does not suffer from the same scaling problem as $t_p(\mathbf{r})$, in fact it is already scaled by $\tau(\mathbf{r})$, it is expected to suffer from the same pathologies as $\chi(\mathbf{r})$ for describing non-covalent interactions. It is worth noting that $\eta^{SCC}(\mathbf{r}) = 1 - g(\mathbf{r})$ introduced in Chapter 1 may be rewritten in terms of $t_p(\mathbf{r})$.

$$\eta^{SCC}(\mathbf{r}) = 1 - g(\mathbf{r}) = \frac{t_p(\mathbf{r})}{\tau(\mathbf{r})}. \tag{3.25}$$

3.4.4 Bonding descriptors from $\tau(\mathbf{r})$ ansatzs

Searching for a density based ansatz of $\tau(\mathbf{r})$, Fintzel defined the ratios [54]

$$f_2(\mathbf{r}) = \frac{\tau(\mathbf{r}) - \tau_{TF}(\mathbf{r})}{\tau_w(\mathbf{r})}, \tag{3.26}$$

$$f_3(\mathbf{r}) = \frac{\tau(\mathbf{r})}{\tau_w(\mathbf{r}) + \tau(\mathbf{r})}. \tag{3.27}$$

She analyzed the ability of these two indicators for revealing atomic shells and chemical bonds. She also showed that all the based kinetic energy density descriptors herein described may be understood as modifying functions for describing $\tau(\mathbf{r})$ (See Table 3.2).

Ansatz	Modifier
$\tau(\mathbf{r}) = \tau_w(\mathbf{r}) + \chi(\mathbf{r})\tau_{TF}(\mathbf{r})$	$\chi(\mathbf{r}) = \frac{\tau(\mathbf{r})-\tau_w(\mathbf{r})}{\tau_{TF}(\mathbf{r})}$
$\tau(\mathbf{r}) = \tau_w(\mathbf{r})f_2(\mathbf{r}) + \tau_{TF}(\mathbf{r})$	$f_2(\mathbf{r}) = \frac{\tau(\mathbf{r})-\tau_{TF}(\mathbf{r})}{\tau_w(\mathbf{r})}$
$\tau(\mathbf{r}) = f_3(\tau(\mathbf{r})_w + \tau_{TF}(\mathbf{r}))$	$f_3(\mathbf{r}) = \frac{\tau(\mathbf{r})}{\tau_w(\mathbf{r})+\tau(\mathbf{r})}$
$\tau(\mathbf{r}) = t_{LOL}(\mathbf{r})\tau_{TF}(\mathbf{r})$	$t_{LOL}(\mathbf{r}) = \frac{\tau(\mathbf{r})}{\tau_{TF}(\mathbf{r})}$
$\tau(\mathbf{r}) = \frac{\tau_w(\mathbf{r})}{g(\mathbf{r})}$	$g(\mathbf{r}) = \frac{\tau_w(\mathbf{r})}{\tau(\mathbf{r})}$

Table 3.2: Kinetic energy density functionals (left) analysed by Fintzel, along with their modifier function (right).

3.5 The local-wave vector

The local-wave vector is defined as $\vec{\mathbf{k}}(\mathbf{r}) = -\vec{\nabla}\rho(\mathbf{r})/\rho(\mathbf{r})$ [63]. It has been shown to reveal the atomic shell structure [64] and characterize atomic and molecular ground states. From the information theory point of view, Nagy and Liu have shown that the the local-wave vector is nothing but the gradient of Shanon's information per particle and the square of Fisher information's per particle [65]. The success of many of the descriptors based on $\tau_w(\mathbf{r})$ may be understood in terms of $\vec{\mathbf{k}}(\mathbf{r})$ and its connection to $\tau_w(\mathbf{r})$

$$\tau_w(\mathbf{r}) = \frac{\rho(\mathbf{r})|\vec{\mathbf{k}}(\mathbf{r})|^2}{8}. \tag{3.28}$$

LED ($\tilde{P}(\mathbf{r})$) is nothing but half the modulus of $\vec{\mathbf{k}}(\mathbf{r})$.

$$\tilde{P}(\mathbf{r}) = -\frac{\vec{\mathbf{k}}(\mathbf{r})}{2}. \tag{3.29}$$

Comparing $|\tilde{P}(\mathbf{r})|$ with that of a suitable reference system such as HEG , one may obtain the reduced density gradient $s(\mathbf{r})$ introduced in the GGA exchange functionals

$$\begin{aligned} s(\mathbf{r}) &= \frac{|\tilde{P}(\mathbf{r})|}{p_{TF}(\mathbf{r})}, && (3.30)\\ &= \frac{|\vec{\mathbf{k}}(\mathbf{r})|}{2k_{TF}(\mathbf{r})}, && (3.31) \end{aligned}$$

where $p_{TF}(\mathbf{r})$ and $k_{TF}(\mathbf{r})$ are the Thomas-Fermi momentum $k_{TF}(\mathbf{r}) = 2p_{TF}(\mathbf{r})$ and the Fermi momentum as defined in Equation 1.157.

Conversely a more elaborated scaling is used by the density overlap regions indicator (DORI) proposed by de Silva *et al.* [66]

LED and $s(\mathbf{r})$ provide very similar chemical pictures for N_2 as displayed in Figure 3.5 As it has been already discussed in Ref [52], core, lone pairs and interatomic bonding regions may be identified as minima of $s(\mathbf{r})$. LED provides a similar picture of that obtained by $s(\mathbf{r})$. Due to the different exponent of $\rho(\mathbf{r})$ in the denominator, 4/3 for $s(\mathbf{r})$ and 1 for LED, the difference between maxima and minima are much more highlighted in the former. This effect is specially notable in the minima associated with lone-pairs. One of the strong points of LED is that it is a bounded function and different chemical entities may be visualized by tuning the LED value. In Figure 3.5 core regions are colored in yellow and they were obtained obtained by a LED=6.0 isosurface, while the cyan isosurface identifying the bonding region was obtained setting LED=0.6.

Since LED, $s(\mathbf{r})$ and DORI use the same basic variable, $\vec{\mathbf{k}}(\mathbf{r})$, it is the local-wave vector who carries all the chemical content.

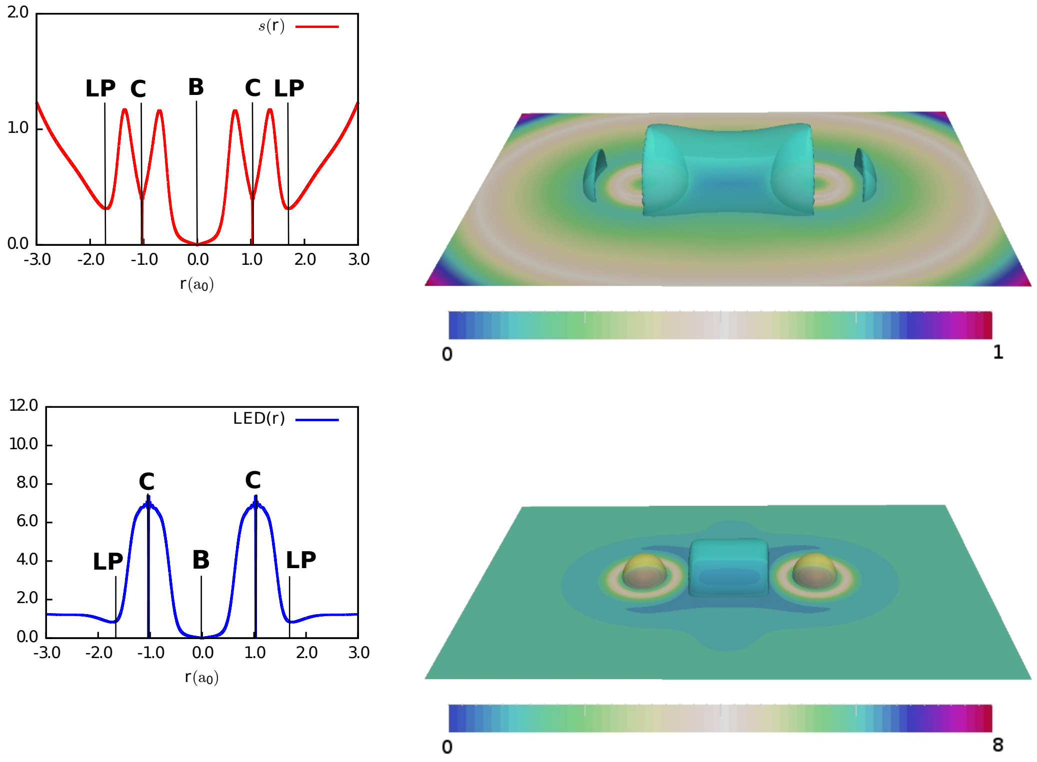

Figure 3.5: $s(\mathbf{r})$ (top), $\mathrm{LED}(\mathbf{r})$(middle) (bottom) for N_2. (Left) Representation along internuclear axis. (Right) $s(\mathbf{r}) = 0.33$, $\mathrm{LED}(\mathbf{r}) = 0.6$(cyan) and $\mathrm{LED}(\mathbf{r}) = 6.0$ (yellow) isosurfaces.

An important property of the local-wave vector, and in general, of any function of the form $|\vec{\nabla}\rho(\mathbf{r})|/\rho^n(\mathbf{r})$, is that the information from the electron density and its Laplacian $\nabla^2\rho(\mathbf{r})$ is added up. Critical points of $\rho(\mathbf{r})$ are identified as zeros of $|\vec{\nabla}\rho(\mathbf{r}|/\rho^n(\mathbf{r})$. Information from $\nabla^2\rho(\mathbf{r})$ may obtained by analyzing its gradient

$$\vec{\nabla}\Big(\frac{|\vec{\nabla}\rho(\mathbf{r})|}{\rho^n(\mathbf{r})}\Big) = \frac{1}{|\vec{\nabla}\rho(\mathbf{r})|\rho^n(\mathbf{r})}\sum_{u=1}^{3}\Big[\sum_{v=1}^{3}\Big(\frac{\partial^2\rho(\mathbf{r})}{\partial x_u\partial x_v}\Big)\Big(\frac{\partial\rho(\mathbf{r})}{\partial x_v} - n\frac{|\vec{\nabla}\rho(\mathbf{r})|^2}{\rho(\mathbf{r})}\Big(\frac{\partial\rho(\mathbf{r})}{\partial x_u}\Big)\Big]\vec{x_u}, \tag{3.32}$$

where u and v run over x, y and z. Because $|\vec{\nabla}\rho(\mathbf{r})|$ appears in the denominator of the right-hand side of Equation 3.32, $|\vec{\nabla}\rho(\mathbf{r})|/\rho^n(\mathbf{r})$ is not differentiable at critical points of $\rho(\mathbf{r})$. However at these points $|\vec{\nabla}\rho(\mathbf{r})|/\rho^n(\mathbf{r})$ behaves formally like a minimum, and this problem may be circumvented by considering these points as minima. Since the Atoms In Molecules Theory focuses on critical points of $\rho(\mathbf{r})$ we will refer to these point as AIM-CPs. By contrast we will call Non-AIM-CPs to points where 3.32 cancels. To analyze them it is convenient to rewrite Equation 3.32 in a matricial form

$$\vec{\nabla}\Big(\frac{|\vec{\nabla}\rho(\mathbf{r})|}{\rho^n(\mathbf{r})}\Big) = \frac{\vec{X}}{|\vec{\nabla}\rho(\mathbf{r})|\rho^n(\mathbf{r})}\Big[\mathbb{H}(\rho(\mathbf{r})) - n\frac{|\vec{\nabla}\rho(\mathbf{r})|^2}{\rho(\mathbf{r})}I\Big]\nabla^t\rho(\mathbf{r}), \tag{3.33}$$

where $\mathbb{H}(\rho(\mathbf{r}))$ is the electron density Hessian matrix (Equation 2.6), I is the identity matrix of order 3, $\vec{X} = (\vec{u}_x, \vec{u}_y, \vec{u}_z)$ contains three unit vectors along direction x, y and z respectively, and $\nabla^t\rho(\mathbf{r})$ is a column vector with elements $\frac{\partial\rho(r)}{\partial x}$ $\frac{\partial\rho(r)}{\partial y}$ and $\frac{\partial\rho(r)}{\partial z}$

$$\nabla^t\rho(\mathbf{r}) = \begin{pmatrix} \frac{\partial\rho}{\partial x} \\ \frac{\partial\rho}{\partial y} \\ \frac{\partial\rho}{\partial z} \end{pmatrix}, \quad \vec{X} = (\vec{x} \quad \vec{y} \quad \vec{z}). \tag{3.34}$$

Since $|\vec{\nabla}\rho(\mathbf{r})| \neq 0$ at Non-AIM-CPs, these points occurs when the remaining terms cancels. That is:

$$\Big[\mathbb{H}(\rho(\mathbf{r})) - n\frac{|\vec{\nabla}\rho(\mathbf{r})|^2}{\rho(\mathbf{r})}I\Big]\nabla^t\rho(\mathbf{r}) = 0. \tag{3.35}$$

Developing the vectorial form of this equation, the following three equalities are obtained:

$$\Big[H_{11} + H_{12} + H_{13}\Big]\Big(\frac{\partial\rho}{\partial x}\Big) = n\frac{|\nabla\rho|^2}{\rho}\Big(\frac{\partial\rho}{\partial x}\Big), \tag{3.36}$$

$$\Big[H_{21} + H_{22} + H_{23}\Big]\Big(\frac{\partial\rho}{\partial y}\Big) = n\frac{|\nabla\rho|^2}{\rho}\Big(\frac{\partial\rho}{\partial y}\Big), \tag{3.37}$$

$$\Big[H_{31} + H_{32} + H_{33}\Big]\Big(\frac{\partial\rho}{\partial z}\Big) = n\frac{|\nabla\rho|^2}{\rho}\Big(\frac{\partial\rho}{\partial z}\Big). \tag{3.38}$$

Following Ref [67], three different cases may be considered:

Case 1 $\frac{\partial\rho}{\partial x_i} \neq 0$ for all i

$$
\begin{aligned}
H_{11} + H_{12} + H_{13} &= n\frac{|\nabla\rho|^2}{\rho}, && (3.39)\\
H_{21} + H_{22} + H_{23} &= n\frac{|\nabla\rho|^2}{\rho}, && (3.40)\\
H_{31} + H_{32} + H_{33} &= n\frac{|\nabla\rho|^2}{\rho}. && (3.41)
\end{aligned}
$$

.

Case 2 Mutual cancellation of all off-diagonal terms: $H_{12} + H_{13} = H_{21} + H_{23} = H_{31} + H_{32} = 0$

$$H_{11} = H_{22} = H_{33} = n\frac{|\nabla\rho|^2}{\rho}. \tag{3.42}$$

Under this condition, the Laplacian of the electron density $\nabla^2\rho(\mathbf{r})$, which is equal to the trace of $\mathbb{H}(\rho(\mathbf{r}))$, becomes positive and equal to $3n\frac{|\vec{\nabla}\rho(\mathbf{r})|^2}{\rho(\mathbf{r})}$. This condition may be satisfied at bond, ring and cage critical points of $\rho(r)$.

Case 3 $\mathbb{H}(\rho(\mathbf{r}))$ is diagonal. Then all off-diagonal terms are zero and Equality 3.42 is obtained. Similarly to Case 2, $\nabla^2\rho(\mathbf{r}) = 3n\frac{|\vec{\nabla}\rho(\mathbf{r})|^2}{\rho(\mathbf{r})}$. In addition, the three eigenvalues of $\mathbb{H}(\rho(\mathbf{r}))$ are positive and equal to $n\frac{|\vec{\nabla}\rho(\mathbf{r})|^2}{\rho(\mathbf{r})}$. Therefore, Case 3 is only satisfied at minima of $\rho(\mathbf{r})$, that is, at cage critical points.

Under Case 2 and 3, Equation 3.35 may be rewritten as:

$$\Big[\frac{\nabla^2\rho(\mathbf{r})}{\rho(\mathbf{r})} - 3n\Big(\frac{|\nabla\rho(\mathbf{r})|}{\rho(\mathbf{r})}\Big)^2\Big] = 0. \tag{3.43}$$

A similar relation to that given by Eq 3.43 is found in the one-electron potential (OEP($\mathbf{r}$)) [56, 68]:

$$
\begin{aligned}
\mathrm{OEP}(\mathbf{r}) &= \frac{1}{4}\Big[\frac{\nabla^2\rho(\mathbf{r})}{\rho(\mathbf{r})} - \frac{1}{2}\Big(\frac{\vec{\nabla}\rho(\mathbf{r})}{\rho(\mathbf{r})}\Big)^2\Big], && (3.44)\\
&= \frac{\nabla^2\sqrt{\rho(\mathbf{r})}}{2\sqrt{\rho(\mathbf{r})}}, && (3.45)
\end{aligned}
$$

Hunter showed that OEP($\mathbf{r}$) is the exact local kinetic energy for a one-electron wave function $\theta(\mathbf{r})$, whose square is proportional to the electron density

$$\rho(\mathbf{r}) = N|\theta(\mathbf{r})|^2, \tag{3.46}$$

where N is a normalization constant. For a one-electron distribution OEP($\mathbf{r}$) is formally identical to Bohm's quantum potential. Kohout found a similar relationship for the many-electron case [69]. Regions of negative OEP($\mathbf{r}$) have been identified as classically allowed regions, in the sense that the kinetic energy takes positive values. Conversely, the regions where OEP($\mathbf{r}$) attains positive values, have negative kinetic energy, and therefore have been identified as classically forbidden regions. This separation has been used to identify atomic shells and bonding regions as the classically allowed ones. Transition between both regions occur at points where $n = 1/6$ in Equation 3.43, thus CPs of $|\vec{\mathbf{k}}(\mathbf{r})|/\rho(\mathbf{r})^6$ match with zeros of OEP($\mathbf{r}$).

3.6 Basin properties

Once the real space is exhaustively partitioned into basins, it is possible to define the basin average of an operator $\widehat{A}$ as

$$A_\Omega = \langle \widehat{A}_\Omega \rangle \quad = \quad \int_\Omega d\mathbf{r} \int \frac{N}{2} [\Psi^* \widehat{A} \Psi + (\widehat{A}\Psi)^* \Psi] d\mathbf{r}'. \tag{3.47}$$

A basin property is therefore determined by the integration of a corresponding property density, $\rho_A(\mathbf{r})$, over the basin Ω

$$A_\Omega = \int_\Omega \rho_A(\mathbf{r}) d\mathbf{r}, \tag{3.48}$$

where

$$\rho_A(\mathbf{r}) \quad = \quad \frac{N}{2} \int [\Psi^* \widehat{A} \Psi + (\widehat{A}\Psi)^* \Psi] d\mathbf{r}'. \tag{3.49}$$

Equations 3.48 and 3.49 can also be expressed in terms of the reduced density matrices. If $\widehat{A}$ is a one-electron operator, Equation 3.48 becomes

$$A_\Omega = \int_\Omega \widehat{A}(\mathbf{r};\mathbf{r}')\rho(\mathbf{r};\mathbf{r}') d\mathbf{r}'|_{\mathbf{r}=\mathbf{r}'}. \tag{3.50}$$

If $\widehat{A}$ is by contrast a two-electron operator

$$A_\Omega = \int_\Omega d\mathbf{r}_1 \int_\Omega \widehat{A}(\mathbf{r}_1, \mathbf{r}_2)\rho_2(\mathbf{r}_1, \mathbf{r}_2) d\mathbf{r}_2. \tag{3.51}$$

The most important consequence of the definition of a basin property is that the average value of any observable may be partitioned into basin contributions

$$\langle \widehat{A} \rangle \quad = \quad \sum_\Omega A_\Omega. \tag{3.52}$$

Equation 3.52 states that each basin makes an additive contribution to any property of the system.

The simplest operator that we can integrate over a basin is the unity, $\widehat{A} = 1$. The property density associated to the unity operator is the charge density and, from Equation 3.49, the basin population of Ω (defined as the average number of electrons in the Ω, N_Ω) is given by

$$\langle N_\Omega \rangle \quad = \quad \int_\Omega \rho(\mathbf{r}) d\mathbf{r}. \tag{3.53}$$

Equivalently the average number of pairs in Ω may be casted as

$$D_2(\Omega, \Omega) = \int_\Omega \int_\Omega \rho_2(\mathbf{r}_1; \mathbf{r}_2) d\mathbf{r}_1 d\mathbf{r}_2. \tag{3.54}$$

Any component of the energy of the system may be also partitioned into basin contributions. For instance the electron-nucleus interaction may be partitioned as

$$V_{en}^{AB} = -\mathbf{Z}_B \int_{\Omega_A} \frac{\rho(\mathbf{r})}{|\mathbf{r} - \mathbf{R}_B|} d\mathbf{r}, \tag{3.55}$$

where V_{en}^{AB} is the interaction between electrons in the basin Ω_A and the nucleus B. The electron-electron interaction may be casted as

$$V_{ee}^{AB} = \frac{1}{2} \int_{\Omega_A} \int_{\Omega_B} r_{12}^{-1} \rho_2(\mathbf{x}_1, \mathbf{x}_2) d\mathbf{x}_1 d\mathbf{x}_2, \tag{3.56}$$

where V_{ee}^{AB} is the electron repulsion between electrons in the basin A and the electrons in the basin B.

Population analysis

Among the aforementioned properties, the most widely used for analysing chemical bonding has been the electron population (Equation 3.53). Undoubtedly chemical concepts were developed in $\mathbb{R}^3$, and are understood in terms of how electrons guard the space, that is, the electron distribution. Along with the average number of electrons in a given region, electronic fluctuations provide insight into the electron localization/delocalization. Many of the modern chemical bond theories are defined in terms of statistics of the electron population after the chemical system of interest has been partitioned according to the QCT methodology.

The probability of finding n electrons in the region Ω and the other $(N-n)$ in the complementary region $\Omega' = \mathbb{R}^3 - \Omega$, $P_n(\Omega)$ is given by [70]

$$P_n(\Omega) = \binom{N}{n} \int_{\boldsymbol{\Omega}} d\mathbf{r}_1 \dots d\mathbf{r}_n \int_{\boldsymbol{\Omega}'} \rho_N(\mathbf{r}_1, \dots . \mathbf{r}_N) d\mathbf{r}_{n+1} \dots d\mathbf{r}_N. \tag{3.57}$$

The average number of electrons and electron pairs in a region Ω were defined by Equation 3.53 and Equation 3.54 and they may rewritten in terms of $P_n(\Omega)$

$$\begin{aligned} \langle N_\Omega \rangle &= \sum\nolimits_n P_n(\Omega) n, & (3.58) \\ D_2(\Omega, \Omega) &= \sum\nolimits_n P_n(\Omega) n(n-1). & (3.59) \end{aligned}$$

From $\rho_2(\mathbf{r}_1, \mathbf{r}_2) = \rho(\mathbf{r}_1)\rho(\mathbf{r}_2) - \rho_{xc}(\mathbf{r}_1, \mathbf{r}_2)$, $D_2(\Omega, \Omega)$ becomes

$$D_2(\Omega, \Omega) = \langle N_\Omega \rangle^2 - \langle N_{\Omega,\Omega} \rangle, \tag{3.60}$$

where

$$\langle N_{\Omega,\Omega} \rangle = \int_\Omega d\mathbf{r}_1 \int_\Omega \rho_{xc}(\mathbf{r}_1, \mathbf{r}_2) d\mathbf{r}_2. \tag{3.61}$$

The quantity $\langle N_{\Omega,\Omega} \rangle$ may be understood as a measure of the total correlation inside the region Ω, since it reduces the number of pairs created by an independent electron distribution. $\langle N_{\Omega,\Omega} \rangle$ is closely connected with the fluctuation in the population of Ω, defined as

$$\begin{aligned} \Lambda(\Omega) &= \sum_{n=0}^{N} P_n(\Omega)(n - \langle N_\Omega \rangle)^2, = \sum_{n=0}^{N} n^2 P_n(\Omega) - \sum_{n=0}^{N} n P_n(\Omega), \\ &= \langle N_\Omega^2 \rangle - \langle N_\Omega \rangle^2. & (3.62) \end{aligned}$$

On the other hand, $D_2(\Omega,\Omega)$ in Equation 3.60 may also be written as

$$D_2(\Omega,\Omega) = \sum\nolimits_n P_n(\Omega) n(n-1) = \langle N_\Omega^2 \rangle - \langle N_\Omega \rangle. \tag{3.63}$$

From Equations 3.62 and 3.63, we have

$$\langle N_\Omega^2 \rangle = \langle N_\Omega \rangle^2 + \langle N_\Omega \rangle - \langle N_{\Omega,\Omega} \rangle, \tag{3.64}$$

and substituting this equation in Equation 3.62 we finally have

$$\Lambda(\Omega) = \langle N_\Omega \rangle - \langle N_{\Omega,\Omega} \rangle. \tag{3.65}$$

$\langle N_{\Omega,\Omega} \rangle$ decreases the fluctuation in the population of Ω, increasing the electron localization in such region. Due to this property, this term receives the name of localization index. When $\langle N_{\Omega,\Omega} \rangle$ attains its maximum value, $\langle N_\Omega \rangle$, the fluctuation $\Lambda(\Omega)$ becomes zero, generating a situation of maximum localization. In such a case, the probability of finding n electrons in Ω, $P_n(\Omega)$, becomes one, $\langle N_\Omega \rangle$ is equal to n, and the average number of pairs in Ω is $\langle N_\Omega \rangle(\langle N_\Omega \rangle - 1)$. This limit situation is known as a pure pair population.

Similarly, one can measure the degree of localization of the electrons in two different regions Ω_1 and Ω_2 by determining the fluctuation in the population of the combined region $\Omega = \Omega_1 + \Omega_2$

$$\Lambda(\Omega) = \Lambda(\Omega_1) + \Lambda(\Omega_2) - 2\langle N_{\Omega_1,\Omega_2} \rangle, \tag{3.66}$$

where

$$\langle N_{\Omega_1,\Omega_2} \rangle \quad = \quad \int_{\Omega_1} d\mathbf{r}_1 \int_{\Omega_2} \rho_{xc}(\mathbf{r}_1,\mathbf{r}_2) d\mathbf{r}_2, \tag{3.67}$$

and $\Lambda(\Omega_1)$ and $\Lambda(\Omega_2)$ are given by Equation 3.62. The quantity $2\langle N_{\Omega_1,\Omega_2} \rangle$ is a measure of the extent to which electrons in Ω_1 are delocalized over Ω_2 and *vice versa* and it is known as delocalization index $\delta^{\Omega_1\Omega_2}$.

If these two regions complete the space, $\Omega_1 \cup \Omega_2 = \mathbb{R}^3$, one finds that

$$\langle N_{\Omega_1,\Omega_1} \rangle + \langle N_{\Omega_2,\Omega_2} \rangle + 2\langle N_{\Omega_1,\Omega_2} \rangle = N. \tag{3.68}$$

Since for a closed system the number of electrons remains constant, maximizing the degree of localization in a given region leads to a minimization of the electron delocalization between different regions. The number of pairs that can be formed between electrons in different regions is given by

$$D_2(\Omega_1,\Omega_2) = \int_{\boldsymbol{\Omega}_1} d\mathbf{r}_1 \int_{\boldsymbol{\Omega}_2} \rho_2(\mathbf{r}_1,\mathbf{r}_2) d\mathbf{r}_2 = \langle N_{\Omega_1} \rangle \langle N_{\Omega_2} \rangle - \langle N_{\Omega_1,\Omega_2} \rangle. \tag{3.69}$$

In the limit of pure pair population, $\langle N_{\Omega_1,\Omega_1} \rangle$ and $\langle N_{\Omega_2,\Omega_2} \rangle$ attain their maximal values, $\langle N_{\Omega_1} \rangle$ and $\langle N_{\Omega_2} \rangle$, respectively. In that case, the delocalization index, $2\langle N_{\Omega_1,\Omega_2} \rangle$, becomes zero and the electrons are perfectly localized in both regions. The number of pairs formed between the two regions, becomes from Equation 3.66 equal to the number of pairs that can be formed with two sets of distinct objects.

If real space is partitioned into several regions, $\cup_{i=a}^{m} \Omega_a = \mathbb{R}^3$ $(m \geq 2)$, the above relations between the delocalization and localization indexes may be generalized. For instance, Eq. 3.69 becomes

$$\sum_a \langle N_{aa} \rangle + 2 \sum_{a \neq b} \langle N_{ab} \rangle = N, \tag{3.70}$$

where the indexes $a, b, \ldots$ run over all the basins. The definitions of localization and delocalization indexes both together with Equations 3.62 and 3.63 show how the inter and intra correlation may be described from the exchange-correlation density, $\rho_{xc}(\mathbf{r}_1, \mathbf{r}_2)$. Indeed, $\rho_{xc}(\mathbf{r}_1, \mathbf{r}_2)$ may be seen as a generator of 2-particle fluctuation in the electron distributions [71]. All these concepts many be generalized, not only for two disjoint domains in real space, but for any number $(m \geq 2)$ of regions by means of n^{th} order cumulants [72, 73].

Chapter 4

The NCI method

Sommaire

The electron density has a fundamental advantage over MO-based descriptors because it is an experimentally accessible scalar field and is a local function defined within the exact-many body theory and supported by the Hohenberg-Kohn theorems [4]. The relationship between electron density topology and physical/chemical properties can be understood from the Hohenberg-Kohn theorem (see Chapter 1), which asserts that a system's ground-state properties are a consequence of its electron density. Furthermore because chemical reactions proceed by redistributions $\rho(\mathbf{r})$, methods that analyze $\rho(\mathbf{r})$ distributions should help to understand the electron structure of molecules and thus chemical reactivity.

Our approach, introduced in the coming sections, uses the density and its derivatives, allowing simultaneous analysis and visualization of a wide range of interaction types as real space surfaces and adds an important tool to the chemist's arsenal [74, 75, 76].

4.1 The reduced density gradient

The reduced density gradient, $s(\mathbf{r})$, or RDG, is a fundamental dimensionless quantity in DFT used to describe the deviation from a homogeneous electron distribution 1.157. Properties of $s(\mathbf{r})$ have been investigated in depth in the process of developing increasingly accurate functionals [10, 15, 77, 78, 79].

The origin of $s(\mathbf{r})$ can be traced back to the generalized gradient contribution to the GGA exchange energy E_x^{GGA} [15]

$$E_x^{GGA} - E_x^{LDA} = -\sum \int F(s)\rho^{4/3}(\mathbf{r})d\mathbf{r}, \tag{4.1}$$

where $F(s)$ is a function of $s(\mathbf{r})$ for a given spin with

$$s(\mathbf{r}) = \frac{1}{C_s}\frac{|\vec{\nabla}\rho(\mathbf{r})|}{\rho(\mathbf{r})^{4/3}}, \tag{4.2}$$

$C_s = 2(3\pi^2)^{1/3}$ and the 4/3 exponent of the density ensures that $s(\mathbf{r})$ is a dimensionless quantity.

The lower bound of the reduced density gradient is zero, as occurs throughout a homogeneous electron gas and at bond critical points.

The effect of bonding on the reduced density gradient is especially easy to visualize when $s(\mathbf{r})$ is plotted as a function of the density. Graphs of $s(\mathbf{r})$ *versus* $\rho(\mathbf{r})$ assume the form $s(\mathbf{r}) = a\rho(\mathbf{r})^{-1/3}$, where a is a constant. This can be easily proven from a Slater orbital model density (STO). For a single atomic orbital $\psi(\mathbf{r}) = e^{-\alpha\mathbf{r}}$, the density is $\rho(\mathbf{r}) = e^{-2\alpha\mathbf{r}}$ and the gradient is $\nabla\rho(\mathbf{r}) = -2\alpha\rho(\mathbf{r})$, such that

$$s^{STO}(\mathbf{r}) = \frac{1}{C_s}\frac{2\alpha\rho(\mathbf{r})}{\rho(\mathbf{r})^{4/3}} = \frac{2\alpha}{C_s}\rho(\mathbf{r})^{-1/3}. \tag{4.3}$$

When there is overlap between atomic orbitals, a spike in the $s(\mathbf{r})$ *versus* $\rho(\mathbf{r})$ diagram appears. The points forming this spike identify the interaction when they are mapped back to real space. This procedure is used to reveal non-covalent interactions, such as hydrogen bonds, steric repulsions, van der Waals interactions, and even covalent and ionic bondings.

To explore the features associated with a small reduced density gradient, we first examine the plots of $s(\mathbf{r})$ *versus* $\rho(\mathbf{r})$. Additionally, plots of $g(\mathbf{r}) = \tau_w(\mathbf{r})/\tau_p(\mathbf{r})$ *versus* $\rho(\mathbf{r})$ are able to reveal regions of orbital overlapping [62]. In "iso-orbital regions" $g(\mathbf{r}) \to 1$, therefore deviations from 1 characterize regions of orbital overlapping, revealing spikes in the $g(\mathbf{r})$ *versus* $\rho(\mathbf{r})$ diagram as $s(\mathbf{r})$ does. These plots were generated by evaluating the reduced density gradient with DFT densities for methane and water dimers (Figure 4.1). Plotting $s(\mathbf{r})$ *versus* $\rho(\mathbf{r})$, reveals the basic pattern of intramolecular and intermolecular interactions. Methane illustrates the typical covalent pattern. The left-side points (small density and large density gradient) corresponds to C-H covalent bonds. Covalent bonds have their characteristic BCP, corresponding to $s \approx 0$. Regions near the nuclei have larger density values and appear beyond the right edge of the plot. Additionally $g(\mathbf{r})$ diagrams disclose the same pattern as $s(\mathbf{r})$ showing spikes at the same positions, revealing regions of high orbital overlapping. $s(\mathbf{r})$ *versus* $\rho(\mathbf{r})$ diagrams have an overall shape of the forms $a\rho^{-1/3}$ because atomic and molecular densities are piecewise exponential. The results for water are very similar. Plots of $s(\mathbf{r})$ *versus* $\rho(\mathbf{r})$ for these systems exhibit a new feature: one or more spikes in the low-density, low-gradient region, a signature of non-covalent interactions. This is the basis of the NCI method.

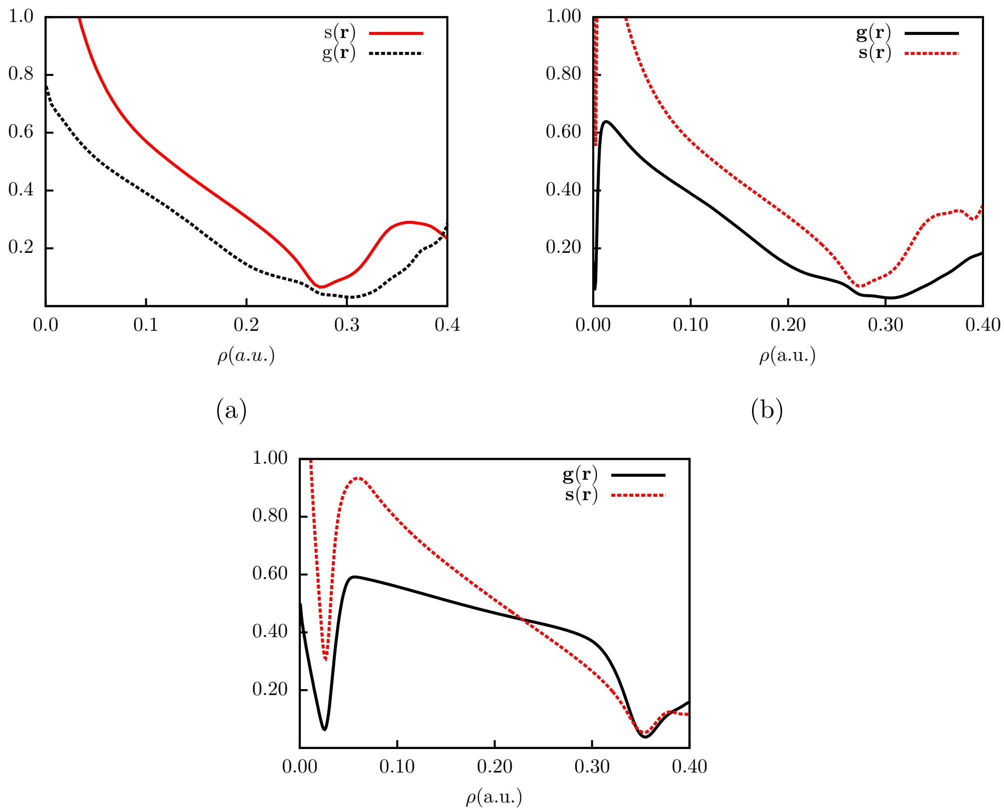

(a)

(b)

(c)

Figure 4.1: $s(\mathbf{r})$ and $g(\mathbf{r})$ *versus* $\rho(\mathbf{r})$ diagrams (a) methane (b) and methane dimer. (c) The water dimer.

4.1.1 Physical interpretation of s(r)

It may be straightforwardly shown that $s(\mathbf{r})$ is the kernel of $t_{bose}(\mathbf{r})$ introduced in Chapter 3 [52]:

$$\begin{aligned} s(\mathbf{r}) &= \left(\frac{3}{10}\right)^{1/2} \frac{1}{2(C_F)^{1/2}} \frac{|\vec{\nabla}\rho(\mathbf{r})|}{\rho(\mathbf{r})^{4/3}}, & (4.4) \\ t_{bose}(\mathbf{r}) &= \frac{\tau_w(\mathbf{r})}{\tau_{TF}(\mathbf{r})} = \left(\frac{5}{3}\right) s(\mathbf{r})^2. & (4.5) \end{aligned}$$

We may notice that its CPs match with those of $t_{bose}(\mathbf{r})$

$$\vec{\nabla} t_{bose}(\mathbf{r}) = \frac{10}{3} s(\mathbf{r}) \vec{\nabla} s(\mathbf{r}). \tag{4.6}$$

Since $s(\mathbf{r})$ is positive semidefinite, at CPs the signs of their laplacians are the same

$$\nabla^2 t_{bose}(\mathbf{r}) = \frac{10}{3} \Big(\vec{\nabla} s(\mathbf{r}) \cdot \vec{\nabla} s(\mathbf{r}) + s(\mathbf{r}) \nabla^2 s(\mathbf{r}) \Big). \tag{4.7}$$

At CPs $|\vec{\nabla} t_{bose}(\mathbf{r_{cp}}|) = |\vec{\nabla} s(\mathbf{r_{cp}})| = 0$, and

$$\nabla^2 t_{bose}(\mathbf{r_{cp}}) = \frac{5}{3} \Big(s(\mathbf{r_{cp}}) \nabla^2 s(\mathbf{r_{cp}}) \Big). \tag{4.8}$$

Thus, the critical points of $s(\mathbf{r})$ and $t_{bose}(\mathbf{r})$ are identical both in location and in nature. Because of the presence of the gradient of ρ in the numerator, and their positive semidefinite condition, at every CP of $\rho(\mathbf{r})$ both functions cancel and have a minimum. This result may be clearly shown, if we develop the explicit expressions for $\nabla t_{bose}(\mathbf{r})$. Inserting Equation 3.35 into 4.6 one obtains

$$\nabla t_{bose}(\mathbf{r}) = \frac{\vec{X}}{4 C_F \rho(\mathbf{r})^{8/3}} \Big[\mathbb{H}(\rho(\mathbf{r})) - \frac{4}{3} \frac{(\vec{\nabla}\rho(\mathbf{r}))^2}{\rho(\mathbf{r})} I \Big] \nabla^t \rho(\mathbf{r}), \tag{4.9}$$

where $\vec{X}$ and $\nabla^t \rho(\mathbf{r})$ were introduced in Equation 3.34. It is worth noticing that in contrast to $s(\mathbf{r})$ (and functions of the form $|\vec{\nabla}\rho(\mathbf{r})|/\rho^n(\mathbf{r})$ in general), $t_{bose}(r)$ is differentiable at critical points of $\rho(\mathbf{r})$. Similarly to $|\vec{\nabla}\rho(\mathbf{r})|/\rho^n(\mathbf{r})$ we may differentiate two different situations where $\nabla t_{bose}(\mathbf{r})$ cancels:

1. AIM-CPs: CPs of $\rho(\mathbf{r})$, for which $|\vec{\nabla}\rho(\mathbf{r})| = 0$.
2. Non-AIM-CPs: Points where

$$\Big[\mathbb{H}(\rho(\mathbf{r})) - \frac{4}{3} \frac{(\vec{\nabla}\rho(\mathbf{r}))^2}{\rho(\mathbf{r})} I \Big] \nabla^t \rho(\mathbf{r}) = 0. \tag{4.10}$$

As pointed out above in Section sec:localwavevector, AIM-CPs correspond to minima of $t_{bose}(\mathbf{r})$ and $s(\mathbf{r})$. In addition, under certain conditions, Non-AIM-CPs may occur when $\mathbb{H}(\rho(\mathbf{r}))$ is diagonal and its eigenvalues, λ_1, λ_2 and λ_3, are identical and equal to $\frac{4}{3}|\vec{\nabla}\rho(\mathbf{r})|^2/\rho(\mathbf{r})$. The Laplacian of the electron density may be then rewritten as:

$$\nabla^2 \rho(\mathbf{r}) = \lambda_1 + \lambda_2 + \lambda_3 = 4 \frac{|\vec{\nabla}\rho(\mathbf{r})|^2}{\rho(\mathbf{r})}. \tag{4.11}$$

As discussed in Section 3.5 the variables in Equation 4.1.1 for the Non-AIM-CPs are also involved in the one-electron potential (OEP($\mathbf{r}$)) [56, 68]

$$\mathrm{OEP}(\mathbf{r}) = \frac{1}{4\rho(\mathbf{r})}\left[\nabla^2\rho(\mathbf{r}) - \frac{1}{2}\frac{|\vec{\nabla}\rho(\mathbf{r})|^2}{\rho(\mathbf{r})}\right], \tag{4.12}$$

When OEP(r) cancels, the ratio between $\nabla^2\rho(\mathbf{r})/\rho(\mathbf{r})$ and $(\vec{\nabla}\rho(\mathbf{r}))^2/\rho^2(\mathbf{r})$ is equal to 1/2, whereas it is 4 when Eq 4.1.1 is satisfied. Thus, any Non-AIM CPs of $t_{bose}(\mathbf{r})$ is anticipated by a zero of OEP(r), and therefore by a transition from a classically allowed to a forbidden region.

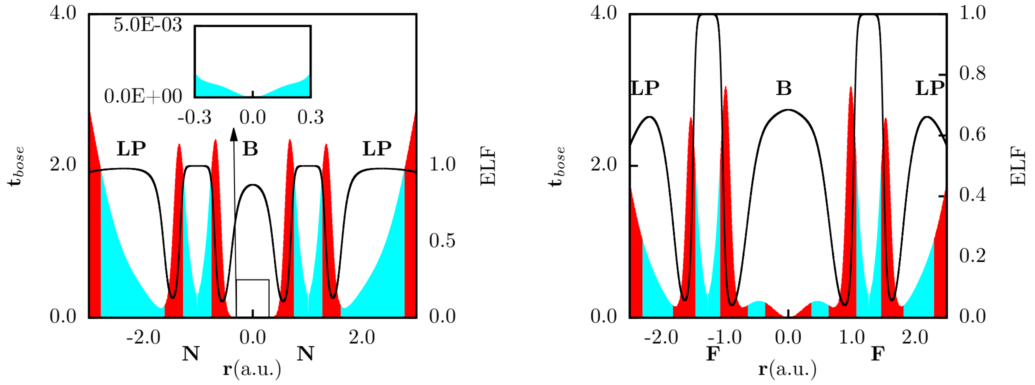

Figure 4.2: $t_{bose}(\mathbf{r})$ along with ELF($\mathbf{r}$) values (solid black line) for N_2(a) and F_2(b). Negative (classically allowed) and positive (classically forbidden) regions of OEP(r) are displayed as cyan and red-colored areas respectively. Labels B and LP stand for bond and lone pair ELF maxima, respectively.

Figure 4.2 displays $t_{bose}(\mathbf{r})$, ELF($\mathbf{r}$) along the internuclear axis for F_2 and N_2. The origin was set at the BCP. The features of $s(\mathbf{r})$ for N_2 have already been discussed in Section 3.5. $t_{bose}(\mathbf{r})$ differentiates the core, lone-pairs and interatomic bonding regions as minima separated by maxima. As revealed by ELF($\mathbf{r}$) maxima, these minima correspond to large electron pair localization. Nuclear and bond critical points of $\rho(\mathbf{r})$ are identified as zeros of $t_{bose}(\mathbf{r})$. Conversely lone pairs are not revealed by critical points of $\rho(\mathbf{r})$, but by critical points of the Laplacian of the electron density. $t_{bose}(\mathbf{r})$ shows minima at such positions driven by the Non-AIM-CP condition (Eq 4.10), following thereby a transition from a classically forbidden region to a classically allowed region, as may be seen in Figure 4.2. We highlight that all CPs of t_{bose} given by Eq 4.10 are anticipated by roots of OEP, but the opposite is not true; not all roots of OEP are followed by Eq 4.10. This situation may be found in N_2. Even though no CP of $t_{bose}(\mathbf{r})$ is found between the external core-maxima and the BCP, the former is localized at regions of positive OEP, whereas the latter is found in a region of negative OEP. We may notice that the BCP for F_2 is localized at a region of positive OEP. It is well known that F_2 exhibits a positive value of the Laplacian of the electron density at the BCP, being thereby identified as a region of electron depletion (thus called charge-shift bond). Since the signs of OEP and $\nabla^2\rho(\mathbf{r})$ are the same at CPs of $\rho(\mathbf{r})$, the BCP for F_2 is localized at a classically forbidden region.

The relationship between $s(\mathbf{r})$ and $\tau_w(\mathbf{r})$ allows to identify regions with a marked bosonic-like character as those where $s(\mathbf{r})$ attains small values and which are characterized by peaks in the $s(\mathbf{r})$ *versus* $\rho(\mathbf{r})$ diagram.

4.2 The electron density Hessian second eigenvalue

According to the divergence theorem, the sign of the Laplacian of the density ($\nabla^2\rho(\mathbf{r})$) indicates whether the net gradient flux is entering ($\nabla^2\rho(\mathbf{r}) < 0$) or leaving ($\nabla^2\rho(\mathbf{r}) > 0$) an infinitesimal volume around a reference point. Hence, it highlights whether the density is concentrated or depleted at that point, relative to the surrounding environment. To understand bonding in more detail, it is often useful to decompose the Laplacian into the contributions along the three particular axes of maximal variation. These components are the three eigenvalues, λ_i, of the electron density Hessian matrix, $\mathbb{H}(\rho)$, such that

$$\mathbf{Tr}(\mathbb{H}(\rho)) = \nabla^2\rho = \lambda_1 + \lambda_2 + \lambda_3 \qquad \lambda_1 < \lambda_2 < \lambda_3. \tag{4.13}$$

where λ_3 is the eigenvalue associated with the eigenvector which expands along the intermolecular axis, and λ_1, λ_2 represents variations in the plane perpendicular to the λ_3 eigenvector.

The sign of $\nabla^2\rho(\mathbf{r})$ determines whether the compression ($\nabla^2\rho(\mathbf{r}) < 0$) or the expansion ($\nabla^2\rho(\mathbf{r}) > 0$) of the electron density is the dominant effect at the reference point. Bader smartly showed that these compressions and expansions are related with the balance between $\tau(\mathbf{r})$ and $\mathcal{V}(\mathbf{r})$

$$\begin{aligned} \mathcal{V}(\mathbf{r}) &= \frac{1}{4}\nabla^2\rho(\mathbf{r}) - 2\tau(\mathbf{r}), \\ &= \frac{1}{4}(\lambda_1 + \lambda_2 + \lambda_3) - 2\tau(\mathbf{r}). \end{aligned} \tag{4.14}$$

He classified chemical interactions as closed-shell, for which $\nabla^2\rho(\mathbf{r}) > 0$ at the BCP and are dominated by the kinetic energy. Conversely, shared interaction implies a lowering of the potential energy and therefore $\nabla^2\rho(\mathbf{r}) < 0$. Weak interactions fall into the category of closed-shell, not being possible to differentiate them using the overall sign of $\nabla^2\rho$. To this purpose it is much more convenient to focus on its eigenvalue contributions.

At nuclei, all the eigenvalues are negative, while at the center of cages or holes (minima of ρ) all the eigenvalues are positive. In the remaining points of space $\lambda_3 > 0$, $\lambda_1 < 0$, and λ_2 can be either positive or negative. In terms of $\tau(\mathbf{r})$ and $\mathcal{V}(\mathbf{r})$, $\lambda_3 > 0$, $\lambda_1 < 0$ represent directions dominated by the kinetic and potential energies respectively, whereas along the direction of λ_2 there is a balance between both terms.

Van der Waals interactions and hydrogen bonds show negatives values of λ_2 at the BCP and can be differentiated by properties at the corresponding BCPs. Characteristic densities of van der Waals interactions are much smaller than densities at which hydrogen bonds appear. However, steric clashes and hydrogen bonds span similar densities ranges and overlap in plots of $s(\mathbf{r})$ *versus* $\rho(\mathbf{r})$. In the cases where λ_2 is positive (as in rings or cages), usually several atoms are confined in the same region interacting through BCPs with positive $\nabla^2\rho(\mathbf{r})$ values, which can correspond to steric crowding according to classical chemistry. Although there is no repulsion in equilibrium systems since $\mathcal{V}(\mathbf{r})$ is negative everywhere, it is often found in the literature that regions of positive λ_2 are said to be repulsive, while regions of negative λ_2 attractive. In what follows we will use this

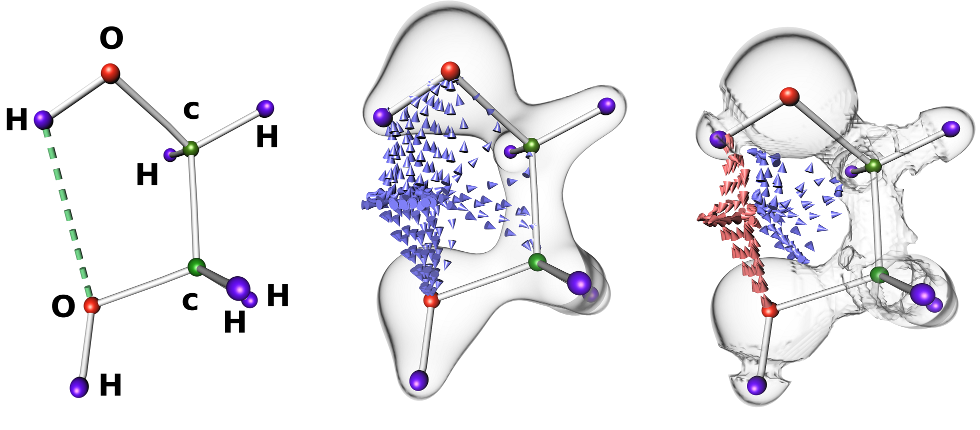

(a) (b) (c)

Figure 4.3: (a) Molecular structure of the 1,2-ethanediol. A hydrogen bond is represented in green. Isosurfaces and gradient flows of (b) $\rho(\mathbf{r})$, $\vec{\nabla}\rho(\mathbf{r})$ (blue) and (c) $\mathrm{sign}(\lambda_2)\rho(\mathbf{r})$, $\vec{\nabla}\mathrm{sign}(\lambda_2)(\rho(\mathbf{r})$. Negative and positive flows are indicated with red and blue arrows, respectively.

last convention, even though it only refers to the balance between $\tau(\mathbf{r})$ and $\mathcal{V}(\mathbf{r})$ along the λ_2 direction.

$\rho(\mathbf{r})$ and the sign of λ_2 information may be added up defining the signed electron density, $\mathrm{sign}(\lambda_2)\rho$, as the product of $\mathrm{sign}(\lambda_2)$ and $\rho(\mathbf{r})$. Contrary to the latter, $\mathrm{sign}(\lambda_2)\rho(\mathbf{r})$ is discontinuous in general. In principle this hurdle may be solved considering $\mathrm{sign}(\lambda_2)\rho(\mathbf{r})$ as a result of a convolution with a mollifier [80]. Figure 4.2 depicts the gradient flow of $\rho(\mathbf{r})$ and $\mathrm{sign}(\lambda_2)\rho(\mathbf{r})$ for 1.2-ethanediol. When analyzing the hydrogen bond between the oxygen and hydrogen atoms (Figure 4.2a) $\vec{\nabla}\rho(\mathbf{r})$ does not identify these interactions, uniformly covering all atoms (Figure 4.2b). By contrast, $\vec{\nabla}\mathrm{sign}(\lambda_2)\rho(\mathbf{r})$ identified a region of incoming flow (attraction) coming from the interacting oxygen and hydrogen atoms (red arrows). This folded conformation also introduces a region of outflow (blue arrows) that covers all the others atoms of the molecule.

4.3 Interpreting NCI

4.3.1 The 2D plot

Interaction types can be distinguished if the $s(\rho)$ diagrams are modified using $\mathrm{sign}(\lambda_2)\rho$ as the ordinate. This is illustrated for the phenol dimer in Figure 4.4. This is a hydrogen-bonded complex that also exhibits non-bonding interactions within each benzene ring and a stacking interaction between the benzene rings. We thus have the three main types of interactions.

Analysis of the sign of λ_2 thus helps to discern the different types of weak interactions, whereas the density itself provides information on their strength; both are combined in the value of $\mathrm{sign}(\lambda_2)\rho$. This is illustrated in Figure 4.4 which shows a modification of the $s(\mathbf{r})$ plot, such that the ordinate is now $\mathrm{sign}(\lambda_2)\rho$. When the Hessian eigenvalues are considered, the different nature of these interactions is made clear. The 2D NCI plots will then be used as inputs to construct 3D NCI plots, consisting in isosurfaces of the reduced gradient of the density enabling the visualization of close contacts. As shown in Table 4.1, the benzene-ring interactions remain at positive value of λ_2 with density value 0.067 a.u., whereas the hydrogen bond now lies at negative value of λ_2 with density value 0.026 a.u. (-0.026 a.u. in terms of sign(λ_2)ρ). The NCI spikes nearest zero density correspond to weakly-attractive dispersion interactions between the phenyl ring (-0.0054 a.u. and 0.0047 a.u.). Therefore the value of the sign(λ_2)ρ at the position of the peaks in s(ρ) plots may be used as the signature of non-covalent interactions.

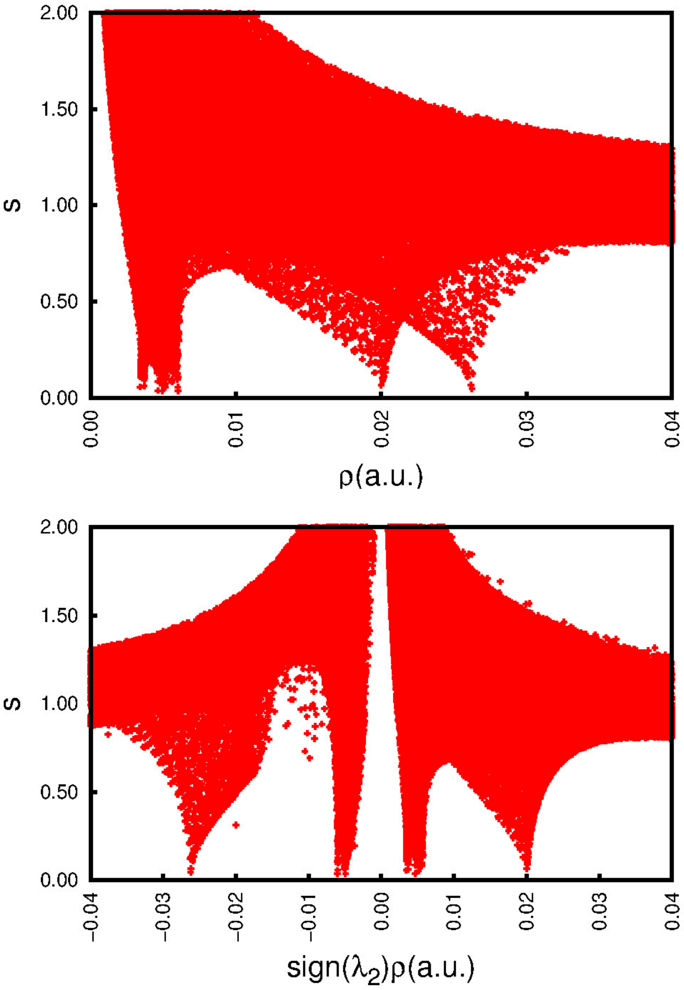

Figure 4.4: NCI analysis for the phenol dimer. (Top) $s(\mathbf{r})$ *versus* $\rho(\mathbf{r})$ diagram. (Bottom) $s(\mathbf{r})$ *versus* sign(λ_2)ρ

	Peak 1	Peak 2	Peak 3	Peak 4
sign(λ_2)(ρ)	-0.026	-0.0054	0.0047	0.067

Table 4.1: sign(λ_2)(ρ) value for each peak of the s *vs* sign(λ_2)(ρ) for the phenol dimer.

In order to facilitate the corresponding between 2D and 3D representation, in Figure 4.5c we use the same coloring scheme on these two representations.

4.3.2 The 3D plot

The 3D spatial visualization of the non-covalent interactions as defined above is done using the data from the 2D plots as input to construct 3D plots composed of reduced density gradient isosurfaces. In a nutshell, a cut-off value of s close to zero, typically $s < 0.5$ is chosen in order to recover all the non-covalent interactions in the system, i.e. all the spikes in the 2D plots. The corresponding reduced density gradient isosurfaces give rise to closed domains in the molecular space which highlight the spatial localization of the interactions within the system (see Figure 4.5a). Since 3D isosurfaces are, by definition, regions of low reduced gradient, the density is nearly constant within these.

The isovalue (or cut-off) of $s(\rho)$ chosen for plotting the 3D isosurface determines which features will appear in the NCI plot as well as their spatial extension. On the one hand, all NCI spikes do not strictly achieve $s = 0$ so that too low a value might miss some of the interaction of interests. In the other hand, too high a value would disclose atomic tails of the density. The cut-off is therefore chosen from the 2D plot so that all spikes, but only spikes, are captured to render a meaningful picture which discovers both attractive and repulsive interactions.

At this stage, however, the types of interaction corresponding to the several isosurfaces are not present. In order to discriminate between them, the density oriented by the sign of λ_2 is further used (as in the 2D plot). A RGB (red-green-blue) coloring scheme is chosen to rank interactions, where red is used for destabilizing interactions, blue for stabilizing interactions and green for delocalized weak interactions (see Figure 4.5b). The deepness of the blue and the red is associated with a higher density and therefore to a strong interaction.

In some cases, noticeable in ring closings, bicolored isosurfaces appear. They result from stabilizing features (revealed by the blue color), counterbalanced by destabilizing interactions due to steric crowding (revealed by the red color), such as ring closure.

It emerges that a one-to-one inverse correlation seems to exist among the directionality (and the strength) of specific non-covalent interaction and the surface/volume ratio of the corresponding s isosurface. In particular, the stronger the interaction is, the smaller and more disc-shaped the s surface appears in real space (and the more negative the ρ sign(λ_2) values are). In Table 4.2 the local shapes of both functions are summarized. NCIs are characterized by $\lambda_1 \approx \lambda_2 << \lambda_3$ and thus are displayed as planar isosurfaces, as may be seen for methane and water dimer. In order to differentiate between the two not only the shape, but also the size of the isosurface should be considered, as we will show latter. This connection between the shape and the nature of the interaction relays on the stability of topological features with the value of the surfaces.

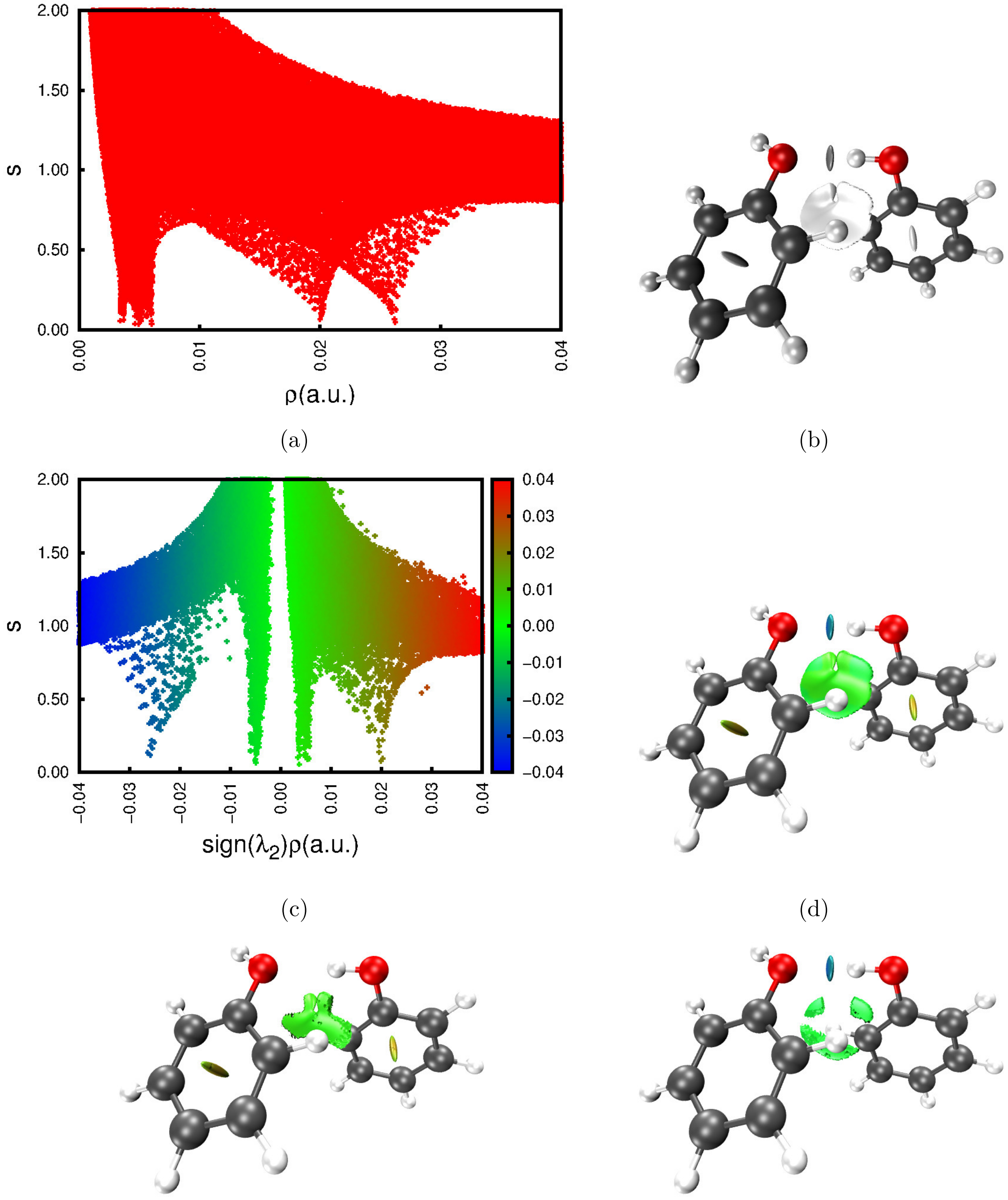

(a) (b)

(c) (d)

(e) (f)

Figure 4.5: NCI analysis for the phenol dimer. (a) $s(\mathbf{r})$ *versus* ρ diagram (b) and $s(\mathbf{r}) = 0.5$ isosurface. (c) $s(\mathbf{r})$ *versus* sign$(\lambda_2)\rho$ diagram (d) and $s(\mathbf{r})$=0.5 isosurface coloured over the range -0.04(blue) < sign$(\lambda_2)\rho$ < 0.04(red). (e) Surface extraction based on sign(λ_2); $\lambda_2 > 0$ isosurface and (f) $\lambda < 0$ isosurface.

Curvature relations	Shape	$\rho(\mathbf{r})$ CP
$\lambda_1 \approx \lambda_2 << \lambda_3$	Planar	BCP, closed-shell interaction
$\lambda_1 << \lambda_2 \approx \lambda_3$	Cylindrical	RCP, BCP shared interaction
$\lambda_1 \approx \lambda_2 \approx \lambda_3$	Spheroidal	BCP shared interactions; CCP, ACP

Table 4.2: Classification of CPs of $\rho(\mathbf{r})$ according to the relative magnitude of the Hessian eigenvalues $|\lambda_1| < |\lambda_2| < |\lambda_3|$, along with the local shape of $s(\mathbf{r})$ around the CP.

4.3.3 Stability

Topological features of the electron density are very stable with respect to the calculation method. The main effect of different methods on the s *vs* ρ diagram is a shift of spikes. The only rule of thumb seems that the same s value should be used when comparing various NCI plots, both in the same or in different systems, provided a single method was employed to obtain the various electron densities. If this is not the case, different s values are seemingly required to compare on similar grounds the s-based results for different computed electron density (e.g. from wave function, promolecular). In other words, a shift of cut-offs is needed to obtain comparable images. This can be related to the fact that s roughly behaves like $\rho^{1/3}$ (Equation 4.3) so that the effect of the method on the density is directly followed by s.

4.3.4 Promolecular densities

Densities are stable to such an extent that their main features are already contained in the sum of atomic densities, ρ^{at}. The resulting molecular density, also known as promolecular density, ρ^{pro}, is then given by:

$$\rho^{pro}(\mathbf{r}) = \sum_i \rho_i^{at}(\mathbf{r}), \tag{4.15}$$

A promolecular density obtained from simple exponential atomic pieces is able to predict low-density, low-reduced-gradient regions qualitatively similar to density-functional results. The free atomic densities used in these calculations consist of one Slater-type function for each electron shell, fit to closely reproduce spherically-averaged, density functional atomic densities.

Resultant plots of $s^{pro}(\mathbf{r})$ *versus* $\rho^{pro}(\mathbf{r})$ for these species show the same 2D features (see Figure 4.6a and Figure 4.7a). Also, 3D isosurfaces generated from the promolecular densities are very similar to those obtained with self-consistent DFT level. For all cases considered, results at the self-consistent and promolecular level are qualitatively equivalent. Quantitative differences are introduced by the density relaxation that, as expected, shift the s *versus* ρ spikes to more bonding regimes. Specifically, a large shift toward smaller density values is obtained in the spikes corresponding to non-bonded overlap, introducing less repulsion and greater stability. This is to be expected, since the approximate promolecular densities used to generate these isosurfaces cannot adjust to alleviate Pauli repulsion in the manner of self- consistent DFT electron densities. However, once the shift is taken into account (by changing the density cut-off), results at the self-consistent and promolecular level are qualitative equivalent. For example, to generate similar isosurfaces using DFT and promolecular densities for the phenol dimer the value of s were set at 0.5 and 0.3, respectively (see Figure 4.6 and Figures 4.7).

The match between SCF and promolecular densities is a consequence of the stepwise exponential behavior of the electron density and the fact that we are analyzing regions of small perturbation, which may be highlighted by the local-wave vector and any related functions. Even though the gross topological features of $\rho(\mathbf{r})$ may be recovered, this is not the case for any operator computed from a promolecular density.

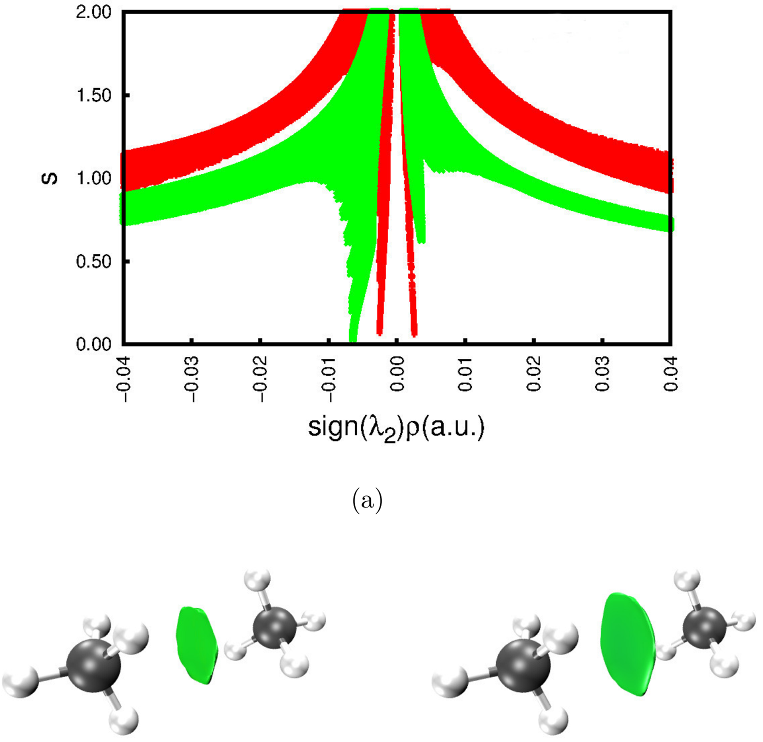

(a)

(b)

(c)

Figure 4.6: Comparison between SCF and promolecular NCI results for the methane dimer. (a) The same $s(\rho)$ features are obtained using self-consistent (green) and promolecular (red) calculations, with a shift toward negative (stabilizing) regimes. Taking the shift in spikes into account (i.e. changing the cut-off), the isosurface shapes remain qualitatively unaltered. (b) For SCF densities $s(\mathbf{r})$=0.6 and color scales of -0.04 < sign(λ_2)ρ) < 0.03 a.u. (c) For promolecular densities $s(\mathbf{r})$=0.5. and -0.04 < sign(λ_2)ρ) < 0.03 a.u.

4.4 Defining NCI regions

Given that chemical interactions are identified as peaks in $s(\rho)$ plots and the visualization of these peaks leads to closed isosufaces of $s(\mathbf{r})$, the integration of different properties within such isosurfaces may lead to some insight into the nature of the interactions. To performs such integration, it is first necessary to establish a unique definition of the NCI region (Ω_{NCI}). Given a proper non-interacting reference system, it is possible to define

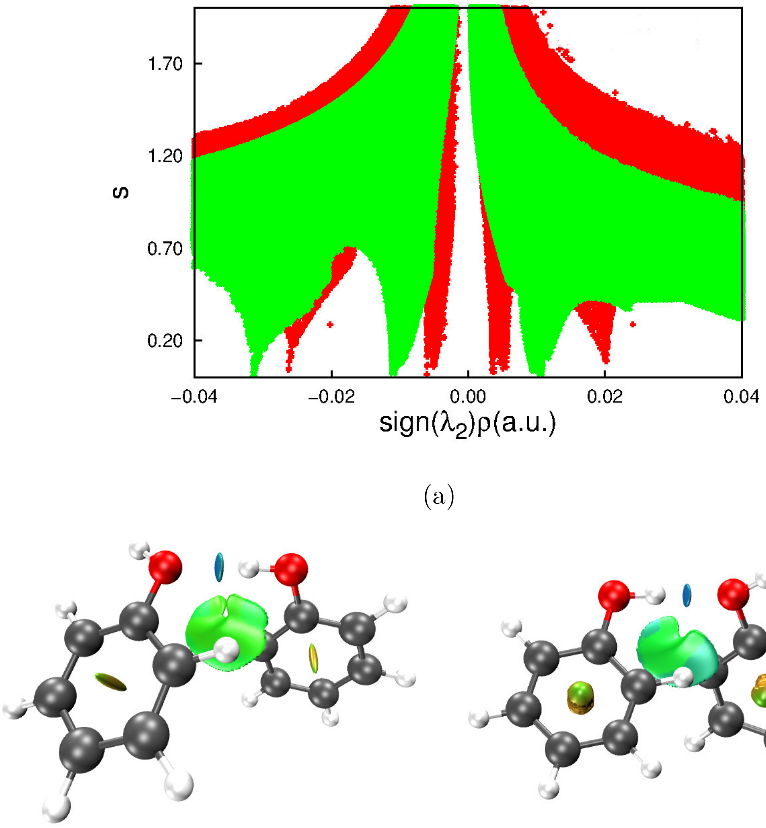

(a)

(b)

(c)

Figure 4.7: Comparison between SCF and promolecular NCI results for the phenol dimer. (a) The same $s(\rho)$ features are obtained using self-consistent (green) and promolecular calculations (red), with a shift toward negative (stabilizing) regimes. Taking the shift in spikes into account (i.e. changing the cut-off), the isosurface shapes remain qualitatively unaltered. (b) For SCF densities $s(\mathbf{r})$=0.6 and color scales of -0.04 $<$ sign$(\lambda_2)\rho$) $<$ 0.03 a.u. (c) For promolecular densities and $s(\mathbf{r})$=0.3. and -0.04 $<$ sign$(\lambda_2)\rho$) $<$ 0.1 a.u.

Ω_{NCI} as the region whose points in the s(ρ) plot lie below the s(ρ) curve for the reference system, $s^{ref}(\mathbf{r})$. Mathematically, NCI regions are defined by the condition

$$s(\mathbf{r}) - s^{ref}(\mathbf{r}) < 0. \tag{4.16}$$

To identify these regions, both the reference and the interacting system must be computed and compared. The lower edge of $s^{ref}(\mathbf{r})$ is splined and all points of the interacting system $s(\mathbf{r})$ lying below the splined curve are localized in real space. In Figure 4.8 Ω_{NCI} is extracted for the methane dimer along with its 3D representation. When the system is composed by different fragments, a hybrid $s^{ref}(\mathbf{r})$ curved is defined as follows: first $s(\mathbf{r})$ is computed for every fragment, then these values are compared at every value of $\rho(\mathbf{r})$ and the lowest $s(\mathbf{r})$ value is taken as reference point for that density.

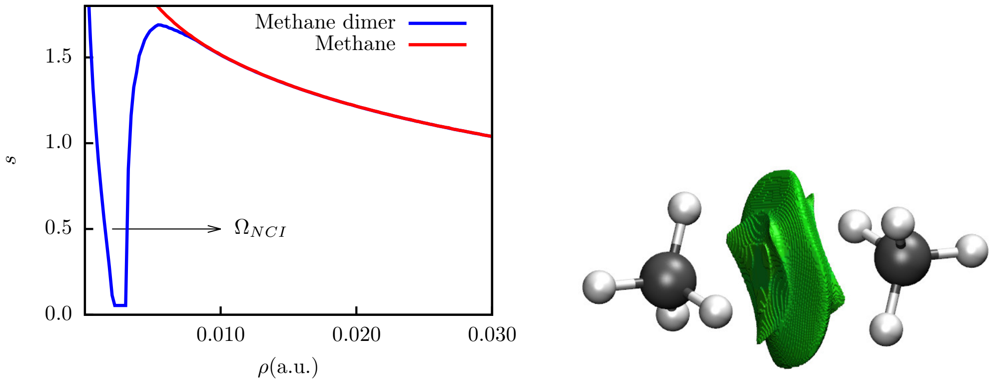

(a) (b)

Figure 4.8: (a) Ω_{NCI} for the methane dimer. (b) $s(\mathbf{r}) = 2.0$ isosurface containing Ω_{NCI}.

Density properties can be then integrated within such region to obtain its volume (V_{NCI}) or its electron population (N_{NCI})

$$V_{NCI} = \int_{\Omega_{NCI}} \mathbf{dr}, \tag{4.17}$$

$$N_{NCI} = \int_{\Omega_{NCI}} \rho(\mathbf{r})\mathbf{dr}, \tag{4.18}$$

Furthemore, attractive (*att*) and repulsive (*rep*) contributions (in the NCI method parlance) may be defined if $sign(\lambda_2)$ is considered:

$$V_{NCI}^{rep} = \int_{\Omega_{NCI}} \mathbf{dr} \qquad \lambda_2(\mathbf{r}) < 0, \tag{4.19}$$

$$V_{NCI}^{att} = \int_{\Omega_{NCI}} \mathbf{dr} \qquad \lambda_2(\mathbf{r}) > 0, \tag{4.20}$$

Contreras *et al.* [76] defined the quantity q^n_{bind} as an indicator of the binding effects in Ω_{NCI}

$$q^n_{bind} = -\int_{\Omega_{NCI}} sign(\lambda_2)\rho^n(\mathbf{r})\mathbf{dr}, \tag{4.21}$$

where the exponent n is a fitting parameter to mimic the hydrogen-bond binding-energy curve.

4.5 Connection with energetics

The kinetic interpretation of $s(\mathbf{r})$ enables a identification of regions of marked bosonic-like character, and therefore, relevant for chemical interactions. Additionally, it allows to connect $s(\mathbf{r})$ with the von Weizäcker kinetic energy density and with the energy density $H(\mathbf{r})$ [81]. For a system in a stationary state, $H(\mathbf{r})$ is defined as

$$H(\mathbf{r}) = \tau(\mathbf{r}) + \mathcal{V}(\mathbf{r}), \tag{4.22}$$

where $\tau(\mathbf{r})$ is the positive definite kinetic energy density and $\mathcal{V}(\mathbf{r})$ is the local virial field

$$\mathcal{V}(\mathbf{r}) = \frac{1}{4}\nabla^2\rho(\mathbf{r}) - 2\tau(\mathbf{r}). \tag{4.23}$$

$\mathcal{V}(\mathbf{r})$ represents the average effective potential field felt by an electron at $\mathbf{r}$, and provides a short-range description for the potential energy density. Since $\mathcal{V}(\mathbf{r})$ is negative everywhere [82] regions with positive $H(\mathbf{r})$ are not repulsive but dominated by $\tau(\mathbf{r})$. Regions where $H(\mathbf{r})$ is negative are dominated by $\mathcal{V}(\mathbf{r})$.

In order to express $H(r)$ in terms of the the von Weizäcker kinetic energy density, $\tau_w(r)$, the relationship between $\tau(\mathbf{r})$ and the Pauli kinetic energy density $t(\mathbf{r})$ is used, $\tau(\mathbf{r}) = \tau_w(\mathbf{r}) + t_p(\mathbf{r})$. Thus Equation 4.22 may be rewritten as:

$$H(\mathbf{r}) = \tau_w(\mathbf{r}) + t_p(\mathbf{r}) + \mathcal{V}(\mathbf{r}). \tag{4.24}$$

Since $H(\mathbf{r})$ integrates to the total electronic energy E, it is plausible to define a local stabilizing energy, $\Delta H(\mathbf{r})$ as the difference between $H(\mathbf{r})$ and that for a system of non-interacting reference fragments in equilibrium $H^{ref}(\mathbf{r})$. $\Delta H(\mathbf{r})$ integrates to the stabilization energy relative to the non-interacting fragments in equilibrium $\Delta E = E - E^{ref}$

$$\begin{aligned} \Delta E = E - E^{ref} &= \int \Delta H(\mathbf{r}) d\mathbf{r} \\ \Delta H(\mathbf{r}) &= \tau_w(\mathbf{r}) - \tau_w^{ref}(\mathbf{r}) + t_p(\mathbf{r}) - t_p^{ref}(\mathbf{r}) + \mathcal{V}(\mathbf{r}) - \mathcal{V}^{ref}(\mathbf{r}) \\ &= \Delta\tau_w(\mathbf{r}) + \Delta t_p(\mathbf{r}) + \Delta\mathcal{V}(\mathbf{r}). \end{aligned} \tag{4.25}$$

Analyzing $\Delta\tau_w(\mathbf{r})$, $\Delta t_p(\mathbf{r})$ and $\Delta\mathcal{V}(\mathbf{r})$ in Ω_{NCI} one may obtain insight into the local energetic contributions and whether they contribute to the stabilization by decreasing the kinetic or potential energy terms. The structural homeomorphism between -$\mathcal{V}(\mathbf{r})$ and $\rho(\mathbf{r})$ [82] states that the increase of the electron density in the interaction regions is followed by a decrease of $\mathcal{V}(\mathbf{r})$, so $\Delta\mathcal{V}(\mathbf{r})$ is expected to be negative in Ω_{NCI}.

As explained in section 4.4, Ω_{NCI} is defined by the condition given by Equation 4.16. Using the relation $\tau_w(r) = (5/3)t_{TF}(\mathbf{r})s^2(\mathbf{r})$, $\Delta\tau_w(\mathbf{r})$ is negative in the NCI regions, and thus the balance between $\Delta t_p(\mathbf{r})$ and $\Delta\tau_w(\mathbf{r}) + \Delta\mathcal{V}(\mathbf{r})$ will indicate whether the stabilization in Ω_{NCI} is locally dominated by the kinetic or the potential energy.

The term $\Delta\tau_w(\mathbf{r})$ is closely connected with the steric energy proposed by Liu [83]. Seeking for a partition of electron energy in terms of steric $E_s[\rho]$, electrostatic $E_e[\rho]$ and quantum effects $E_q[\rho]$, Liu proposed a partition of electron energy where $T_w = \int \tau_w(\mathbf{r})d\mathbf{r}$ accounts for the steric energy.

$$E_[\rho] = E_s[\rho] + E_e[\rho] + E_q[\rho], \tag{4.26}$$

In this context, one may understand Ω_{NCI} as those regions where the steric effects decrease.

$$\begin{aligned} E_e[\rho] &= V_{ne}[\rho] + J[\rho] + V_{nn}[\rho], \\ E_q[\rho] &= E_{xc}[\rho] + T_s[\rho] - T_w[\rho]. \end{aligned} \tag{4.27}$$

From the van der Waals DFT framework, it is found that non-local van der Waals density functionals are defined in terms on models of the static polarizability $\alpha(iu, 0)$ based on s [84],

$$\alpha(iu, 0) \propto \frac{1}{k_F^4 F(s)^4}, \tag{4.28}$$

where $F(s)$ is some function of s^2. For instance in vdW-DF-09 a particular simple choice is made $F = 1 + \mu s^2$. The dispersion interaction energy between two systems A and B can be written in terms of local polarizabilities

$$E_{disp} = -\frac{3\hbar}{\pi}\int_0^\infty du \int_A d\mathbf{r} \int_B \frac{\alpha(\mathbf{r}, iu), \alpha(\mathbf{r}', iu)}{|\mathbf{r} - \mathbf{r}'|^6} d\mathbf{r}', \tag{4.29}$$

where iu is an imaginary frequency, $\mathbf{r}$ is within the domain of system A, and $\mathbf{r}$' is within the domain of B. Regions of lower s, contribute larger to the local polarizabilites and therefore, to the overall dispersion energy. This result is supported by the correlation found between the volume of such regions V_{NCI} and E_{disp} [85].

A very interesting example where we can first cast from a visual approach the relative energies is found in 4-́Methyl,-5́' -Phenyl-[1,1' ;2' ,1"; 3", 1" ',2" ',1" ",3" ",1" " ']-sexiphenyl (See Figure 4.9). This system is formed by a central toluene ring with other six rings placed in three branches, one with one ring, another one with two rings and the last one with three rings. We have analyzed the effect of rotating two dihedral angles in order to release T-shape interactions. Rotation φ_5 gives rise to structures 1-2 (Figure 4.9b and 4.9c respectively); whereas structures 3-4 (Figure 4.9d and 4.9e respectively) result from the rotation of φ_3. Structures 1 and 3 present a T-shape interaction, whereas it has been respectively released in 2 and 4. A first look to Table 4.3 shows a good agreement between relative volumes and the stability of the system, in such a way that energetic ordering corresponds to the same ordering in NCI volumes (the more stable, the bigger volume). Moreover, NCI enables to detect the presence of the T-shape interactions in 1 and 3 that explain their greater stability over structures 2 and 4, respectively (see Figure 4.10 and Table 4.3). It should be noted that this kind of structural-stability information is a necessary step in inverse design and in the rationalization of chemistry.

This relation is not completely unexpected since the stabilization through dispersion interaction is proportional to the overlap area between molecular surfaces. One may

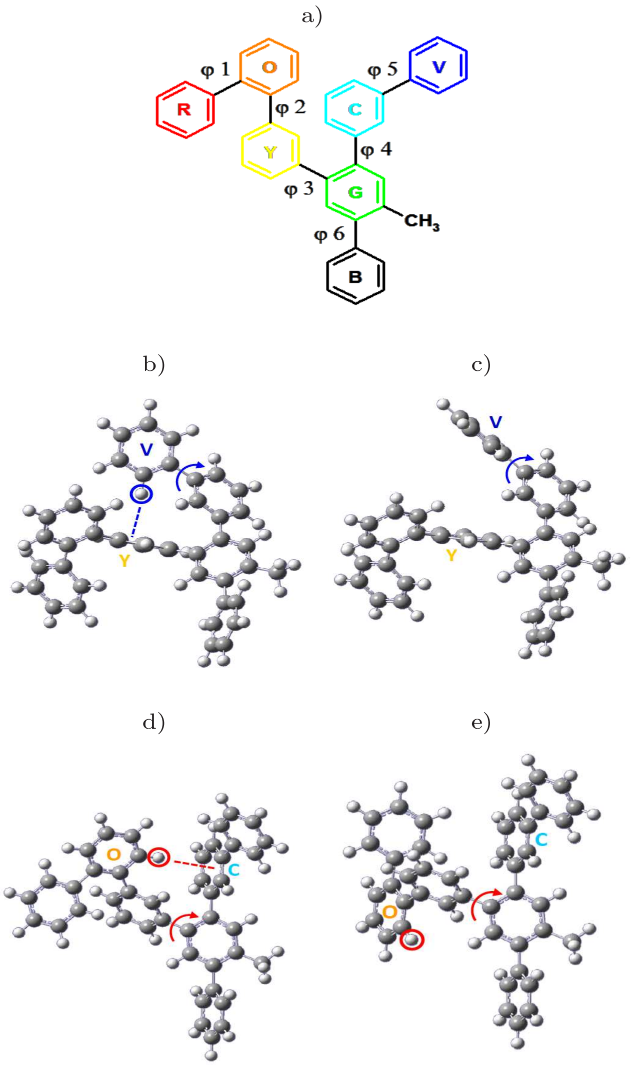

Figure 4.9: a) Numbering of the conformationally relevant dihedral angles φ=1 to 6 in sexiphenyl, b) and c) pair of structures differing by orientation of the $\varphi 5$ dihedral angle (designated by blue arrow): b) structure sexiphenyl-1 , where ring “V” forms a T-shape contact with ring “Y” and c) structure sexiphenyl-2, where the T shaped contact is absent. d) and e) pair of structures differing by orientation of the $\varphi 3$ dihedral angle (designated by red arrow): d) structure sexiphenyl-3, where ring “O” forms a T-shaped contact (red dashed line) with ring “C” and e) structure sexiphenyl-4, where the T shaped contact is absent.

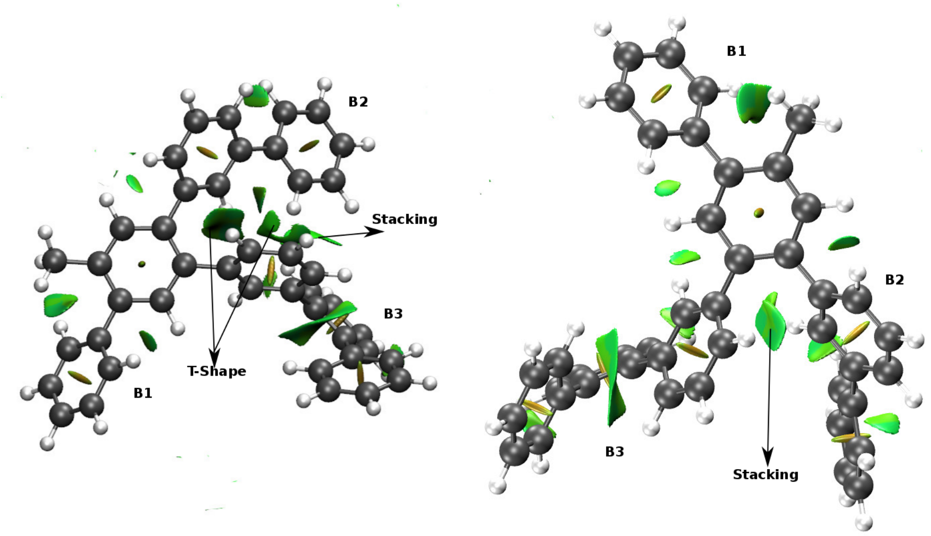

(a) Structure 1

(b) Structure 2

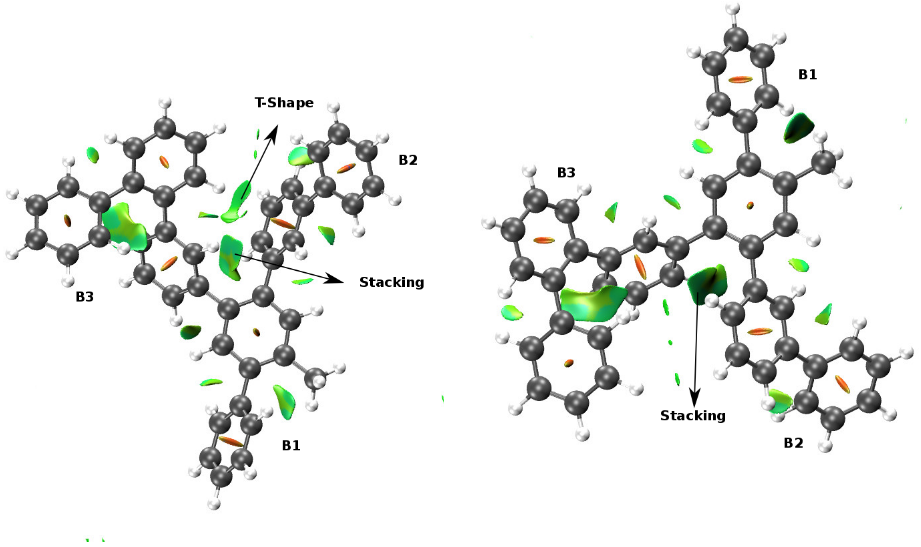

(c) Structure 3

(d) Structure 4

Figure 4.10: NCI results for the four sexiphenyl conformers. NCI regions corresponding to stacking and T-Shape interactions have been labeled a) structure 1, b) structure 2. c) structure 3 and d) structure 4. $s(\mathbf{r}) = 0.5$ isosurfaces colored over the range and color scale -0.04(blue) > sign$(\lambda_2)\rho$)< 0.04 (red).

Structure	1	2	3	4
T-shape	✓	×	✓	×
E_{int}	0.00	9.46	1.29	8.12
V_{NCI}	110.54	86.60	100.87	87.74

Table 4.3: Relative energy (E_{int}, kJ/mol) NCI volumes (V_NCI, a.u.) for the four rotamers (1 to 4) of sexiphenyl at the M06-2X/6-31g(d,p) level.

conclude that dispersion interactions occur through large regions of marked bosonic character. However, this correlation only holds for systems mainly stabilized by dispersion. Using the parameter q^n_{bind} (Equation 4.21) Contreras-García *et al* were able to mimic the potential energy curve of several hydrogen-bonded complexes [76], showing that it is possible to correlate interaction energies with properties computed within regions provided by the NCI method.

In the same line, Saleh *et al* analyzed the correlation between the stabilization energy and the energy density computed in regions with $s(\mathbf{r})$ lower than a given constant cut- off δ ($s(\mathbf{r}) < \delta$) [86]. They analyzed the correlation of $H(\mathbf{r})$, $\mathcal{V}(\mathbf{r})$ and $\tau(\mathbf{r})$ in such regions with the stabilization energies, and they found that $\tau(\mathbf{r})$ presents the best fitting.

Chapter 5

NCIPLOT: A program for plotting and computing properties within non-covalent interaction regions

Sommaire

In this chapter we describe the algorithms implemented in our principal code for performing NCI calculations: NCIPLOT. The first version of the code was realized in 2010 and developed by Julia Contreras-García, Erin R. Johnson, S. Keinan and W. Yang. This first code was mainly focused on the visualization of NCI regions, as extracted from the s *vs* ρ diagrams, as shown in Chapter 4. The recruit of Alberto Otero-de-la-Roza to the NCIPLOT project lead to a parallelized version of the code, NCIPLOT3. Moreover it added some new keywords to the original code. In order to compute properties within NCI regions as shown in Chapter 4, we developed a new version of NCIPLOT3. For the sake of simplicity we divided this chapter in three parts: i) algorithm for visualizing NCI regions, ii) algorithm for computing properties within NCI regions, iii) we perform several benchmark calculations to outline the possibilities and limitations of the algorithms hereby presented.

5.1 Algorithm for visualising NCI regions

Figure 5.1 shows the protocol for visualizing non-covalent interaction in NCIPLOT, and it is used in all versions of the code. Two basic types of data constitute the input: the density information (based on wave functions or molecular geometries) and the analysis options, which determine the non-covalent interactions to be plotted. Four algorithms analyze the data: i) the selection of interactions (through the input), ii) the construction of the cube and the grid, iii) the calculation of properties at each point (using a number of routines), and iv) the calculation of visualization data (carried by the main routine, NCIPLOT). Since the input is keyword oriented, the program includes a number of parsing routines. These main features are discussed in the following sections.

5.1.1 Building the cube

Interaction analysis is based on examination of local properties on a cubic grid constructed within the program. This procedure was found to be extremely efficient for computing stable properties (as is the case of NCI). Furthermore, this approach enable us to discard contributions from high-density points in the construction of isosurfaces. The spatial region to be analyzed is determined by default, in terms of the molecular geometry. Unless otherwise noted, a cube is constructed for the outermost *x,y,z* coordinates for all the molecules in the input. An extra radial threshold in each directions is added to ensure that the isosurfaces are contained within the cube (no intermolecular interactions are expected in those regions, but isosurfaces can spread beyond the atoms. A practical threshold was defined as 2 Å:

$$x_i(0) = min[x_i] - 2\text{Å} \tag{5.1}$$

$$x_i(1) = max[x_i] + 2\text{Å}, \tag{5.2}$$

where $x_i = x, y, z$. This step eliminates spurious symmetry-related cancellations in case of planar systems.

It can be useful to construct a user-defined cube or to analyze the interactions only around one point or molecule. With this purpose in mind, two possibilities when choosing a given interaction from its location in 3D space have been implemented:

- An appropriate choice of the cube boundaries enables the selection of individual interactions (CUBE keyword). The cube boundaries may be defined by cartesian

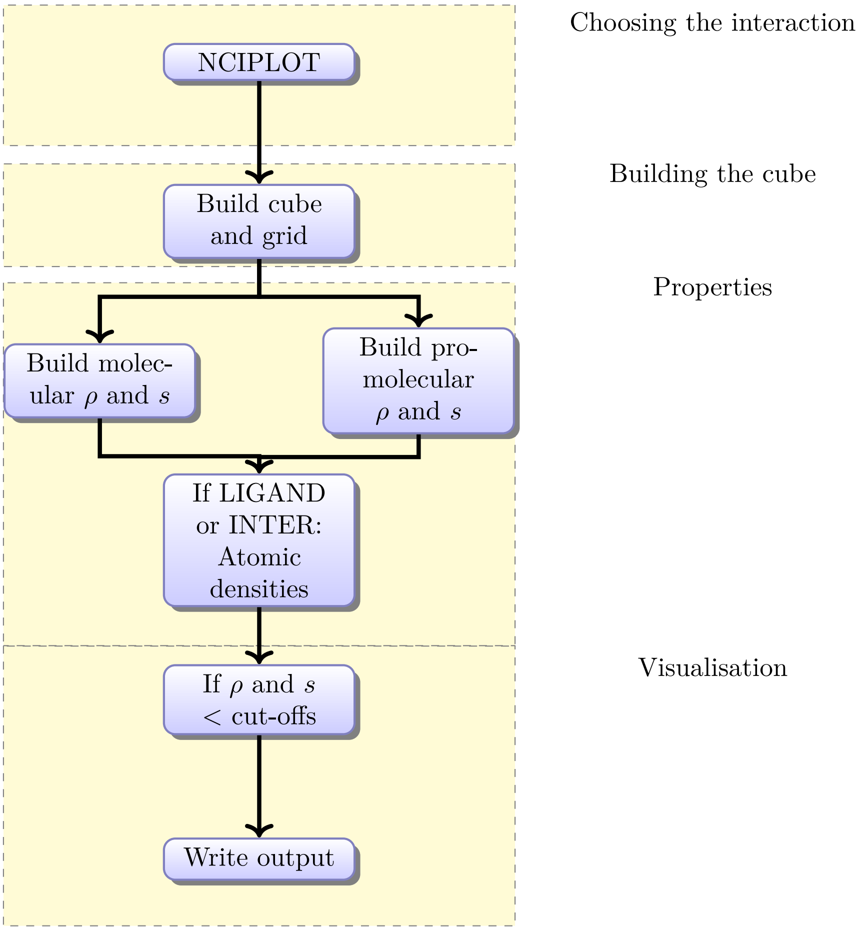

Figure 5.1: Flowchart for program routines for non-covalent interactions visualization in NCIPLOT. The flow is divided into four main algorithmic parts: input, cube construction, properties, and visualisation.

coordinates or by choosing a list of atoms (ATCUBE and LIGAND keywords) (See Figure 5.2c). This selection by atoms was found to be chemically more useful and intuitive than the initial CUBE keyword, so it is a simple but very useful addition to the code.

- An alternative implementation for the geometric criterion consists on defining the center of the cube instead of its boundaries (RADIUS keywords). This option used the origin and length of the box sides as input rather that the Cartesian coordinates themselves.

5.1.2 Pure intermolecular interactions

All of the interactions with at least, a specified fraction (e.g., $f = 0.9$) of the density from a single molecule are turned off:

$$\frac{\rho_{monomer}}{\rho_{tot}} = \begin{cases} \geq f & \text{intramolecular} \\ < f & \text{intermolecular} \end{cases}$$

This choice causes only intermolecular interactions to be plotted, screening out the intermolecular interactions. This is readily automated if each monomer is uploaded in different files. This procedure enables the characterization of monomers and the construction of $\rho_{monomer}$.

5.1.3 Promolecular densities

The features of promolecular densities have been already discussed in Section 4.3.4 of Chapter 4. In NCIPLOT, promolecular densities are constructed from the atomic positions stored in an xyz coordinate file(s). In order to store atomic densities, two sets of promolecular densities can be used; exponential and radial fits. The former are generated by fully numerically LSDA free-atomic densities for the neutral atom H to Ar, spherically averaged over space and summed over spins. The latter are build by fitting to one (H,He), two (Li-Ne), or three (Na-Ar) Slater-type functions of the form $\rho^{at} = \sum_j c_j e^{-\mathbf{r}/\zeta_j}$. Once these densities are written as simple sums of exponential functions, the NCI surfaces can be calculated very efficiently for each (supra)molecule, since all of the necessary data $(\rho, s\lambda_2)$ can be obtained analytically. Radial fits were added to the NCIPLOT3 are available up to Pu.

5.1.4 Visualization: The cut-offs

The ρ, s coordinates of the density peaks define the appropriate cut-offs for non-covalent interactions. For example, in the formic acid dimer a cut-off of $\rho < 0.05$ a.u. is appropriate for recovering all the non-covalent interactions. All points giving rise to ρ values above this threshold need to have their s values set to a large value. This enables the user to recover only the non-covalent interactions when $s \leq S$ (for some isosurface value S). Tuning the cut-off value, the non-covalent interactions of the system may be recovered as individual isosurfaces. The formic acid dimer peaks appear at $\rho = 0.01$ a.u. for vdW contacts, and $\rho = 0.05$ a.u. for hydrogen bonds. If the cut-off is set to $\rho = 0.01$ a.u. the isosurface will only recover the vdW interactions in the system (Figure 5.2b). Furthermore, placing a threshold for the interval $\rho = [0.01 - 0.06]$ a.u. enables the user to isolate the hydrogen bonds in a similar manner.

It is convenient, therefore, to perform a preliminary run, where only $s(\rho)$ values are produced, then the user can use these data to determine optimal cut-offs. A second run can subsequently target the non-covalent interactions in a given molecule with no interference from other density regions. For this reason, the current implementation enables the user to decide which file types are to be output.

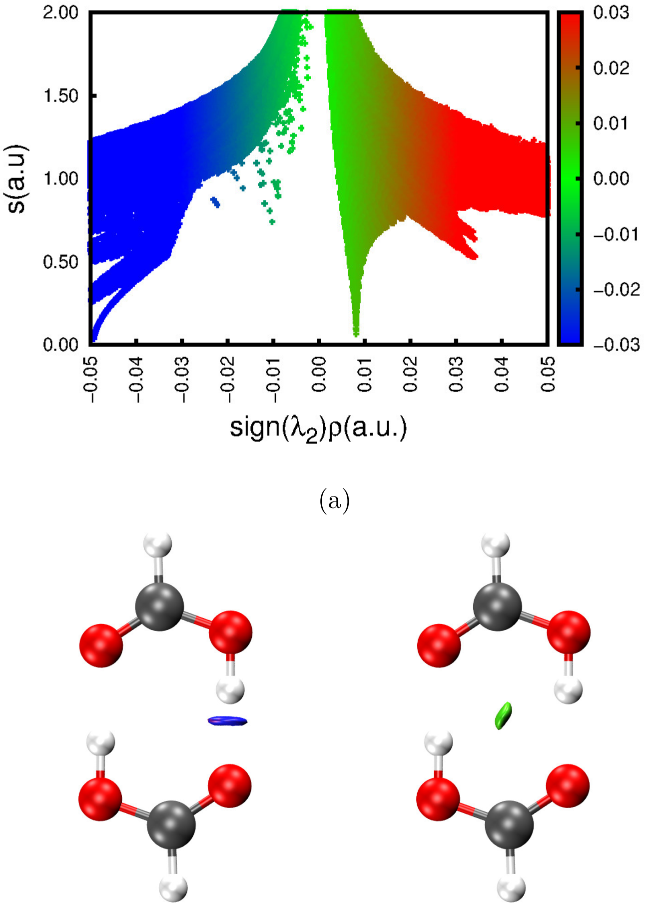

(a)

(b) (c)

Figure 5.2: NCI analysis of formic acid dimer. (a) $s(\rho)$ plot for CCSD/6-311G density. Peaks appear at 0.05 for vdW (green) and 0.008 a.u. for hydrogen bonds (blue). Isosurface extraction with the ATCUBE keyword: (b) Hydrogen bonds may be selected by setting the cube boundaries around the hydrogen and oxygen atoms, (c) vdW interactions may be recovered by setting a thin cube boundaries around the carbon atoms. The NCI color scale is -0.05 < $\text{sign}(\lambda_2)\rho$ < 0.05 a.u.

5.2 Computing properties within NCI regions

Quantitative calculations have been added to the code. As shown in Section 4.4 of Chapter 4, the NCI regions (Ω_{NCI}) may be directly defined from the s *vs* ρ diagram, as the domain(s) in $\mathbb{R}^3$ with ρ and s values lying in the $s(\rho)$ peak. To identify this region, the reference, the interest system densities and their reduced density gradients must be computed and compared. The lowest edge of the reference $s^{ref}(\rho)$ curve is splined. A point r_i is said to belong to Ω_{NCI} if it satisfies the following three conditions;

$$\mathbf{r}_i \in \Omega_{NCI} \begin{cases} s(\mathbf{r}_i) & < s^{ref}(\mathbf{r}_i) \\ s(\mathbf{r}_i) & < s_{cut-off} \\ \rho(\mathbf{r}_i) & < \rho_{cut-off}, \end{cases}$$

where $s^{ref}(\mathbf{r}_i)$ is the reference value of s at r_i, and $s_{cut-off}$ and $\rho_{cut-off}$ are the reduced density gradient and the density cutoffs respectively.

Density properties can be then integrated within Ω_{NCI}, as defined in Equations 4.4-4.21. Although in principle any integration method is valid, the current version of the code performs a mere sum over volume elements contained in Ω_{NCI}

$$A_{NCI} = \sum_{i \in \Omega_{NCI}} A(r_i) \Delta x_i \Delta y_i \Delta z_i, \tag{5.3}$$

where $A(r_i)$ is the value of the property A at r_i and $\Delta x, \Delta y$ and Δz stand for the increments along the x, y and z direction. Their product $\Delta x_i \Delta y_i \Delta z_i$ defines a volume element around r_i. For visualization purposes, the property values are set to very big values for such points not belonging to Ω_{NCI}. The simplest property one can compute is the volume of the NCI region V_{NCI} which is given by the sum of all the elements $\Delta x_i \Delta y_i \Delta z_i$ contained in Ω_{NCI}. Besides s and ρ which should be computed in all points of the grid in order to define the NCI regions, all the other properties are only computed in those points belonging to Ω_{NCI}.

5.2.1 Selecting s^{ref}

We have implemented three possible choices of the NCI regions; i) selecting only one of the constituent fragments of the system (See Figure 5.3), ii) building a hybrid reference reduced density gradient from the constituent fragments, and iii) fixing an upper cut-off for s. The first and the second have more physical grounds, and they are therefore highly recommended. The latter gains importance when monomer (or fragments in general) structures are not available or not defined, e.g. intramolecular interactions. Its validity has only been confirmed *ad hoc* by comparison with interaction energies [86].

5.3 Benchmark

One of the most striking and controversial points of the NCI method is the match between the results obtained with promolecular and self-consistent densities. As discussed in Section 4.3.4 of Chapter 4, this result may be traced back to the stepwise exponential behavior of the electron density. This raises a theoretical issues: *"What it the influence of the method and the basis set on the NCI index? How trustworthy are promolecular results?"*. To explore the dependence of the NCI method with the quality of the electron density, we have performed a number of benchmark calculations.

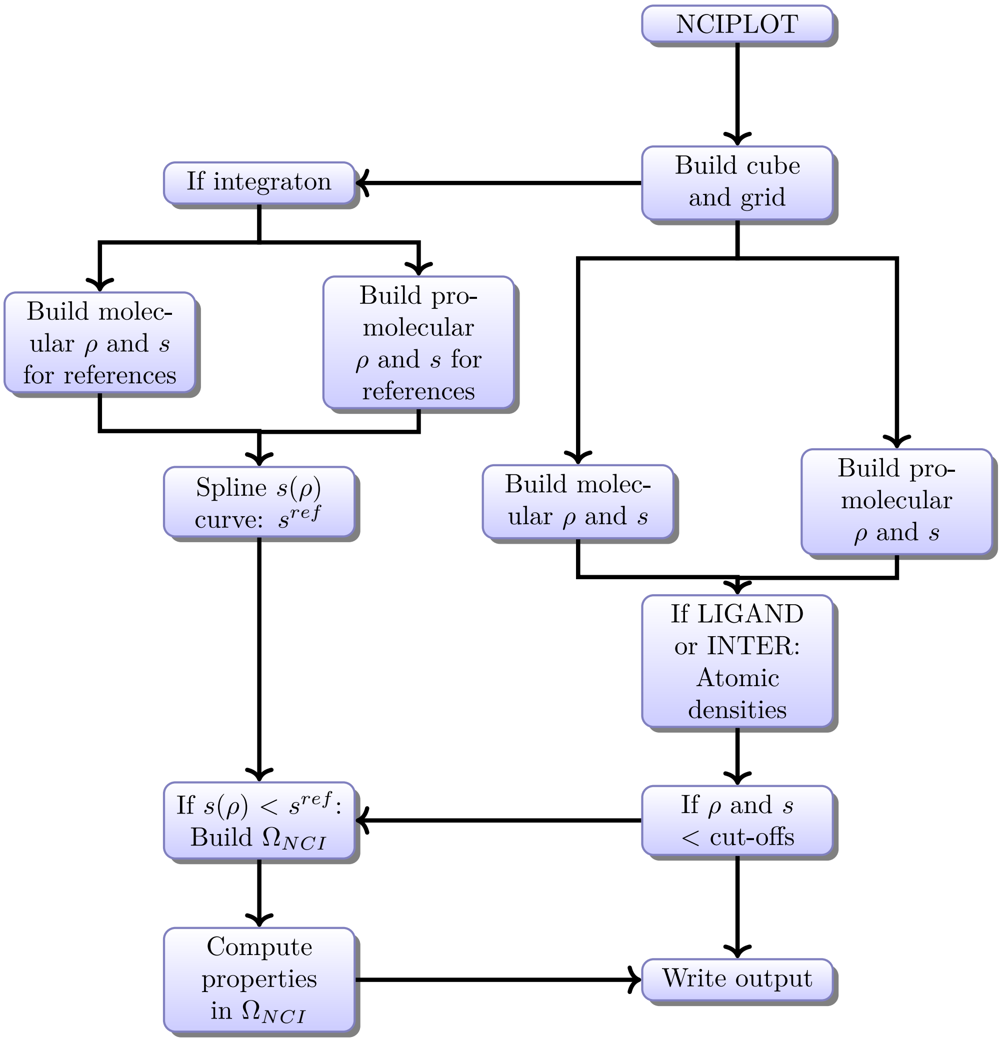

Figure 5.3: Flowchart for program routines for non-covalent interactions visualisation and integration in NCIPLOT.

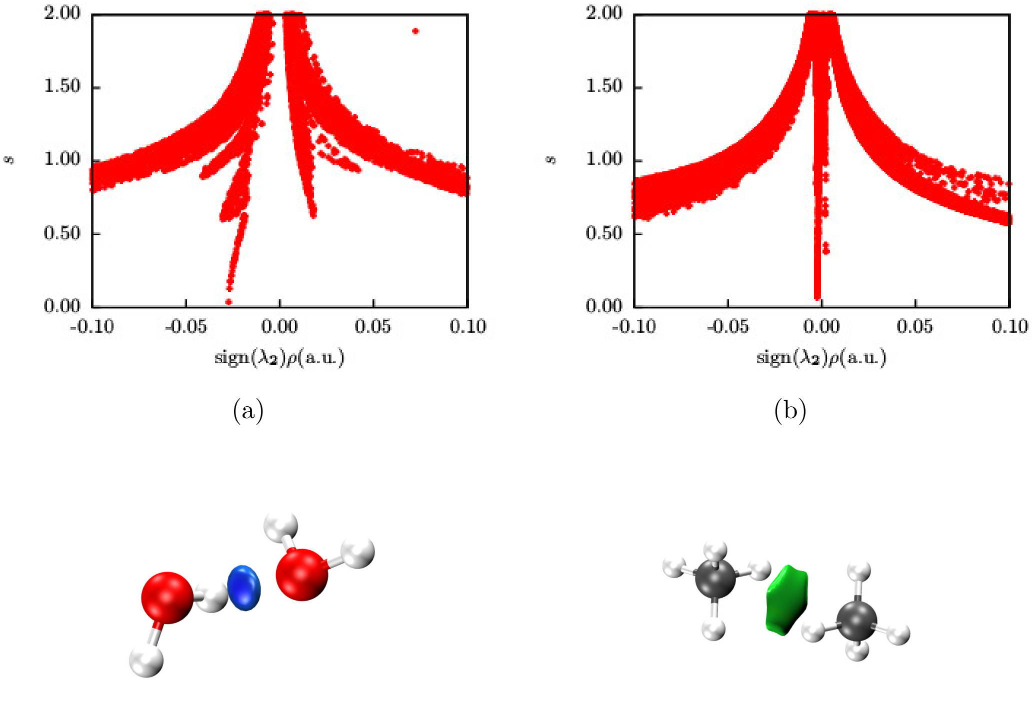

(a)

(b)

(c)

(d)

Figure 5.4: 2D ((a), (b)) and 3D ((c),(d)) NCI plots of water ((a), (c)) and methane ((b), (d)) dimers (computed at CCSD/6-311G level of theory):The $s = 0.5$ isosurfaces are coloured on a blue-green-red according to the sign$(\lambda_2)\rho$ value over the range -0.03 to 0.03 a.u.

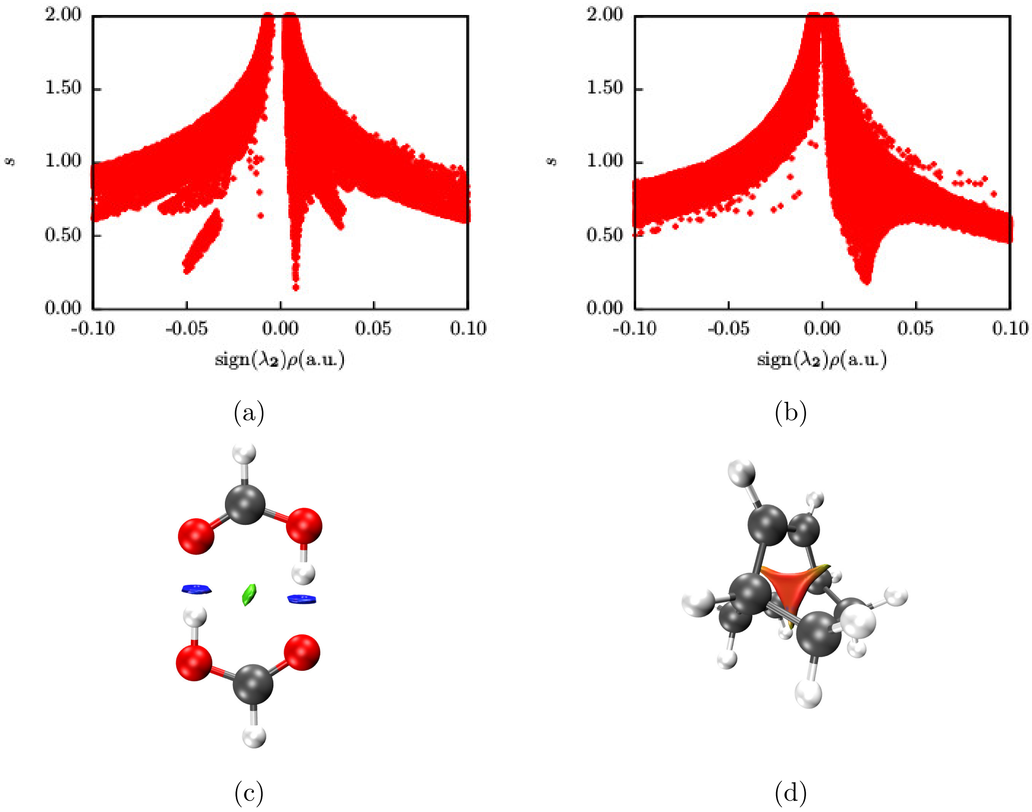

(a)

(b)

(c)

(d)

Figure 5.5: 2D ((a), (b)) and 3D ((c),(d)) NCI plots of formic acid dimer ((a), (c)) and bicyclootene ((b), (d)) dimers (computed at CCSD/6-311G level of theory):The $s = 0.5$ isosurfaces are coloured on a blue-green-red according to the sign$(\lambda_2)\rho$ value over the range -0.03 to 0.03 a.u.

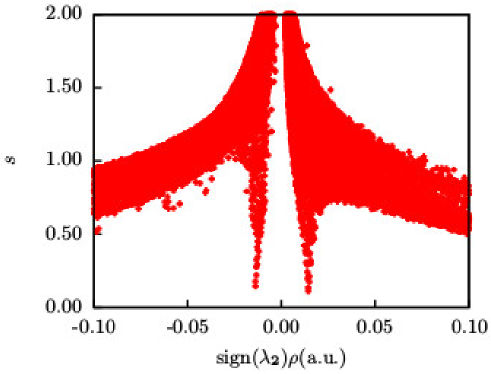

(a)

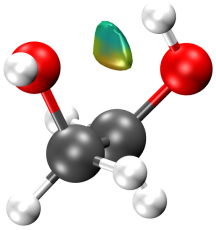

(b)

Figure 5.6: 2D (a) and 3D (b) NCI plots of ethanediol (computed at CCSD/6-311G level of theory):The $s = 0.5$ isosurfaces are coloured on a blue-green-red according to the $\text{sign}(\lambda_2)\rho$ value over the range -0.03 to 0.03 a.u.

5.3.1 Computational details

All the geometries were taken from the S22 set and not reoptimized. Wave functions were obtained with the Gaussian09 package. In order to compare the results from different SCF methods, we have included in our study Hartree-Fock(HF), post-HF methods (MP2, CISD, CCSD) and density functional approaches.

Second-order Möller-Plesset perturbation theory (MP2) is the most affordable wave function-based method beyond the HF approximation that provides an approximate description of all relevant vdW interactions, electrostatics, induction and dispersion. Furthermore, MP2 is free from spurious electron self-interaction, which leads to noticeable improvements for hydrogen bond description. However, one of the serious shortcomings of MP2 theory is a noticeable overestimation of the dispersion interaction energy. As a reference, we have included the quantum chemistry gold standard: coupled cluster theory with single and double excitations. Perturbative triple excitation have not been included since they do not affect the underlying electron density and the output of *wfn* files is not yet implemented in Gaussian. CISD has been included for completeness.

Since nowadays calculation of big systems, where NCIs are extremely relevant, are usually performed with density functional theory (DFT) methods, we have also included two of the most common functionals: B3LYP and B97D. B3LYP is by far the most popular density functional in chemistry, but there is growing evidence showing that B3LYP degrades as the systems becomes larger and fails to bind van der Waals systems. Last years have been marked by an intense research of new DFT variants accounting for dispersive effects. From the comparative benchmark studies emerges that the M06-2X, w-B97X-D, and B97-D functionals significantly outdo B3LYP in estimating interaction energies in π-complexes. Since these studies are done at fixed geometry, a posteriori corrections become a fair test for the results. Pople basis sets have been used to test the dependence with the basis, including separately polarization and diffuse functions to independently analyze their effect.

NCI isosurfaces were obtained using grids of 0.1 Å along each axis. Electron densities at the AIM critical points were obtained with promolden. Non-AIM critical points were obtained from 2D graphs with increments of 0.05 bohr along each axis. For the sake of simplicity we shall refer to both AIM and Non-AIM critical points as Interaction Critical Point (ICPs). As aforementioned, volume and electron density integrations, are performed using pseudo-densities (approximated monomer densities from the dimer wave functions) for each of the monomers and performing a cubic spline interpolation of the resulting $s(\rho)$ curve. We used the following default value: grids of 0.09 bohr along each axis, and threshold of 0.05 a.u. and 0.5 in the density and s, respectively.

5.3.2 The effects of the method

In order to understand the effect of the method we will analyze a set of representative molecular systems:

- a hydrogen bond (water dimer), a dispersive interaction (CH_4 dimer) and a repulsive clash (bicyclo[2.2.2], from now on, bicyclooctene) showing critical points of the electron density.
- formic acid dimer as an example of mixed interactions of different strength (hydrogen bonds and dispersion).
- ethanediol where the hydrogen bond does not have an associated AIM critical point.

A stand-alone section is included on the analysis of promolecular (non-relaxed densities) at the end of the chapter Since the main objective of this section is to analyze the effects of the method on NCI results, we will use fixed geometries in all cases.

Figures 5.4-5.6 collect the 2D and 3D NCI diagrams of the selected molecules. The hydrogen bond in water dimer shows a negative value of λ_2 at the critical point (Figures. 5.4a,c), whereas $\lambda_2 \approx 0$ (either positive or negative) for van der Waals interaction in methane dimer (Figures. 5.4b,d). Non-bonding interactions in bicyclooctene result in density depletion, so that $\lambda_2 > 0$ (Figures. 5.5b, d). It can be observed that both hydrogen bonds and steric clashes appear at greater densities (although different λ_2 sign) that van der Waals (see Figures. 5.5a-c and Table 5.1). Both strong and weak interactions are present in formic acid dimer (Figs. 5.5a, c). The case of non-AIM-CPs is illustrated with ethanediol (Figs. 5.6a-b). As highlighted in the previous section, it corresponds to a very weak interaction where both positive and negative eigenvalues of the electron density Hessian matrix are present in the absence of AIM critical points.

SCF method

Table 5.1 collects the electron density at the ICP for our test systems. Except for HF, the influence of the electronic structure method is rather small. In general, peaks at the HF level appear at smaller densities. This is due to the localizing effect of HF. Hartree-Fock densities localize the electrons within molecular units, so that the electron density at ICP diminishes in all the interaction types. Inclusion of correlation, either directly (MP2, CISD) or by parametrization (functionals re-establish values similar to the CCSD reference. It is interesting to note how the method failures are translated into the electron density. MP2 leads to overbinding, with slightly overestimation of densities at the ICP, specially (as noted in the literature) in dispersion interactions. As far as DFT calculations are concerned, they have an effect contrary to that of HF, since functionals tend to delocalize. Thus, the electron density at the ICP is always larger than for CCSD in attractive interactions. The effect however is not as well behaved due to the parametrizations. B97D seems to specially overbind the strong hydrogen bonds, whereas it behaves better in methane dimer (but not in formic acid dimer). The case of bicyclooctene is interesting: both functionals find smaller densities at the ICP than CCSD, which seems to indicate that they underestimate steric repulsion probably due to self-interaction errors.

It is interesting to note that the calculations have been carried out at the S22 fixed geometry, so that the over(under)binding is not translated into the geometry, but only into the electron density. These effects are small and do not yield qualitative (not even quantitative) differences in the NCI picture of the systems. Two main conclusions can be extracted.

On the one hand, global quantities are more affected by the method (see Table 5.2), but the qualitative behavior remains. This is related to the stability of NCI results, and backs up the fact that NCI can be applied in spite of the method used of evaluating the density. Even non-dispersive methods, such as HF or B3LYP give global result that qualitatively agree with CCSD calculations. Changes in the global quantities confirm that NCI does change with the calculation method, but the changes are not very important (even for the volume) and conserve the trends, as long as the geometry is fixed.

On the other hand, the same behavior in ICPs and NCI volumes is observed in all cases. This is a very interesting observation since the calculation of electron densities at the ICP is much faster than the integration of volumes, so the former can be directly taken as an indicator of the quantitative deviations that should be expected. As observed

Method	H_2O dimer	CH_4 dimer	Bicyclooctene[a]	Formic acid dimer		Ethanediol[b]
CCSD	0.027328	0.0025130	0.023781	0.049234	0.0081382	0.014290[†]
HF	0.025641	0.0023633	0.023113	0.046651	0.0072130	0.013501[†]
MP2	0.027456	0.0025443	0.024157	0.049405	0.0084400	0.014479[†]
CISD	0.027025	0.0024832	0.023535	0.048359	0.0077967	0.014072[†]
B3LYP	0.027572	0.0025944	0.023394	0.049895	0.0082705	0.014206[†]
B97D	0.027872	0.0025270	0.023435	0.050661	0.0083902	0.014206[†]

Table 5.1: Method dependency of the ICP electron density for test molecules: water dimer, methane dimer, bicyclooctene, formic acid dimer (HB in first column, vdW in the second) and ethanediol.[a] All calculations with 6-311G basis set. [b] Due to their similarty (Ref [87]) only attractive points is shown in ethanediol. [†] Approximated value obtained from 2D plot due to the absence of AIM critical point.

Method	H_2O dimer	CH_4 dimer	Bicyclooctene[a]	Formic acid dimer	Ethanediol
CCSD	0.24	0.86	1.55	0.80	0.36
HF	0.21	0.79	1.33	0.69	0.28
MP2	0.25	0.88	1.64	0.84	0.38
CISD	0.24	0.85	1.48	0.76	0.33
B3LYP	0.25	0.90	1.50	0.82	0.37
B97D	0.25	0.88	1.48	0.81	0.37

Table 5.2: Method dependency of the NCI volume (pseudomolecules as reference) for test molecules at the 6-311G level: water dimer, methane dimer, bicyclooctene, formic acid dimer and ethanediol. [a] Grid increments of 0.09 bohr along each axis and a threshold of 0.05 a.u. and 0.5 in the density and s, respectively, were used in the integrations.

in Chapter 4, volumes confirm that the same s value should be used when densities have been calculated with the same method and shifted otherwise.

No relaxation: promolecular densities

Promolecular densities lack the relaxation introduced in a SCF Hartree-Fock or DFT calculation; but are very fast to compute. Thus, qualitative NCI analysis is applicable to large systems, including biosystems, where the description of the interplay of structure and reactivity is crucial. Because the calculation of the electron density in these subsystems becomes extremely computationally expensive, the promolecular density becomes an attractive option.

Of course, it is important in these cases to understand how to use of promolecular densities affects the NCI calculation. When relaxed densities are compared to promolecular ones, a shift in the peak is observed, with the promolecular approximation yielding bigger values in all cases (Table 5.3). The largest shift is observed in the non-bonded overlap cases, whereas it is moderate in the case of stabilizing interactions. This can be understood as the process of relaxing densities at a fixed geometry: steric clashes play the major role, which affects the whole interacting region, and to a smaller extent the stabilizing ones. As an example, the electron density at the peak in bicyclooctene changes from 0.053 to 0.023 a.u. upon convergence, whereas it only changes from 0.023 to 0.027 a.u. and from 0.018 to 0.014 a.u. in water dimer and ethanediol, respectively. Non-bonded dispersive interactions also show big relative changes (e.g. from 0.006 to 0.002 a.u. in methane dimer), but since these densities are smaller in absolute value, the absolute difference stays negligible from a visual point of view. This same behavior is reproduced when the interaction pattern becomes more complicated, as is the case of formic acid dimer.

Since in the promolecular case, the changes are not negligible, cut-off values need to be changed if we want to obtain similar pictures to SCF ones: the electron density cut-off needs to be bigger and the s isovalue smaller. The isosurface value need to be diminished because reduced densities are contracted around the ICPs upon relaxation. This is reflected in Figure 5.7-5.9 for all interaction types. As already observed in the analysis of ICPs, the greatest change is observed in steric clashes, where the repulsive region is greatly reduced upon convergence.

In the same line, all volumes are bigger in the promolecular approximation (Table 5.4). Indeed, values start to look of the same order when $s = 0.4$ in the promolecular calculation (except in bicyclooctene), whereas $s = 0.5$ is used in the SCF ones. As a guiding line, the default values for visualization in the NCIPLOT code go from $\rho = 0.05$ a.u. and $s = 0.5$ in SCF calculations to $\rho = 0.07$ a.u. and $s = 0.3$ in the promolecular case.

5.3.3 The basis set

Table 5.5 shows the variation of the electron density with the basis set on going from double to triple zeta, and on adding diffuse and polarization functions. CCSD has been used in all cases. Linear dependency problems were found with the convergence for Dunning basis sets (and also for 6-311G** calculations of bicyclooctene), so we have restricted ourselves to Pople basis set as a proof of principle of basis set dependency. It has been observed in the study of benzene dimers with Dunning basis sets, the influence

Method	H_2O dimer	CH_4 dimer	Bicyclooctene^a	Formic acid dimer		Ethanediol^b
CCSD(6-31G)	0.027328	0.0025130	0.023781	0.049234	0.0081382	0.014290
Promolecular	0.029861†	0.0063881†	0.053456†	0.051855†	0.0013996†	0.018327†

Table 5.3: Variation from promolecular to CCSD in the ICP electron density for test molecules: water dimer, methane dimer, bicyclooctene, formic acid dimer (HF in first column, vdW in the second) and ethanediol. ^{a} Approximated values obtained from 2D plot with 0.05 a.u. grids except for ethanediol, where a 0.01 grid along each axis was used to increase accuracy due to the planarity of the electron density. ^{b} Due to their similarity, only attractive ICS is shown in ethanediol (Ref [87]). † Approximated value obtained from 2D plot.

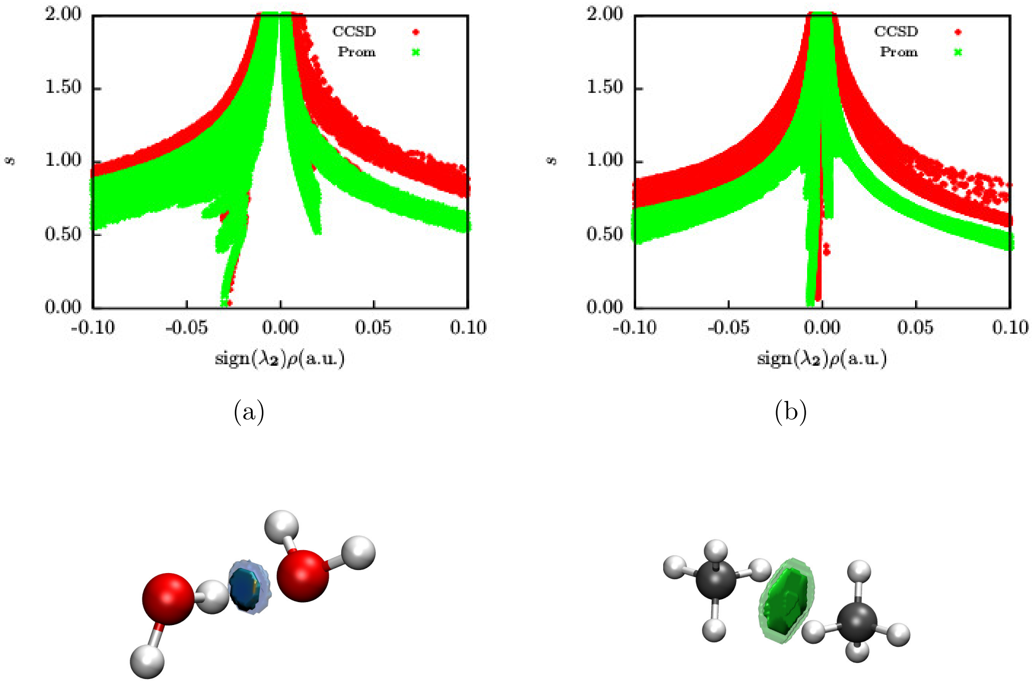

(a)

(b)

(c)

(d)

Figure 5.7: Comparison of NCI CCSD/6-311G and promolecular for test molecules. CCSD and promolecular integrated volumes are displayed as solid and transparent isosurfaces respectively: (a, c) water dimer and (b, d) methane dimers

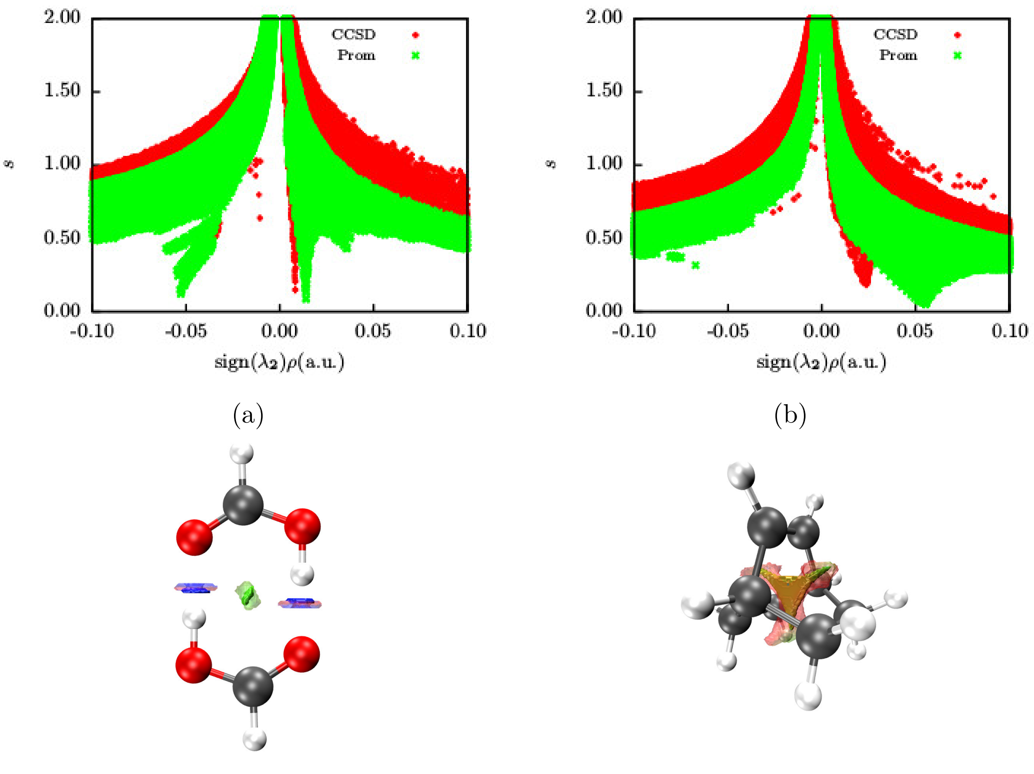

(a) (b)

(c) (d)

Figure 5.8: Comparison of NCI CCSD/6-311G and promolecular for test molecules. CCSD and promolecular integrated volumes are displayed as solid and transparent isosurfaces respectively: (a, c) formic acid dimer and (b, d) bicyclooctene.

Method	H_2O dimer	CH_4 dimer	Bicyclooctene^{a,c}	Formic acid dimer	Ethanediol
CCSD^b	0.24	0.86	1.55	0.80	0.36
Promolecular $s = 0.5$	0.63	17.28	9.17	2.22	1.53
Promolecular $s = 0.4$	0.30	8.05	3.28	0.98	0.22

Table 5.4: Variation of the NCI volume between CCSD(pseudo-densities of monomers are used as reference) and the promolecular approach for test molecules at the 6-311G level: water dimer, methane dimer, bicyclooctene, formic acid dimer and ethanediol. Two different thresholds for s where used in the integrations of the volume for promolecular densities: 0.5 and 0.4. ^{a} Grid increments of 0.09 bohr, ρ <0.05 a.u. ^{b} A threshold of 0.5 in s was used in the integrations for the CCSD volumes. ^{c} $s < 0.6$ in bicyclooctene due to the big shift in the peaks.

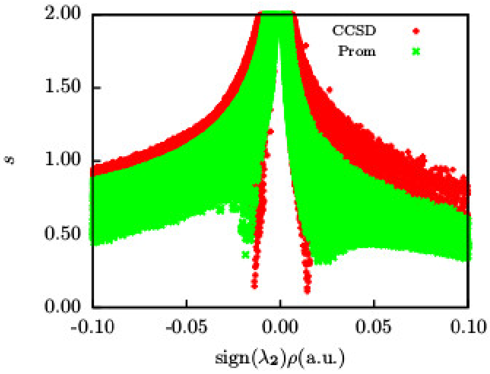

(a)

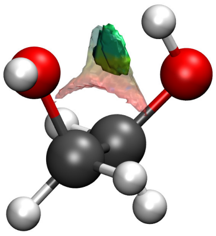

(b)

Figure 5.9: Comparison of NCI CCSD/6-311G and promolecular for test molecules. CCSD and promolecular integrated volumes are displayed as solid and transparent isosurfaces respectively for ethanediol.

Method	H_2O dimer	CH_4 dimer	Bicyclooctene[a]	Formic acid dimer		Ethanediol[b]
6-31G	0.28449	0.0025736	0.023113	0.049204	0.0075955	0.014496
6-311G	0.027328	0.0025130	0.023781	0.049234	0.0081382	0.014290
6-311G**	0.023977	0.0023279	†	0.046353	0.0074230	0.014234
6-311G++	0.026571	0.0025064	0.024020	0.049072	0.0083187	0.001403

Table 5.5: Basis set dependence of the ICP electron density for test molecules :water dimer, methane dimer, bicyclooctene, formic acid dimer (HF in first column, vdW in the second) and ethanediol. [a] All calculations at the CCSD level. [b] Due to their similarity, only attractive point is shown in ethanediol. [†] The calculation did not converge due to nearly linear dependency. [‡] Approximated value obtained from 2D plot due to the absence of AIM critical point.

of adding diffuse functions was negligible, since an almost identical distribution of low-gradient spikes was obtained for the aug-cc-VTZ and cc-VTZ basis sets.

As in the previous section, we have focused on electron densities at the ICP and NCI volumes to quantify changes. It is important to separate attractive and repulsive interactions here, and to make a joint analysis of ICP densities and NCI volumes. As a general trend, in attractive interactions, the increase of the basis set leads to a diminution of the electron density at the ICP. This is clearly observed in water and methane dimers. In both cases, polarization functions have the greatest effect. This can probably be attributed to the match between the method and the base: since CCSD allows for correlation to take place, the use of higher order angular momenta functions is favored. It also highlights the relevance of a well balancing method and basis set. Correlation diminishes bond order in general and reduces the electron density at the critical points, but has different effects on the total NCI volume.

A localized interaction, such as the one in the water dimers leads to smaller NCI volumes along with the diminution of ICP density. However, the effect in methane dimer volume is the opposite. Due to the nature of dispersion, the main effect of the basis set in methane dimer is a delocalization of the electron density, an increase in its planarity, leading to bigger NCI volumes. So the bigger basis variability reduces the density at the ICP and increases the NCI volume in vdW interactions. A similar effect is observed in ethanediol, although in this case the biggest effect is by inclusion of diffuse functions. Since these two effects are opposite, they are more difficult to analyze when interactions are mixed in the same system, as in the formic acid dimer example. However, the larger NCI volumes due to an electronic delocalization in the interaction region remain. Finally, repulsive interactions like the one in bicyclooectene yield both and increase in density and volume as the basis set increased.

All in all, this highlights the need for a compensated basis set, which can have an important role in providing the variability necessary for electronic delocalization. However, this is only relevant for a quantitative description, and does not yield important qualitative differences in the NCI picture.

Baiss	H_2O dimer	CH_4 dimer	Bicyclooctene^a	Formic acid dimer	Ethanediol
6-31G	0.28	0.83	1.28	0.77	0.32
6-311G	0.25	0.90	1.50	0.82	0.36
6-311G**	0.24	0.97	1.43	†	0.32
6-311G^{++}	0.24	0.85	1.57	0.84	0.38

Table 5.6: Basis set dependency of the NCI volume (pseudo-densities of monomers are used as reference) for test molecules at the CCSD level: water dimer, methane dimer, bicyclooctene, formic acid dimer and ethanediol.^{a} All calculations at the CCSD level. Grid increments of 0.09 bohr along each axis and a threshold of 0.05 a.u. and 0.5 in the density and s, respectively, were used in the integrations.† The calculation did not converge due to nearly linear dependency.

Chapter 6

Bonding analysis by means of the NCI method I: Covalent and ionic interactions

Sommaire

In Chapter 4 we have presented an interpretation of the reduced density gradient in terms of the von Weiszäcker kinetic energy and how this term may be understood as an indicator of regions where the bosonic character is more important. Moreover this link connects the reduced density gradient with other bonding descriptors already introduced in the literature such as the local-wave vector, the electron localization function or the localized orbitals locator. Although a quick look at the shape of the reduced density gradient should be enough for differentiating between interaction types, the mapping of another scalar field over a given s isosurface may help to characterize interactions. This practice is quite common in the chemistry community. For instance, the mapping of the molecular electrostatic potential over a electron density isosurface is widely used for analyzing non-covalent interactions. In the same spirit, the NCI method maps the product of the sign of second eigenvalue of the electron density Hessian matrix and the electron density on a given reduced density gradient isosurface. In a nutshell, the reduced density gradient isosurfaces grow from the minima of such function, which identifies core, and interaction regions, then these regions are characterized by the shape of the isosurface along with the mapping of $\text{sign}(\lambda_2)\rho(\mathbf{r})$.

It is well known that interaction strength grows with the electron density values in the interaction region, so $\text{sign}(\lambda_2)\rho(\mathbf{r})$ differentiates interaction types by their relative electron density values on the reduced density gradient isosurfaces. The sign of λ_2 provides information on the flux of the electron density along the $\vec{e}_2$ eigenvector of the electron density Hessian. When passing from a bond critical point to a ring critical point ((3,-1) and (3, 1) critical points of the electron density respectively) only λ_2 changes its sign. The former are usually related to favored exchange channels, the latter appear in regions where many atoms interact and have been classically identified with steric clashes. Independently of the local potential energy contribution, regions of positive and negative λ_2 values have been characterized as attractive and repulsive, respectively.

In this chapter we will apply the NCI method to the analysis of bonding in small molecules. We have selected a small set of diatomic molecules which involve from covalent to ionic interaction passing through the more challenging charge-shift bonding. After describing the computational information, we will characterize the bonding in these systems only by the bare reduced density gradient in Section 6.2. In Section 6.3 we will complement the previous analysis by adding information of $\text{sign}(\lambda_2)\rho$, that is, by the NCI method.

6.1 Computational details

The electron density and the reduced density gradient have been computed for several chemically representative systems in their ground states: H_2, O_2, F_2, CO, FCl, FBr, HF, LiH, NaF, NaCl and KCl. The wave functions were calculated at the restricted B3LYP level with the aug-cc-pVTZ basis as implemented in the GAUSSIAN 09 package [88]. To explore the topography of the reduced density gradient along with other functions related to any of the forms of the kinetic energy density we have developed our own code CHECKIN. Whereas the later code is used for exploratory works, a modified version of NCIPLOT3 is used for performing NCI calculations Scalar field visualization was performed with ParaView version 4.3.1. [89] and VMD version 1.9.1 [90]

6.2 Chemical bonding by means of the $s(\mathbf{r})$ topography

Figure 6.1 shows the color-coded map of $s(\mathbf{r})$, where blue color corresponds to $s(\mathbf{r}) = 0$, and red color to $s(\mathbf{r}) \geq 1$. As shown in Figure 6.1a the hydrogen molecule is characterized by a bonding region that expands from one hydrogen nucleus to the other. Core and bonding regions are barely separated by $s(\mathbf{r})$ maxima in the hydrogen molecule. Figure 6.1b shows the result for the nitrogen molecule. RDG unveils the whole electronic pairing distributions: core, lone-pairs and interacting bonding regions are shown as minima of RDG. Contrary to N_2, O_2 and F_2 which are characterized by a narrowing of the bonding region along the interatomic axis and an expansion along the perpendicular direction (see Figures 6.1c and 6.1d). Along with this compression in the interatomic direction, $s(\mathbf{r})$ minima appear between the core-valence maxima and the BCP (see Figures 6.2c and 6.2d). Atomic shell structure for group II atoms is depicted by only one maximum, therefore this additional region of bosonic behavior may be attributed to the charge-shift character of O_2 and F_2 [91].

Turning to polar bonds, the symmetry of the bonding region is broken by a shift of the BCP. Additionally, the core region of the less electronegative atom occupies larger areas as may be seen in Figure 6.2. For CO (Figures 6.1e and 6.2e), the carbon core region is larger than that of the oxygen atom, and is strongly compressed along the internuclear direction. This results in an effect of the additional minima between the BCP and the oxygen core-valence maxima; the Pauli repulsion between electrons localized in that region and the bonding electron pair is strong enough to push the latter against the carbon atom.

For FCl (Figures 6.1f and 6.2f) and FBr (Figures 6.1g and 6.3a) the compression around the core regions comes from a perpendicular direction to the internuclear axis. Comparing CO, FCl and FBr, one may notice that there is a narrowing of the bonding region, which correlates with their increasing charge-shift nature. This effect is boosted in ionic interactions. Figures 6.1h and 6.3b, and 6.1i and 6.3c show the bonding pattern of HF and LiH, respectively. They are completely different to precedent plots. The hydrogen cation and the bonding region for HF are completely merged with the fluorine anion valence. For LiF the bonding region and the hydride anion are embedded in a large flat region. By contrast, the lithium cation is so strongly polarized that it is completely surrounded by a region of $s(\mathbf{r}) > 1$. The bonding pattern for NaF, reflects what is expected for an ionic interaction, two disconnected ions with a thin interacting region. As soon as the hardness of the anion decrees, its valence starts to merge with the interacting regions resulting in a picture akin to that found for LiH, as it is also found for NaCl and KCl.

6.3 Bonding analysis by means of the NCI method

In the following section we will apply the NCI method to analyse the diatomic molecules in Figures 6.4, 6.5 and 6.6. Following the prescription of Chapters 4 and 5, we use a red-green-blue color scale ranging from sign(λ_2) -0.5 a.u. to 0.5 a.u. This range allows us to compare on equal footing all the chemical interactions herein presented. The selection of the $s(\mathbf{r})$ depends on what regions one wants to visualize. Extracting core, lone-pairs and bonding regions as separated connected components requires a fine tuning of the values of $s(\mathbf{r})$, and it is very system dependent. For all these reasons we prefer to set the

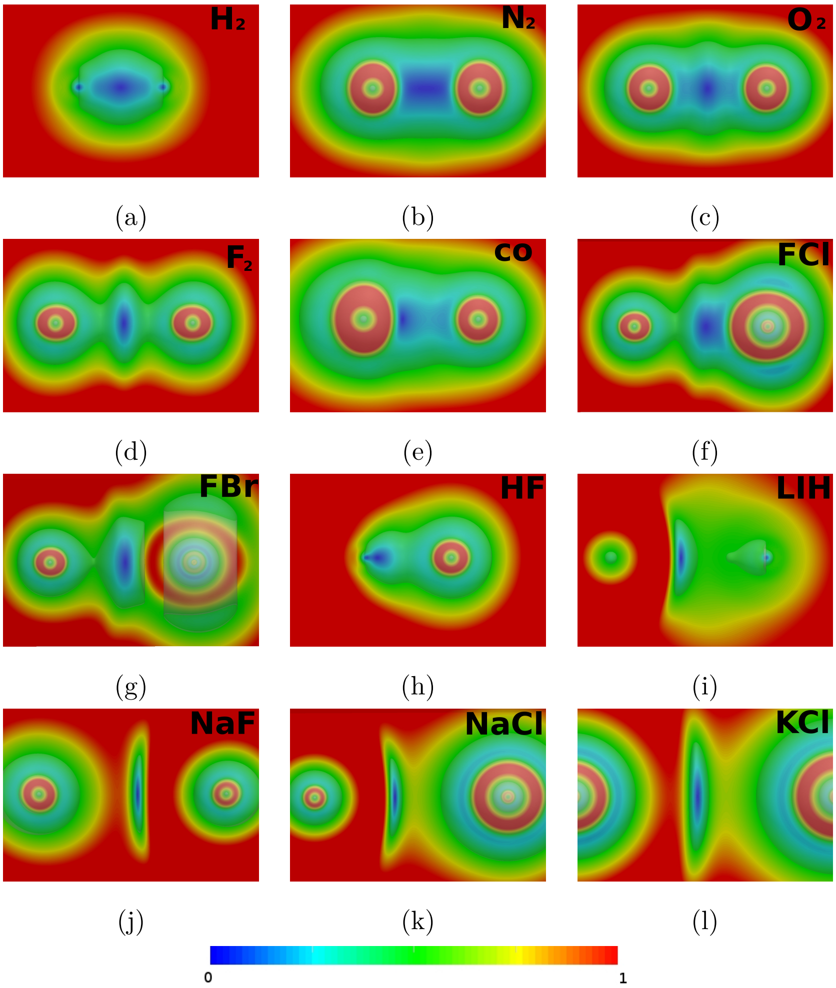

Figure 6.1: $s(\mathbf{r})$ contours for (a) H_2, (b) N_2, (c) O_2, (d) F_2, (e) CO, (f) FCl, (g) FBr, (h) HF, (i) LiH, (j) NaF, (k) NaCl and (l) KCl. Atoms in the same order as in the notation on the top-left corner.

value of $s(\mathbf{r})$ to 0.5 and only pinpoint the distribution of $\text{sign}(\lambda_2)\rho(\mathbf{r})$ on these $s(\mathbf{r})$=0.5 isosurfaces.

Let us start with the homoatomic systems: H_2, N_2, O_2 and F_2. $s(\mathbf{r})$ *versus* $\text{sign}(\lambda_2)\rho(\mathbf{r})$ diagrams (see Figure 6.4) display three peaks, two in the negative part corresponding to the nuclear positions and the BCP, and another one in the positive (repulsive) part. The nuclear peaks are often out of our $\text{sign}(\lambda_2)\rho(\mathbf{r})$ range, it can only be seen for H_2 (Figure 6.4a)is shown since it appears at almost the same density as the BCP. When displayed over the $s(\mathbf{r})$ isosurfaces, the negative regions cover almost all the isosurface, except for a region around the BCP where the electron density tends to “swell away” from the BCP along the λ_2 direction. This pairing between peaks in the negative and positive parts of the diagram is found in all the systems here analyzed. Another noticeable effect is that the stronger the density at BCP peak (more negative $\text{sign}(\lambda_2)\rho(\mathbf{r})$), the stronger the repulsive peak (more positive $\text{sign}(\lambda_2)\rho(\mathbf{r})$). As shown in Figures 6.6c

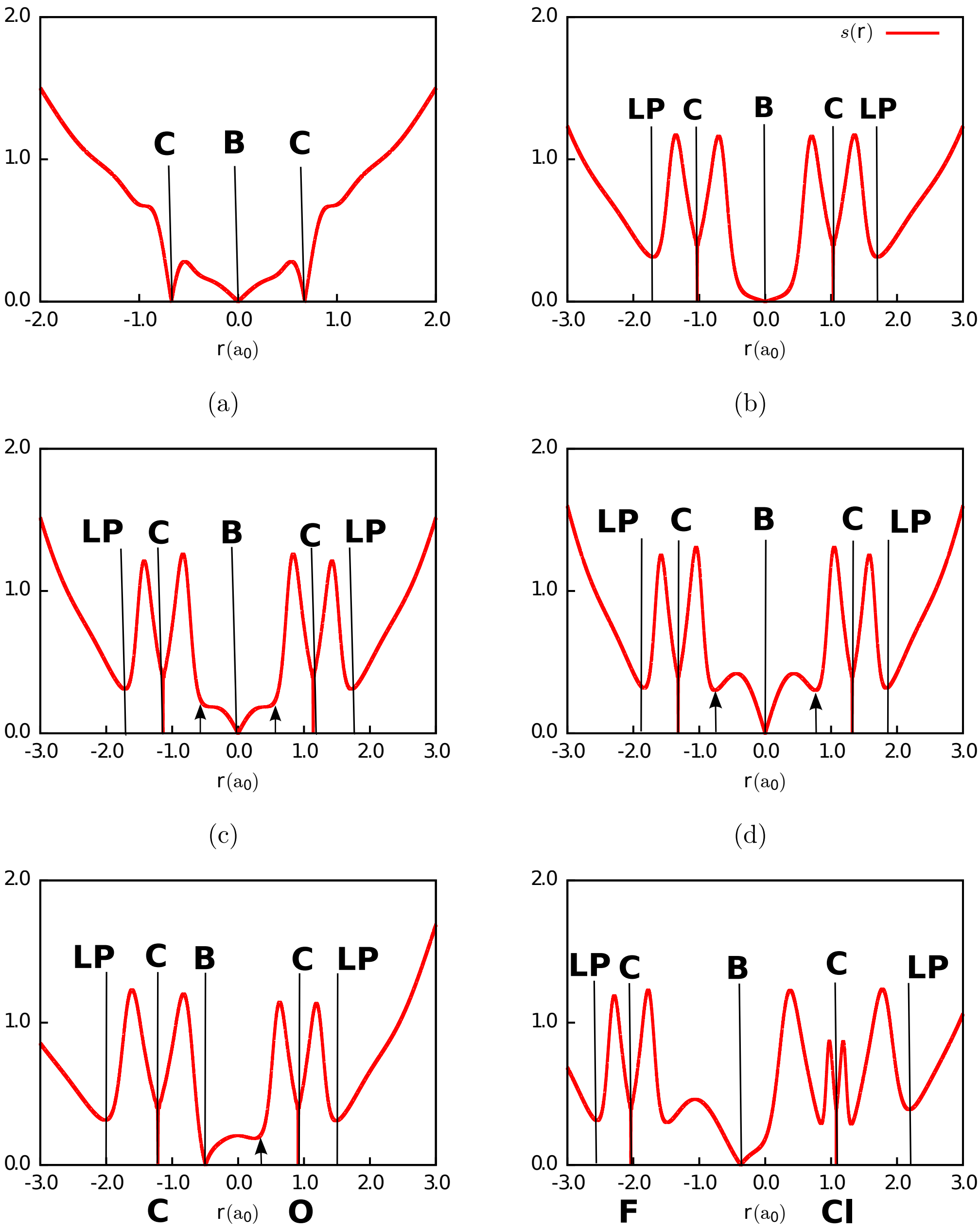

(a) (b) (c) (d) (e) (f)

Figure 6.2: $s(\mathbf{r})$ along intermolecular axis for a) H_2, b) N_2, c) O_2, d) F_2, e) CO, f) FCl. Labels C, B and LP stand for core, bonding and lone-pair minima respectively. Arrows in O_2, F_2 and CO plots indicate additional minima in the bonding region.

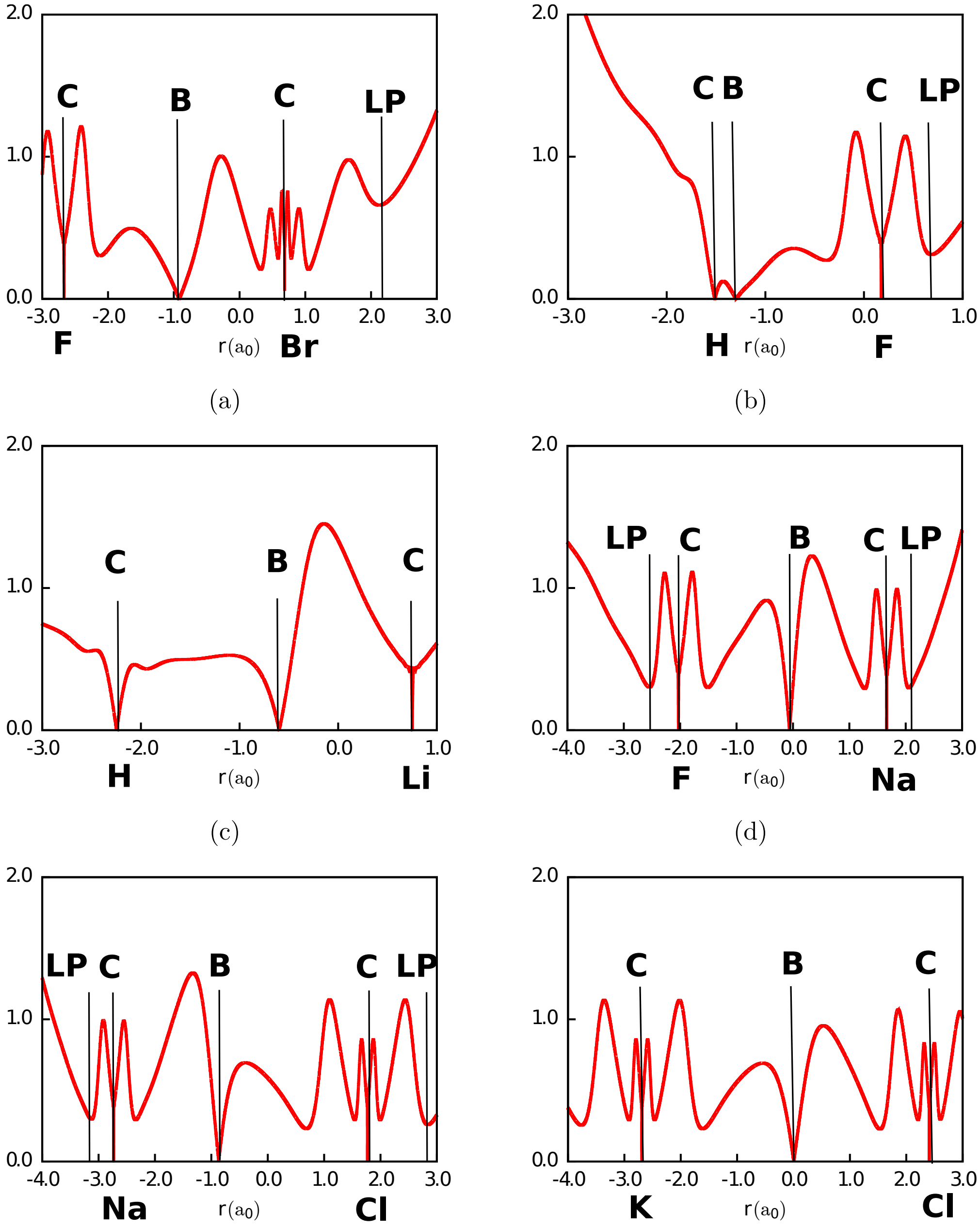

(a) (b)

(c) (d)

(e) (f)

Figure 6.3: $s(\mathbf{r})$ along intermolecular axis for a) FBr, b) HF, c) LiH, d) NaF, e) NaCl, f) KCl. Labels C, B and LP stand for core, bonding and lone-pair minima respectively.

and 6.6d the narrowing of the interaction regions for O_2 and F_2 is easily visualized as an expansion of the isosurface perpendicular to the internuclear axis.

A split of both positive and negative branches of the $s(\mathbf{r})$ *versus* $\text{sign}(\lambda_2)\rho(\mathbf{r})$ diagrams is found when moving towards heteronuclear systems. In regions where $\rho(\mathbf{r})$ is dominated by one of the atoms, such as regions close to nuclear positions, $\rho(\mathbf{r})$ may be approximated by a sum of atomic contributions, that is, by a promolecular density. As explained in Chapter 4, atomic densities can be modeled by exponential basis functions

$$\rho_{at}^{prom}(\mathbf{r}) = \sum_n c_n e^{-\zeta_n \mathbf{r}}, \tag{6.1}$$

where n, c_n and ζ_n stand for the number of shells, the expansion coefficient and exponent corresponding to the shell n, respectively. In the interaction regions, this is reduced to the outermost shell, so the density for a A B pair at mutual distance $\mathbf{R}$ is given by

$$\rho(\mathbf{r}) = \rho_A^{prom}(\mathbf{r}) + \rho_B^{prom}(\rho) = ae^{-\alpha\mathbf{r}} + be^{-\beta(\mathbf{R}-\mathbf{r})}, \tag{6.2}$$

where a, α, b and β are positive constants characteristic of A and B ions, respectively. As $\mathbf{r} \to A$, we can assume that $\rho(\mathbf{r})$ approximates to $\rho_A(\mathbf{r}) = e^{-\alpha\mathbf{r}}$, and analogously for $\mathbf{r} \to B$. In these cases, the reduced density gradient reduces to the free-ion behavior:

$$s_A(\mathbf{r}) = \frac{1}{2(3\pi^2)^{1/3}} \frac{|\vec{\nabla}\rho_A(\mathbf{r})|}{\rho_A(\mathbf{r})^{4/3}}, \tag{6.3}$$

Thus, these regions give rise to two curves in the $s(\mathbf{r})$ *versus* $\rho(\mathbf{r})$ diagram. Although promolecular densities describe fairly well ionic interactions, these models also account for the splitting in polar bonds, being more important as the polarity of the bond increases. Within the promolecular approximation, the polarity of the bond is taken into account by the exponents α and β, which for ionic systems are associated with the hardness of the ions. The relative position of the curves can be associated with the relative hardness of the ions, or with the relative electronegativity in general. This is exactly what is observed in the heteronuclear systems here analyzed (Figures 6.4e-6.5e). The upper curves correspond to the carbon, chloride and bromine atoms in CO, FCl and FBr, respectively (Figures 6.4f, 6.5a), and to the cationic species in all the other systems. The hardness difference between the fluorine anion and a proton is not enough to observe this effect in HF, as disclosed in Figure 6.5b. It is worth noticing that all systems with chlorine, FCl, NaCl and KCl exhibit atomic shell structure as an additional peak with $s(\mathbf{r})$ value higher than 0 (Figures 6.5e- 6.5f). This peak is ascribed to the outermost shell of the Cl atom, the L shell. The M shell of potassium in KCl is also displayed. For all the other systems the valence shell occurs at higher densities than 1.0 a.u and thus, out of the selected $\text{sign}(\lambda_2)\rho(\mathbf{r})$ range.

In Figure 6.6 it is observed that the red branches enclosing the interacting regions are shifted towards C, Cl and Br in CO, FCl and FBr, respectively. Along with this effect, it is observed that the larger the core region, the bumpier the isosurface around it, and the more compressed around the bonding regions. This effect is already noticeable for CO, and much more accused for FCl. Eventually, for FBr the isosurface is broken in three components, two around core regions and one around the BCP. This change in the number of connected components of the isosurface is a consequence of the apparition of CPs of $s(\mathbf{r})$ as stated by the Morse theory. In all the other systems the increase in the number of connected components occurs at values of $s(\mathbf{r})$ lower than 0.5, therefore a fine tuning of the isosurface value is necessary for extracting core and bonding regions separately, as it has been already commented.

Figures 6.6i-6.6l show $s(\mathbf{r})$ isosurfaces for LiH, NaF, NaCl and KCl respectively. A similarly split into three components to that found in FBr is observed. HF is an exception in this regard, the low density at the hydrogen core, prevents the appearance of CPs between core and bonding regions with value 0.5.

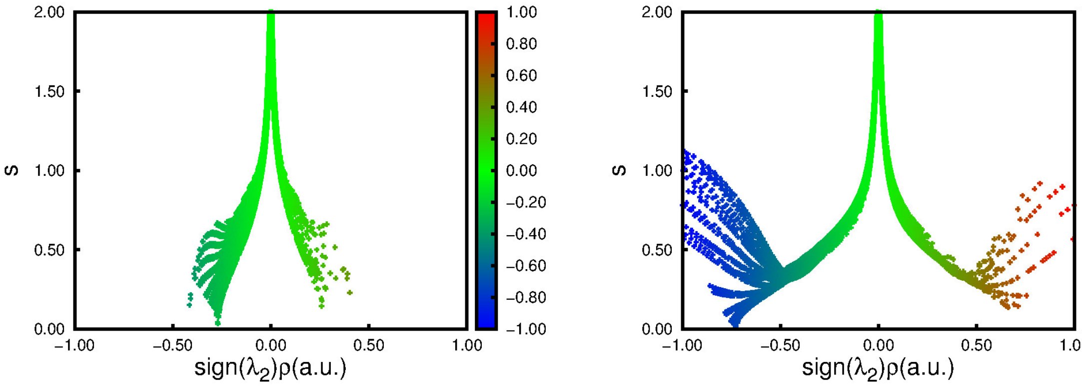

(a) H_2 (b) N_2

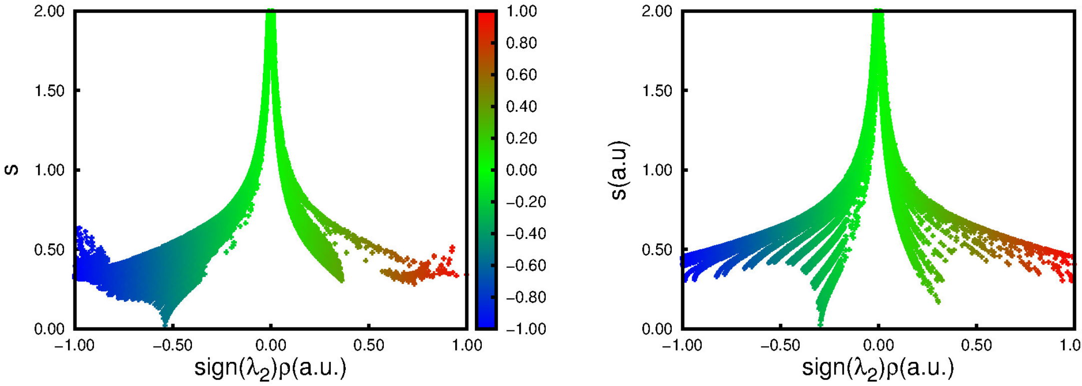

(c) O_2 (d)F_2

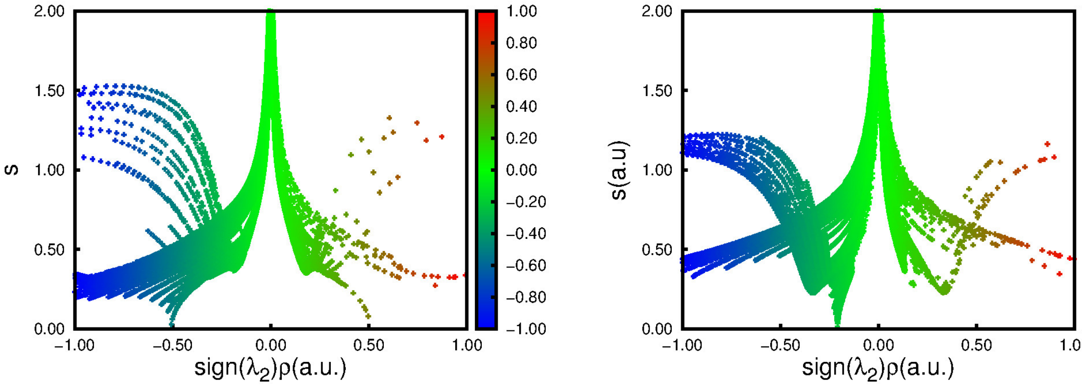

(e)CO (f) FCl

Figure 6.4: $s(\mathbf{r})$ along intermolecular axis for a) H_2, b) N_2, c)O_2, d)F_2, e) CO.

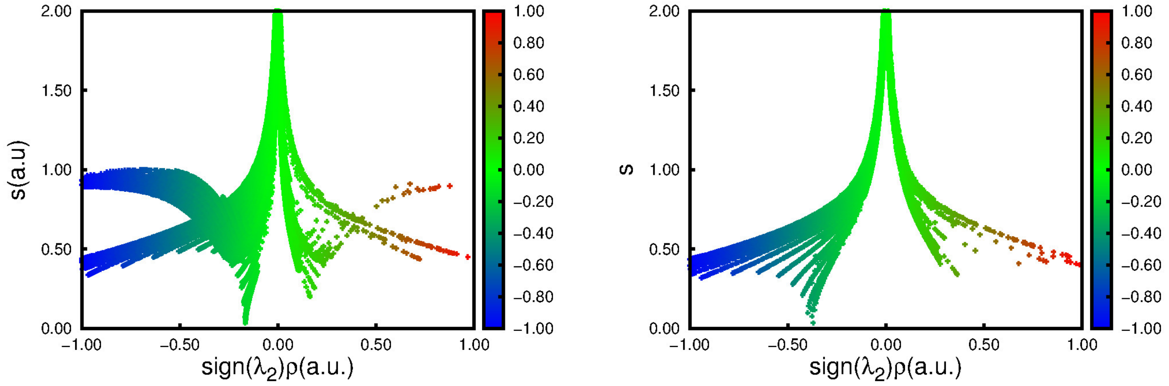

(a) FBr

(b) HF

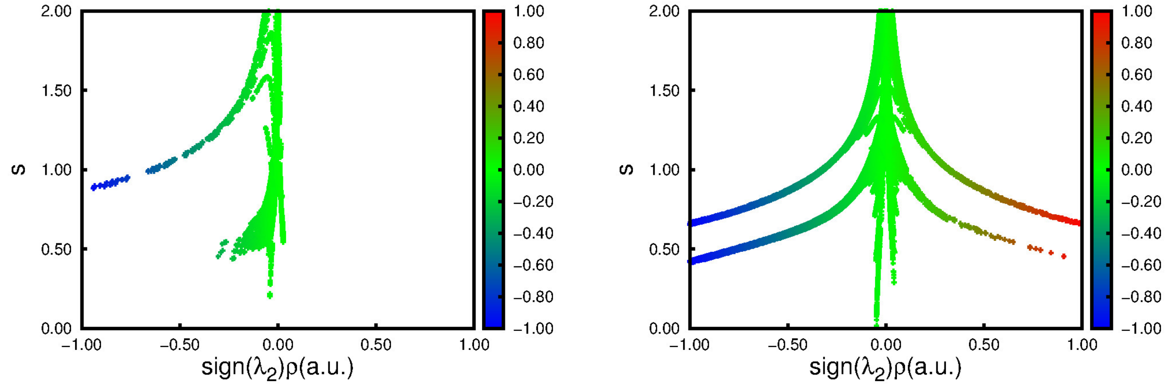

(d) LiH

(c) NaF

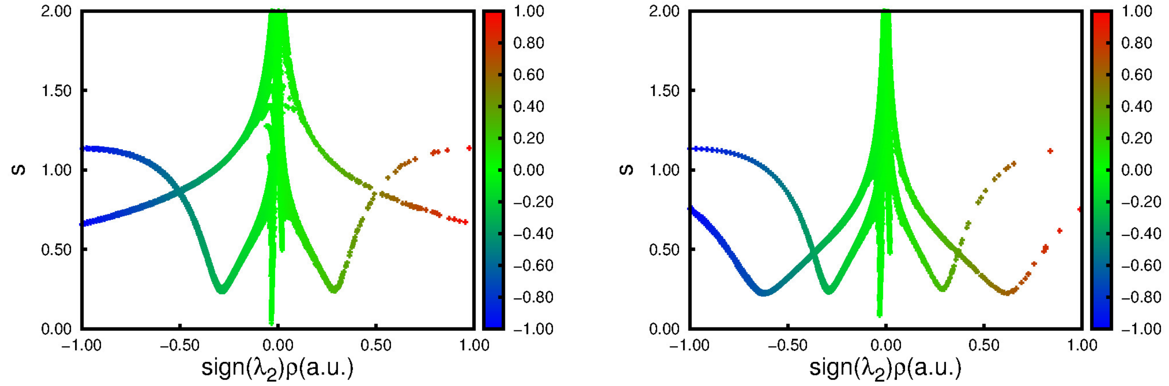

(e) NaCl

(f) KCl

Figure 6.5: $s(\mathbf{r})$ along intermolecular axis for a) FBr, b) HF, c) LiH, d) NaF, e) NaCl, f) KCl.

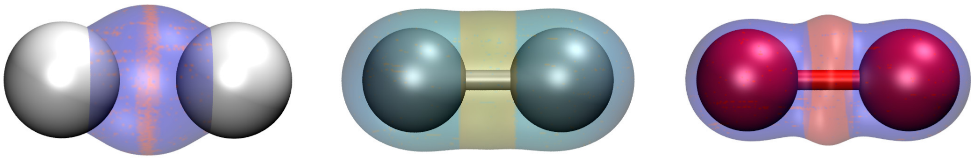

(a) H_2 (b) N_2 (c) O_2

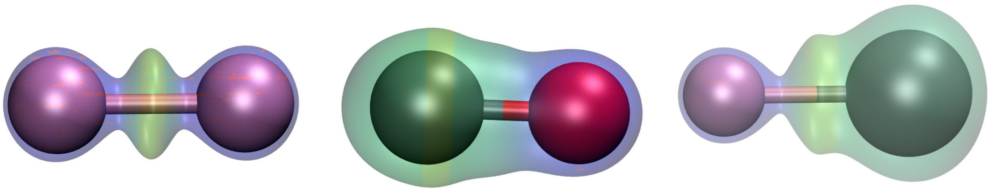

(d) F_2 (e) CO (f) FCl

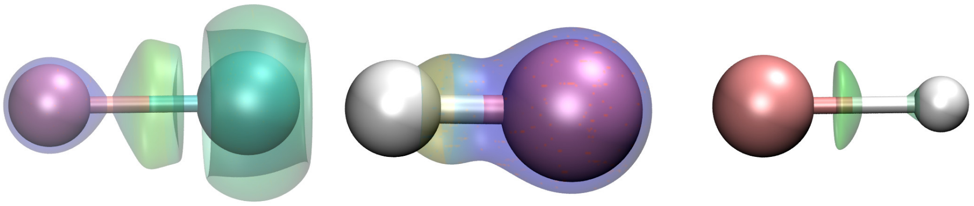

(g) FBr (h) HF (i) LiH

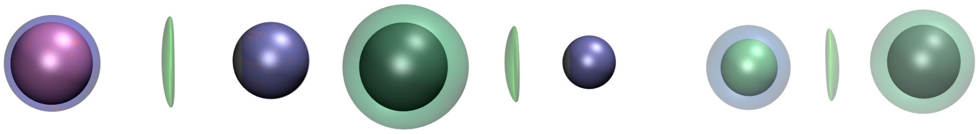

(j) NaF (k) NaCl (l) KCl

Figure 6.6: $s(\mathbf{r}) = 0.5$ contours colored on a blue-green-red according to the sign$(\lambda_2)\rho$ value over the range -0.03 to 0.03 a.u.for a) H_2, b) N_2, c) O_2, d) F_2, e) CO, g) FCl, h) FBr, i)HF, j) LiH, k) NaF, l) NaCl and k) KCl.

Chapter 7

Bonding analysis by means of the NCI method II: Non-covalent interactions

Sommaire

At this stage, we hope the reader becomes acquainted with the main subject of this manuscript, the NCI method. As it was aforementioned, it was envisaged as a tool for a fast qualitative analysis of non-covalent interactions. The subsequent work on this topic revealed that behind beautiful pictures there is some chemical content; regions of relatively high bosonic character. After having applied the NCI method for analyzing covalent and ionic bondings, we will revisited its prime playground, NCIs.

Among NCIs, hydrogen bonding (HB) has always received special attention, since it appears in almost all biological, solvation and crystallization processes. Its existence was first postulated in the early 20^{th} century based on the stunning macroscopic differences between the first and second row hydrides, i.e. water is a high temperature boiling liquid without which there would be no life, while hydrogen sulphide is a stinking gas under ambient conditions [92].

With the advent of molecular beam and cryogenic experimental methods as well as the ever advancing theoretical methods, HBs have been proved to exist in H_2S as well [93]. Its elusive nature motivated the International Union of Pure and Applied Chemists (IUPAC) to revisit its definition. The result of such task was a set of guidelines to characterize hydrogen bonds not only from practical perspectives, but also from theoretical considerations, enlarging considerably its original definition. In a nutshell, we may define a hydrogen bond X-H $\cdots$ Y-Z as an attractive interaction between a positive charged hydrogen and two electronegative species X and Y. X is termed proton donor and Y proton acceptor. Traditionally, the role of Y has been undoubtedly assigned to O or N, however less electronegative atoms, such as C, or even negatively charged regions, such as σ or π bonds, are now also accepted as proton acceptors.

But things go even further. About a century later, chemists have identified a wealth of new bonding types along the periodic table. Halogen bonds (XBs) (group 17) are frequently exploited for crystal engineering [94]. Recently, similar bonding mechanisms have been proposed for adjacent main-group elements, such as non-covalent "chalcogen bonds" (group 16) [95] and "pnictogen bonds" (group 15) [96, 97] have also been identified in crystal structures. Even carbon bonding (group 14) [98] has been proposed as a stabilizing interaction.

But not only the concept of HB has been enlarged, also new interactions have appeared in the chemist vocabulary. Some of these interactions even break down the assumption that HB entails "special characteristics". Hydrogen bonding was usually characterized by been highly directional, in the sense that X, H and Z form an angle of almost 180°. This preference for a linear orientation is usually considered a consequence of its electrostatic nature, and it was taken as a unique feature among other NCIs which are much more isotropic.

On the one hand, the new definition of HBs lets in much less anisotropic interactions fall into the definition (e.g. very weak HBs) [99]. On the other hand, the venue of halogen bonding broadened the spectrum of directional NCIs. In a halogen bond, the halogen atom plays the role of H in a hydrogen atom X-Hal $\cdots$Y-Z where Hal termed an electropositive halogen atom and X, Y, and Z fulfil the same roles as they do in a hydrogen bond. The counterintuitive origin of halogen bonding was explained in terms of the concept of σ-hole i.e. a region of positive electrostatic potential along the X-Hal bond [95]. Similar to hydrogen bonding, these interactions are driven by electrostatic forces, though some authors state that dispersion and induction are the crucial energetic contributions [96].

Although with some exceptions, specially pnictogen bonding, the unexpected directionality of the great majority of the aforementioned NCIs has found a common origin; the σ-hole concept. As shown by Murray *et al.* [100], directional interactions are not limited to linear arrangements of atoms but they are also found in perpendicular ones. In analogy with the σ-hole, they introduced the concept of π-hole: a region of low electronic density that is perpendicular to a portion of a molecular framework. Regardless their geometry, all these interactions can be regarded as electrostatic in nature.

In other words, the panorama of weak interactions is lately suffering a continuous update, and it is difficult to tell where it will stop. Although it might look just an epistemological question, it is far from being just so. Molecular force fields are parametrized for pair-wise atomic contacts. These interatomic potentials have to be tuned so as to recognize these interactions and reproduce the corresponding potential energy surface reliably. If one depends on the "naming" of an interaction, force fields are as prone to error and interaction oblivions as our interaction dictionary. One such example in the recent literature is the cation-π interaction. Jorgensen found that OPLS parameters that are quite successful in modeling benzene-water and water-TMA (tetramethylammonium), could not properly model benzene-TMA [101]. This defect was due to their inability to describe cation-π interactions. As a consequence, the description of potentials was re-adapted in AMBER, which is now able to account for this type of interactions.

In words of Desiraju, *"a term is acceptable if the largest number of chemists are in a maximum degree of agreement about what it means"* [93]. Thus in the absence of general consensus, the chemical community has the verdict. In other words, the unabated research on NCI is expected to enlarge the realm of known chemical interactions This is showing to be a never ending quest. Or at least very prolific. But an alternative can be proposed.

Traditionally, chemical interactions have been classified in terms of their nature no matter which atoms are involved in them. Whereas covalent interactions occur through electron sharing, ionic interactions are electrostatic in nature. Differences are not so well defined in the case of non-covalent interactions. The relative weights of the different terms in the multipolar expansion can be used to identify different interaction types. Another approach is to look at the electron density. Before and beyond the identification and characterization of an interaction, the signature on the electron density will be present. It can provide a distinct approach, where interactions are categorized by their characteristics and not by their atomic composition, which can become limiting and cumbersome.

In this chapter we will first perform a quantitative NCI analysis of some model systems classified by interaction types: pnictogen, weak-hydrogen and halogen bonding. In section II, we will apply the NCI method to shed some light on the source of some complex systems as the self-assembled monolayers and metallocenes systems. We will conclude by addressing a philosophical question: **if so similar in nature, do all these interactions deserve distinctive names?** Beyond philosophy, this question has great implications in theoretical chemistry, in the construction of models and in the development of methods.

7.1 Model systems

7.1.1 Computational details

All the geometries were optimized at MP2 level using aug-cc-pVDZ basis set as implemented in the GAUSSIAN 09 package [88]. Structures were verified as minima having all real vibrational frequencies. Interaction energies were computed as the difference between the dimer and the sum of the monomers when they have the same structure as in the complex. These quantities were corrected for basis set superposition error by the counterpoise procedure [102]. The optimized geometries were used to compute the electron density at B3LYP/aug-cc-pVTZ level of theory combined with the Grimme D3 dispersion correction and with the Becke-Johnson damping function [103]. Dispersion energies were calculated at the same level with the DFTD3 code version 3.1 Rev 1 [104, 105]. NCI isosurfaces were obtained with a modified version of the NCIPLOT code [75] with grids of 0.1 Å along each axis. In order to improve the visualization of FH$\cdots$ HLi the grid step was reduced to 0.05 Å. To assure the convergence of NCI volumes (V_{NCI}) a 0.05 Å grid along each axis was used. The NCI isosurfaces were visualised with VMD version 1.9.2 [90].

7.1.2 Pnictogen bonds

The simplest example of pnictogen bonding is the complex between NH_3 and PH_3, where the N atom is the donor of electron density [96]: the two molecules are oriented such that the P and the N atom face one another directly, without the intermediacy of a H atom. Natural bonding orbital analysis has revealed that this attraction is due in part to the charge transfer of electron density from the N lone pair to the P-H σ^* antibonding orbital [96]. Unlike the hydrogen bonds, the pertinent hydrogen is oriented about 180° away from the N (instead of toward), and the N lone pair overlaps with the lobe of the P-H σ^* orbitals that is closest to the P atom. Surprisingly, the binding energy of the pnictogen bonded complex is larger than the hydrogen bonded complex formed between the same two molecules where the N atom is the proton acceptor (see Table 7.1).

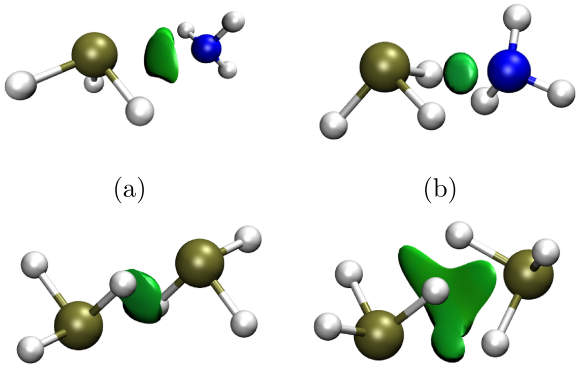

(a) (b)

(c) (d)

Figure 7.1: NCI isosurfaces of the PH_3-NH_3(top) and PH_3-PH_3 (bottom) complexes. (a) , (c) pnictogen bonded, (b) PH_3-NH_3 hydrgogen bonded configuration and (d) PH_3-NH_3 secondary minima. 3D isosurfaces were produced using cut-off values of $s(\mathbf{r}) = 0.5$ colored over the range -0.05(blue) $<$ sign$(\lambda_2)\rho$ $<$ 0.05(red).

The NCI analysis of the NH_3-PH_3 complexes shows the presence of a NCI and this is illustrated by the 3D isosurfaces of both complexes as shown in Fig. 7.1. The green color of both interactions indicate that the two types of bonding have similar bonding strengths corresponding to that of the van der Waals interactions. Whereas for the H-mediated complex, a typical picture of the hydrogen bond is obtained, a thick surface is

System	V_{NCI}	E_{int}	E_{disp}
$H_3P\cdots NH_3$	32.33	-1.60	-3.70
$PH_3\cdots NH_3$	12.72	-0.81	-2.97
$H_3P\cdots PH_3$	52.86	-1.10	-4.83
$PH_3\cdots PH_3$	49.80	-0.70	-4.83

Table 7.1: NCI volumes(V_{NCI}, a.u.), interaction (E_{int}, kcal/mol) and dispersion energies (E_{disp}, kcal/mol) of $PH_3\cdots PH_3$, the pnicogen ($PH_3\cdots NH_3$ and $H_3P\cdots PH_3$) and hydrogen ($H_3P\cdots NH_3$)bonded complexes.) complexes.

obtained in the case of pnictogen bonding, which is extended like in the case of the van der Waals, but thick like the hydrogen bonded ones. Scheiner has shown that there is a gain of electron density in the N lone pair of both PH_3/NH_3 configurations. Additionally energetics show that all interactions herein analyzed are in the typical range of dispersion interactions [96].

It is interesting to note that in contrast to halogen bonds, there is no requirement for a σ-hole nearby the P atom, nor it is necessary for the two interacting atoms to be of differing potential. In fact, the two atoms can be identical, as the global minimum of the PH_3 homodimer has the same structure, characterized by a $P\cdots P$ attraction. Indeed, for the complex between PH_3 and PH_3 the P atoms posses a partial positive charge and none of the located minima found on the potential energy surface corresponds to a hydrogen-bonded complex [96]. The two minima that were located correspond to complexes where the P atoms approach one another. The complex with the symmetric geometry was found to be dominated by electrostatic interactions, corresponding to pnictogen bonding, whereas the second structure was found to be dominated by dispersion. This shows in the NCI isosurfaces where the interaction region in Figure 7.1d) occupies a larger volume than that of Figure 7.1c). This is in agreement with the more diffuse character of the dispersion interaction compared to the pnictogen bond which is more concentrated along the bonding direction. As showed in Table 7.1, V_{NCI} correlates with this effect.

Although the PH_3/NH_3 and PH_3/PH_3 complexes do not show σ-hole, it is worth noting that generally as soon as any of the hydrogen atoms is replaced by some electron-withdrawing group, such as CN or F, a σ-hole is formed along the R-X bond strengthening the X–Y interaction. A similar effect is observed when N or P are substituted with a more polarizable atom as At [95].

7.1.3 Weak-hydrogen bonds

We have also studied a series of six complexes presenting “weak hydrogen bonds”: $HCCH\cdots OH_2$, $HOH\cdots\pi$, $HCCH\cdots\pi$, $HCCH\cdots HLi$, $FH\cdots\pi$, $FH\cdots HLi$. We have divided them in two groups $HOH\cdots\pi$, $HCCH\cdots\pi$ and $FH\cdots\pi$ represent T-shaped complexes where the π electrons of the acetylene are the proton acceptor. $HCCH\cdots HLi$, $FH\cdots HLi$ and $HCCH\cdots OH_2$ are linear complexes where the proton acceptor and donor are hydrogens $X\text{-}H^{-\delta}\cdots{}^{+\delta}H\text{-}Y$. Figure 7.2 and Table 7.2 display NCI surfaces and V_{NCI} respectively for all the hydrogen bonded systems herein analyzed. Energetic and NCI results were obtained with the same methods and parameters used to obtain those of the pnictogen bonded data. The results show that NCI allows to follow the evolution of the interaction strength for different systems. The NCI isosurfaces range from those similar to dispersive interactions (HOH$\cdots\pi$, HCCH$\cdots\pi$, FH$\cdots\pi$) characterized for having more diffuse character and therefore bigger volumes than those much more localized typical of strong hydrogen bonds. As the electrostatic contribution to energetics increases V_{NCI} decreases and the NCI isosurfaces become more localized around the bond critical point.

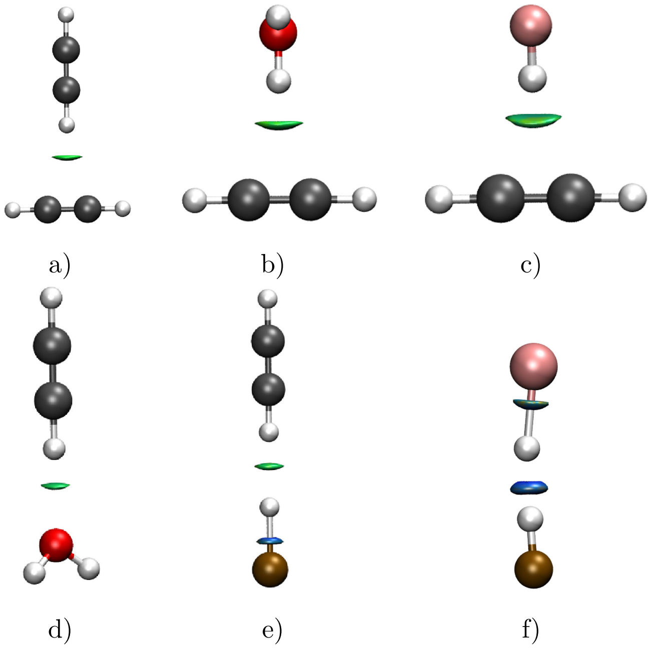

Figure 7.2: NCI isosurfaces for (*a*) HCCH$\cdots\pi$, (*b*) HOH$\cdots\pi$, (*c*) FH$\cdots\pi$, (*d*) (HCCH)$\cdots$OH$_2$, (*e*) HCCH$\cdots$HLi and (*f*) FH$\cdots$HLi. 3D isosurfaces were produced using cut-off values of $s(\mathbf{r}) = 0.5$ and coloured over the range -0.05(blue) $<$ sign$(\lambda_2)\rho <$ 0.05(red).

7.1.4 Halogen bonds

Halogen bonds (XBs) occur between a halogen atom, playing the role of Lewis acid, and a Lewis base. This non-covalent interaction is analogous to hydrogen bonding (HB) in the sense that in both cases an atom or group of atoms with high electron density donates an electron to an acceptor which is electron poor. We have studied a series of complexes of the type CF$_3$X$\cdots$B, with X=Cl, Br and B=dimethylether (DME), trimethylamine (TMA) and dimethylthiol (DMS).

Table 7.3 contains V_{NCI}, E_{int} and E_{disp} for the selected halogen bonded systems. Although the interaction energies are of the same order as in the pnictogen and weak hydrogen bonded system, the dispersion is much stronger. Nevertheless, these complexes have been characterized for having a σ hole and have been said to be dominated by electrostatics [106]. The disc-shaped NCI isosurface supports the electrostatic origin of halogen interactions. The mismatches between V_{NCI} and E_{int} may be ascribed to the fact that electrostatic and not dispersion is the driving force in halogen bonding.

System	V_{NCI}	E_{int}	E_{disp}
$(HCCH)\cdots OH_2$	21.34	-2.62	-2.37
$HOH\cdots\pi$	38.05	-2.16	-2.80
$HCCH\cdots\pi$	38.65	-1.19	-3.88
$HCCH\cdots HLi$	3.28	-3.99	-2.22
$FH\cdots\pi$	27.61	-0.17	-2.48
$FH\cdots HLi$	0.71	-10.74	-0.87

Table 7.2: NCI volumes ($V_{NCI}, (a.u.)$), interaction (E_{int}, kcal/mol) and relative dispersion energies (E_{disp}, kcal/mol) of the hydrogen bonded systems investigated here. complexes.

System	V_{NCI}	E_{int}	E_{disp}
$CF_3Br\cdots DME$	10.73	-3.73	-9.97
$CF_3Br\cdots TMA$	30.7	-5.81	-15.60
$CF_3Cl\cdots DME$	9.63	-2.69	-9.23
$CF_3Cl\cdots DMS$	8.50	-10.83	-11.74
$CF_3Cl\cdots DMS^a$	2.27		

Table 7.3: NCI volumes ($V_{NCI}, (a.u.)$), interaction energies (E_{int}, kcal/mol) and relative dispersion energies (E_{disp}, kcal/mol) of the halogen bonded systems investigated here. *a* V_{NCI} correspoding to the $Cl\cdots S$ interaction.

7.2 Complex systems

After analyzing model systems, we have decided to check the ability and utility of the NCI method in bigger systems.

7.2.1 Binding in self-assembled monolayers

Another challenging binding mode is that existing between long alkyl chains molecules in self-assembly monolayers (SAM). The stability of such systems is mainly due to a competition between metal-molecule and molecule-molecule interactions. Understanding the nature and the strength of the interaction between surfaces and long chain molecules is thus of great importance and may help in the design of systems with specific molecule-surface and molecule-molecule strengths. The intermolecular interactions in SAMs come from the vicinity of the neighboring molecules that form an ordered two-dimensional layer and are mainly caused by dispersion forces. This molecular arrangement exhibits

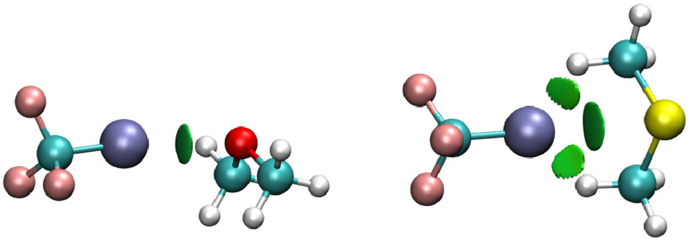

a) CF_3Cl-DME b) CF_3Cl-DMS

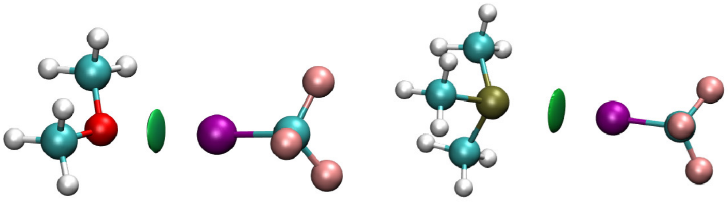

c) CF_3Br-DME d) CF_3Br-TMP

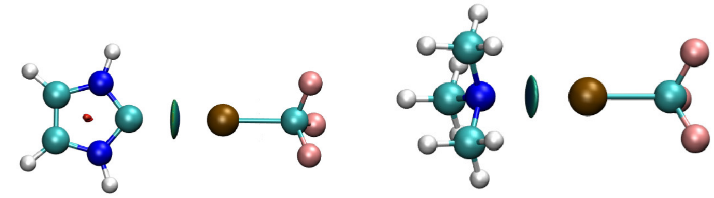

e) CF_3I-NHC f) CF_3I-TMA

Figure 7.3: 3D plots for halogen bonded complexes: a) CF_3Cl-DME b) CF_3Cl-DMS c) CF_3Br-DME d) CF_3Br-TMP e) CF_3I-NHC f) CF_3I-TMA. NCI isosurfaces correspond to s=0.5 and a color scale of $-0.04 < \mathrm{sign}(\lambda_2)\rho < +0.04$ a.u.

an extra stabilization when compared with the corresponding isolated molecular dimer, known as *packing*. The role of the dispersion forces between the alkyl chains is poorly understood although it may become crucial in the stabilization of SAMs.

As example of SAM system the platinium (100)-octylamine system ($NH_2C_8H_{17}$) has been chose because it has been recently reported to lead to stable cubic platinum nanoparticles [107, 108]. The calculations were carried out with the revised PBE functional (rPBE) [15, 109] as implemented in the VASP code [110, 111]. Projector Augmented Wave (PAW) pseudopotentials [112, 113] combined with plane wave (cut-off=400 eV) represent the electron distribution. Periodic boundary conditions apply and a vacuum of at least 15 Å is included to avoid interaction between successive layers. Starting from the gas-phase optimized geometry at the rPBE level, calculations are done without geometrical optimization for the gas-phase studies and with the conjugate-gradient algorithm for the surface-molecule interaction studies, with the geometrical constrains specified in each case. The interactions energies were calculated by the formula:

$$\mathbf{A} + \mathbf{B} = [\mathbf{AB}] \quad \text{where} \quad E_{int} = E_{[AB]} - E_A - E_B, \tag{7.1}$$

whereby $E_{int} < 0$ for exothermic reactions and E_A stand for the energy of the octylamine in the complex geometry. Dispersion interaction were included by using the Grimme D2 approach as implemented in the VASP code (parameters for Pt: radius=1.676Å and C_6=19.46 Jnm^{6}mol^{-1} obtained from [104]). As notice in the literature [114], the problem of metal screening of dispersive forces can be roughly corrected by including dispersion only on the uppermost slab layer. We have considered this possibility together with the pure rPBE and full D2, denoted as 1L, rPBE and D2, respectively. Tests on the propylamine dimer potential energy curve have been carried out at MP2/6-311g(3df,2pd), BSSE corrected, together with the rPBE and rPBE+D2 levels, and show very good agreement with the rPBE+D2 results. Contrary to the previous systems, the NCI analysis has been carried out with the critic2 code [115] where NCI is implemented for solids.

An in-depth analysis of the factors that determine the stability of octyalmine/Pt was carried out by Calatayud *et al* [116]. They concluded that a proper description of packing in SAM systems requires accounting for dispersion effects, since only the rPBE+D2 functional is able to explain the additional stability of octyalmine SAM when compared to the octylamine dimer (see Figure 7.4). The interaction between alkyl chains depends on their relative orientation. Figure 7.5 displays the relative orientation of two neighboring octylamines in the x and y directions. It can be observed that they are not equivalent since they involve different H-H interactions. Along the y directions, octylamine molecules are oriented in such a way that the hydrogen atoms in the chains face those of the neighboring molecule. Instead, there is no such orientation when molecules are arranged along the x direction and hydrogens are not face to face. In order to gain more information on the role of the relative orientation of the two chains, we have considered polymers of octylamine in the x and y directions separately. For the octyalmine dimer in the gas phase the most favorable situation is found when the molecules are rotated 80 degrees in the z-axis. This orientation is similar to the one obtained for the y-polymer that would correspond to 90 degrees.

Figure 7.4 shows the energetic profile of 1D polymers alongs x and y directions as a function of the distance between neighboring molecules d_{NN}. It can be observed that the stabilization in the alignment along the y direction is higher than in the x direction with and without dispersion correction. Comparing now the 2D pattern to the addition of x and y polymers (Figure 7.4) the result is a net stabilization of the 2D square pattern with respect to the addition of x plus y, almost inexistent for rPBE but significant when using the D2 approach. Although the method used overstabilizes the interactions in the y direction, the overall stabilization of the 2D pattern compared to the sum of the polymers is significant. This result highlights the key role of second neighbors in the stabilization of the squared superstructure.

The differences along x and y are also evident from the NCI isosurfaces as shown in Figure 7.5. The symmetric arrangement along the y direction gives rise to localized H-H interactions between alkyl molecules. Similarly to that found for all directional interactions previously analyzed, the directionality of H-H interactions is characterised within the NCI approach by the small, round shape of the regions and the strength by the relatively large accumulation of electron density. Weak interaction such as the ones found in the x polymer give rise to interacting regions, rather than localized NCI domains, and present a relatively low electron density. In both cases, the color of the NCI isosurfaces reveals the weak non-bonding nature of all the interactions, which agrees with the need to resort to D2 corrections to account for them. The shapes of the NCI isosurfaces point that the dispersion and electrostatic contribution to E_{int} are at least as important as in the pnictogen, halogen and weak-hydrogen bonded systems analyzed so far.

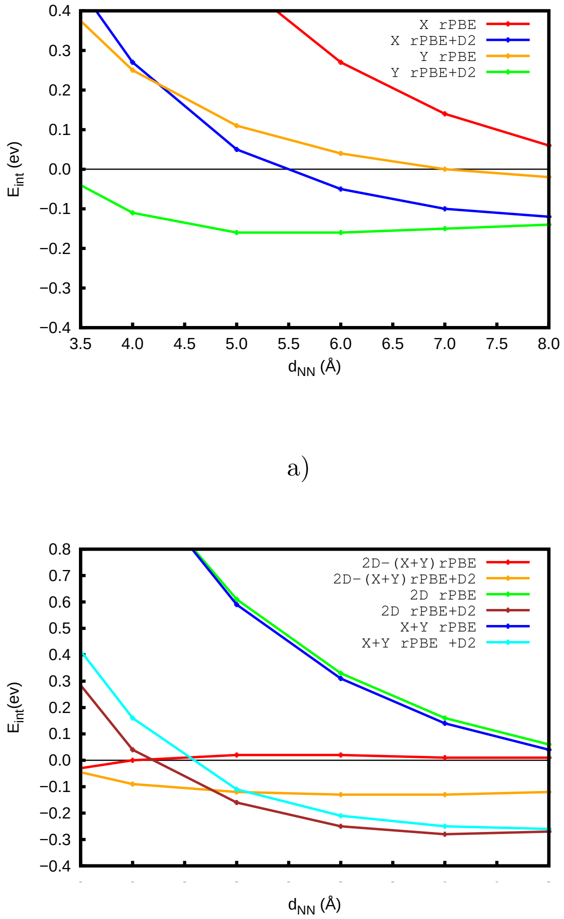

a)

b)

Figure 7.4: (a) Energy profile for the molecule-molecule interaction along the x and y directions and (b) energy diference between the 2D polymer and the x and y separately as a function of the d_{NN}.

Moreover, the stabilizing effect of H-H interactions along x and y directions raises a fundamental problem in crystal packing, which is still an open question. These interactions are usually assumed to give rise to steric clashes, and contribute to the destabilisation of the crystal. However, topological approaches such as QTAIM point towards their stabilising nature.

The H-H BCPs were first interpreted by Cioslowsky and Mixon in kekulene [117] and ortho-substituted biphenyls [118] and assigned to "non-bonded repulsive contacts", a view supported by later studies with a different energy partition [119, 120]. QTAIM atomic energies, on the other hand, predict a stabilisation caused by H-H contacts of up to 10 kcal/mol in the general case of polybenzenoid molecules [121]. It should be noted that the weakness of dihydrogen interactions and the arbitrariness in the choice of energy partition precludes determining how much these interactions contribute to the total binding energy of a crystal, so it would be extremely difficult to determine in an unbiased manner the strength and character of these interactions, except in those cases where the total stabilization is to a good approximation, only given by those interactions. This is the case of the y polymer. Being hydrogen interactions the main source of interactions in the y direction (very little dispersion is observed), the attractive interaction observed in this polymer can only be attributed to H-H interactions. This highlights the advantage of local approaches in complex systems

From the visual analysis of NCI isosurfaces of the linear polymers and the 2D arrangement, the x and y components are perfectly recovered, along with an extra region between interactions along x and y direction. This interaction between diagonal elements of the arrangements, may be identified as the responsible of its relative stability. In other words, the diagonal interaction is related to packing. It is interesting to note that once again, these interactions are dispersive-like, which explains why the are so difficult to track in solids.

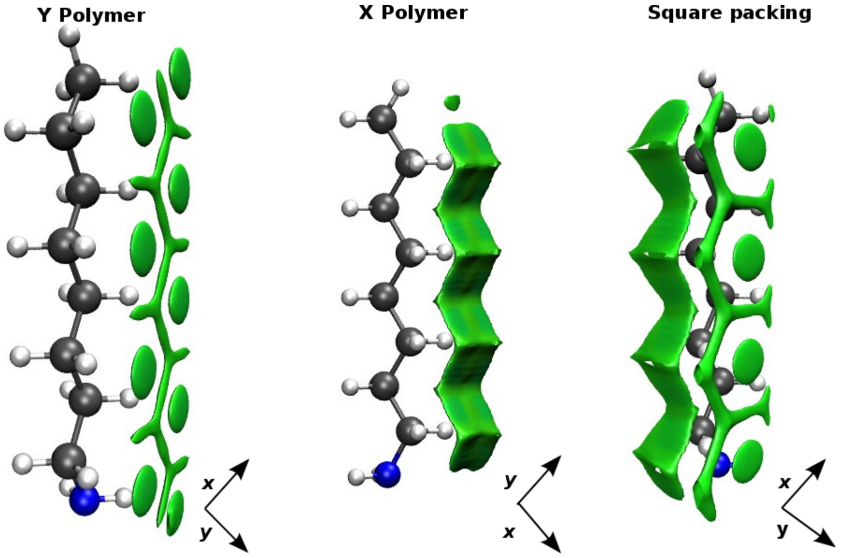

a) b) c)

Figure 7.5: NCI isosurfaces of the (a) y-polymer, (b) the x-polymer and (c) the 2 dimension polymer. Only the monomers are plotted. The linear polymers grow in the plane.

7.2.2 Binding in metallocenes

Dispersion interactions plays an outstanding role in metallocenes dimers. Vargas-Caamal *et al* [122] have performed an in-depth survey of the nature of the bonding in different metallocene dimers: ferrocene, ruthenocene, osmocene. These systems exhibit higher dissociation energies than the water dimer at low temperatures. The additional stability of metallocene dimers was ascribed to the collective action of very weak interactions of dispersive nature. An EDA analysis reveals that in these systems the contribution of the dispersion term to the energy is larger than in the parallel-displaced benzene dimer, the prototype example of system stabilized by dispersion interactions.

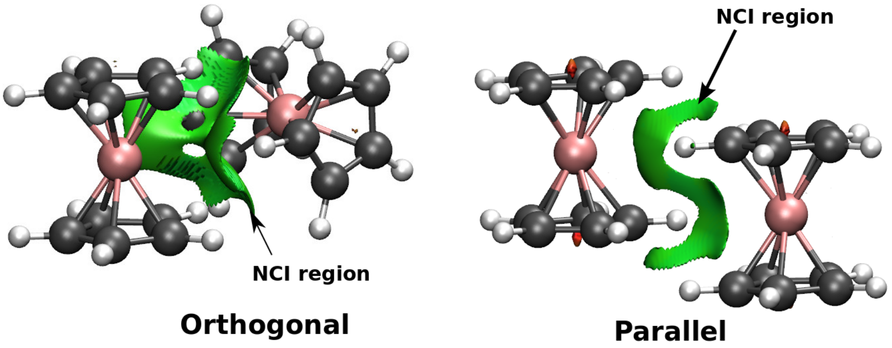

a) b)

Figure 7.6: NCI isosurfaces for: a) orthogonal and b) parallel ferrocene dimers. A density cut-off of $\rho = 0.01$ a.u. was applied and the pictures were created for an isosurface value of $s = 0.5$ and coloured in the [-0.03, 0.03]a.u. sign$(\lambda_2)\rho$.

As shown in Figure 7.6 the NCI analysis of the most stables conformations of the ferrocene dimer correspond to a typical dimer stabilized mainly by dispersion where attractive surfaces cover a very large area between both monomers. Similar results are found for osmocene and ruthenocene dimers. Once again, a correlation is found between the size and the electron population within the NCI region and the relative stability of the two conformers as shown in Table 7.4.

	$\Delta E^{\dagger}_{total}$(kcal/mol)	$V_{\Omega_{NCI}}$(a.u.)	$N_{\Omega_{NCI}}$(a.u.)
Orthogonal	-7.7	104.03	1.90
Parallel	-5.7	87.47	1.78

Table 7.4: Interaction energy (ΔE_{total}), NCI volume ($V_{\Omega_{NCI}}$(a.u.)) and NCI electron population ($N_{\Omega_{NCI}}$(a.u.)) for the ferrocene dimers.
† Energies extracted from [122].

7.3 Do all these interactions deserve distinctive names?

The energetic statements here conveyed reveal that with a few exceptions, pnictogen, halogen and weak-hydrogen bonds and even H-H interactions expand over the same range of energy. The NCI picture sorts this interactions between those characterized by having small and round-shaped isosurfaces and those exhibiting large and thin isosurfaces. The former are very directional and the electrostatic contribution to the stabilization of the complex is at least as large as the dispersion term. The latter are mainly driven by the dispersion contribution to the energy and expand large areas, being the consequence of the collective action of very weak dispersion interactions.

Given the correlation between the "directionality" of the interaction and the weights of the dispersion and electrostatic contributions to the interaction energy, it seems more convenient to refer to these interactions as dispersive, electrostatic or both, forgetting any reference to the composition of the interacting fragments. Since the "directionality" is transcribed into the shape of the NCI regions, the NCI method allows, with some caveats, a first estimation of the localization and energetic nature of the interaction. For instance, it is expected that the electrostatic contribution to E_{int} is larger in the interaction between the alkyl chains in the SAM systems (specially along the y direction) than in metallocene dimers. This approach has the advantage of being fast and applicable to big systems, including the difficult-to-characterize intramolecular interactions.

Chapter 8

Bonding analysis by means of the NCI method III: Reactivity

Sommaire

As defined by Linus Pauling “Chemistry is the science of substances: their structure, their properties, and the reactions that change them into other substance” [92]. The first aspects, structure and properties, are clearly associated with the arrangement of atoms in a molecule, i.e. the chemical bond. These bonds determine Pauling’s third aspect, chemical reactivity.

In the precedent chapters it was shown how bonding is defined within the NCI method. Qualitatively, chemical interactions are displayed as isosurfaces of the reduced density gradient around the minima of this function. Chemical bonds may be characterized by the shapes of such isosurfaces and differentiated by the mapping of $\mathrm{sign}(\lambda_2)\rho$ on them. A more quantitative characterization may be achieved by computing the volume and the electron population within NCI regions. One of most appealing features of the NCI method is the simultaneous visualization of interactions of any energetic range, from strong covalent interactions to very weak non-covalent interactions. In chemical reactions interactions of different strength interplay during bond breaking and formation. The transition from weak to strong interactions (or the opposite) that occurs during chemical reactions may be casted by following the evolution of the NCI isosurfaces.

In this chapter, we apply the NCI method to qualitatively understand the outcome of different chemical reactions. We have chosen two reactions that have been crucial in the history of theoretical chemistry: the thermal ring-opening of disubstituted cyclobutenes as example of the success of Woodward-Hoffmann rules in rationalisation from orbital grounds, and the Houk-List reaction as one of the first achievements in reactivity of computational chemistry.

8.1 Torquoselectivity

Pericyclic reactions represent the favorite playground for quantum chemistry reactivity models since Woodward and Hoffmann proposed their seminal list of rules [123]. By definition, pericyclic reactions evolve via a cyclic aromatic transition state of delocalized electrons where bond making and bond breaking occurs simultaneously in a cyclic array. Using the orbital symmetry conservation, Woodward and Hoffmann proposed a list of rules of thumb able to predict the mechanism and, hence the stereoselectivity of pericyclic reactions. Examples include cycloadditions, electrocyclisations, sigmatropic rearrangements, and chelotropic reactions. Much work has been devoted to show that electron circulation of the pericyclic transitions states may be smartly characterized by the topology of ELF [124].

One example of application of NCI to predict the outcome of pericyclic reaction is provided by the thermal ring-opening of *trans*-1,2,3,4-tetrafluoro-3,4- bis(pentafluorosulfanyl)cyclobutene (see figure 8.1). As a thermal, $4n$ electron process, the Woodward-Hoffmann rules predict that the conrotatory opening is more favorable than the disrotatory one [123]. Additionally, a given terminal substituent may either rotate “outwards” leading to (Z,Z)-1,2,3,4-tetrafluoro-1,4-bis(pentafluorosulfanyl)butadiene (from now on *outward* compound) or “inwards” yielding (E,E)-1,2,3,4-tetrafluoro-1,4-bis(pentafluorosulfanyl)butadiene (from now on *inwards* compound). Activation energies obtained at ωB97X-D/6-31G* level for *outwards* and *inwards* transition states are 41.55 kcal/mol and 21.12 kcal/mol respectively. Because this kind of stereoselectivity is related to the direction of the twist, it was named *torquoselectivity* by Houk and co- workers [125].

Rondan and Houk proposed in 1984 a widely accepted orbital model able to explain *torquoselectivity* [126, 127]. Since only certain orbitals are included in the model, a wrong selection of the interacting orbitals leads to wrong predictions. This shortcoming is com-

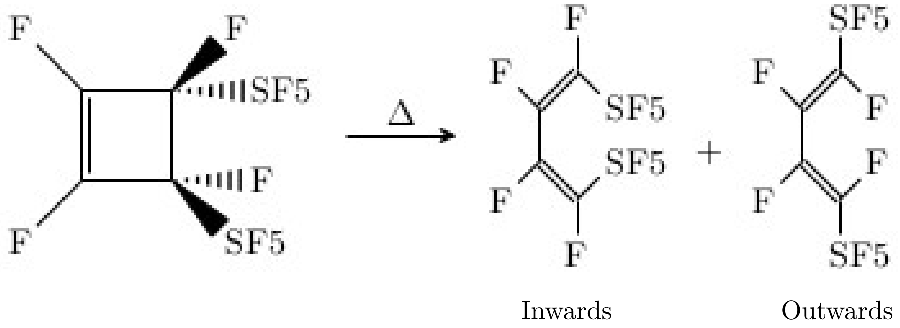

Figure 8.1: "Inwards" and "outwards" conrotatory product for the thermal ring opening of *trans*-1,2,3,4-tetrafluoro-3,4-bis(pentafluorsulfanyl)cyclobutene.

mon for all theories based on a selected group of orbitals, such as the frontier orbital theory [128]. To avoid this flaw, Ponec decided to reinvestigate the problem in terms of an electron density based indicator, such as the molecular similarity approach [129]. He showed that the origin of the *torquoselectivity* underlies on the low electron reorganization required to transform reactants into products. Additionally, NCI analyses of both *outwards* and *inwards* transition states provide us with the topological arguments to understand this differential selectivity.

As shown in Figure 8.2, apart from the breaking carbon-carbon covalent interaction (blue isosurface) and its repulsive counterpart ring tension (red isosurface), we can differentiate three types of non-covalent interactions (green isosurfaces):

Type 1 Fluor-fluor interaction between pentafluorosulfanyl groups.

Type 2 Pentafluorosulfanyl-carbon interaction.

Type 3 Fluor-fluor interaction between pentafluorosulfanyl and fluoro groups.

All of them are present in the *inwards* transition state, whereas only interactions of type 3 are found in the *outwards* one (See Figure 8.2). Thus, dispersion interactions between pentafluorosulfanyl groups and those with the carbon cycle should be the driving force of the process. Thus, *torquoselectivity* can also be understood in terms of neighbor interactions as revealed by NCI: within this approach products are driven by the stabilization through non-covalent interactions in the transition state.

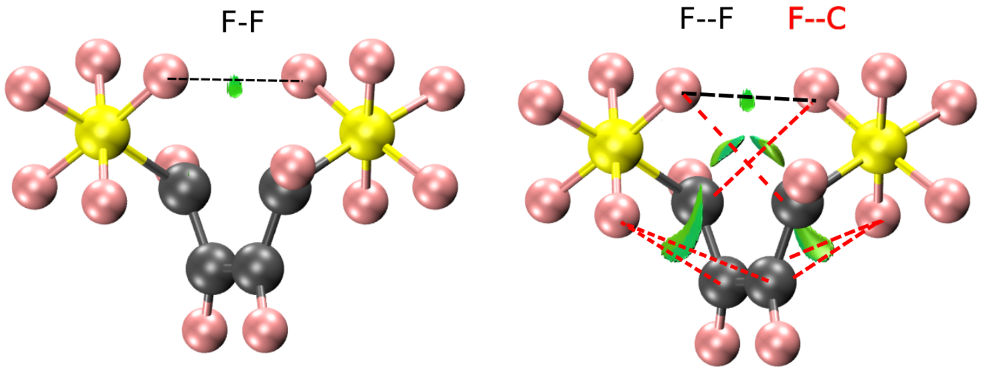

a) Type 1

b) Type 1 + 2

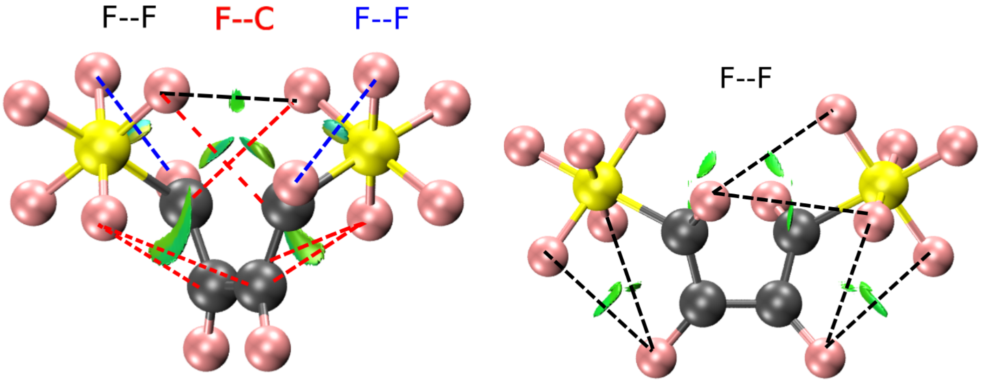

c) Type 1 + 2 +3

d) Type 3

Figure 8.2: Non-covalent interaction types in *outwards* and *inwards* transition states. Black, read and blue dashed lines represent type 1, 2 and 3 interactions respectively. The reduced density gradient isosurfaces (s=0.3) are colored on blue-green-red scale according the sign$(\lambda_2)\rho$ over the range -0.03 to 0.03 a.u.

8.2 The Houk-List transition states

Organocatalysed intermolecular aldol additions (see Figure 8.3) have been nicely rationalised by the Houk-List model, which involves a one-proline mechanism based on enamine activation [130, 131, 132, 133, 134]. The carbon-carbon bond formation is the rate-determining step of the intermolecular aldol catalytic cycle in which the catalytic active enamine attacks an electrophile.

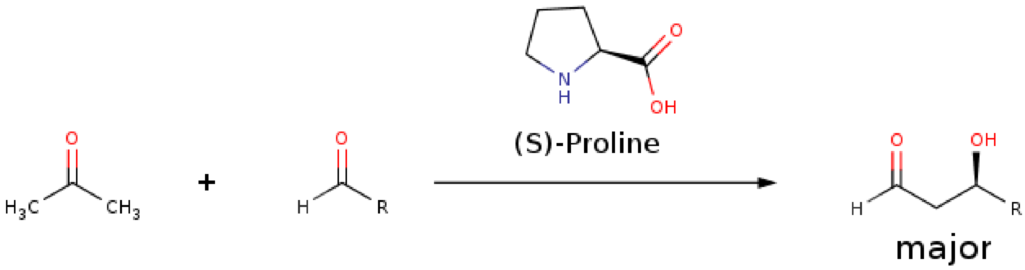

Figure 8.3: Scheme of a generic proline-mediated assymetric intermolecular aldol reaction.

Following Figure 8.4 the carboxylic acid group of proline plays a central role in the model, directing the electrophilic to the *Re* face of the enamine. The enamine can be either *anti* or *syn*, relative to the acid, and the electrophile can offer two prochiral faces for attack, *Re* or Si resulting in four different stereochemical outcomes.

Houk and Bahmanyar suggested that the energy differences between these transition states, and so the origin and degree of stereoselectivity displayed by the reaction, depends on two critical structural elements: the relative degree to which each transition state can adopt a planar enamine, and the degree of electrostatic stabilization provided to the forming alkoxide. A planar enamine allows for the greatest possible nucleophilicity of the terminal olefin while also reducing the geometric distortion experienced by the forming iminium group. The proton transfer from the carboxylic acid to the forming alkoxide was suggested to provide the majority of the electrostatic stabilization and is key to the Houk-List model. Smaller, yet important, stabilizing contributions also result from $NCH^{\delta+} \cdots O^{\delta-}$ interactions from the pyrrolidine ring.

In order to reproduce and expand the original calculations performed by Houk and List for R=Ph and R=*i*Pr,"chair" and "twist-boat" conformations for the cyclohexene ring and puckering of the proline ring away from or towards the proton transfer (Figure 8.5) were considered for each stereochemical outcome shown in Figure 8.4 for both R=Ph and R=*i*Pr, resulting in 16 transition states for each. Several computational aspects such as the quality of the functional, basis set, the need for dispersion corrections and the effect of solvent have been in-depth scrutinized in Ref [135]. Our collaborators concluded that geometries obtained at the larger triple-ζ-quality TZVP basis set with inclusion of the CPCM solvation model at B3LYP+D3 level were reliable enough to be considered as our base standard.

It is worth to note the importance of considering dispersion correction in the DFT functional, which results in a increase of the planarity of the enamine. Examining the enamine geometries for R=Ph, a correlation between the planarity of the enamine and the relative stability is found; the lowest energy structure, (S,R) conformation 2, has

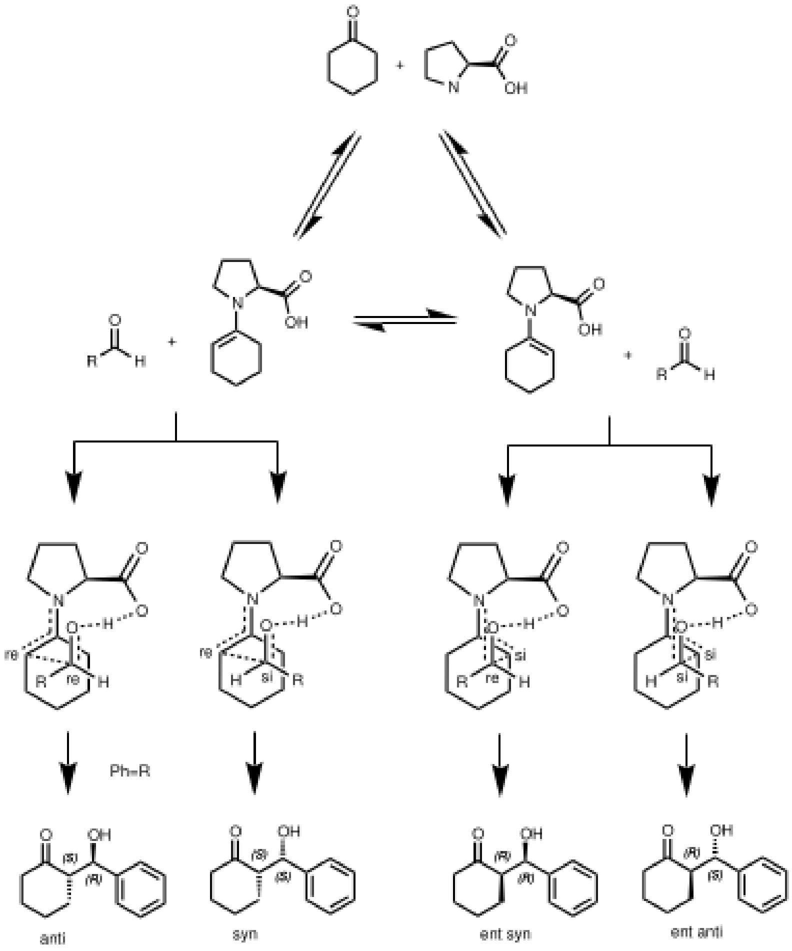

Figure 8.4: The stereochemical possibilities for the asymmetric aldol reaction. Cahn-Ingold-Prelog conventions are shown for R=Ph.

an almost totally planar enamine (177.2°) whereas the highest energy structure (R,S) conformation 3 is highly pyramidalised (167.0°). Once the geometries were optimized including dispersion corrections, further insights into the role of non-covalent interactions in the relative stability of transition states may be disclosed by applying the NCI method. In order to highlight certain features, three representative examples from the R=Ph reaction have been chosen. Figure 8.6 dissects the diastereoisomer with the highest energy ($ent - anti$), the diastereoisomer with the lowest energy (*anti*), and the diastereoisomer with the highest dispersion correction (*syn*). The cut-off ($\rho = 0.1a.u$) has been chosen to isolate the purely non-covalent interactions along the C-C formation. At first glance, both the *anti* and the *syn* conformers show greater NCI isosurfaces, which confirms the role of non-covalent interactions in stabilizing the diastereoisomeric transition states. For a more detailed analysis, the most relevant interaction have been highlighted in Figure 8.6. The deep blue feature corresponds in all three cases to the forming C-C bond. It corresponds to a mid-range interaction, in-between covalent and non-covalent.

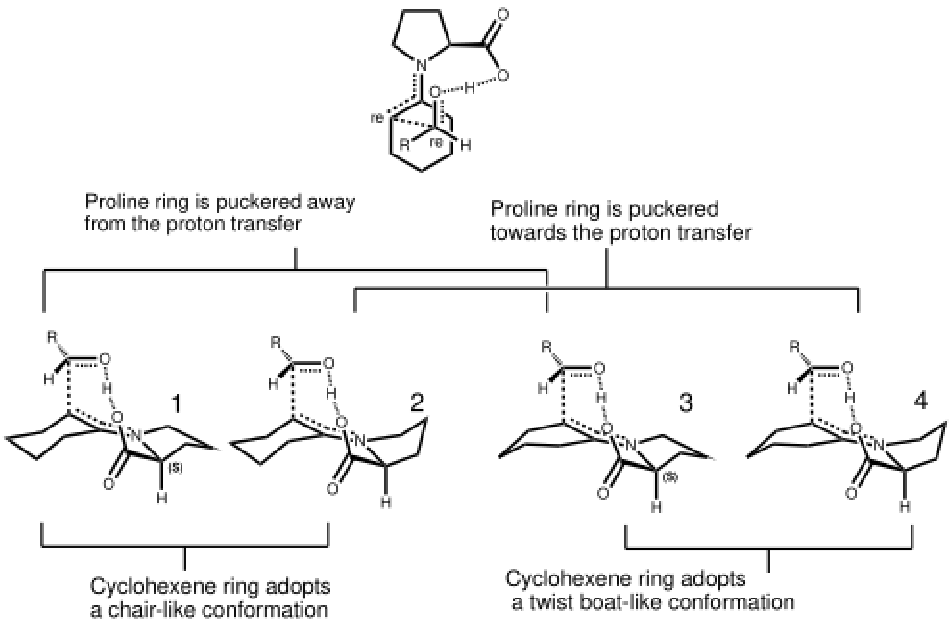

Figure 8.5: The four considered conformational possibilities for the asymmetric aldol condensation.

Along with the C-C formation, two purely non-covalent regions appear:

- The region around the heteroatoms (C=O$\cdots$N) shows stabilizing features in all the conformers, whereas it is most important in *anti* and *syn* conformers, it is much weaker in the $ent-anti$ and $ent-syn$ ones. This 3D view coincides with the previous approaches, which locate the relevance in the NCH$^{\delta+}\cdots O^{\delta-}$ interaction. However, along with the electrostatic interactions, green dispersive interactions appear elongating the NCI feature which highlights the importance of the planarity of this region and which cannot be merely explained by electrostatics.
- An extra region in the *syn* conformer, a green surface between the proline and the R=Ph group. This interaction can be identified as tilted T-shape interaction or as π-facial hydrogen bond. It is important to note that this interaction, which stabilizes the *syn* conformers, had not been identified before by mere geometric inspections. However, its presence enables us to explain the fact that the *syn* conformers are the ones with largest dispersion correction.

Thus, a combination of NCH$^{\delta+}\cdots$ O$^{\delta-}$ electrostatics and dispersion (either in the NCH$^{\delta+}\cdots$ O$^{\delta-}$ or T-shape/π-facial H-bond in the ring region) determine the outcome of the reaction, with only *anti* and *syn* as observable diasteroisomers. It should be noted that this balance between electrostatic and dispersive interactions highlights, once again, the necessity to include dispersion effects in the calculations, else the correct energetics and geometrics would not be obtained.

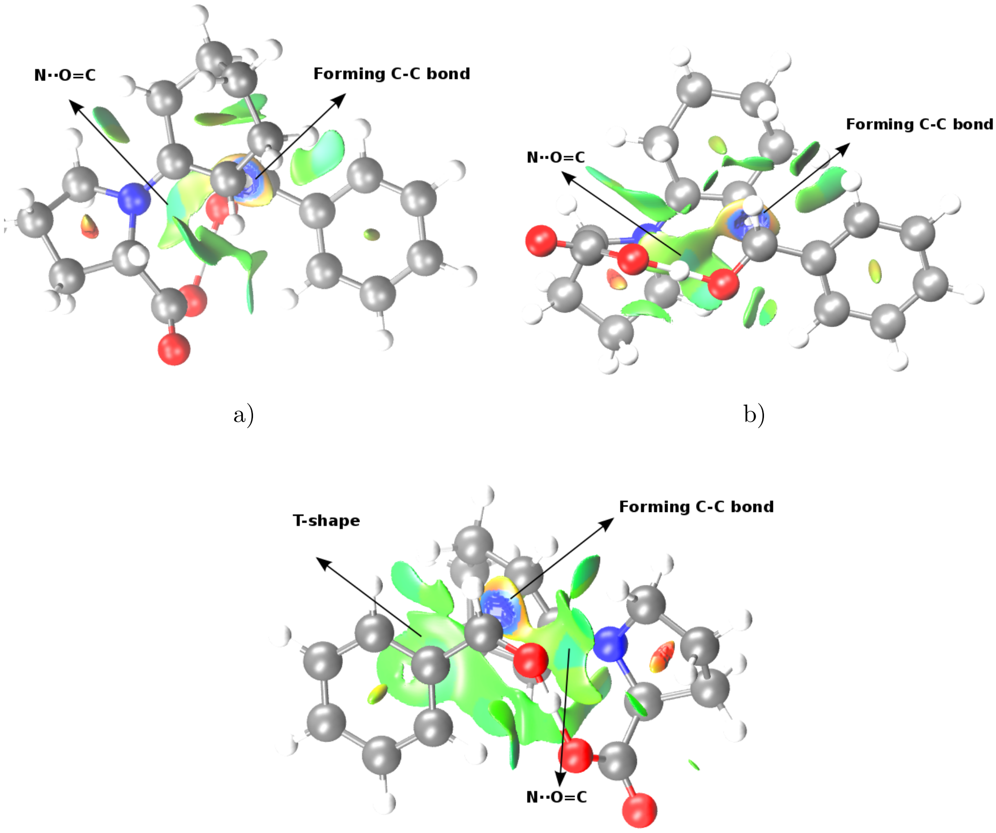

a)

b)

c)

Figure 8.6: NCI analysis of several conformers of the computed transition state: a) the lowest energy isomer, b) the highest energy isomer, c) the highest D3 corrections isomer. The reduced density gradient isosurfaces ($s = 0.5$) are colored on a blue-green-red scale according to the $\text{sign}(\lambda_2)\rho$ over the range -0.03 to 0.03 a.u.

Chapter 9

Conclusions and outlook

This thesis is intended to present the current state of the art of the NCI method and its applications to understand structural stability and chemical reactivity. Following the QCT spirit, the NCI method focuses on the properties of the electron density and its derivatives to obtain some insight into chemical bonding, namely of the reduced density gradient (RDG) and the electron density Laplacian eigenvalues.

On the one hand, RDG is used as an indicator of chemical interactions, critical points, namely its minima, match with those of the electron density, and with very weak interactions not revealed by BCPs. This gain of RDG respect to the electron density is related to the fact that the former adds up information from the gradient and the Laplacian of the latter. Since the origin of the reduced density gradient is traced back to the DFT development of GGA functionals, it was interpreted as a measure of the local inhomogeneity of the system, which is not very appealing from a chemical point of view. A conceptual laguna arose regarding the chemical content of the NCI pictures. The connection with QTAIM foresaw that minima of RDG may be ascribed with changes in the electron density Laplacian, and therefore with some kind of interaction. The strength of these changes may determine whether these interactions occur through a BCP or not. A more satisfactory interpretation has been given in terms of the von Weiszäcker kinetic energy. Minima of this term identify regions more prone to exhibit a bosonic behaviour. For a fermionic system this occurs in regions with low Pauli repulsion accounted by the Pauli kinetic energy. This happens in regions well described by a single orbital, i.e. where there is a strong electron pairing, or like-spin electron repulsion is relatively small.

Independently of the NCI method, different functions have been proposed which exhibit similar results than those of the reduced density gradient. We refer to LED and DORI. The former is derived from the local quantum theory of momentum and it uses a formula equivalent to that of the local-wave vector. The latter is based on the geometrical features of the electron density, and it uses an elaborated scaled form of the local-wave vector. Since the reduced density gradient may be viewed as a scaled form of LED, the three descriptors turn around the same function, the local-wave vector. Once again the importance of the gradient of the electron density is stressed.

Additionally, the NCI method came up with a new type of diagram scarcely used in the chemistry community. RDG *versus* ρ representations collect a lot of information of the system in two dimensions. By tuning the ρ range, one can tune which kind of interaction to visualize, non-covalent interactions appear at low values of ρ (typically $\rho < 0.1$ a.u.), covalent interactions at intermediated values and core regions at higher densities. When plotting $s(\rho)$ values, troughs in the diagram may be ascribed to some kind of chemical interaction. These peaks represent deviations from a single exponential decay density model, which is used as reference of non-interacting system. The points in the diagrams forming these peaks are then represented in real space for some value of s inside the peak, and visualized as isosurfaces. These are very similar to some kind of spectra, where transitions have been replaced with chemical interactions. Since each peak is the signature of some chemical interactions, resolving such spectra is the main issue. Since a peak is a very vague definition, a unique definition of the region should be provided, that is a baseline in the spectroscopy jargon. This first problem has been circumvented by defining a reference pseudodensity whose reduced density gradient will define the baseline, points under such reference curve defined what we have called throughout this manuscript, NCI regions. The use of pseudodensities defined from real fragments of the system resolves the problem of the arbitrariness on the choice of the isosurface value. This approach has been already implemented in our main code for performing NCI analysis, NCIPLOT.

Once chemical interactions are identified, we proposed different criteria for differentiating beetween interaction types based on the curvature of the electron density. i) The shape of the s isosurfaces representing such interactions ii) the electron density Laplacian eigenvalues.

i) Since minima of the reduced density gradient usually appear at low values of the electron density gradient, the shape of the isosurfaces encompassing such minima are determined by the behavior of the eigenvalues of the Laplacian of the electron density. Shared shell interactions are characterized by cylindrical shapes. Among closed shell interaction, highly localized interaction involving only a pair of atoms, such as hydrogen or pnictogen bonding are characterized by a disc-shape isosurface, while dispersion interactions result of a sum of several weak interactions and are disclosed as extended misshaped isosurfaces. Isosurfaces around ring critical points and cage critical points, which have been ascribed to steric classes, appears as ellipsoidal shapes. Among closed shell interactions, highly localized interactions involving only a pair of atoms, such as hydrogen or pnictogen bonding are characterized by a disc-shape interaction, while dispersion interactions, which result of a sum of several weak interactions, are disclosed as extended misshaped surfaces

ii) Since non-covalent interactions involve a positive value of the electron density Laplacian in the interaction region it is not possible to sort non-covalent interaction only with the sign of the Laplacian. Instead, one may focus on the eigenvalue responsible of the different signature of BCP and ring critical points, that is, the second eigenvalue of the electron density Laplacian λ_2, ($\lambda_1 < \lambda_2 < \lambda_3$). Due to the fact that ring critical points occur traditionally where it is said to be steric crowing, regions with positive value of λ_2 have been said to be repulsive and regions with negative value of λ_2 attractive.

Mapping the values of $\text{sign}(\lambda_2)\rho$ over the reduced density gradient isosurfaces one may identify and differentiate chemical interactions. The relative strength of a interaction is given by the ρ values, and therefore, the strongest interactions are represented as isosurfaces with the purest red or blue color.

Contributions

The main contributions of this manuscript are the following:

- A novel physical interpretation of the reduced density gradient based on its connection with the von Weizsäcker kinetic energy density. Additionally the critical points of the reduced density gradient have been connected with the AIM theory and one-electron potential.

- An algorithm for defining NCI regions and computing properties within them has been implemented in NCIPLOT. The results thereby obtained reveal a close correlation between the size the NCI regions and the stabilization energy in that systems mainly stabilized by dispersion forces.

- We asses the dependence of the NCI method with the theory level. From a visual point of view, results are very stable with respect to the geometry, but from the quantitative point of view, NCI is able to reveal changes in the geometry and electron distribution when very subtle effects are at play.

- We demonstrate the ability of the NCI method for analyzing covalent bonds. The close relationship between the reduced density gradient and other widely used bonding descriptors enables the application of the NCI method for analyzing any interaction type.

- A characterization of non-covalent interactions in terms of the shapes of the NCI domains, the values of the $\mathrm{sign}(\lambda_2)\rho(\mathbf{r})$ and energetics.

- We apply the NCI method for assessing the role of dispersion interactions in complex systems: SAMs, methallocene dimers and transition states. The relative stability of such systems is often analyzed in terms of energy partitions, which provide global quantities. Local approaches such as NCI have the advantage of revealing the key interactions of the systems.

Setbacks

So far so good, but then comes the poison arrow. In the zoo of methods which are nowadays available for analyzing chemical bonding, we have selected quantum chemical topology (QCT) as our main approach. QCT embraces all those methodologies that used the dynamical system induced by the gradient field of some physical meaningful scalar field as partition engine. Along Chapter 2 we introduced the theory required for understanding the topological aspects behind QCT. The reader may have realized that a topological partition of the reduced density gradient has not been presented yet, so this excludes the NCI method and many of the analysis herein presented from QCT.

Despite my commitment to perform such task, I found two main hurdles I could not overcome:

- Due to the absolute value in the numerator of the reduced density gradient, this function is piecewise smooth, and therefore, analytical searching for critical points are not accurate enough to guarantee that the relation between number of different critical points satisfies the Morse rule.

- The implementation of the combinatorial methods introduced in Chapter 2 needs for rewriting our main code NCILOT from FORTAN to C++, in order to profit from the libraries already implement for such kind of task.

Despite these limitations, all is not lost! As commented in Chapter 2 the split and merge of the connected components of an isosurface is related to the presence of critical points. This information is nicely collected into the Reeb graphs. This approach has already been implemented for analyzing ELF and RDG under the name of bifurcation trees. In a nutshell, a rough idea of the localization and value of critical points may be obtained by tuning the isosurface value. When visualising RDG, an isosurface of $s = 0.5$ is often enough to grasp all the RDG minima.

Regarding the second aspect of QCT, chemical meaningful scalar fields, we expect to have convinced the reader of the connection between regions of marked bosonic character and the minima of the reduced density gradient, and so with relevant chemical features.

Turning back to the spectroscopy analogy, the ability for extracting different regions from $s(\rho)$ diagrams, depends on how well resolved are the peaks, i.e. symmetric regions will be represented by the same peak in the diagram and they cannot be extracted as separate isosurfaces by mere observation of the diagram. This hurdle is intrinsic to the method and no solution has been envisaged. Some improvements have been made from the visualization community. Recently Carr *et al* have proposed an algorithm for extracting surfaces from arbitrary regions of the $s(\rho)$ diagrams, and for any two scalar fields in general [136].

Open issues

It is hard to put a final point to this thesis when there are so many things to do. Considering that the conceptual basis of the NCI method has been already established, the future research lines within NCI project should be focused in the implementation part. Although the NCI method has been adopted by the QCT community, it is far from being a “full member”. Efforts in such direction should be taken. In what follows I will try to list the tasks that still remain not only in my “TO DO” list but also for future members of the NCI project:

1. The first step is to perform a robust code able to compute the Morse complex of RDG. Despite having outlined the shape of such partition, as far as I know no one has performed it yet. Such code will develop the NCI method up to the other QCT approaches. Moreover, such basins of RDG (namely its negative since basins are developed around maxima of a scalar field) will split the real space into atomic and interaction regions. With this methodology in hand, $s(\rho)$ diagrams will be pushed into the background, since critical points will be directly localized in real space.

2. In order to compute average properties within RDG basins, improvements of the integration methods is mandatory. In this regard, integration algorithms over grid points are already available. Although the target of the NCI method are big systems, an step by step test of the RDG topology should be performed starting from atoms, then small molecules and gradually increasing the size of the system.

3. If we success in the previous two points, we should deal with the main difficulty of the QCT approach, big systems. Although QCT algorithms have been sped up during the last decade, they are far from being a real possibility in dealing with big systems coming from other disciplines such as Biology and Material Sciences. This is one of the main advantage of RDG: it is fast to compute and robust in such extent that promolecular densities retain the main signatures of the NCI method. Given these two points, one may envisage a two steps algorithm for dealing with

big systems; a first quick NCI analysis for localizing the interaction regions, and a second step in which accurate topological analyses are performed within them. Tierny *et al* [137] have made some progress in this direction. They proposed an algorithm for searching critical points of the electron density, within NCI regions.

4. Last but not least. Working with researches from the visualization community I realized the potential applications of the topology to tackle with our main issue, chemical bonding. In words of Popelier the number of concepts handled by QCT is so limited that sometimes it is closer to topography than to topology [138]. Since the seminal work of Bader, little improvement has been done in applying new topological concepts to the analysis of chemical bonding. In this regard, there are a plenty of choices. For instance the simultaneous analysis of several scalar fields is available through the notions of Jacobi sets or continuous scatter plots. A close collaboration between both communities is mandatory for the success of this endeavor.

The list could probably be longer and I am pretty sure it will be. Although I am running out of time for facing all these fascinating challenges, I wish they would be solve in the near future either by me or my collaborators.

List of publications

Articles

- *The Houk List transition state for organocatalytic mechanism revisited.*
  A. Armstrong, R. A. Boto, P. Dingwall, J. Contreras-García, M. J. Harvey, N. J. Mason and H. S. Rzepa.
  Chemical Science, 2014, 5, 2057-2071.

- *Characterizing Molecular Interactions in Chemical Systems.*
  R. A. Boto, D. Günther, J. Contreras-García, J.P. Piquemal, J. Tierny.
  IEEE Transactions on Visualization and Computer Graphics, 2014, 20, 2476-2485.

- *The role of dispersion forces in metal-supported self-assembled monolayers.*
  R. A. Boto, J. Conteras-García, M. Calatayud.
  Computation and Theoretical Chemistry, 2015, 1053, 322-327.

- *How Strong is a Metallocene Dimer (Metal= Fe, Ru, Os)?*
  A. Vargas, S. Pan, F. Ortiz-Chi, J. L. Cabellos, R. A. Boto, J. Contreras-García, A. Restrepo, P. M. Chattaraj, G. Merino.
  Physical Chemistry Chemical Physics, 2016, 18, 550-556.

- *Interpretation of the reduced density gradient.*
  R. A. Boto, J. Contreras-García, J. Tierny, J-P Piquemal.
  Molecular Physics, 2016, 114, 1406-1414.

- *A benchmark for the Non-Covalent Interaction index (NCI) or…is it really all in the geometry?*
  J. Contreras-García, R. A. Boto, F. Izquierdo-Ruiz, I. Reva, T.Woller, M.Alonso.
  Theoretical Chemistry Accounts, 2016, 135, 252-254.

- *Revealing strong interactions with the reduced density gradient: a benchmark for covalent, ionic and charge-shift bonds.*
  R. A. Boto. J-P Piquemal, J. Contreras-García.
  Theoretical Chemistry Accounts, 2017, 136,139-146.

- *Do bonds need a name?.*
  R. A. Boto, C. Narth, Z. Maroun, J. Contreras-García.
  in preparation.

Book chapters

- *Chemical Bonding under Pressure.*
  In *An Introduction to High Pressure Science and Technology.*
  R. A. Boto, M. Marqués, A. Beltrán, L. García, Juan Andrés, V. Riffet, V. Labet, and J. Contreras-García.
  Eds. J. Manuel Recio, José Manuel Menéndez, Alberto Otero-de-la-Roza.
  CRC Press Taylor & Francis Group: Boca Raton, FL, 2015.

- *A complete NCI perspective: from new bonds to reactivity.*
  In *Applications of Topological Methods in Molecular Chemistry.*
  C. Narth, Z. Maroun, R. A. Boto, R. Chaurdret, M-L Bonet, J-P Piquemal, Julia Contreras-García.
  Eds. Remi Chauvin, Christine Lepetit, Bernard Silvi, Esmail Alikhani.
  Challenges and Advances in Computational Chemistry and Physics. Volume 22.
  Springer International Publishing Switzerland 2016.

- *Analysis of reactivity from the non-covalent interactions perspective.*
  R. A. Boto, I. Woller, Julia Contreras-García and I. Fernandez.
  submitted.

Bibliography

[1] D. Danovich, P. C. Hiberty, W. Wu, H. S. Rzepa, and S. Shaik, “The nature of the fourth bond in the ground state of c2: The quadruple bond conundrum,” *Chemistry–A European Journal*, vol. 20, no. 21, pp. 6220–6232, 2014.

[2] A. Szabo and N. S. Ostlund, *Modern quantum chemistry: introduction to advanced electronic structure theory.* Courier Corporation, 1989.

[3] C. J. Cramer, *Essentials of computational chemistry: theories and models.* John Wiley & Sons, 2013.

[4] P. Hohenberg and W. Kohn, “Inhomogeneous electron gas,” *Physical review*, vol. 136, no. 3B, p. B864, 1964.

[5] R. McWeeny and B. Sutcliffe, “Methods of molecular quantum mechanics (academic, london, 1989),” *Vol. XV*, 1959.

[6] W. Koch and M. C. Holthausen, *A chemist’s guide to density functional theory.* John Wiley & Sons, 2015.

[7] R. G. Parr, *Density functional theory of atoms and molecules.* Springer, 1980.

[8] M. Levy, “Universal variational functionals of electron densities, first-order density matrices, and natural spin-orbitals and solution of the v-representability problem,” *Proceedings of the National Academy of Sciences*, vol. 76, no. 12, pp. 6062–6065, 1979.

[9] M. Levy, “Electron densities in search of hamiltonians,” *Physical Review A*, vol. 26, no. 3, p. 1200, 1982.

[10] V. Sahni, J. Gruenebaum, and J. Perdew, “Study of the density-gradient expansion for the exchange energy,” *Physical Review B*, vol. 26, no. 8, p. 4371, 1982.

[11] W. Kohn and L. J. Sham, “Self-consistent equations including exchange and correlation effects,” *Physical review*, vol. 140, no. 4A, p. A1133, 1965.

[12] D. M. Ceperley and B. Alder, “Ground state of the electron gas by a stochastic method,” *Physical Review Letters*, vol. 45, no. 7, p. 566, 1980.

[13] S. Vosko, L. Wilk, and M. Nusair, “Accurate spin-dependent electron liquid correlation energies for local spin density calculations: a critical analysis,” *Canadian Journal of physics*, vol. 58, no. 8, pp. 1200–1211, 1980.

[14] J. P. Perdew and Y. Wang, “Accurate and simple analytic representation of the electron-gas correlation energy,” *Physical Review B*, vol. 45, no. 23, p. 13244, 1992.

[15] J. P. Perdew, K. Burke, and M. Ernzerhof, "Generalized gradient approximation made simple," *Physical review letters*, vol. 77, no. 18, p. 3865, 1996.

[16] A. D. Becke, "Density-functional exchange-energy approximation with correct asymptotic behavior," *Physical review A*, vol. 38, no. 6, p. 3098, 1988.

[17] C. Lee, W. Yang, and R. G. Parr, "Development of the colle-salvetti correlation-energy formula into a functional of the electron density," *Physical review B*, vol. 37, no. 2, p. 785, 1988.

[18] A. Becke, "Hartree–fock exchange energy of an inhomogeneous electron gas," *International journal of quantum chemistry*, vol. 23, no. 6, pp. 1915–1922, 1983.

[19] A. D. Becke, "Correlation energy of an inhomogeneous electron gas: A coordinate-space model," *The Journal of chemical physics*, vol. 88, no. 2, pp. 1053–1062, 1988.

[20] J. Jaramillo, G. E. Scuseria, and M. Ernzerhof, "Local hybrid functionals," *The Journal of chemical physics*, vol. 118, no. 3, pp. 1068–1073, 2003.

[21] A. D. Becke, "Thermochemical tests of a kinetic-energy dependent exchange-correlation approximation," *International Journal of Quantum Chemistry*, vol. 52, no. S28, pp. 625–632, 1994.

[22] J. P. Perdew, S. Kurth, A. Zupan, and P. Blaha, "Accurate density functional with correct formal properties: A step beyond the generalized gradient approximation," *Physical review letters*, vol. 82, no. 12, p. 2544, 1999.

[23] J. Tao, J. P. Perdew, V. N. Staroverov, and G. E. Scuseria, "Climbing the density functional ladder: Nonempirical meta–generalized gradient approximation designed for molecules and solids," *Physical Review Letters*, vol. 91, no. 14, p. 146401, 2003.

[24] J. Krieger, J. Chen, G. Iafrate, A. Savin, A. Gonis, and N. Kioussis, "Electron correlations and materials properties," *Kluwer Academic, New York*, pp. 463–477, 1999.

[25] A. D. Becke, "Density-functional thermochemistry. iii. the role of exact exchange," *Chem. Phys*, vol. 96, p. 2155, 1992.

[26] A. D. Becke, "A new mixing of hartree–fock and local density-functional theories," *The Journal of Chemical Physics*, vol. 98, no. 2, pp. 1372–1377, 1993.

[27] A. Beck, "Density-functional thermochemistry. iv. a new dynamical correlation functional and implications for exact-exchange mixing," *J Chem Phys*, vol. 109, pp. 1040–1047, 1996.

[28] C. Adamo and V. Barone, "Toward reliable density functional methods without adjustable parameters: The pbe0 model," *The Journal of chemical physics*, vol. 110, no. 13, pp. 6158–6170, 1999.

[29] T. Leininger, H. Stoll, H.-J. Werner, and A. Savin, "Combining long-range configuration interaction with short-range density functionals," *Chemical physics letters*, vol. 275, no. 3, pp. 151–160, 1997.

[30] A. Savin and H.-J. Flad, "Density functionals for the yukawa electron-electron interaction," *International Journal of Quantum Chemistry*, vol. 56, no. 4, pp. 327–332, 1995.

[31] J. Toulouse, F. Colonna, and A. Savin, “Long-range–short-range separation of the electron-electron interaction in density-functional theory,” *Physical Review A*, vol. 70, no. 6, p. 062505, 2004.

[32] J.-D. Chai and M. Head-Gordon, “Systematic optimization of long-range corrected hybrid density functionals,” *The Journal of chemical physics*, vol. 128, no. 8, p. 084106, 2008.

[33] K. Sharkas, J. Toulouse, and A. Savin, “Double-hybrid density-functional theory made rigorous,” *The Journal of chemical physics*, vol. 134, no. 6, p. 064113, 2011.

[34] J. Heyd, G. E. Scuseria, and M. Ernzerhof, “Hybrid functionals based on a screened coulomb potential,” *The Journal of Chemical Physics*, vol. 118, no. 18, pp. 8207–8215, 2003.

[35] J. Heyd and G. E. Scuseria, “Efficient hybrid density functional calculations in solids: assessment of the heyd–scuseria–ernzerhof screened coulomb hybrid functional,” *The Journal of chemical physics*, vol. 121, no. 3, pp. 1187–1192, 2004.

[36] J. Heyd and G. E. Scuseria, “Assessment and validation of a screened coulomb hybrid density functional,” *The Journal of chemical physics*, vol. 120, no. 16, pp. 7274–7280, 2004.

[37] A. V. Krukau, O. A. Vydrov, A. F. Izmaylov, and G. E. Scuseria, “Influence of the exchange screening parameter on the performance of screened hybrid functionals.,” *The Journal of chemical physics*, vol. 125, no. 22, pp. 224106–224106, 2006.

[38] P. L. Popelier and F. M. Aicken, “Atomic properties of amino acids: Computed atom types as a guide for future force-field design,” *ChemPhysChem*, vol. 4, no. 8, pp. 824–829, 2003.

[39] T. Kato, “On the eigenfunctions of many-particle systems in quantum mechanics,” *Communications on Pure and Applied Mathematics*, vol. 10, no. 2, pp. 151–177, 1957.

[40] M. Hoffmann-Ostenhof and T. Hoffmann-Ostenhof, “" schrödinger inequalities" and asymptotic behavior of the electron density of atoms and molecules,” *Physical Review A*, vol. 16, no. 5, p. 1782, 1977.

[41] R. F. W. Bader, *Atoms in Molecules: A Quantum Theory.* Oxford, UK: Oxford Science Publications, 1990.

[42] A. D. Becke and K. E. Edgecombe, “A simple measure of electron localization in atomic and molecular systems,” *The Journal of chemical physics*, vol. 92, p. 5397, 1990.

[43] B. Silvi, “The synaptic order: a key concept to understand multicenter bonding,” *Journal of molecular structure*, vol. 614, no. 1, pp. 3–10, 2002.

[44] B. Silvi, A. Savin, *et al.*, “Classification of chemical bonds based on topological analysis of electron localization functions,” *Nature*, vol. 371, no. 6499, pp. 683–686, 1994.

[45] W. Kutzelnigg, “Chemical bonding in higher main group elements,” *Angewandte Chemie International Edition in English*, vol. 23, no. 4, pp. 272–295, 1984.

[46] K. Ruedenberg and M. W. Schmidt, “Why does electron sharing lead to covalent bonding? a variational analysis,” *Journal of computational chemistry*, vol. 28, no. 1, pp. 391–410, 2007.

[47] T. Bitter, K. Ruedenberg, and W. Schwarz, “Toward a physical understanding of electron-sharing two-center bonds. i. general aspects,” *Journal of computational chemistry*, vol. 28, no. 1, 2007.

[48] L. Cohen, “Local kinetic energy in quantum mechanics,” *The Journal of Chemical Physics*, vol. 70, no. 2, pp. 788–789, 1979.

[49] L. Cohen, “Representable local kinetic energy,” *The Journal of chemical physics*, vol. 80, no. 9, pp. 4277–4279, 1984.

[50] C. v. Weizsäcker, “On the theory on nuclear masses,” *Journal of Physisc*, vol. 96, 1935.

[51] H. J. Bohórquez and R. J. Boyd, “A localized electrons detector for atomic and molecular systems,” *Theoretical Chemistry Accounts*, vol. 127, no. 4, p. 393, 2010.

[52] R. A. Boto, J. Contreras-García, J. Tierny, and J.-P. Piquemal, “Interpretation of the reduced density gradient,” *Molecular Physics*, pp. 1–9, 2015.

[53] H. Schmider and A. Becke, “Chemical content of the kinetic energy density,” *Journal of Molecular Structure: THEOCHEM*, vol. 527, no. 1, p. 51, 2000.

[54] K. Finzel, “Elf and its relatives a detailed study about the robustness of the atomic shell structure in real space,” *International Journal of Quantum Chemistry*, vol. 114, no. 22, p. 1546, 2014.

[55] Y. Tal and R. Bader, “Studies of the energy density functional approach. i. kinetic energy,” *International Journal of Quantum Chemistry*, vol. 14, no. S12, pp. 153–168, 1978.

[56] G. Hunter, “The exact one-electron model of molecular structure,” *International Journal of Quantum Chemistry*, vol. 29, no. 2, p. 197, 1986.

[57] A. Savin, O. Jepsen, J. r. Flad, O. K. Andersen, H. Preuss, and H. G. von Schnering, “Electron localization in solid-state structures of the elements: the diamond structure,” *Angewandte Chemie International Edition in English*, vol. 31, no. 2, p. 187, 1992.

[58] A. Savin, “The electron localization function (elf) and its relatives: interpretations and difficulties,” *Journal of Molecular Structure: THEOCHEM*, vol. 727, no. 1, p. 127, 2005.

[59] H. J. Bohorquez, *Local Quantum Chemistry.* PhD thesis, Dalhousie University, 2012.

[60] C. Gatti, “Chemical bonding in crystals: new directions,” *Zeitschrift für Kristallographie*, vol. 220, no. 5/6/2005, p. 399, 2005.

[61] H. L. Schmider and A. D. Becke, “Two functions of the density matrix and their relation to the chemical bond,” *The Journal of chemical physics*, vol. 116, no. 8, p. 3184, 2002.

[62] T. Schmidt, E. Kraisler, L. Kronik, and S. Kümmel, “One-electron self-interaction and the asymptotics of the kohn–sham potential: an impaired relation,” *Physical Chemistry Chemical Physics*, vol. 16, no. 28, pp. 14357–14367, 2014.

[63] A. Nagy and N. March, "Ratio of density gradient to electron density as a local wavenumber to characterize the ground state of spherical atoms," *Molecular Physics*, vol. 90, no. 2, pp. 271–276, 1997.

[64] M. Kohout, A. Savin, and H. Preuss, "Contribution to the electron distribution analysis. i. shell structure of atoms," *The Journal of chemical physics*, vol. 95, no. 3, pp. 1928–1942, 1991.

[65] A. Nagy and S. Liu, "Local wave-vector, shannon and fisher information," *Physics Letters A*, vol. 372, no. 10, pp. 1654–1656, 2008.

[66] P. De Silva and C. Corminboeuf, "Simultaneous visualization of covalent and noncovalent interactions using regions of density overlap," *Journal of chemical theory and computation*, vol. 10, no. 9, pp. 3745–3756, 2014.

[67] R. A. Boto, J.-P. Piquemal, and J. Contreras-García, "Revealing strong interactions with the reduced density gradient: a benchmark for covalent, ionic and charge-shift bonds," *Theoretical Chemistry Accounts*, vol. 136, no. 12, p. 139, 2017.

[68] R. P. Sagar, A. C. Ku, and V. H. Jr, "An examination of the shell structure of atoms and ions as revealed by the one-electron potential," *Canadian journal of chemistry*, vol. 66, no. 4, p. 1005, 1988.

[69] M. Kohout, "On the relationship between the one-electron and bohm's quantum potential," *International journal of quantum chemistry*, vol. 87, no. 1, pp. 12–14, 2002.

[70] R. F. Bader and M. E. Stephens, "Spatial localization of the electronic pair and number distributions in molecules," *Journal of the American Chemical Society*, vol. 97, no. 26, pp. 7391–7399, 1975.

[71] P. Ziesche, "Attempts toward a pair density functional theory," *International journal of quantum chemistry*, vol. 60, no. 7, pp. 1361–1374, 1996.

[72] E. Francisco, A. M. Pendás, M. García-Revilla, and R. Á. Boto, "A hierarchy of chemical bonding indices in real space from reduced density matrices and cumulants," *Computational and Theoretical Chemistry*, vol. 1003, pp. 71–78, 2013.

[73] M. Menéndez, R. Álvarez Boto, E. Francisco, and Á. Martín Pendás, "One-electron images in real space: Natural adaptive orbitals," *Journal of computational chemistry*, vol. 36, no. 11, pp. 833–843, 2015.

[74] E. R. Johnson, S. Keinan, P. Mori-Sanchez, J. Contreras-Garcia, A. J. Cohen, and W. Yang, "Revealing noncovalent interactions," *Journal of the American Chemical Society*, vol. 132, no. 18, p. 6498, 2010.

[75] J. Contreras-García, E. R. Johnson, S. Keinan, R. Chaudret, J.-P. Piquemal, D. N. Beratan, and W. Yang, "Nciplot: a program for plotting noncovalent interaction regions," *Journal of chemical theory and computation*, vol. 7, no. 3, pp. 625–632, 2011.

[76] J. Contreras-García, W. Yang, and E. R. Johnson, "Analysis of hydrogen-bond interaction potentials from the electron density: integration of noncovalent interaction regions," *The Journal of Physical Chemistry A*, vol. 115, no. 45, p. 12983, 2011.

[77] E. W. Pearson and R. G. Gordon, "Local asymptotic gradient corrections to the energy functional of an electron gas," *The Journal of Chemical Physics*, vol. 82, no. 2, p. 881, 1985.

[78] A. Zupan, K. Burke, M. Ernzerhof, and J. P. Perdew, “Distributions and averages of electron density parameters: Explaining the effects of gradient corrections,” *Journal of Chemical Physics*, vol. 106, no. 24, p. 10184, 1997.

[79] V. Tognetti, P. Cortona, and C. Adamo, “A new parameter-free correlation functional based on an average atomic reduced density gradient analysis,” *The Journal of chemical physics*, vol. 128, no. 3, p. 034101, 2008.

[80] S. Voronin, G. Ozkaya, and D. Yoshida, “Convolution based smooth approximations to the absolute value function with application to non-smooth regularization,” *arXiv preprint arXiv:1408.6795*, 2014.

[81] R. F. Bader, “A bond path: a universal indicator of bonded interactions,” *The Journal of Physical Chemistry A*, vol. 102, no. 37, pp. 7314–7323, 1998.

[82] T. Keith, R. Bader, and Y. Aray, “Structural homeomorphism between the electron density and the virial field,” *International journal of quantum chemistry*, vol. 57, no. 2, pp. 183–198, 1996.

[83] S. Liu, “Steric effect: A quantitative description from density functional theory,” *The Journal of chemical physics*, vol. 126, no. 24, p. 244103, 2007.

[84] M. A. Marques, N. T. Maitra, F. M. Nogueira, E. K. Gross, and A. Rubio, *Fundamentals of time-dependent density functional theory*, vol. 837. Springer Science & Business Media, 2012.

[85] M. Alonso, T. Woller, F. J. Martín-Martínez, J. Contreras-García, P. Geerlings, and F. De Proft, “Understanding the fundamental role of π/π, σ/σ, and σ/π dispersion interactions in shaping carbon-based materials,” *Chemistry-A European Journal*, vol. 20, no. 17, p. 4931, 2014.

[86] G. Saleh, C. Gatti, and L. L. Presti, “Energetics of non-covalent interactions from electron and energy density distributions,” *Computational and Theoretical Chemistry*, vol. 1053, p. 53, 2015.

[87] J. R. Lane, J. Contreras-García, J.-P. Piquemal, B. J. Miller, and H. G. Kjaergaard, “Are bond critical points really critical for hydrogen bonding?,” *Journal of Chemical Theory and Computation*, vol. 9, no. 8, p. 3263, 2013.

[88] M. J. Frisch, G. W. Trucks, H. B. Schlegel, G. E. Scuseria, M. A. Robb, J. R. Cheeseman, G. Scalmani, V. Barone, B. Mennucci, G. A. Petersson, H. Nakatsuji, M. Caricato, X. Li, H. P. Hratchian, A. F. Izmaylov, J. Bloino, G. Zheng, J. L. Sonnenberg, M. Hada, M. Ehara, K. Toyota, R. Fukuda, J. Hasegawa, M. Ishida, T. Nakajima, Y. Honda, O. Kitao, H. Nakai, T. Vreven, J. A. Montgomery, Jr., J. E. Peralta, F. Ogliaro, M. Bearpark, J. J. Heyd, E. Brothers, K. N. Kudin, V. N. Staroverov, R. Kobayashi, J. Normand, K. Raghavachari, A. Rendell, J. C. Burant, S. S. Iyengar, J. Tomasi, M. Cossi, N. Rega, J. M. Millam, M. Klene, J. E. Knox, J. B. Cross, V. Bakken, C. Adamo, J. Jaramillo, R. Gomperts, R. E. Stratmann, O. Yazyev, A. J. Austin, R. Cammi, C. Pomelli, J. W. Ochterski, R. L. Martin, K. Morokuma, V. G. Zakrzewski, G. A. Voth, P. Salvador, J. J. Dannenberg, S. Dapprich, A. D. Daniels, Farkas, J. B. Foresman, J. V. Ortiz, J. Cioslowski, and D. J. Fox, “Gaussian09 Revision E.01.” Gaussian Inc. Wallingford CT 2009.

[89] J. Ahrens, B. Geverci, and L. Charles, “Paraview: An end-user tool for large data visualization, visualization handbook,” 2005.

[90] W. Humphrey, A. Dalke, and K. Schulten, "VMD – Visual Molecular Dynamics," *Journal of Molecular Graphics*, vol. 14, p. 33, 1996.

[91] S. Shaik, D. Danovich, B. Silvi, D. L. Lauvergnat, and P. C. Hiberty, "Charge-shift bonding a class of electron-pair bonds that emerges from valence bond theory and is supported by the electron localization function approach," *Chemistry-A European Journal*, vol. 11, no. 21, p. 6358, 2005.

[92] L. Pauling, *General Chemistry.* Dover Publications, Inc., 1947.

[93] G. R. Desiraju, "A bond by any other name," *Angewandte Chemie International Edition in English*, vol. 50, no. 1, pp. 52–59, 2011.

[94] P. Metrangolo and G. Resnati, "Halogen bonding: a paradigm in supramolecular chemistry," *Chemistry–A European Journal*, vol. 7, no. 12, pp. 2511–2519, 2001.

[95] J. S. Murray, L. Pat, and P. Politzer, "A predicted new type of directional noncovalent interaction," *International Journal of Quantum Chemistry*, vol. 107, no. 12, pp. 2286–2292, 2007.

[96] S. Scheiner, "A new noncovalent force: Comparison of p $\cdots$ n interaction with hydrogen an halogen bonds," *The Journal of Chemical Physics*, vol. 134, no. 9, p. 094315, 2011.

[97] S. Scheiner, "The pnicogen bond: Its relation to hydrogen, halogen, and other noncovalent bonds," *ACCOUNTS of chemical research*, vol. 46, no. 2, pp. 280–288, 2012.

[98] D. Mani and E. Arunan, "The x–cy (x= o/f, y= o/s/f/cl/br/n/p)'carbon bond'and hydrophobic interactions," *Physical Chemistry Chemical Physics*, vol. 15, no. 34, pp. 14377–14383, 2013.

[99] S. C. Kui, N. Zhu, and M. C. Chan, "Observation of intramolecular c h f c contacts in non-metallocene polyolefin catalysts: Model for weak attractive interactions between polymer chain and noninnocent ligand," *Angewandte Chemie International Edition*, vol. 42, no. 14, pp. 1628–1632, 2003.

[100] J. S. Murray, P. Lane, T. Clark, K. E. Riley, and P. Politzer, "$\sigma - holes$,π-holes and electrostatically-driven interactions," *Journal of Molecular Modeling*, vol. 18, pp. 541–548, 2012.

[101] E. M. Duffy, P. J. Kowalczyk, and W. L. Jorgensen, "Do denaturants interact with aromatic hydrocarbons in water?," *Journal of the American Chemical Society*, vol. 115, no. 20, pp. 9271–9275, 1993.

[102] S. F. Boys and F. d. Bernardi, "The calculation of small molecular interactions by the differences of separate total energies. some procedures with reduced errors," *Molecular Physics*, vol. 19, no. 4, pp. 553–566, 1970.

[103] E. R. Johnson and A. D. Becke, "A post-hartree–fock model of intermolecular interactions," *The Journal of chemical physics*, vol. 123, no. 2, p. 024101, 2005.

[104] S. Grimme, J. Antony, S. Ehrlich, and H. Krieg, "A consistent and accurate ab initio parametrization of density functional dispersion correction (dft-d) for the 94 elements h-pu," *The Journal of chemical physics*, vol. 132, no. 15, p. 154104, 2010.

[105] S. Grimme, S. Ehrlich, and L. Goerigk, "Effect of the damping function in dispersion corrected density functional theory," *Journal of computational chemistry*, vol. 32, no. 7, pp. 1456–1465, 2011.

[106] P. Politzer and J. S. Murray, "Halogen bonding: An interim discussion," *A European Journal of Chemical Physics and Physical Chemistry*, vol. 14, no. 2, pp. 278–294, 2013.

[107] C. Salzemann and C. Petit, "Influence of hydrogen on the morphology of platinum and palladium nanocrystals," *Langmuir*, vol. 28, no. 10, pp. 4835–4841, 2012.

[108] N. Aguilera-Porta, M. Calatayud, C. Salzemann, and C. Petit, "Understanding how in situ generated hydrogen controls the morphology of platinum nanoparticles," *The Journal of Physical Chemistry C*, vol. 118, no. 17, pp. 9290–9298, 2014.

[109] Y. Zhang and W. Yang, "Comment on "generalized gradient approximation made simple"," *Physical Review Letters*, vol. 80, no. 4, p. 890, 1998.

[110] G. Kresse and J. Hafner, "Ab initio molecular-dynamics simulation of the liquid-metal–amorphous-semiconductor transition in germanium," *Physical Review B*, vol. 49, no. 20, p. 14251, 1994.

[111] G. Kresse and J. Hafner, "Ab initio molecular dynamics for liquid metals," *Physical Review B*, vol. 47, no. 1, p. 558, 1993.

[112] P. E. Blöchl, "Projector augmented-wave method," *Physical Review B*, vol. 50, no. 24, p. 17953, 1994.

[113] G. Kresse and D. Joubert, "From ultrasoft pseudopotentials to the projector augmented-wave method," *Physical Review B*, vol. 59, no. 3, p. 1758, 1999.

[114] G. Mercurio, E. R. McNellis, I. Martin, S. Hagen, F. Leyssner, S. Soubatch, J. Meyer, M. Wolf, P. Tegeder, F. S. Tautz, *et al.*, "Structure and energetics of azobenzene on ag (111): benchmarking semiempirical dispersion correction approaches," *Physical review letters*, vol. 104, no. 3, p. 036102, 2010.

[115] A. Otero-de-la Roza, M. Blanco, A. M. Pendás, and V. Luaña, "Critic: a new program for the topological analysis of solid-state electron densities," *Computer Physics Communications*, vol. 180, no. 1, pp. 157–166, 2009.

[116] R. A. Boto, J. Contreras-García, and M. Calatayud, "The role of dispersion forces in metal-supported self-assembled monolayers," *Computational and Theoretical Chemistry*, vol. 1053, pp. 322–327, 2015.

[117] J. Cioslowski, S. T. Mixon, and W. D. Edwards, "Weak bonds in the topological theory of atoms in molecules," *Journal of the American chemical society*, vol. 113, no. 4, pp. 1083–1085, 1991.

[118] J. Cioslowski and S. T. Mixon, "Topological properties of electron density in search of steric interactions in molecules: electronic structure calculations on ortho-substituted biphenyls," *Journal of the American Chemical Society*, vol. 114, no. 11, pp. 4382–4387, 1992.

[119] J. Poater, M. Solà, and F. M. Bickelhaupt, "Hydrogen–hydrogen bonding in planar biphenyl, predicted by atoms-in-molecules theory, does not exist," *Chemistry–A European Journal*, vol. 12, no. 10, pp. 2889–2895, 2006.

[120] J. D. Dunitz and A. Gavezzotti, “Molecular recognition in organic crystals: directed intermolecular bonds or nonlocalized bonding?,” *Angewandte Chemie International Edition*, vol. 44, no. 12, pp. 1766–1787, 2005.

[121] C. F. Matta, J. Hernández-Trujillo, T.-H. Tang, and R. F. Bader, “Hydrogen–hydrogen bonding: a stabilizing interaction in molecules and crystals,” *Chemistry–A European Journal*, vol. 9, no. 9, pp. 1940–1951, 2003.

[122] A. Vargas-Caamal, S. Pan, F. Ortiz-Chi, J. L. Cabellos, R. A. Boto, J. Contreras-Garcia, A. Restrepo, P. K. Chattaraj, and G. Merino, “How strong are the metallocene–metallocene interactions? cases of ferrocene, ruthenocene, and osmocene,” *Physical Chemistry Chemical Physics*, vol. 18, no. 1, pp. 550–556, 2016.

[123] R. B. Woodward and R. Hoffmann, “The conservation of orbital symmetry,” *Angewandte Chemie International Edition in English*, vol. 8, no. 11, pp. 781–853, 1969.

[124] E. Matito, J. Poater, M. Duran, and M. Solà, “Electron fluctuation in pericyclic and pseudopericyclic reactions,” *ChemPhysChem*, vol. 7, no. 1, pp. 111–113, 2006.

[125] K. N. Houk, Y. Li, and J. D. Evanseck, “Transition structures of hydrocarbon pericyclic reactions,” *Angewandte Chemie International Edition in English*, vol. 31, no. 6, pp. 682–708, 1992.

[126] W. Kirmse, N. G. Rondan, and K. Houk, “Stereoselective substituent effects on conrotatory electrocyclic reactions of cyclobutenes,” *Journal of the American Chemical Society*, vol. 106, no. 25, pp. 7989–7991, 1984.

[127] N. G. Rondan and K. Houk, “Theory of stereoselection in conrotatory electrocyclic reactions of substituted cyclobutenes,” *Journal of the American Chemical Society*, vol. 107, no. 7, pp. 2099–2111, 1985.

[128] M. J. Dewar, “A critique of frontier orbital theory,” *Journal of Molecular Structure: THEOCHEM*, vol. 200, pp. 301–323, 1989.

[129] R. Ponec, G. Yuzhakov, and J. Pecka, “Similarity approach to chemical reactivity. torquoselectivity in pericyclic reactions,” *Journal of Mathematical Chemistry*, vol. 20, no. 2, pp. 301–310, 1996.

[130] S. Bahmanyar and K. Houk, “Transition states of amine-catalyzed aldol reactions involving enamine intermediates: theoretical studies of mechanism, reactivity, and stereoselectivity,” *Journal of the American Chemical Society*, vol. 123, no. 45, pp. 11273–11283, 2001.

[131] S. Bahmanyar and K. Houk, “The origin of stereoselectivity in proline-catalyzed intramolecular aldol reactions,” *Journal of the American Chemical Society*, vol. 123, no. 51, pp. 12911–12912, 2001.

[132] S. Bahmanyar, K. Houk, H. J. Martin, and B. List, “Quantum mechanical predictions of the stereoselectivities of proline-catalyzed asymmetric intermolecular aldol reactions,” *Journal of the American Chemical Society*, vol. 125, no. 9, pp. 2475–2479, 2003.

[133] S. Bahmanyar and K. Houk, “Origins of opposite absolute stereoselectivities in proline-catalyzed direct mannich and aldol reactions,” *Organic letters*, vol. 5, no. 8, pp. 1249–1251, 2003.

[134] L. Hoang, S. Bahmanyar, K. Houk, and B. List, "Kinetic and stereochemical evidence for the involvement of only one proline molecule in the transition states of proline-catalyzed intra-and intermolecular aldol reactions," *Journal of the American Chemical Society*, vol. 125, no. 1, pp. 16–17, 2003.

[135] A. Armstrong, R. A. Boto, P. Dingwall, J. Contreras-García, M. J. Harvey, N. J. Mason, and H. S. Rzepa, "The houk–list transition states for organocatalytic mechanisms revisited," *Chemical Science*, vol. 5, no. 5, pp. 2057–2071, 2014.

[136] H. Carr, Z. Geng, J. Tierny, A. Chattopadhyay, and A. Knoll, "Fiber surfaces: Generalizing isosurfaces to bivariate data," *Computer Graphics Forum*, vol. 34, no. 3, p. 241, 2015.

[137] D. Gunther, R. A. Boto, J. Contreras-Garcia, J.-P. Piquemal, and J. Tierny, "Characterizing molecular interactions in chemical systems," *Visualization and Computer Graphics, IEEE Transactions on*, vol. 20, no. 12, pp. 2476–2485, 2014.

[138] P. L. Popelier, "Quantum chemical topology: on bonds and potentials," pp. 1–56, 2005.